UNIVERSITAT POLITÈCNICA DE VALÈNCIA

Departamento de Máquinas y Motores Térmicos

DOCTORAL THESIS:

"On the analysis and design of series hybrid distributed electric propulsion with boundary layer ingestion of remotely piloted aircraft"

Presented by: D. PAU VARELA MARTÍNEZ
Supervised by: DR. D. LUIS MIGUEL GARCÍA-CUEVAS GONZÁLEZ

in fulfillement of the requisites for the degree of

Doctor of Philosophy

Valencia, February 2023

PhD. Thesis

“On the analysis and design of series hybrid distributed electric propulsion with boundary layer ingestion of remotely piloted aircraft”

AUTHORS

Presented by: D. Pau Varela Martínez
Supervised by: Dr. D. Luis Miguel García-Cuevas González

DEFENSE COMMITTEE

Chairman: Dr. D. Jaime Alberto Broatch Jacobi
Secretary: Dr. D. Sebastián Franchini Longhi
Member: Dr. D. Murat Bronz

Valencia, February 2023

On the analysis and design of series hybrid distributed electric propulsion with boundary layer ingestion of remotely piloted aircraft

Pau Varela Martínez

Abstract

The present work explores possible solutions to two correlated events that could compromise our future to some extent.

On the one hand, the growth of the fleet of small aircraft in the coming years, whether manned or not, is a reality. Access to these aircraft by an increasing majority of the public grows year after year and at the same time, manufacturers adapt their aircraft to missions that we could not contemplate a few years ago.

On the other hand, and unfortunately, climate change is also a reality that compromises not only our future but also our present. Today the climate alert is and must be elevated. If we do not find solutions that help alleviate this problem, life on the planet could irremediably change for the worse.

Both facts are implicitly related. The manufacture and operation of vehicles contribute significantly to increasing the carbon footprint, so the increase in the fleet in the coming years may have an extremely negative impact on global polluting and greenhouse gas emissions. That is why official organizations and scientific and technological development sectors promote research for possible solutions.

This work tries to do its bit to minimize this common problem. Multiple technologies are proposed to reduce the fuel required by 25kg aircraft at takeoff and, thus, reduce the emissions associated with their operation.

The applied technologies are electric series hybridization, distributed electric propulsion, and boundary layer ingestion. Separately, these technologies have shown multiple advantages, especially in terms of improving aircraft propulsion and aerodynamics, which directly affects fuel consumption. Nevertheless, this work proposes the simultaneous use of all of them to reduce fuel consumption further and, therefore, polluting and greenhouse gas emissions. To do this, after these pages, the main parameters of this aircraft are chosen and accompanied by an exhaustive analysis of the fluid dynamic behavior. With an understanding of its behavior, it is possible to optimize its components' selection so that significant fuel consumption improvements are obtained. This fuel saving is shown in comparison with similar aircraft in size and weight, but that does not include these technologies, achieving a saving of 16 % of fuel weight for the same range.

This work's conduction focuses on employing computational tools mainly based on computational fluid dynamics (CFD). This primary tool will be complemented by the use of modal decomposition to carry out the analyses, and the creation of a database that will help create quick models useful in future conceptual and preliminary designs of this type of aircraft.

Resumen

En el presente trabajo se explora posibles soluciones a dos hechos correlacionados que podrían comprometer hasta cierto punto nuestro futuro.

Por un lado, el crecimiento de la flota de aeronaves pequeñas en los próximos años, ya sean tripuladas o no, es una realidad. El acceso a estas aeronaves por parte de un público cada vez más mayoritario crece año a año y, al mismo tiempo, los fabricantes adaptan sus aeronaves a misiones que hace unos años no éramos capaces de contemplar.

Por otro lado, y por desgracia, el cambio climático también es una realidad que no solo compromete nuestro futuro, sino también nuestro presente. Hoy en día la alerta climática es y debe ser elevada, y si no encontramos soluciones que ayuden a paliar este problema, la vida en el planeta podría cambiar irremediablemente para peor.

Ambos hechos se encuentran implícitamente relacionados. La fabricación y operación de vehículos contribuye notablemente a aumentar la huella de carbono. Por lo tanto, el aumento de flota en los próximos años puede tener un impacto notablemente negativo en las emisiones contaminantes y gases de efecto invernadero globales. Es por ello por lo que organismos oficiales y sectores de desarrollo científico y tecnológico impulsan la investigación de posibles soluciones.

Este trabajo intenta poner su grano de arena para minimizar este problema común. Se propone la utilización de múltiples tecnologías con el objetivo de disminuir el combustible requerido por aeronaves de 25kg al despegue, y de esta forma, disminuir las emisiones asociadas a su operación.

Las tecnologías aplicadas son la hibridación eléctrica en serie, la propulsión eléctrica distribuida y la ingestión de capa límite. Por separado, estas tecnologías han demostrado múltiples ventajas, especialmente en términos de mejora propulsiva y aerodinámica de las aeronaves, lo que repercute directamente en el consumo de combustible. Sin embargo, este trabajo propone la utilización simultánea de todas ellas con el objetivo de disminuir aún más el consumo de combustible y, por tanto, las emisiones contaminantes y gases de efecto invernadero. Para ello, tras estas páginas se eligen los parámetros principales de esta aeronave y se acompaña de un exhaustivo análisis del comportamiento fluidodinámico. Con la comprensión de su comportamiento, es posible optimizar la selección de sus componentes, de forma que se obtienen mejoras importantes en el consumo de combustible. Este ahorro de combustible se muestra en comparación con aeronaves similares en tamaño y peso, pero que no incluyen estas tecnologías, logrando para un mismo alcance un ahorro del 16 % del peso del combustible.

La realización de este trabajo se centra en el empleo de herramientas computacionales apoyándose sobre todo en la dinámica de fluidos computacional (CFD). Esta herramienta principal se verá complementada con el uso de descomposición modal para realizar los análisis y de la creación

de una base de datos que ayude a crear modelos rápidos útiles en futuros diseños preliminares y conceptuales de aeronaves de este tipo.

Resum

En aquest treball s'exploren possibles solucions a dos fets correlacionats que podrien comprometre d'alguna manera el nostre futur.

Per un costat, el creixement de la flota d'aeronaus de xicoteta dimensió en el futur, tant tripulades com no tripulades, és una realitat. L'accés a aquestes aeronaus per part d'un públic cada cop més majoritari creix any rere any i, al mateix temps, els fabricants adapten les aeronaus a feines que anys enrere no eren capaços d'assolir.

Per l'altre costat, malauradament, el canvi climàtic és un fet que compromet tant el nostre futur com el nostre present. Hui en dia l'alerta climàtica és elevada i, si no trobem solucions per a pal·liar aquest problema la vida al nostre planeta, podria canviar irremeiablement a pitjor.

Ambdós fets es troben implícitament relacionats. La fabricació i l'operació de vehicles contribueix notablement a augmentar l'empremta de carboni. Per tant, l'increment de flota en els pròxims anys pot tindre un efecte negatiu molt notable en les emissions contaminants i gasos d'efecte hivernacle globals. És per això que organismes oficials i sectors de desenvolupament científic i tecnològic impulsen la investigació de possibles solucions.

Aquest treball intenta aportar el seu granet de sorra per minimitzar aquest problema comú. Es proposa la utilització de múltiples tecnologies amb l'objectiu de reduir el combustible emprat per aeronaus de fins a 25kg i, per tant, disminuir les emissions associades a la seua operació.

Les tecnologies aplicades són la hibridació elèctrica en sèrie, la propulsió elèctrica distribuïda i la ingestió de capa límit. Separadament, aquestes tecnologies han demostrat múltiples avantatges, especialment en termes de millora propulsiva i aerodinàmica de les aeronaus, repercutint directament en el consum de combustible. No obstant, aquest treball proposa la utilització simultània de totes elles amb l'objectiu de reduir encara més el consum de combustible i, per tant, les emissions contaminants i gasos d'efecte hivernacle. Per fer-ho, en les darreres pàgines es trien els paràmetres principals de l'aeronau i s'acompanyen d'una exhaustiva anàlisi del comportament de la dinàmica de fluids. Comprenent el seu comportament, és possible optimitzar la selecció dels seus components, de manera que s'obtenen millores importants en el consum de combustible. L'estalvi de combustible es mostra en comparació amb aeronaus similars en mida i pes, però que no inclouen aquestes tecnologies, aconseguint per a un mínim abast un estalvi del 16 % del pes del combustible.

La realització d'aquest treball es centra en l'ús d'eines computacionals recolzant-se sobretot en la dinàmica de fluids computacional (CFD). Aquesta eina principal es veurà complementada amb l'ús de descomposició modal per a elaborar les anàlisis i de la creació d'una base de dades que ajude a crear models ràpids i útils en futurs dissenys conceptuals i preliminars d'aeronaus d'aquest tipus.

List of publications

The papers presented here are the basis of this thesis:

- "Optimisation of the flight speed in a hybrid RPAS with distributed electric propulsion and boundary layer ingestion", in *1st INGENIADRON conference* (2021) by García-Cuevas, Quintero, Bares and Varela [1].
- "Computational Study of the Propeller Position Effects in Wing-Mounted, Distributed Electric Propulsion with Boundary Layer Ingestion in a 25 kg Remotely Piloted Aircraft", in *Drones* (2021) by Serrano, Tiseira, García-Cuevas and Varela [2].
- "Series-hybridisation, distributed electric propulsion and boundary layer ingestion in long-endurance, small remotely piloted aircraft: Fuel consumption improvements", in *Aerospace Science and Technology* (2022) by Tiseira, García-Cuevas, Quintero and Varela [3].
- "Propeller position effects over the pressure and friction coefficients over the wing of an UAV with distributed electric propulsion: a Proper Orthogonal Decomposition analysis", in *Drones* (2022) by Serrano, García-Cuevas, Bares and Varela [4].

Division of work between authors

The mentioned publications have been done in cooperation with additional researchers from CMT – Motores Térmicos. The author signatures of these publications are in order of seniority. The respondent carried out all the CFD simulations and the corresponding post-process, analysis, and data curation as described in the document. The results discussions were performed in collaboration with Prof. García-Cuevas, his supervisor. All the co-authors helped in the editing and final results discussion.

Funding acknowledgements

The respondent would like to acknowledge the financial support received through contract FPI-UPV PREDOCFD/19 of Subprograma 2 of Universitat Politècnica de València.

Acknowledgements

Me voy a tomar la libertad de escribir esta página en castellano, ya que, en el plano de las emociones, me expreso (un poco) mejor en mi lengua de origen. Cuando echo la vista atrás veo a tantísima gente que me ha apoyado que esta sección podría alargarse casi infinitamente, y como no queremos quitarle protagonismo a las aeronaves híbridas en serie con propulsión eléctrica distribuida e ingestión de capa límite, intentaré acotarlo todo lo que pueda.

En primer lugar, me gustaría agradecer este trabajo a mi tutor Luis Miguel García-Cuevas por su paciencia sin límite y por depositar su confianza en mí a la hora de enfrascarnos en este proyecto. Ya te lo dije una vez, pero eres un verdadero ejemplo a seguir.

Por supuesto, este trabajo hubiera sido imposible sin el CMT y la Universitat Politècnica de València. Dentro de este grupo me gustaría destacar la labor del equipo técnico, en especial de Valentín Ucedo, Vicente Esteve "Vicentón" y Adolfo Guzmán "Fito" por sacarme las castañas del fuego, y de secretaría, ya que sin Amparo Cutillas la burocracia nos hubiera engullido a todos en algún momento. Gracias también al autodenominado tutor en la sombra Andrés Tiseira por ser una mano amiga desde que entré en la carrera (y por venderme tan bien a Luismi), y a todos los doctores y profesores que me han aconsejado durante estos años, especialmente a su compañero de despacho Vicente Dolz.

Debo decir que sin todos los que habéis estado a mi alrededor en el despacho, el trabajo hubiera sido mucho más aburrido. Gracias al sector Colombia formado por Fabio, Juancho y Miguel Ángel, a Miguel, Guille y Natalia, y muy especialmente a Alberto, por aguantarme en el trabajo y en casa, y enseñarme a tomar buenas decisiones, y a Nicolás, al que más allá de su amistad, debería darle crédito en todos mis papers por ayudarme a sacarlos adelante. Muchas gracias también a los miembros del "pseudo despacho", Alejandro, Borja, David, Alicia y sobre todo a Lucas, por acogerme y hacerme reír en cualquier circunstancia.

No puedo olvidarme de mis amigos de Alicante, gente maravillosa con la que evadirte del trabajo, en especial a Andrés, que lleva distrayéndome desde los dos años, y a Marco, Vicente, Pala y Alberto. Gracias por ser fans incondicionales de todo lo que he escrito.

Hubiera sido muy difícil completar esta etapa de mi vida sin el apoyo y amor total y absoluto de mi familia. Gracias a mis padres, tíos, abuelos y a mi hermano Joan por hacer esto posible y por seguir igual de curiosos.

Por último y más importante, gracias a Nerea, llegaste a mi vida a la mitad de este sendero para quedarte y te has convertido en la pieza clave para terminarlo. Ten claro que, sin ti, esto no hubiera sido posible. Te quiero muchísimo.

"All tradition must be questioned"

Contents

List of Figures

List of Tables

Nomenclature

Abbreviations

1D	One-dimensional
2D	Bi-dimensional
3D	Three-dimensional
AC	Alternating current
BCG	Boston Consulting Group
BEMT	Blade Element Model Theory
BLI	Boundary layer ingestion
BSFC	Brake-specific fuel consumption
BWB	Blended Wing Body
CFD	Computational fluid dynamics
CFL	Courant–Friedrichs–Lewy
CO_2	Carbon dioxide
CO	Carbon oxide
DC	Direct current
DEP	Distributed electrical propulsion
DJBW	Distributed jet blowing wing
DNS	Direct numerical simulation
EASA	European Union Aviation Safety Agency
EM	Extra mass
ERA	Environmentally Responsible Aviation
ESC	Electronic speed controller
FDS	Flux-difference splitting scheme
FM	Initial fuel mass
FR	Fuel reduction mass
GCI	Grid convergence index
ICE	Internal combustion engines
ITDS	Information Technology Development Solutions
LES	Large eddy simulation
LHS	Latin hypercube sampling
LSB	Laminar separation bubble
MIT	Massachusetts Institute of Technology
MSE	Mean squared error
MTOM	Maximum take-off mass

NASA National Aeronautics and Space Administration

NO_x Nitrogen oxides

OEM Operative empty mass

OEW Operative empty weight

PID Proportional-integral-derivative

PIV Particle image velocimetry

PL Payload mass

POD Proper Orthogonal Decomposition

RANS Reynolds-averaged Navier-Stokes

RF Fuel reserve mass

SESAR Single European Sky ATM Research

SST Shear stress transport

TKE Total fluctuating kinetic energy

UAV Unmanned aerial vehicle

UIUC University of Illinois Urbana-Champaign

URANS Unsteady Reynolds-averaged Navier-Stokes

VFM Variable fidelity model

Greek Symbols

α Angle of attack

β Specific range

η Efficiency

γ Draft angle

λ Eigenvalue, tunning lasso parameter

Λ Eigenvalues matrix

μ Dynamic viscosity

ϕ Eigenvector

Φ Eigenvector matrix

ρ Air Density

τ Torque

ξ Rate of change of the velocity with the aircraft mass

Roman symbols

A Area

a Configuration coefficient

$\mathbf{A}$ Configuration coefficient matrix

AR Aspect ratio

b Wingsapn

C Coefficient

c Airfoil chord length

$\mathbf{C}$ Covariance matrix

D Drag

d Diameter

E Energy

e Oswald efficiency factor

f Mass fraction

g Gravity acceleration

h	Relative height
J	Advance ratio
L	Lift
$\dot{m}$	Mass flow
M	Mass
m	Mass
Ma	Mach number
n	Number of engines, rotational speed
P	Power
R	Range
r	Radius
Re	Reynolds number
u	Sound velocity at sea level, vector field
S	Wing surface
T	Thrust
t	Time
U	Velocity, axial velocity
$\mathbf{U}$	Dataset matrix
V	Velocity, vertical velocity
W	Weight
x	Distance between shafts

Subscripts and superscripts

0	Inlet, undisturbed upstream, initial
$0,1,\ldots$	Coefficient number
1	Final
∞	Undisturbed upstream
airfoil	Relative to the airfoil
avg	Average
baseline	Baseline
BL	Boundary Layer
BLI	Boundary Layer Ingestion
D	Drag
D0	Parasitic drag
e	Electric
EM	Extra mass
extra	Relative to the aircraft component without the wing
f	Friction
FM	Initial fuel mass
FR	Fuel reduction mass
hybrid	Hybrid
i	Induced
j	Trefftz plane
L	Lift
m	Mechanic
modes	Relative to the POD
OEM	Operative empty mass
P	Power
p	Propulsive, pressure
PL	Payload mass

pressure side Pressure side

prop Propeller

props Propellers

RF Fuel reserve mass

s Sound

suction side Suction side

T Thrust

tot Total

w,wake Wake

wing Relative to the wing

CHAPTER 1

Introduction

Contents

1.1 Background and Motivation

In past years, the use and commercialization of small civil aircraft listed as Remotely Piloted Aircraft Systems (RPAS), Unmanned Aerial Vehicles (UAV), or merely "drones" have exponentially grown. This information is collected in multiple studies centered on Europe, highlighting the "Study on the societal acceptance of Urban Air Mobility in Europe" developed by the European Union Aviation Safety Agency (EASA) [5], the "European drones outlook study" carried out by the Single European Sky ATM Research (SESAR) [6], and the study of the Boston Consulting Group (BCG) which also expands the analysis to the Unite States of America [7]. In these documents, it is predicted that the small aircraft civil fleet will reach hundreds of thousands of units in the following years, which leads to new concerns. As the fleet size increases, the research on more efficient aircraft through its aerodynamic and power plant design and optimization becomes necessary, reducing the fuel consumed and the derivated pollutant and greenhouse gas emissions. This need for more efficient and environmentally-friendly aircraft is collected in the Environmentally Responsible Aviation (ERA) projected by the National Aeronautics and Space Administration (NASA) as a possible solution inside the Technology Development Solutions (ITDS) [8]. Following the necessity to design more efficient small aircraft, novel configurations have emerged, as can be seen in the work of Rostami et al. [9], in which the UAV performance is improved thanks to the design and interaction of tandem ducted propellers, or the results of Zhang et al. [10] showing a power plant improvement through the optimization of the propulsion in a quadrotor fixed-wing hybrid UAV.

The project of Zhang et al. is encompassed in the electric hybridization (HE) technology trend. Full-electric battery power plants remain one of the popular choices in small aircraft design, thanks to their ease of implementation and control, along with low maintenance cost. Of course, batteries reduce direct point of use pollutant and greenhouse gas emissions compared with a traditional fuel-based powertrain, removing combustion from the equation. However, as described by McKinney in his thesis [11], battery-based power plants have a low energy density and specific energy compared to fuel-based powertrain, not making them suitable for every mission.

The low energy density and specific energy of batteries compared to fuel-based powertrains leads to the research for alternatives. Internal combustion engines (ICE) are employed when heavy and faster aircraft are projected or in cases where the proposed mission seeks to optimize and extend the aircraft's range or endurance. ICE also has applications in very small RPAS with extreme thrust-to-weight ratios, as in competition or acrobatic aircraft, where the thrust needed outweighs the disadvantages of small ICEs. As described in the works of Fredericks et al. [12], Payri et al. [13] and Heywood [14], small ICEs suffer

from big thermal losses that impair engine performance.

It is true that combining the ICE with new technology advancements can mitigate pollutant emissions. Usually, the ICEs used in aircraft use spark-ignition, where the torque obtained is controlled by means of a throttle valve. This type of ICE has stoichiometric combustion, leading to high fuel consumption when a partial load is needed. Some novel approaches to overcome this problem are being developed; for example, burning in a controlled lean condition can control the output torque and at the same time maintain high efficiencies, thus reducing the emissions of unburnt hydrocarbons, CO and NOx, as suggested by the work of Benajes et al. [15]. Another solution studied by Nagasawa et al. [16] proposes piston water insulation to reduce heat transfer with high efficiencies and compression ratios. Nevertheless, these solutions come with a high weight penalty, limiting their application in aeronautics.

Considering the limitations of using only ICE as a propulsive plant, the electric hybridization technology has been extensively studied to combine the advantages of electric and combustion propulsion systems, as mentioned by McKinney [11]. On the one hand, the aircraft and range are increased thanks to the higher energy density and specific energy of the fuel, regarding the use of a purely electric propulsion plant. On the other hand (assuming perfect combustion), HE allows reducing the CO_2 emissions regarding the use of a traditional ICE propulsion plant.

The electric hybridization and its inclusion in UAVs and RPAS have been widely studied in recent years. To highlight some works, Harmon et al. [17] developed a conceptual design of small UAV using parallel HE propulsion, optimizing the selection of components and propulsion plant. Ausserer and Harmon [18] integrated and validated with experimental data a parallel HE optimization focused on optimizing the components, final weight and endurance of an aircraft projected in Hiserote's thesis [19]. On their behalf, Kim et al. [20] optimized the fuel economy of a parallel HE, finding strategies that can be used in power plant design to lower pollutant emissions. Most works focus on parallel hybridization, where both ICE and electric engine are connected to the propeller shaft. As Mengistu mentioned in his thesis [21], this HE configuration has some advantages, outlining that the ICE can be disconnected in cruise flight using it only to provide power in specific maneuvers. This way, fuel consumption and pollutant emissions decrease. At the same time, it is possible to reduce the acoustic footprint by flying in a pure-electric configuration, a major necessity in some surveillance and military missions. Although this has evident advantages, a series HE configuration can also be attractive. Lieh et al. [22] showed in their work this hybrid configuration, where the main advantage of this setting is that there is no mechanical coupling between the electric and the ICE engine, only electrical coupling. Without a battery, an ICE working at an almost optimum point feeds an electric generator during all the flight, not permitting a full-

electric flight, but the mechanical decoupling allows to configure of the power plant in a novel way that new advantages are obtained. One of these novel configurations is distributed electric propulsion (DEP).

In simple terms, DEP consists of distributing the total propulsion in more than one electric engine allocated along the wingspan. This solution has been studied for both conventional and small aircraft due to its optimization capabilities. Stoll et al. [23, 24] have researched this configuration numerically and experimentally, where various advantages have been proved, highlighting an improved aerodynamic efficiency thanks to better vorticity control and vectored thrust. Continuing the aerodynamic improvement research, Xen and Zhou [25] also demonstrate both computationally and experimentally that there is a margin to increase the lift-to-drag ratio through the correct design and integration of propulsion on the wing.

Additionally, the investigation of Ko [26] reports gains in propulsive efficiency by increasing the wing area swept by propellers. The benefits also include the reduction of noise footprint, as pointed out in the work of Moore and Ning [27], and Kirner et al. [28], and upgrades in wing structural stability from an aeroelastic point of view as the work of Amoozgar et al. [29] shows. as highlighted by Kim et al. [30] highlight in an extensive review various improvements, as better resilience in case of impact against foreign objects, or the utilization of the distributed propulsion as control platform reducing the size of aerodynamic actuators.

As Moore and Ning [27] also point out, the location of the distributed propulsion's electric engines directly impacts the aerodynamic and propulsion benefits. All the mentioned studies are focused on the distribution over the wing leading edge. However, a setting over the trailing edge can also unlock further benefits. As every propeller is set in the correct position behind the wing, a boundary layer ingestion (BLI) is produced.

BLI is based on the flow reacceleration around the wing and especially near the propulsion system. The reacceleration is produced by the ingestion of the boundary layer produced over a body by the engine or propulsion plant. As a great area of the propulsive system is swept by the boundary layer, the velocity of the intake air decreases; this way, less power is needed to produce the same amount of thrust. This idea was studied by Budziszewski and Friedrichs [31], modeling the asymmetric BLI of a compressor fan over a 2D airfoil and achieving power savings but also a drag reduction. For their part, Lv et al. [32] have studied the benefits of BLI experimentally in comparison with wake ingestion (setting the propeller at a major distance from the body) and obtaining a significant power saving.

Additionally, because the flow around the airfoil changes, the aerodynamic efficiency can also vary. BLI usually increases the suction peak near the wing leading edge and reduces the lift-induced drag. However, the skin friction drag

is grown on the surfaces near the propulsors due to the flux reacceleration, counterbalancing the positive effects. Hall et al. [33] conclude in their work of BLI applied to civil aircraft fuselages that this propulsion configuration has both propulsion and aerodynamic benefits.

Also, in the aerodynamic field, Teperin et al. [34] analyze the BLI impact on an axisymmetric UAV body using simulations with an actuator disk approach and concludes that setting the propeller behind the trailing edge involves less drag and power consumption than a leading edge setting. Martinez and Smith [35] and, Samuelsson and Grönstedt [36] reached a similar conclusion by analyzing the BLI application on a commercial aircraft fuselage and determining a significant drag reduction.

On the other hand, using the same simulation approach simulation approach, Elsalamony et al. [37] point out that by applying BLI behind an airfoil, the lift decreases and drag increases compared with a clean airfoil. However, they remark that BLI is helpful due to power savings and boundary layer stabilization. The change in the trend of their results when compared with those of others might be explained by changes in the geometrical configuration.

The combination of the benefits produced by DEP and BLI technologies has also been studied. Leifsson et al. [38] and Goldberg et al. [39] showed the combination of both DEP and BLI in the design of a blended-wing-body aircraft, where a higher lift-to-drag ratio was estimated.

Nevertheless, the combination of DEP and BLI together with hybridization in small aircraft has not been previously found in the literature. The primary motivation of this work lies in studying the combination of these technologies, with the hope of offering solutions that help mitigate the polluting and greenhouse gas emissions associated with the growing future fleet of UAVs and RPAS. To carry out the main motivation, this work contributes to studying the possible positive effects of improving aerodynamical efficiency, propulsive efficiency and fuel consumption, combining the described technologies and focusing on the importance of the position of the propeller relative to the wing.

1.2 Objectives

This work can be divided into two main objectives.

The first objective consists of analyzing the feasibility of small aircraft that combines serial hybridization, distributed electric propulsion and boundary layer ingestion. The analysis compares DEP BLI aircraft with a more classic configuration, specifically single-propeller aircraft with ICE as the only powertrain and single-propeller with electric hybridization, both without including DEP or BLI.

A secondary goal starts from the first objective, consisting of creating and manipulating tools and environments to analyze those aircraft. The aircraft will be analyzed using different tools, mainly in terms of propulsive efficiency, aerodynamic efficiency, and specific fuel consumption. In addition, to validate the viability of aircraft with DEP and BLI, the optimization of the range of the aircraft is chosen as an objective.

The second main objective starts after having analyzed the feasibility of the aircraft to be treated. It consists of providing tools for conceptual and preliminary design of aircraft that combine these systems so that the problem can be extended to various design situations and required missions.

1.3 Working plan

The present work begins with the definition of the aircraft, setting the most important characteristics in terms of geometry, weight, and propulsive plant. At this point, the mission to be optimized is chosen and a first quick calculation is made to study the feasibility of a DEP BLI aircraft. This first calculation is made with data from similar aircraft and off-the-shelf components.

Once indications of improvement in range and fuel consumption have been obtained by combining DEP, BLI and serial hybridization technologies, a computational fluid mechanics (CFD) work environment is defined. CFD simulations are the core of this work. The simulations are performed for both the wing and the propeller, and their interaction. In this environment, the most critical variables of the problem are parameterized, and optimal solutions are sought in terms of propulsive and aerodynamic efficiencies. External experiments and independence analysis validate the simulations.

Now that optimal configurations are obtained, an in-depth analysis is carried out to understand how the improvements are produced, focusing on a detailed analysis of the influence of the position of the propeller with respect to the wing. On the one hand, the data coming directly from the CFD is analyzed. On the other hand, tools are developed to perform modal analysis that can later also be applied as the first tools in pre-design.

Returning to earlier range improvement calculations, the data obtained in the simulations are used to identify potential fuel improvement when using DEP BLI aircraft realistically. The optimized aircraft is compared with more classic options in terms of fuel reduction for the same-range mission. These options comprise single-propellers with ICE as the primary power system and single-propeller hybrid electric aircraft, neither option featuring distributed propulsion or boundary layer ingestion.

Finally, additional simulations have been carried out with the aim of having a broad database that can be used to make simple models. In this way, it is

possible to develop tools to contribute to design and optimize aircraft with DEP and BLI.

1.4 Contents

The current work has been structured as follows:

Chapter 2 presents a literature review of the most relevant technologies involved in aircraft design that this work is about. It also introduces a theoretical framework of the methods applied to fulfill this work.

Chapter 3 presents the main selection of components and design parameters in terms of the aircraft's geometry, weight and power plant. This chapter finishes with a quick study that proves the feasibility of combining technologies to design new small aircraft.

Chapter 4 develops the whole methods applied in this work. The first half is focused on the primary tool: CFD simulations. The complete computational setup and models selected are widely explained, along with a detailed section of the propeller disk models and the validation of the simulations with studies and external experiments. The chapter continues by explaining how the modal method is applied for analysis and developing pre-designing tools. It finishes with a description of how the mission is optimized, following the quick study basis presented in the previous chapter.

Chapter 5 focuses on the results. A significant part of this chapter is dedicated to analyze the simulations obtained, focusing on the aerodynamic and propulsive behavior due to the propeller position. Also, the study is accompanied by a modal analysis to understand this aircraft's behavior better. This study allows selecting a first optimal configuration, with which a range mission will be optimized later. In this optimization, significant improvements in fuel consumption are obtained compared to classic propulsive configurations. Finally, some tools for designing and optimizing aircraft with DEP and BLI are developed.

Chapter 6 summarizes all the conclusions reached in this work. Additionally, this chapter discusses the limitations of the work and possible future works derived from this thesis.

1.5 References

[5] E. U. A. S. Agency. *Study on the societal acceptance of Urban Air Mobility in Europe*. 2021 (cit. on p. 2).

[6] Single European Sky ATM Research. *European Drones Outlook Study*. Last accessed: 2022-01-12. 2016. URL: http://www.sesarju.eu/sites/default/files/documents/reports/European_Drones_Outlook_Study_2016.pdf (cit. on p. 2).

[7] A. Amoukteh, J. Janda, and J. Vicent. "Drones Go to work". In: *Harvard Business Review* (2017), pp. 77–94. URL: https://hbr.org/cover-story/2017/05/drones-go-to-work (cit. on p. 2).

[8] C. L. Nickol and W. J. Haller. "Assessment of the performance potential of advanced subsonic transport concepts for NASA's environmentally responsible aviation project". In: *54th AIAA Aerospace Sciences Meeting*. San Diego, CA, USA: AIAA, Jan. 2016, pp. 1–21. DOI: 10.2514/6.2016-1030 (cit. on p. 2).

[9] M. Rostami and A. hamzeh Farajollahi. "Aerodynamic performance of mutual interaction tandem propellers with ducted UAV". In: *Aerospace Science and Technology* 108 (2021), p. 10. ISSN: 12709638. DOI: 10.1016/j.ast.2020.106399 (cit. on p. 2).

[10] H. Zhang, B. Song, F. Li, and J. Xuan. "Multidisciplinary design optimization of an electric propulsion system of a hybrid UAV considering wind disturbance rejection capability in the quadrotor mode". In: *Aerospace Science and Technology* 110 (2021), p. 20. ISSN: 12709638. DOI: 10.1016/j.ast.2020.106372 (cit. on p. 2).

[11] K. E. McKinney. "Evaluation of Hybrid-Electric Power System Integration Challenges for Multi-rotor UAS". B.Sc. thesis. Stilwater, OK, USA: Oklahoma State University, 2018 (cit. on pp. 2, 3).

[12] W. J. Fredericks, M. D. Moore, and R. C. Busan. "Benefits of hybrid-electric propulsion to achieve 4x increase in cruise efficiency for a VTOL aircraft". In: *2013 International Powered Lift Conference*. Los Angeles, California, USA, 2013, pp. 1–21. DOI: 10.2514/6.2013-4324 (cit. on p. 2).

[13] F. Payri and J. Desantes. *Motores de Combustión Interna Alternativos*. Valencia, Spain: Editorial Reverté and Editorial UPV, 2011, pp. 800–822. ISBN: 978-84-291-4802-2 (cit. on p. 2).

[14] J. Heywood. *Internal Combustion Engine Fundamentals*. McGraw-Hill Education, 1988, pp. 668–712. ISBN: 978-1259002076 (cit. on p. 2).

[15] J. Benajes, R. Novella, J. Gómez-Soriano, I. Barbery, C. Libert, F. Rampanarivo, and M. Dabiri. "Computational assessment towards understanding the energy conversion and combustion process of lean mixtures in passive pre-chamber ignited engines". In: *Applied Thermal Engineering* 178 (2020). DOI: 10.1016/j.applthermaleng.2020.115501 (cit. on p. 3).

[16] T. Nagasawa, Y. Okura, R. Yamada, S. Sato, H. Kosaka, T. Yokomori, and N. Iida. "Thermal efficiency improvement of super-lean burn spark ignition engine by stratified water insulation on piston top surface". In: *International Journal of Engine Research* 22 (5 2021), pp. 1421–1439. DOI: 10.1177/1468087420908164 (cit. on p. 3).

[17] F. G. Harmon, A. A. Frank, and J. J. Chattot. "Conceptual design and simulation of a small hybrid-electric unmanned aerial vehicle". In: *Journal of Aircraft* 43.5 (2006), pp. 1490–1498. ISSN: 00218669. DOI: 10.2514/1.15816 (cit. on pp. 3, 40, 42).

[18] J. K. Ausserer and F. G. Harmon. "Integration, validation, and testing of a hybrid-electric propulsion system for a small remotely-piloted aircraft". In: *10th Annual International Energy Conversion Engineering Conference*. Atlanta, GA, USA: AIAA, Aug. 2012, pp. 1–11. ISBN: 9781624101908. DOI: 10.2514/6.2012-4239 (cit. on pp. 3, 40).

[19] R. M. Hiserote. "Analysis of Hybrid-Electric Propulsion System Designs for Small Unmanned Aircraft Systems". MA thesis. 2010. URL: https://scholar.afit.edu/etd/2044 (cit. on p. 3).

[20] C. Kim, E. Namgoong, S. Lee, T. Kim, and H. Kim. *Fuel economy optimization for parallel hybrid vehicles with CVT*. SAE Technical Paper 1999-01-1148. SAE International, 1999. DOI: 10.4271/1999-01-1148 (cit. on p. 3).

[21] I. H. Mengistu. "A small internal combustion engine testing for a hybrid-electric remotely-piloted aircraft". MA thesis. Wright-Patterson Air Force Base, OH, USA: Air Force Institute of Technology, 2011, p. 124 (cit. on pp. 3, 40).

[22] J. Lieh, E. Spahr, A. Behbahani, and J. Hoying. "Design of hybrid propulsion systems for unmanned aerial vehicles". In: *47th AIAA/ASME/SAE/ASEE Joint Propulsion Conference and Exhibit 2011*. San Diego, California, USA, Aug. 2011, pp. 1–14. DOI: 10.2514/6.2011-6146 (cit. on pp. 3, 14).

[23] A. M. Stoll, J. Bevirt, M. D. Moore, W. J. Fredericks, and N. K. Borer. "Drag Reduction Through Distributed Electric Propulsion". In: *14th AIAA Aviation Technology, Integration, and Operations Conference*. Atlanta, GA, USA: AIAA, June 2014, pp. 1–10. DOI: 10.2514/6.2014-2851 (cit. on p. 4).

[24] A. M. Stoll. "Comparison of CFD and experimental results of the leap tech distributed electric propulsion blown wing". In: *15th AIAA Aviation Technology, Integration, and Operations Conference*. Dallas, TX, USA: AIAA, June 2015, pp. 22–26. ISBN: 9781624103698. DOI: 10.2514/6.2015-3188 (cit. on pp. 4, 61, 63).

[25] C. Xue and Z. Zhou. "Propeller-wing coupled aerodynamic design based on desired propeller slipstream". In: *Aerospace Science and Technology* 97 (2020), p. 16. ISSN: 12709638. DOI: 10.1016/j.ast.2019.105556 (cit. on p. 4).

[26] Y.-Y. A. Ko. "The Multidisciplinary Design Optimization of a Distributed Propulsion Blended-Wing-Body Aircraft". PhD thesis. Virginia Tech, 2003, pp. 1–222. URL: https://vtechworks.lib.vt.edu/handle/10919/27257 (cit. on p. 4).

[27] K. R. Moore and A. Ning. "Distributed electric propulsion effects on traditional aircraft through multidisciplinary optimization". In: *AIAA/ASCE/AHS/ASC Structures, Structural Dynamics, and Materials Conference*. Kissimmee, FL, USA: AIAA, Jan. 2018. ISBN: 9781624105326. DOI: 10.2514/6.2018-1652 (cit. on pp. 4, 42).

[28] R. Kirner, L. Raffaelli, A. Rolt, P. Laskaridis, G. Doulgeris, and R. Singh. "An assessment of distributed propulsion: Part B - Advanced propulsion system architectures for blended wing body aircraft configurations". In: *Aerospace Science and Technology* 50 (2016), pp. 212–219. ISSN: 12709638. DOI: 10.1016/j.ast.2015.12.020. URL: http://dx.doi.org/10.1016/j.ast.2015.12.020 (cit. on p. 4).

[29] M. Amoozgar, M. I. Friswell, S. A. Fazelzadeh, H. H. Khodaparast, A. Mazidi, and J. E. Cooper. "Aeroelastic stability analysis of electric aircraft wings with distributed electric propulsors". In: *Aerospace* 8.4 (2021), pp. 1–12. ISSN: 22264310. DOI: 10.3390/aerospace8040100 (cit. on pp. 4, 42).

[30] H. D. Kim, A. T. Perry, and P. J. Ansell. "A Review of Distributed Electric Propulsion Concepts for Air Vehicle Technology". In: *AIAA/IEEE Electric Aircraft Technologies Symposium*. Cincinnati, OH, USA: AIAA/IEEE, July 2018, pp. 1–21. ISBN: 9781624105722. DOI: 10.2514/6.2018-4998 (cit. on p. 4).

[31] N. Budziszewski and J. Friedrichs. “Modelling of a boundary layer ingesting propulsor”. In: *Energies* 11.4 (2018). ISSN: 19961073. DOI: 10.3390/en11040708 (cit. on p. 4).

[32] P. Lv, D. Ragni, T. Hartuc, L. Veldhuis, and A. G. Rao. “Experimental investigation of the flow mechanisms associated with a wake-ingesting propulsor”. In: *AIAA Journal* 55.4 (2017), pp. 1332–1342. ISSN: 00011452. DOI: 10.2514/1.J055292 (cit. on p. 4).

[33] D. K. Hall, A. C. Huang, A. Uranga, E. M. Greitzer, M. Drela, and S. Sato. “Boundary layer ingestion propulsion benefit for transport aircraft”. In: *Journal of Propulsion and Power* 33.5 (2017), pp. 1118–1129. ISSN: 15333876. DOI: 10.2514/1.B36321 (cit. on pp. 5, 21).

[34] L. Teperin. “Investigation on Boundary Layer Ingestion Propulsion for UAVs”. In: *International Micro Air Vehicle Conference and Flight Competition (IMAV)*. Aug. 2017, pp. 293–300 (cit. on pp. 5, 45, 63).

[35] A. Martínez Fernández and H. Smith. “Effect of a fuselage boundary layer ingesting propulsor on airframe forces and moments”. In: *Aerospace Science and Technology* 100 (2020), p. 105808. ISSN: 12709638. DOI: 10.1016/j.ast.2020.105808 (cit. on p. 5).

[36] S. Samuelsson and T. Grönstedt. “Performance analysis of turbo-electric propulsion system with fuselage boundary layer ingestion”. In: *Aerospace Science and Technology* 109 (2021), p. 10. ISSN: 12709638. DOI: 10.1016/j.ast.2020.106412 (cit. on p. 5).

[37] M. Elsalamony and L. Teperin. “2D Numerical Investigation of Boundary Layer Ingestion Propulsor on Airfoil”. In: *7th European Conference for Aeronautics and Space Sciences (EUCASS)* (2017), pp. 1–11. DOI: 10.13009/EUCASS2017-67 (cit. on pp. 5, 21, 46, 102).

[38] L. Leifsson, A. Ko, W. H. Mason, J. A. Schetz, B. Grossman, and R. T. Haftka. “Multidisciplinary design optimization of blended-wing-body transport aircraft with distributed propulsion”. In: *Aerospace Science and Technology* 25.1 (2013), pp. 16–28. ISSN: 12709638. DOI: 10.1016/j.ast.2011.12.004 (cit. on p. 5).

[39] C. Goldberg, D. Nalianda, D. MacManus, P. Pilidis, and J. Felder. “Installed performance assessment of a boundary layer ingesting distributed propulsion system at design point”. In: *52nd AIAA/SAE/ASEE Joint Propulsion Conference*. Salt Lake City, Utah, USA, 2016, pp. 1–22. DOI: 10.2514/6.2016-4800 (cit. on p. 5).

CHAPTER 2

Literature review and theoretical framework

Contents

2.1 Introduction

The previous chapter introduces the principal aspects that shape this work. This research employs three different technologies: Series electric-internal combustion engine hybridization, distributed electric propulsion, and boundary layer ingestion. Below these lines, previous works and the classification of these technologies are studied. The main objective is to understand the possible benefits of simultaneous integration of all three technologies.

Additionally, the main tools of analysis applied in this work are also advanced in this chapter, remarking the use and application of computational fluid dynamics and the proper orthogonal decomposition method.

2.2 Aircraft hybridization

Hybrid electric aircraft combine the benefits of the high energy power supply compared with fully electric vehicles, and lower pollutant and greenhouse gas emissions compared with ICE-based aircraft.

In general, every hybrid electric setting consists of the use of at least one electric engine and one non-electric engine. Usually, this second engine is a reciprocating combustion engine or ICE based on the Otto cycle with 2 o 4 strokes, but electric hybridization is possible with different systems. Capata et al. in their investigation of hybrid UAVs have studied the use of a radial gas turbine as main ICE [40]. Jurecka and Bencalik point out in their review of electric airplanes [41] the importance in the future of the inclusion of fuel cells in small aircraft. Their conclusions are reinforced by the first flight of a UAV in Taiwan in 2010 performed by The National Cheng Kung University, implementing hybridization with fuel cells [42].

Multiple configurations arise depending on how the HE drive train is connected. In the description, only ICE as a non-electric engine will be explained, being the system equivalent if this power source is changed. The following descriptions of different configurations of hybridization according to their drive train is not new and are listed in detail in the investigation of Lieh et al. [22], the assestment on aircraft hybridization realized by Hoogreef and de Vries [43], and the book of Ehsani et al. [44].

One of the most popular is the parallel configuration, described in Fig. 2.1. This configuration is called “parallel” because the electric motor and ICE supply mechanical power to the propeller through the transmission. This way, both energy sources are mechanically coupled and need two power supplies, a battery for the electric engine and a fuel tank for the ICE. Usually, the ICE is the main power source and the battery acts as an energy buffer. This configuration makes different operating modes possible because the aircraft may use a single mode

with one engine (electric or ICE) or a dual mode with both. A popular mode decision is to use only the ICE when a large amount of power is needed, for example, during take-off and reserving the single electric mode for the cruise. This mode is called in the literature "electric flight" as Schömann mentions in his thesis [45], and allows to keep a low noise footprint which is perfect for surveillance missions and low pollutant emissions.

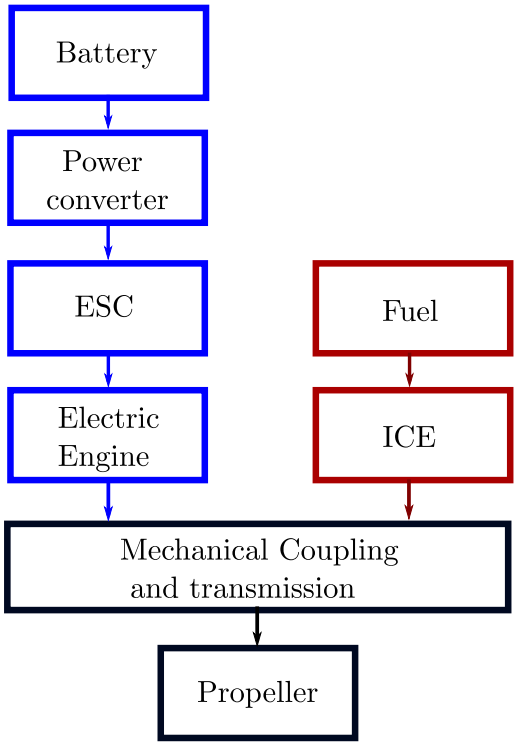

Figure 2.1: Hybrid parallel drive configuration. The part of the system related to the ICE is highlighted in red, while the electrical part is highlighted in blue. The output is shown in black.

The opposite setting is the series configuration, represented in Fig. 2.2. The series hybrid configuration does not have a mechanical coupling between engines but electrical coupling. In this case, a generator is needed as an additional system, which transforms the mechanical power produced by the ICE into electrical power. The electricity is led to the electric engines that drives the propeller. In this configuration, the mechanical transmission only exists between the electric motor and the propeller. In this system, the ICE is the primary power supply. The only way to unplug the ICE is to employ an additional battery directly connected to the electric engine, allowing the electrical flight if

the mission requires it. The battery may even be used to provide extra power during some flight phases, or it may even be charged midflight using the electric generator. Despite not allowing electric flight if batteries are not inserted since the ICE is working throughout the flight, it can work at an optimal point in its motor map. This is possible due to the mechanical decoupling since the ICE does not need to maintain a rotational velocity proportional to the propeller's rotational velocity. The ICE can generate the required power with the lowest possible fuel consumption by changing its rotational speed and shaft torque accordingly.

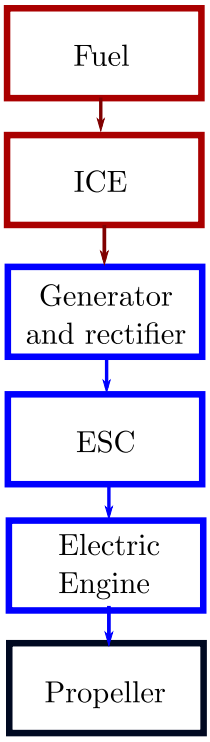

Figure 2.2: Hybrid series drive configuration. The part of the system related to the ICE is highlighted in red, while the electrical part is highlighted in blue. The output is shown in black.

Also, this configuration is suitable for installing a fuel cell instead of the ICE. As the fuel cell produces not mechanical but electrical power, the generator is not needed in this setting. Hybrid fuel cells have some advantages against ICEs, such as negligible noise levels and pollutant and greenhouse gas emissions during the flight, although with much lower specific energy and power.

A rectifier and electronic speed control (ESC) are needed in both configura-

tions. The rectifier converts the alternating current (AC) of the generator to direct current (DC) needed to power the electric engine controller. The ESC is an electronic circuit that allows the control of the electric engine's velocity.

More complex configurations are possible, usually known as "series-parallel" hybridization, which is represented in Fig. 2.3.

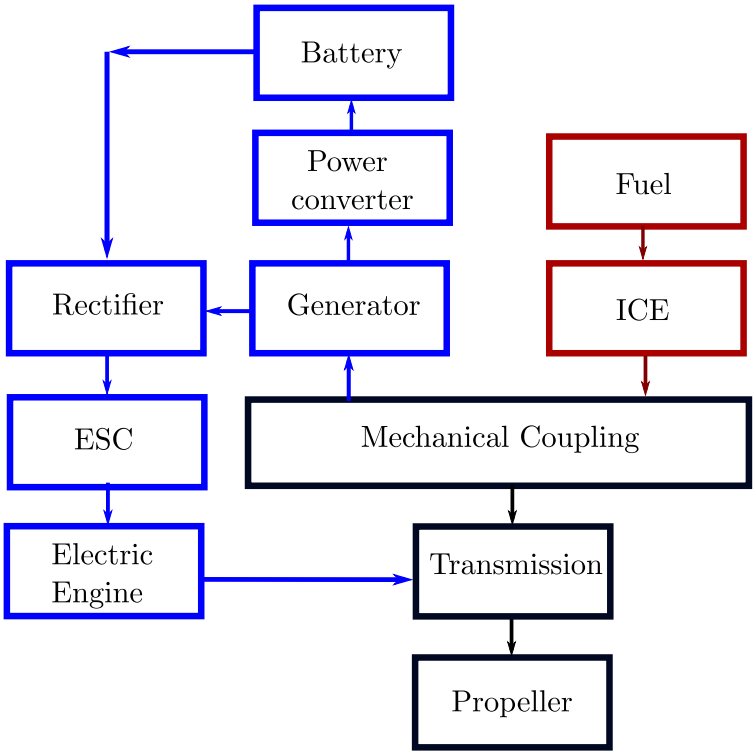

Figure 2.3: Complex hybrid series-parallel drive configuration. The part of the system related to the ICE is highlighted in red, while the electrical part is highlighted in blue. The output is shown in black.

This configuration combines series and parallel settings, meaning that mechanical and electrical couplings are employed to drive the propeller. In the simpler case shown in Fig. 2.3, the only difference from the series case is that the ICE is in direct drive with the propeller, including the battery to power the electric motor. All the operating modes already described are possible. Fig. 2.3 shows a complex variant, where an additional power converter is applied to charge the battery pack. This variant enables a new operating mode that charges the batteries using the ICE. The complexity of this system, together with the additional weight of adding components, means that it is relegated to heavier aircraft.

2.3 Distributed electric propulsion

As explained previously in chapter 1, a distributed electric propulsion setting usually consists of the distribution of electric engines along the wing with the objective of gaining some benefits. But, in reality, the distribution does not have to be purely electric; different possible configurations exist in distributed propulsion, where three different settings stand out.

The first configuration handles multiple small propulsors that are powered independently. Because many aircraft employ more than one self-powered engine, only the cases where the propulsion integration carries out some benefits are considered in this definition. One example of this configuration is the widely studied NASA's Blended Wing Body (BWB) aircraft (Fig. 2.4). On this aircraft, various propulsion distributions have been studied that fit in this category, for example the research of Kim et al. [46] represented in Fig. 2.4, or the SAX-40 proposed by a colaboration between the Cambridge University and the MIT [47, 48] represented in Fig. 2.5.

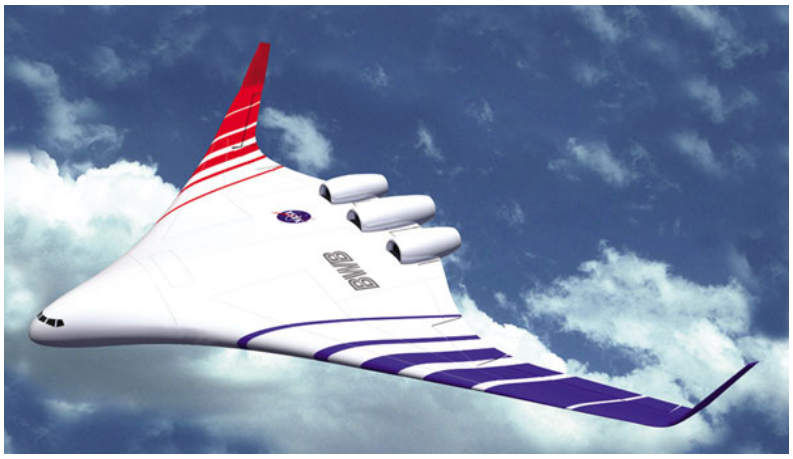

Figure 2.4: NASA's Blended Wing Body (BWB) aircraft.

The second configuration is known as distributed jet or jet flap. This propulsion layout sets multiple slots or jets near the trailing edge. The jet is usually produced on a centered propulsor or engine, and its usual application is to provide additional thrust in fighter planes. Some novel examples of this are the DJBW (Distributed jet blowing wing) aircraft presented by Siliang et al. [49] or the distributed air-breathing plasma jet propulsion aircraft researched by Goeksel [50].

The last configuration consists of distributed propulsors which are driven only by a primary power source through a transmission system, and it is the setting applied in this work. Not all the designs that are within this classifi-

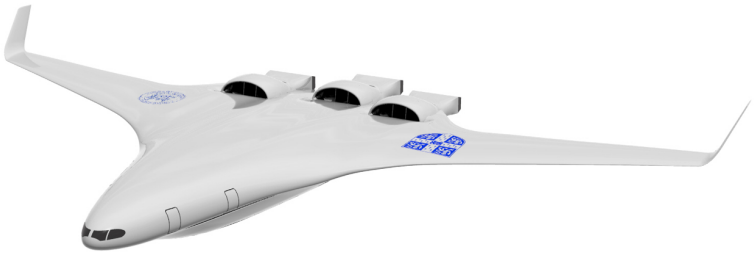

Figure 2.5: SAX-40 concept for silent aircraft proposed by the Cambridge University and the MIT.

cation are distributed electric propulsion or DEP. For example, some designs of BWB have multiple fans but a single combustion chamber, as presented by Gohardani [51]. Returning to DEP, electric engines are used as propulsors in this configuration without sharing any mechanical coupling. However, the main source of power does not have to be a battery. As mentioned in Section 2.2, an ICE or a fuel cell can be used to impose DEP with hybridization.

Felder et al. [52] presented a similar integrated wing propulsion design, where hybridization is the basis of distributed electric propulsion mounted on the NASA's N3-X aircraft (Fig. 2.6).

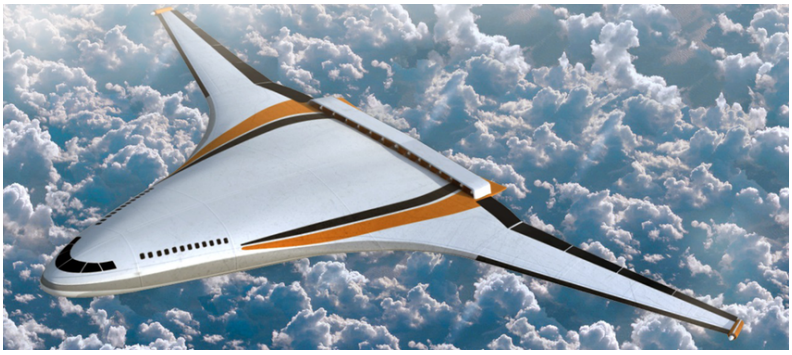

Figure 2.6: Trailing edge distributed electric propulsion with boundary layer ingestion applied to NASA's N3-X aircraft.

An example of a smaller size would also be the NASA aircraft X-57 Maxwell [53](Fig. 2.7), which employs a full electric distributed propulsion.

Multiple advantages of using this system have been discussed in the introduction. In summary, the main advantages collected by Kim et al. [54] should be noted. DEP systems allow high-efficiency electric engines while a centered power train is run in high-efficiency conditions. It can be combined with bound-

Figure 2.7: Leading edge distributed electric propulsion applied to NASA's X-57 Maxwell aircraft.

ary layer ingestion, which is described in the Section 2.4, if the engines are set behind the fuselage or the wing, enabling additional benefits such as wake filling or vortex suppression. If the distribution is applied in the wing leading edge, like in the X-57 Maxwell, the distribution could increase the dynamic pressure over the wing, reducing this way the required wing area. Additionally, DEP has been presented as a measure to reduce noise pollution and as a possible control platform, reducing the need to implement other actuators.

2.4 Boundary Layer Ingestion

As mentioned in the previous chapter, boundary layer ingestion is based on the ingestion of a boundary layer formed around a body by a propulsor, improving this way the propulsor efficiency and lowering the fuel needed to propel it.

The BLI has been studied for over 70 years, as can be seen in the publication conducted by Smith and Howard in 1947 [55], where BLI is studied to reduce the drag of a large conventional airplane. Because its propulsion benefit in different transport areas, the BLI concept was originally applied to both aircraft and naval fields. As seen in Douglass' research [56], a performance improvement can be achieved on torpedoes, submarines and ships thanks to locating by design the propeller motors behind the propelled bodies. Following those principles, multiple investigations have emerged in recent years on applying BLI to aircraft. The field that stands out the most is the study of boundary layer ingestion applied to the study of ducted fans coupled behind aircraft fuselages, as can be seen in the research of Uranga et al. [57, 58], Hardin et al. [59], Welstead and Felder [60] or Plas [61].

In Section 2.4.1 there is an explanation of the theoretical framework of the

operation of the BLI, based principally on the research of Smith [62], Lv et al. [63], Elsalamony et al. [37], Hall et al. [33] and the thesis of Sato [64].

2.4.1 Propeller and airfoil without BLI

The first approach is to define how a free stream propeller works. To simplify things, the propeller is going to be considered as an actuator disk without thickness. This actuator or virtual disk simulates the propeller by creating a surface that applies a pressure difference between its sides, generating a velocity difference between the incoming and outgoing far field flow and, hence, thrust.

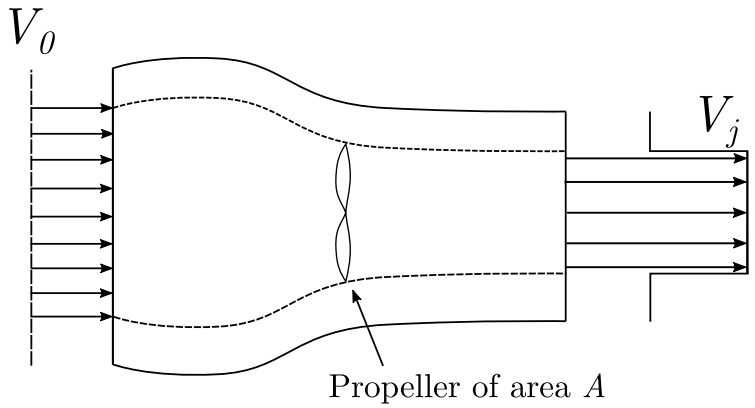

Figure 2.8: Control volume for a freestream propeller.

Fig. 2.8 serves as an aid of visualization to explain the thrust (T) integration. Considering that the flow is axisymmetric, the air density is constant, and the virtual disk has the same properties on all its surface, the integration in the Trefftz plane in which the pressure is the same as the undisturbed upstream pressure gives the T equation in eqn. 2.1.

$$T = \iint \rho \cdot V_j \cdot (V_j - V_0)\,\mathrm{d}A = \dot{m}(V_j - V_0), \tag{2.1}$$

where V_0 and V_j are the air velocity upstream and downstream the propeller respectively. the mass flow rate at the propeller section $\dot{m}$ is defined as $\dot{m} = \rho A V_p$, being A the propeller area, and $V_p = (V_j + V_0)/2$ the velocity at the virtual disk.

The propulsive power (P_p) is defined as the difference between the flow of kinetic energy upstream and downstream of the stream tube. With the same considerations taken into account when calculating the thrust, the power is represented in eq. 2.2.

$$P_p = \iint \frac{1}{2} \cdot \rho \cdot V_j \cdot (V_j^2 - V_0^2)\,\mathrm{d}A = \frac{\dot{m}}{2}(V_j^2 - V_0^2). \tag{2.2}$$

If Drela Power Balance Method is applied [65, 66], the total propulsive power can be separated into two sources. On the one hand, in eq. 2.3 the power produced by the thrust and the velocity flow is represented.

$$T \cdot V_0 = \iint \rho \cdot V_j \cdot V_0 \cdot (V_j - V_0)\,\mathrm{d}A\,. \tag{2.3}$$

On the other hand, the wake generated behind the propeller requires extra energy ($E_{wake,prop}$) to be evened by the viscous stresses. The power wasted by the wake is represented in eq. 2.4.

$$E_{\text{wake,prop}} = \iint \frac{1}{2} \cdot \rho \cdot V_j \cdot (V_j - V_0)^2\,\mathrm{d}A\,. \tag{2.4}$$

The propulsive efficiency (η_p) can be defined in eq. 2.5 as the power involved in the thrust divided by the total power.

$$\eta_p = \frac{T \cdot V_0}{P_p} = \frac{T \cdot V_0}{T \cdot V_0 + E_{\text{wake,prop}}} < 1. \tag{2.5}$$

In this case, the shaft power is greater than the propulsive power since different sources of losses are not being considered, such as viscous losses, induced losses due to a finite number of blades in the propeller, or kinetic energy in the jet having both radial and azimuthal components, and not only an axial one.

In eq. 2.6, the drag is expressed as a function of the velocity distribution near the airfoil wake according to the momentum equation.

$$D = \iint \rho \cdot V_w \cdot (V_w - V_0)\,\mathrm{d}A\,. \tag{2.6}$$

Now, the isolated airfoil is studied and the drag is defined. The airfoil drag can be summed up as the loss in momentum between the flow upstream and downstream of the airfoil, as explained by Meseguer and Sanz in [67].

As with the propeller, a simplified figure is provided to aid the visualization in Fig. 2.9.

The power consumed by this force is expressed in the eq. 2.7 by multiplying the drag by the speed of flight.

$$D \cdot V_0 = \iint \rho \cdot V_w \cdot V_0 \cdot (V_w - V_0)\,\mathrm{d}A = P_{BL} + E_{\text{wake,airfoil}}. \tag{2.7}$$

As the propeller power described in eq. 2.2, the power associated with the drag force can also be divided into two sources. On the one hand, the power is

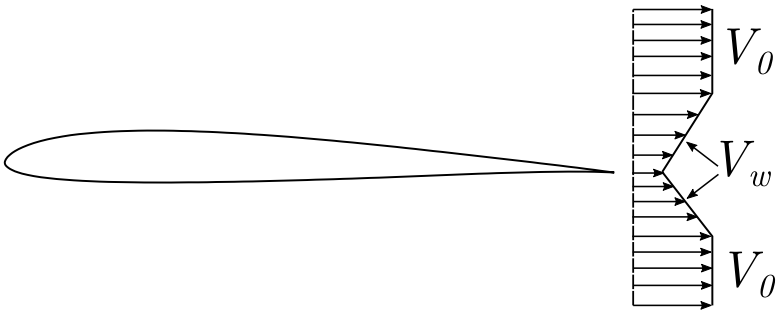

Figure 2.9: Airfoil and simplified velocity distribution downstream.

consumed due to the dissipated energy in the boundary layer (P_{BL}) around the airfoil. This power is computed in eq. 2.8.

$$P_{BL} = \iint \frac{1}{2} \cdot \rho \cdot V_w \cdot (V_0^2 - V_w^2) \, \mathrm{d}A \, . \tag{2.8}$$

On the other hand, the energy related to the wake perturbations is calculated in eq. 2.10.

$$E_{\text{wake,airfoil}} = \iint \frac{1}{2} \cdot \rho \cdot V_w \cdot (V_0 - V_w)^2 \, \mathrm{d}A \, . \tag{2.9}$$

2.4.2 Ideal BLI

The ideal boundary layer ingestion propulsion is now defined as the combination of propeller and airfoil in an ideal integration. This configuration can be seen in a simplified sketch in Fig. 2.10.

The idea is that if the propulsor ingests part of the boundary layer grown on the body, it can provide the same thrust with less cost in power consumption. Notionally, the propulsor is set, occupying the momentum gap in the wake of the airfoil. This way, the wake behind the body can be minimized, decreasing the associated power loss. If this setting is considered, the complete wake produced behind the airfoil is ingested and flattened. Also, the jet velocity has the same velocity as the undisturbed flow. With this, the body's wake is suppressed, and the energy added by the propeller will equal the boundary layer losses. This energy is also evaluated as a difference in kinetic energy upstream and downstream of the body in eq. 2.10, giving the same result as eq. 2.8.

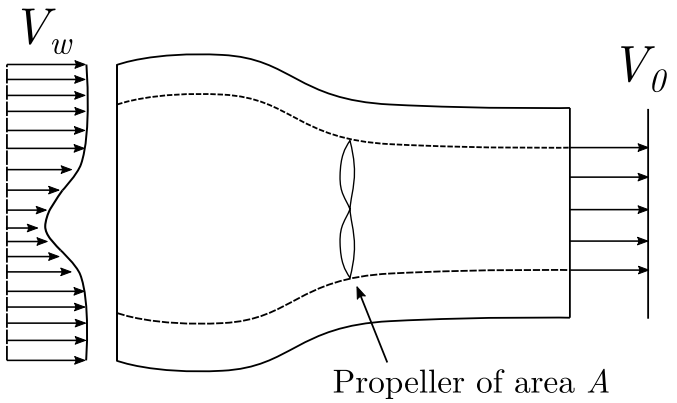

Figure 2.10: Propeller in a idealistic boundary layer ingesting setting.

$$E_{\text{prop,BLI}} = \iint \frac{1}{2} \cdot \rho \cdot V_w \cdot (V_0^2 - V_w^2)\,\mathrm{d}A = P_{BL}. \tag{2.10}$$

The power balance in the ideal case is collected in equation 2.11, where both the actuator and the wake produced by the airfoil contribute to the total power.

$$D \cdot V_0 = E_{\text{prop,BLI}} + E_{\text{wake,airfoil}}. \tag{2.11}$$

In this ideal case the propulsive efficiency is collected and shown in eq. 2.12, considering that the thrust produced is equal to the airfoil drag.

$$\eta_p = \frac{D \cdot V_0}{E_{\text{prop,BLI}}} = \frac{E_{\text{prop,BLI}} + E_{\text{wake,airfoil}}}{E_{\text{prop,BLI}}} > 1. \tag{2.12}$$

The result of eq. 2.12 is an efficiency higher than one but, of course, in a real case there would be an interaction between airfoil and propulsor, and the propulsor does not have to fill completely the airfoil wake, which is not considered here.

2.4.3 Real BLI

In a real BLI configuration, an interaction between the airfoil and the propeller always exists, modifying the overall pressure field around both elements. This way, a realistic design will impact the airfoil drag and the propeller's power.

Because in this configuration, the propeller is set very close to the airfoil trailing edge, both propeller and airfoil are in a pressure field unequal to the inlet pressure. This condition has a direct impact on both propeller and airfoil,

modifying, on the one hand, the aerodynamic performance and, on the other hand, the power needed to propel the system.

As Hendricks [68] reviews in his BLI modeling research, there exist multiple options when modeling this kind of problem. The author classifies these approaches by their degree of coupling when studying propulsor and body, but highlights that despite the existence of decoupled models, that is, that study these two mediums separately, they are not faithful to reality.

In the present work, a Reynolds-averaged Navier-Stokes CFD code with an actuator disk as the source term takes care of the calculation of both aerodynamics and propeller. Consequently, the system is considered strongly coupled because both models share a high level of interaction during the calculation.

2.5 Computational Fluid Dynamics

Computational Fluid Dynamics, widely known as CFD, is a set of techniques based on fluid mechanics that, through numerical methods and algorithms, can simulate the behavior of fluids and their interaction with solids and surfaces. The resolution basis of CFD is built around the Navier-Stokes equations. Those equations are written in terms of nonlinear partial derivatives and describe the movement of a (in the case described in this work) Newtonian fluid, as described by Anderson in [69].

Navier-Stokes equations are derived from principles of conservation of mass, momentum and energy in its integral formulation. Although some authors use the term Navier-Stokes equations for only the momentum conservation equations, this document will use the term for the set that includes also the continuity and energy conservation. The resolution of the set of equations is only possible analytically in a reduced number of cases under strict assumptions and hypotheses. CFD offers a numerical approximation to the Navier-Stokes resolution, allowing to model fluid problems of very different types, which is why it has become a widely used tool.

CFD can be divided into three categories by the method applied when the turbulence is solved. The first category is Direct Numerical Simulation (DNS). With DNS, CFD completely solves the Navier-Stokes equations without any turbulence model. This way, all the spatial turbulence scales are solved; therefore, highly refined meshes are required to resolve the smallest scales. Due to its mode of operation, DNS is expensive in resources and time, being today relegated to simple geometries, as remarked by Verstappen and Veldman [70].

The second category is called Large Eddy Simulation (LES). This method includes the turbulence modeling of the smaller scales, but solves the larger turbulence scales. In this way, costs are reduced concerning the use of DNS.

The last category is the less expensive using resources in an equal problem and is the method employed in this work: Reynolds-averaged Navier-Stokes equations (RANS). Appling RANS, as the name implies, the Navier-Stokes equations are solved in a time-averaged way, modeling the turbulence completely. RANS models can also be used for non-steady problems, which gives rise to Unsteady Reynolds-averaged Navier-Stokes simulations (U-RANS). In U-RANS simulations, there is an extra implicit assumption: the time scale associated to the mean flow that is being resolved is much bigger than the time scale of the turbulent fluctuations, so even if the time step used during the numerical integration is small, the turbulence can not be resolved.

In RANS, the solution for each variable (velocity, pressure, energy, or species concentration) is separated into a mean component and a fluctuating component. An additional term is found in the momentum equation in the averaging process. This term is known as the Reynolds stress tensor, and it needs an extra set of equations to close the problem.

Different models are selected to close the system; some of them are listed below. The first one is the K-Epsilon ($k-\epsilon$) model, which applies two extra transport equations to solve the problem and allows for balancing the accuracy and the computational cost: one equation for the turbulent kinetic energy (k) and another one for the turbulent dissipation (ϵ). This model is inherently not able to resolve the viscous sublayer of the boundary layer and is somehow insensitive to adverse pressure gradients.

Another typical model with two transport equations is the K-Omega model. While $k-\epsilon$ is typically applied to free stream simulations, $k-\omega$ stands out near walls. A combination of both can also be applied, called $k-\omega\,SST$. This model applies to the simulation a $k-\omega$ near the wall and $k-\epsilon$ far from it, producing adequate results both near the walls and in the far field.

In this work a less complex model is selected, known as Spalart-Allmaras. This model only adds one extra transport equation to solve the problem, and it was formulated for external aerodynamic problems. It is employed to lower the computational cost when a low Reynolds number is present, and in its present formulation is able to reproduce complex phenomena such as laminar-turbulent boundary layer transitions. The equations formulation are collected in the original work of Spalart and Allmaras [71]. Although there exist the possibility to include extra transport equations for the laminar-to-turbulent transition, for which maybe the Langtry-Menter two equations model is the most used ([72]), the Spalart-Allmaras one equation model usually produces good transition results.

The propeller is modeled using a virtual disk approach. This model sets a source term distributed in the disk in the momentum equations of the flow, and simplifies the simulation, not needing a body-fitted mesh around the complex propeller geometry. There are different approaches to modeling a virtual disk:

- Body Force propeller method: this model was designed originally to model marine propellers, setting an induced flow depending on the flow around the ship hull. It requires knowing the propeller performance curve and the position where the thrust is produced.

- 1D Momentum Method: this model was created to calculate wind turbine problems. It is based on one-dimensional momentum theory with wake rotation. The momentum equation's source term represents axial and tangential effects. This method requires knowing the thrust and power coefficients of the propeller as a function of the inflow velocity.

- Blade Element Method (BEMT): It was first designed to capture the aerodynamic interaction between elements when modeling helicopters, as mentioned in the work of Rajagopalan and Mathur [73]. In this method, the propeller is modeled as a distribution of momentum sources. The real propeller geometry and the local velocity field determine each source's strength. It is necessary to know the number of blades and blade geometry exactly, including the chord and twist angle of each section of the blade. Of course, in this method the geometry is not explicitly resolved. The influence of the blade on the flow is possible by imposing the aerodynamic behavior of each blade section. The aerodynamic characteristics are set in terms of lift and drag coefficients of each two-dimensional airfoil that corresponds to each blade cross-section, as a function of the Reynolds number and the angle of attack. During each iteration, the local angle of attack of each propeller section is computed and, with this, the lift and drag distribution. The method also takes into account the induced speed over the blades due to their circulation. The resultant force and torque are used to compute the thrust and power consumption of the propeller, and the results are also used to generate source terms for the rest of the finite-volume CFD simulation. BEMT also allows for trimming the propeller using a non-linear iterative approach. This is the method applied when modeling the propeller in this work.

2.6 Proper Orthogonal Decomposition

A proper orthogonal decomposition (POD) method has been used as an additional tool of analysis in this work. POD is defined as an instrument that tries to simplify a complex problem into a series of deterministic functions that are easier to analyze. Those deterministic functions can be used in modeling the mentioned problem, so in the end, POD can be a pre-design tool.

POD is not a new tool in the fluid dynamic field. It was first introduced by Lumley [74] past half of the last century. Since this moment, this method has been widely used in both numerical and experimental fluid mechanic problems.

Hereunder, some works are highlighted where POD is employed to analyze diverse fluid dynamic problems. In Torregrosa et al.'s [75] work, POD has been used to characterize the unsteady flow inside a combustion chamber. As in this last work, the use of POD proliferates in the field of combustion and thermal engines. Zhu et al. [76] obtained a reduced order model using POD to predict the temperature distribution in a three-way catalytic converter, Shen et al. [77] applied modal decomposition to understand experimental optical measures of the flow inside an ICE cylinder, and in the same vein, Rulli et al. [78] reviewed different flow analysis methods based on POD and applied to PIV application in combustion engines. Outside the combustion field, in the aerodynamic area and ICE related, the proper decomposition is also used, as Broatch et al. [79] investigation where the acoustic field of a radial compressor is characterized.

As in this last work, in the aerodynamic field, the use of POD is also widely used. In the work of Malouin et al. [80], the method is used to interpolate the performance of a transonic flow around an airfoil at different Mach numbers and angles of attack. In the investigation of Mifsud et al. [81], a variable-fidelity model based on POD (VFM) is employed to generate three-dimensional flow models applied to supersonic aircraft to reduce the number of simulations needed and thus limit both the calculation time and the cost. The same first author has a work in Mifsud et al. [82] where uses a reduced order method (ROM) extracted using POD to characterize a high angle of attack flying aircraft.

Usually, the final goal of POD is to decompose a space vector into a series of spatial functions. Those spatial functions are modulated by means of other coefficients, known as time coefficients (if the problem is time-dependent) or configuration coefficients. Each spatial function will be orthonormal regarding the other functions. This way, the set of functions will be independent since their vector product is zero. Also, they share an interesting property. It is possible to order the functions or modes according to how much of the problem's total fluctuating kinetic energy (TKE) explain, which is the sum of the variances of all the studied vectors. In other words, how much of the problem can be represented by each mode. Choosing the first modes that best describe the problem and ignoring the rest, reduced-order models can be built that simplify what has been studied.

The POD application with this work's conditions is developed in section 4.7.

2.7 Summary

All the technologies that this work involves and were first introduced in Chapter 1 are reviewed in this chapter. For this purpose, the principal components and analysis of electric hybridization, distributed electric propulsion, and boundary layer ingestion are explained with the support of a literature review.

Once the operation and application of the technologies above are understood, as well as the advantages and disadvantages associated with their use, it will be possible to define an aircraft that combines them, as seen in the next chapter 3.

Finally, the main aspects of the methods with the purpose of both analyzing and analyzing aircraft that combine these technologies are reviewed from a theoretical point of view. This chapter focuses, always supported by a bibliographical study, on the choice of methods and models when using CFD and on the application of POD. These methods can be seen applied in chapter 4.

2.8 References

[22] J. Lieh, E. Spahr, A. Behbahani, and J. Hoying. "Design of hybrid propulsion systems for unmanned aerial vehicles". In: *47th AIAA/ASME/SAE/ASEE Joint Propulsion Conference and Exhibit 2011*. San Diego, California, USA, Aug. 2011, pp. 1–14. DOI: 10.2514/6.2011-6146 (cit. on pp. 3, 14).

[33] D. K. Hall, A. C. Huang, A. Uranga, E. M. Greitzer, M. Drela, and S. Sato. "Boundary layer ingestion propulsion benefit for transport aircraft". In: *Journal of Propulsion and Power* 33.5 (2017), pp. 1118–1129. ISSN: 15333876. DOI: 10.2514/1.B36321 (cit. on pp. 5, 21).

[37] M. Elsalamony and L. Teperin. "2D Numerical Investigation of Boundary Layer Ingestion Propulsor on Airfoil". In: *7th European Conference for Aeronautics and Space Sciences (EUCASS)* (2017), pp. 1–11. DOI: 10.13009/EUCASS2017-67 (cit. on pp. 5, 21, 46, 102).

[40] R. Capata, L. Marino, and E. Sciubba. "A hybrid propulsion system for a high-endurance UAV: configuration selection, aerodynamic study, and gas turbine bench tests". In: *Journal of Unmanned Vehicle Systems* 02.01 (2014), pp. 16–35. ISSN: 2291-3467. DOI: 10.1139/juvs-2013-0005 (cit. on p. 14).

[41] R. Jurecka and K. Bencalik. "Airplanes with an electric motor". In: *Aviation* 16.3 (2012), pp. 63–68. ISSN: 16487788. DOI: 10.3846/16487788.2012.732304 (cit. on p. 14).

[42] "Fuel cell/battery hybrid UAV takes off in Taiwan". In: *Fuel Cells Bulletin* 2010.6 (2010), pp. 4–5. ISSN: 1464-2859. DOI: https://doi.org/10.1016/S1464-2859(10)70177-2. URL: https://www.sciencedirect.com/science/article/pii/S1464285910701772 (cit. on p. 14).

[43] M. F. Hoogreef, R. Vos, R. de Vries, and L. L. Veldhuis. "Conceptual assessment of hybrid electric aircraft with distributed propulsion and boosted turbofans". In: *AIAA Scitech 2019 Forum* May 2020 (2019). DOI: 10.2514/6.2019-1807 (cit. on p. 14).

[44] G. S. Ehsani M. Gao Y. and E. A. *Modern Electric, Hybrid Electric, and Fuel Cell Vehicles*. CRC Press, 2010, pp. 120–136. ISBN: 0-8493-3154-4 (cit. on p. 14).

[45] J. Schömann. *Hybrid-electric Propulsion Systems for Small Unmanned Aircraft*. Verlag Dr. Hut, 2014. ISBN: 9783843918473. URL: https://books.google.es/books?id=idECrgEACAAJ (cit. on p. 15).

[46] H. D. Kim, J. J. Berton, and S. M. Jones. “Low noise cruise efficient short take-off and landing transport vehicle study”. In: *Collection of Technical Papers - 6th AIAA Aviation Technology, Integration, and Operations Conference* 1.February (2006), pp. 362–372. DOI: 10.2514/6.2006-7738 (cit. on p. 18).

[47] T. C.-M. Insititute. *The ‘Silent’ Aircraft Initiative*. Last accessed: 2022-09-01. URL: %7Bhttp://silentaircraft.org/%7D (cit. on p. 18).

[48] Y. Liu, A. P. Dowling, J. I. Hileman, and A. R. Quayle. “Surface roughness noise prediction for silent aircraft experimental design SAX-40”. In: *46th AIAA Aerospace Sciences Meeting and Exhibit* January (2008). DOI: 10.2514/6.2008-45 (cit. on p. 18).

[49] D. Siliang, Z. Qijun, and W. Bo. “Research on Distributed Jet Blowing Wing Based on the Principle of Fan-Wing Vortex-Induced Lift and Thrust”. In: *International Journal of Aerospace Engineering* 2019 (2019). ISSN: 16875974. DOI: 10.1155/2019/7561856 (cit. on p. 18).

[50] B. Goeksel. “Novel Distributed Air-Breathing Plasma Jet Propulsion Concept for All-Electric High-Altitude Flying Wings”. In: April. 2017, pp. 2016–2017 (cit. on p. 18).

[51] A. S. Goharadani. *Distributed Propulsion Technology*. Nova Science Publishers, 2014, pp. 173–1174 (cit. on p. 19).

[52] J. L. Felder, H. D. Kim, and G. V. Brown. “Turboelectric distributed propulsion engine cycle analysis for hybrid-wing-body aircraft”. In: *47th AIAA Aerospace Sciences Meeting including the New Horizons Forum and Aerospace Exposition*. Orlando, Florida, USA, 2009, pp. 1–25. ISBN: 9781563479694. DOI: 10.2514/6.2009-1132 (cit. on p. 19).

[53] S. Clarke and S. Redifer. “NASA ’ s X -57 Maxwell All-Electric Aircraft”. In: 2020 (cit. on p. 19).

[54] H. D. Kim, A. T. Perry, and P. J. Ansell. “A Review of Distributed Electric Propulsion Concepts for Air Vehicle Technology”. In: *2018 AIAA/IEEE Electric Aircraft Technologies Symposium, EATS 2018* (2018). DOI: 10.2514/6.2018-4998 (cit. on p. 19).

[55] A. M. O. Smith and H. E. Roberts. “The Jet Airplane Utilizing Boundary Layer Air for Propulsion”. In: *Journal of the Aeronautical Sciences* 14.2 (1947), pp. 97–109. DOI: 10.2514/8.1273 (cit. on p. 20).

[56] W. M. Douglass. *Propulsive Efficiency with Boundary Layer Ingestion*. 1970 (cit. on p. 20).

[57] A. Uranga et al. “Boundary layer ingestion benefit of the D8 transport aircraft”. In: *AIAA Journal* 55.11 (2017), pp. 3693–3708. ISSN: 00011452. DOI: 10.2514/1.J055755 (cit. on p. 20).

[58] A. Uranga, M. Drela, D. K. Hall, and E. M. Greitzer. "Analysis of the aerodynamic benefit from boundary layer ingestion for transport aircraft". In: *AIAA Journal* 56.11 (2018), pp. 4271–4281. ISSN: 00011452. DOI: 10.2514/1.J056781 (cit. on p. 20).

[59] L. W. Hardin, G. Tillman, O. P. Sharma, J. Berton, and D. J. Arend. "Aircraft system study of boundary layer ingesting propulsion". In: *48th AIAA/ASME/SAE/ASEE Joint Propulsion Conference and Exhibit 2012* December 2015 (2012). DOI: 10.2514/6.2012-3993 (cit. on p. 20).

[60] J. R. Welstead and J. L. Felder. "Conceptual design of a single-aisle turboelectric commercial transport with fuselage boundary layer ingestion". In: *54th AIAA Aerospace Sciences Meeting* 0.January (2016), pp. 1–17. DOI: 10.2514/6.2016-1027 (cit. on p. 20).

[61] P. Angelique. "Performance of a Boundary Layer Ingesting Propulsion System by Angelique Plas". MA thesis. 2006, p. 114 (cit. on p. 20).

[62] L. H. Smith. "Wake ingestion propulsion benefit". In: *Journal of Propulsion and Power* 9.1 (1993), pp. 74–82. ISSN: 07484658. DOI: 10.2514/3.11487 (cit. on pp. 21, 59).

[63] P. Lv, A. G. Rao, D. Ragni, and L. Veldhuis. "Performance analysis of wake and boundary-layer ingestion for aircraft design". In: *Journal of Aircraft* 53.5 (2016), pp. 1517–1526. ISSN: 15333868. DOI: 10.2514/1.C033395 (cit. on p. 21).

[64] S. Sato. "The Power Balance Method For Aerodynamic Performance Assessment". MA thesis. 2012. ISBN: 978-1-4244-7992-4. DOI: 10.1109/ICIP.2010.5649226 (cit. on p. 21).

[65] M. Drela and T. J. Kohler. "Power balance in aerodynamic flows". In: *AIAA Journal* 47.7 (2009), pp. 1761–1771. ISSN: 00011452. DOI: 10.2514/1.42409 (cit. on p. 22).

[66] M. Drela. "Version Terms of Use Power Balance in Aerodynamic Flows". In: *AIAA Journal* 47 (2009). ISSN: 1533-385X. DOI: http://dx.doi.org/10.2514/1.42409 (cit. on p. 22).

[67] J. Meseguer and A. Sanz. *Aerodinámica básica*. Universidad Politécnica de Madrid, 2005. ISBN: 84-921113-8-0 (cit. on p. 22).

[68] E. S. Hendricks. "A Review of Boundary Layer Ingestion Modeling Approaches for use in Conceptual Design". In: July 2018 (2018). URL: http://www.sti.nasa.gov (cit. on p. 25).

[69] J. John D. Anderson. *Computational Fluid Dynamics: The Basics with Applications*. McGraw-Hill, 1995. ISBN: 0-07-113210-4 (cit. on p. 25).

[70] R. Verstappen and A. Veldman. “Direct Numerical Simulation of Turbulence at Lower Costs”. In: *Journal of Engineering Mathematics* 32 (Oct. 1997). DOI: 10.1023/A:1004255329158 (cit. on p. 25).

[71] P. Spalart and S. Allmaras. “A One-Equation Turbulence Model for Aerodynamic Flows”. In: *AIAA* 439 (Jan. 1992). DOI: 10.2514/6.1992-439 (cit. on p. 26).

[72] F. R. Menter, R. Langtry, and S. Völker. “Transition Modelling for General Purpose CFD Codes”. In: *Flow, Turbulence and Combustion* 77.1-4 (2006), pp. 277–303. ISSN: 15731987. DOI: 10.1007/s10494-006-9047-1 (cit. on p. 26).

[73] R. Rajagopalan and S. R. Mathur. *Three dimensional analysis of a rotor in forward flight*. 1989. DOI: 10.2514/6.1989-1815 (cit. on p. 27).

[74] J. Lumley. “The structure of inhomogeneous turbulent flows.” In: *Atmospheric turbulence and radio wave propagation* (1967). DOI: 10.2514/1.C033395 (cit. on p. 28).

[75] A. J. Torregrosa, A. Broatch, J. García-Tíscar, and J. Gomez-Soriano. “Modal decomposition of the unsteady flow field in compression-ignited combustion chambers”. In: *Combustion and Flame* 188 (2018), pp. 469–482. ISSN: 15562921. DOI: 10.1016/j.combustflame.2017.10.007. URL: https://doi.org/10.1016/j.combustflame.2017.10.007 (cit. on p. 28).

[76] Z. Zhu, S. Midlam-Mohler, and M. Canova. “Development of physics-based three-way catalytic converter model for real-time distributed temperature prediction using proper orthogonal decomposition and collocation”. In: *International Journal of Engine Research* 22.3 (2021), pp. 873–889. ISSN: 20413149. DOI: 10.1177/1468087419876127 (cit. on p. 28).

[77] L. Shen, K. Y. Teh, P. Ge, F. Zhao, and D. L. Hung. “Temporal evolution analysis of in-cylinder flow by means of proper orthogonal decomposition”. In: *International Journal of Engine Research* 22.5 (2021), pp. 1714–1730. ISSN: 20413149. DOI: 10.1177/1468087420917246 (cit. on p. 28).

[78] F. Rulli, S. Fontanesi, A. D’Adamo, and F. Berni. “A critical review of flow field analysis methods involving proper orthogonal decomposition and quadruple proper orthogonal decomposition for internal combustion engines”. In: *International Journal of Engine Research* 22.1 (2021), pp. 222–242. ISSN: 20413149. DOI: 10.1177/1468087419836178 (cit. on p. 28).

[79] A. Broatch, J. García-Tíscar, F. Roig, and S. Sharma. "Dynamic mode decomposition of the acoustic field in radial compressors". In: *Aerospace Science and Technology* 90 (2019), pp. 388–400. ISSN: 12709638. DOI: 10.1016/j.ast.2019.05.015. URL: https://doi.org/10.1016/j.ast.2019.05.015 (cit. on p. 28).

[80] B. Malouin, J. Y. Trépanier, and M. Gariépy. "Interpolation of transonic flows using a proper orthogonal decomposition method". In: *International Journal of Aerospace Engineering* 2013 (2013). ISSN: 16875966. DOI: 10.1155/2013/928904 (cit. on p. 28).

[81] M. J. Mifsud, D. G. MacManus, and S. T. Shaw. "A variable-fidelity aerodynamic model using proper orthogonal decomposition". In: *International Journal for Numerical Methods in Fluids* 82.10 (2016), pp. 646–663. ISSN: 10970363. DOI: 10.1002/fld.4234 (cit. on p. 28).

[82] M. Mifsud, R. Zimmermann, and S. Görtz. "Speeding-up the computation of high-lift aerodynamics using a residual-based reduced-order model". In: *CEAS Aeronautical Journal* 6.1 (2015), pp. 3–16. ISSN: 18695590. DOI: 10.1007/s13272-014-0125-0 (cit. on p. 28).

CHAPTER 3

Aircraft design and component selection

Contents

Figures

Tables

3.1 Introduction

BEFORE running any calculation, it is crucial to know the kind of aircraft that will be optimized. The selection of a proper plane is not a trivial matter. The final design depends strongly on the mission selection, and, likewise, the mission depends on flight regulation and all the components of which the aircraft is composed and available.

Now that the different technologies that contribute to the aircraft design (series HE, DEP and BLI) have been introduced in the previous chapter, it is possible to select the different components that will be part of the aircraft.

This chapter focuses on selecting all components and parameters that influence the final design, and all the components available to build the aircraft. Last, a preliminary study about range gain and fuel benefits in HE DEP BLI aircraft is presented.

3.2 Aircraft main design parameters

Regarding the main research topic of this work, the use of DEP technology with BLI applied on the wing is more readily applicable to a "classic" or "fixed-wing" aircraft architecture. For this reason, the design will revolve around an aircraft of these characteristics. The use of fixed-wing UAVs is usually linked to applications with long endurance or a wide operational range, such as border surveillance, fire control, etc., as Sayler shows in her drone review [83].

Additionally, the maximum take-off mass (*MTOM*) is set as a parameter and a design limit at 25 kg. This limitation is chosen based on civil unmanned aircraft regulations of Spanish legislation [84], being a similar limitation in the rest of European territories such as France or Poland [85]. It is perfectly possible to extend this limit up to 150 kg; however, new flight permissions are needed at the administrative level. Also, the civil flight operation can only be carried out in a segregated flight space, so limits higher than 25 kg are reserved for military application aircraft. Setting the *MTOM*, both aerodynamical design parameters and a propulsive plant can also be arranged.

In the European Union, the operation of a drone of this *MTOM* obeys the "open" operational category. Inside this category, due to the maximum *MTOM*, they fall in the subcategory A3. The operation in this subcategory must be performed in areas with a horizontal safety of 150 m from any inhabited or industrial area and ensure that no one is at risk. Inside the A3 subcategory, there are two possible classes to classify these aircraft, C3 and C4. The main difference between the two classes is that the C3 class is reserved for drones with an electric power supply. If due to the solicited mission, any point of the "open" category could not be accomplished, the aircraft must follow the "specific"

category of UAS operation, class C6. Further information about the operational categories can be found in the EASA regulations of 2019/947 [86] and 2019/945 [87], and summarized by Alamouri et al. [88].

There are several RPAS or UAVs on the market with characteristics similar to those desired. Some examples are the Penguin C from UAV Factory [89] (Fig. 3.1) , with a wingspan of similar weight and cruise speeds between 20 m/s and 30 m/s, or the TARSIS 25 from AERTEC Solutions [90] (Fig. 3.2), which has a wingspan of 2 m. The main design parameters of these two aircraft are collected in Table 3.1.

Figure 3.1: Penguin C MIL UAS manufactured by UAV Factory.

	Penguin C	**Tarsis 25**
Wingspan	3.3 m	2 m
MTOM	23 kg	25 kg
Cruise Speed	19-22 m/s	27 m/s
Ceiling	5000 m	4000 m
Propulsion	28cc EFI engine	50 cc

Table 3.1: Penguin C and TARSIS 25 main design parameters.

Considering these aircraft, the first geometric parameters applied in the design of the aircraft presented in this work can be defined. A wingspan (b) of 2 m is set with a wing aspect ratio ($\mathcal{R} = b^2/S$) of 10, which sets the chord length of the airfoil (c) to 0.2 m considering that the wing is rectangular.

As the main airfoil, a Selig-Donovan 7003 is employed with a constant chord along the entire wing. This airfoil was designed by Selig et al. [91] for middle

Figure 3.2: RPAS TARSIS 25 manufactured by AERTEC Solutions.

and low Reynolds numbers and is popular in the literature, so it turns out easy to find experimental and CFD performance and geometrical data. Some examples can be found in the reserach of Schmidt and Breuer [92], Hain et al. [93], Burgmann et al. [94], Galbraith and Visbal [95], just to name a few. The Reynolds number is defined in 3.1:

$$Re = \frac{\rho \cdot U \cdot c}{\mu}, \tag{3.1}$$

where ρ, and μ are, respectively, the density and the dynamic viscosity of the air, U is the flight velocity, and c is a characteristic length, in this definition it is the airfoil chord length.

Using the same example data and the *MTOM* equal to 25 kg, the power needed (P) can be calculated in equation 3.2.

$$P = D \cdot U + W \cdot V. \tag{3.2}$$

In this equation the aircraft weight is W, and considering a low ascensional velocity V, the power leads to a maximum value near of 1 kW. Additionally D

represents the airplane drag, and can be expressed as:

$$D = \frac{1}{2} \cdot \rho \cdot U^2 \cdot S \cdot \left(C_{D0,\text{wing}} + C_{D0,\text{extra}} + \frac{C_L^2}{\pi \cdot \mathcal{AR} \cdot e} \right) \tag{3.3}$$

where, $S = b \cdot c$ is the wing surface, $C_{D0,\text{wing}}$ is the parasitic drag coefficient of the wing, and $C_{D0,\text{extra}}$ is the parasitic drag coefficient due to the rest of the components, such as the fuselage, the landing gear, the vertical and horizontal stabilizers, etc.; C_L is the lift coefficient which causes the induced part of the drag, defined for this case in equation 3.4.

$$C_L = \frac{MTOM}{\rho \cdot S \cdot U^2} \tag{3.4}$$

The values of $C_{D0,\text{wing}}$ is computed using quick numerical panel methods using XFLR5 [96], which gives results consistent with the experimental data found in the literature. This software is based on XFOIL [97] to compute a solution of the airfoil using a potential flow method with interactive boundary layer corrections. The value of $C_{D0,\text{extra}}$ is computed using geometrical information of similar mission aircraft, including the mentioned Penguin C and the Harmon and Hiserote's aircraft [18, 17]. The Oswald efficiency factor e has been calculated using also the information of similar aircraft. Taking into account the different methods described by Hoerner [98], and Niţă and Scholz [99], an e factor of 0.8 is set.

Providing this power, GX-35 designed by Honda [100] has been selected as ICE. This ICE can be found in multiple UAV design studies of similar power requirements and *MTOM*, as can be seen in the works of Ausserer et al. [18], Harmon et al. [17], and Schoemann and Hornung [101]. The application of the Honda GX-35 is desirable for multiple reasons. The low specific weight of the engine compared to other ICE makes it suitable for this kind of application. Also, this engine has been tested on a test bench and the data is readily availabe in the literature, so its brake-specific fuel consumption (*BSFC*) for different operations can be used. In Mengistu's thesis [21], the *BSFC* map has been measured between 0 % and 60 % of its maximum torque. The author was unable to specify data at maximum load due to instabilities in the measurement with his test bench, but these data can be completed with those obtained by Semcon company [102].

A DA4052 designed and tested in a wind tunnel by the University of Illinois Urbana-Champaign (UIUC) [103] has been employed as a two-blade propeller. In addition to a wide operating range, the UIUC provides complete geometric data, making it suitable for implementing a future blade-element method theory model (BEMT) or scaling the propeller. Below these lines, the geometry employed to model the actuator disk with a radius R of 0.04 m is provided in Table 3.2.

r/R	c/R	θ_0 [°]	c [mm]
0.02	0.110	38.79	4.4
0.15	0.110	38.79	4.4
0.16	0.065	38.79	2.6
0.2	0.065	38.79	2.6
0.3	0.352	38.79	14.1
0.35	0.352	33.75	14.1
0.4	0.352	30.82	14.1
0.45	0.352	27.89	14.1
0.5	0.317	25.63	12.7
0.55	0.283	23.37	11.3
0.6	0.255	21.75	10.2
0.65	0.228	20.12	9.1
0.7	0.204	18.89	8.1
0.75	0.180	17.66	7.2
0.8	0.155	16.87	6.2
0.85	0.131	16.09	5.2
0.9	0.101	15.42	4.1
0.95	0.071	14.75	2.8
1	0.041	14.07	1.6

Table 3.2: Propeller geometry provided by the University of Illinois Urbana-Champaign (UIUC) [103] scaled to a radius of 0.04 m.

In Table 3.2, c is the chord length and θ_0 is the twist angle of each blade section. The main design parameters already described are collected in Table 3.3.

3.3 Design discretization and component selection

Three different designs are defined with the same wing, engine, and propeller model. In the first place, the baseline case is determined. The baseline correspons to a UAV with a single propeller with the ICE as the only propulsive plant system, similar to what can be seen in Fig. 3.1 or Fig. 3.2, but it would also be valid to think of an aircraft whose propeller is located in the nose. For the dimensions already described and listed in Table 3.3, a propeller with a diameter of 0.229 m is estimated as necessary. The propeller is directly coupled to the ICE through a gearbox that allows the rotation to be multiplied at a ratio of 2.75 with an efficiency of 90 %, and it is not affected by BLI conditions.

Then, a pure hybrid case is defined. This case uses the same baseline propeller and ICE, but these both are mechanically decoupled. In the pure

Design parameters	
Aspect ratio	10
Wing area	$0.4\,\mathrm{m}^2$
Wing span	$2\,\mathrm{m}$
Wing chord	$0.2\,\mathrm{m}$
Maximum takeoff mass	$25\,\mathrm{kg}$
Aerodynamic parameters	
$C_{D0,\mathrm{extra}}$ (fuselage, empennage, others)	0.011
Oswald efficiency factor (e)	0.8
Engine data	
Stroke	4
Displacement	$35.8\,\mathrm{cm}^3$
Net power (at 7000 rpm)	$1\,\mathrm{kW}$
Max. net torque (at 5500 rpm)	$1.6\,\mathrm{N\,m}$
Dry mass	$3.33\,\mathrm{kg}$

Table 3.3: Aerodynamic, design parameters and engine data

hybrid, the ICE is coupled with an electric generator. The electric generator powers the ESC that controls an electric engine coupled with the propeller. This way, the rotational velocity of the propeller is totally decoupled from the ICE torque.

Finally, this work's central configuration is defined as an aircraft that combines HE technology with DEP and BLI. The power plant layout is the same as the pure hybrid case but includes multiple small electric engines and propellers distributed near the wing's trailing edge.

The propulsive plant change can be translated into important changes in the operating empty mass of the airplane. Looking for commercial components that meet the characteristics of each design, the weight gain due to hybridization is estimated at 3 % for the pure hybrid case and 5 % for the hybrid case with DEP and BLI, which is consistent with the hybrid RPAS design conducted by Harmon [17].

Some of the increased weight of the DEP system with BLI could be mitigated by a clever distribution of the engines along the wing, as noted in the investigation of Moore and Ning [27], and the research of Amoozgar et al.[29]. Thanks to a correct distribution of engines along the wing, the bending moment of the wing can be decreased, which would allow the use of a lighter wing. However, this design has not been taken into account since the same type of wing has been maintained for all designs. Table 3.4 shows the different commercial elements

taken for the weight calculation, assuming the use of 13 engines in the DEP with BLI case. In no case do the elements selected here or the use of 13 electric motors respond to an optimized final design, so there could be small variations in weight.

HE + DEP + BLI			
Element	**Name**	**Mass [kg]**	**Price [€]**
Generator	Turnigy Aerodrive SK3 - 4250-410kv	0.260	41.35
Motor	Turnigy 4500kv 2610 EDF Outrunner	0.054	11.39
ESC	Turnigy Multistar 32 bits 12 A Race Spec ESC	0.006	5.23
Rectifier	3 Phase Rectifier Bridge Powersem PSD 82	0.160	50.92
Wire	AWG 22 and AWG12	0.100	47.95
Propeller	APC 4.1x4.1E	0.003	5.46
	Total extra increase for 13 propellers	1.351	427.26
	Increase relative to baseline case [%]	5.40	
HE single engine			
Element	**Name**	**Mass [kg]**	**Price [€]**
Generator	9225-160KV Turnigy Multistar	0.329	92.84
Motor	NTM Prop Serie Drive 35-36A 1800KV/875W	0.126	25.06
ESC	YEP 80A SBEC	0.070	43.99
Rectifier	3 Phase Rectifier Bridge Powersem PSD82	0.160	50.92
Wire	AWG 12	0.018	47.95
Propeller	APC B9x9E	0.018	8.43
	Total extra increase	0.721	260.76
	Increase relative to baseline case [%]	2.9	

Table 3.4: Off-the-shelf components with masses and prices

In the same table, the indicative price of every component is shown. Although this work does not revolve around economic costs, it is important to point out that a hybrid aircraft adaptation with DEP and BLI can double the cost of a pure hybrid adaptation. The extra cost only takes into account commercial off-the-shelf components and does not include skilled labour costs.

As an aid to visualization, a sketch of the UAV configuration with HE DEP BLI has been added in Fig. 3.3. It must be taken into account that this sketch does not obey the final design nor is it to scale.

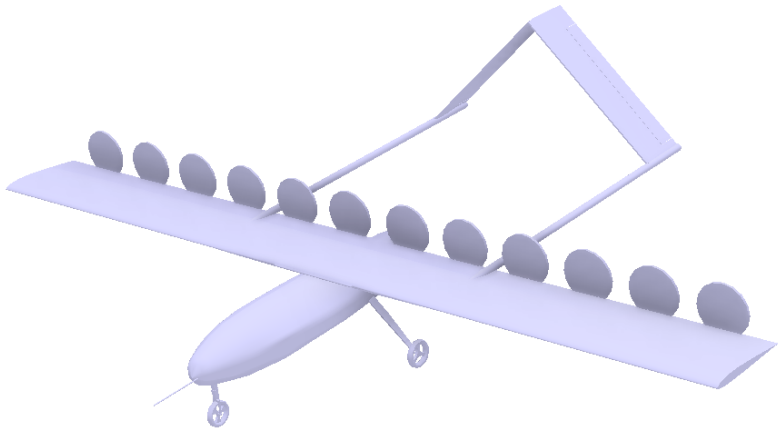

Figure 3.3: HE DEP BLI UAV sketch. Behind the trailing edge each disc represents the possible position of the distributed propellers. This sketch does not obey the final design nor is it to scale.

3.4 Preliminary study on range gains and fuel benefits

Considering the weight gain of the DEP and BLI configuration, the question arises as to whether this system is still interesting to achieve increased aircraft operating range or fuel savings. A quick preliminary study is proposed, comparing the range and total fuel required between the baseline and HE DEP BLI configuration.

Some concessions are applied to simplify the study that takes it away from a realistic case, but they help to give a rough idea of the problem:

- Average cruise conditions with constant velocity are considered for all parameters and efficiencies.
- The ICE's brake-specific fuel consumption ($BSFC$) is constant at all moments.
- The aerodynamic efficiency or lift-to-drag ratio (L/D) is constant at all moments.
- The propulsive efficiency (η_p) of the propeller is constant at all moments.

- The effect of weight loss from burning fuel does not affect any efficiency.

The integral form of the Breguet equation, as presented by Nygren and Shulz [104] in eq. 3.5, is used to analyze the baseline aircraft range.

$$R_{\text{baseline}} = \left(\frac{\eta_p \cdot \eta_m}{g \cdot BSFC} \cdot \frac{L}{D} \right)_{\text{avg,baseline}} \log \frac{M_0}{M_1}, \tag{3.5}$$

where η_m is a mechanical efficiency due to the use of a gearbox to supply the difference of torque between the ICE and the propeller and g is the gravity acceleration. Masses M_0 and M_1 are respectively, the initial and final aircraft mass, developed in eq. 3.6.

$$\begin{aligned} M_0 &= MTOM_{\text{baseline}} = OEM_{\text{baseline}} + PL + FM \\ M_1 &= OEW_{\text{baseline}} + PL + RF, \end{aligned} \tag{3.6}$$

where OEM_{baseline} is the operative empty mass, PL is the mass that corresponds to the payload, FM is the initial mass of fuel, and RF is a possible fuel reserve at the end of the flight.

Following eq. 3.5, the same equation can be presented in a series hybrid case in eq. 3.7.

$$R_{\text{hybrid}} = \left(\frac{\eta_p \cdot \eta_e}{g \cdot BSFC} \cdot \frac{L}{D} \right)_{\text{avg,hybrid}} \log \frac{MTOM_{\text{hybrid}}}{OEM_{\text{hybrid}} + PL + RF}. \tag{3.7}$$

In this case, no gearbox is needed because there is no mechanical coupling between the ICE and the propeller. However, an electrical efficiency η_e due to the energy conversion and all electrical components is introduced. In the hybrid case, the operative empty mass is defined in eq. 3.8.

$$OEM_{\text{hybrid}} = OEM_{\text{baseline}} + EM, \tag{3.8}$$

where EM is the additional mass due to the use of extra electrical components and propellers.

Comparing the range between configurations, Fig. 3.4 is obtained.

Fig. 3.4 represents the range gain as a function of the increase in weight and the global efficiency increase due to using a HE DEP BLI configuration. Global efficiency refers to the product of aerodynamic efficiency, propulsive efficiency, specific fuel consumption and additional parameters that affect the performance.

It may seem like a high product of efficiencies is needed at first since, if the OEM increases by 3 %, more than 10 % of the global efficiency is required in order to gain range in a new design. Considering an increase of the OEM in the new design of 5 %, the global efficiency required increases up to almost 25 %.

However, authors such as Teperin [34] point out an improvement in efficiency of more than 20 % in their work. Also, Atinault et al. [105] experimentally

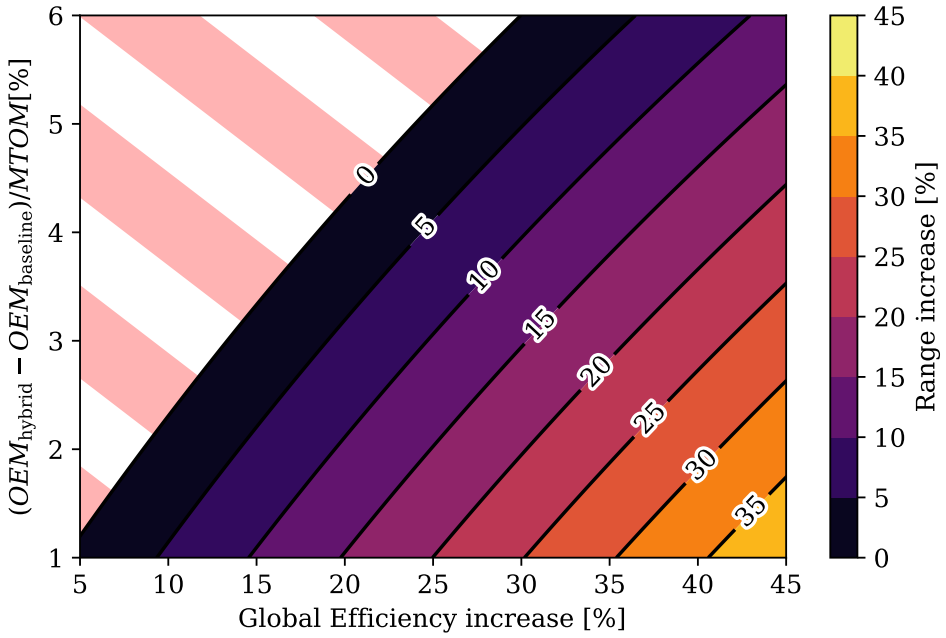

Figure 3.4: Range increase as a function of the increase in weight and global efficiency.

find improvements between 10 % and 45 % depending on the operating point. However, Elsamony et al. [37] point out that the increase in drag diminishes the power savings gain, obtaining improvements slightly greater than 12 %.

Nevertheless, in the mentioned studies, no improvement in efficiency due to the use of hybridization or distributed electric propulsion is considered. Presumably, the ICE set in a series hybrid configuration will work at a more optimal point of the ICE's map compared with a baseline configuration due to the mechanical decoupling between ICE and propeller, as introduced in the section 2.2.

The same problem can be seen from other perspective. From another point of view, it is possible to study the fuel weight decrease using a HE DEP BLI configuration to fly the same range as a baseline aircraft. In this case, equations 3.5 and 3.7 are written in terms of mass fraction f in eq. 3.9 and eq. 3.10 respectively.

$$R_{\text{baseline}} = \left(\frac{\eta_p \cdot \eta_m}{g \cdot BSFC} \cdot \frac{L}{D}\right)_{\text{avg,baseline}} \log \frac{1}{f_{OEM,\text{baseline}} + f_{PL} + f_{RF}}, \tag{3.9}$$

$$R_{\text{hybrid}} = \left(\frac{\eta_p \cdot \eta_e}{g \cdot BSFC} \cdot \frac{L}{D}\right)_{\text{avg,hybrid}} \log \frac{1}{f_{OEM,\text{hybrid}} + f_{PL} + f_{RF}}. \tag{3.10}$$

The hybrid case, the eq. 3.10 can be written in terms of the fuel reduction mass fraction f_{FR} in eq. 3.11.

$$R_{\text{hybrid}} = \left(\frac{\eta_p \cdot \eta_e}{g \cdot BSFC} \cdot \frac{L}{D}\right)_{\text{avg,hybrid}} \log \frac{1 - f_{FR}}{f_{OEM,\text{baseline}} + f_{PL} + f_{RF} + f_{EM}}. \tag{3.11}$$

This fuel reduction can be referred to the initial fuel mass in the baseline case as f'_{FR} in eq. 3.12.

$$f'_{FR} = \frac{f_{FR}}{f_{FM}} = \frac{f_{FR}}{1 - f_{OEM,\text{baseline}} - f_{PL}}. \tag{3.12}$$

Comparing both eq. 3.9 and eq. 3.11, the f'_{FR} can be calculated in eq. 3.13.

$$f'_{FR} = \frac{1 - \left(f_{OEM,\text{baseline}} + f_{PL} + f_{RF} + f_{EM}\right) \cdot \left(\frac{1}{f_{OEM,\text{baseline}} + f_{PL} + f_{RF}}\right)^{\frac{\left(\frac{\eta_p \eta_m}{gBSFC} \frac{L}{D}\right)_{\text{avg,baseline}}}{\left(\frac{\eta_p \eta_e}{gBSFC} \frac{L}{D}\right)_{\text{avg,hybrid}}}}}{1 - f_{OEM,\text{baseline}} - f_{PL}}. \tag{3.13}$$

The fuel weight decrease can now be plotted as a function of the global efficiency increase and the penalization in weight using a HE DEP BLI configuration in Fig. 3.5.

In Fig. 3.5 a similar conclusion is extracted compared with the range increase of Fig. 3.4. To achieve a decrease in fuel, and therefore to reduce pollulant and greenhouse emissions in the same range mission, the HE DEP BLI system needs to improve the global efficiency of the system by around 25 % if the weight increases a 5 %.

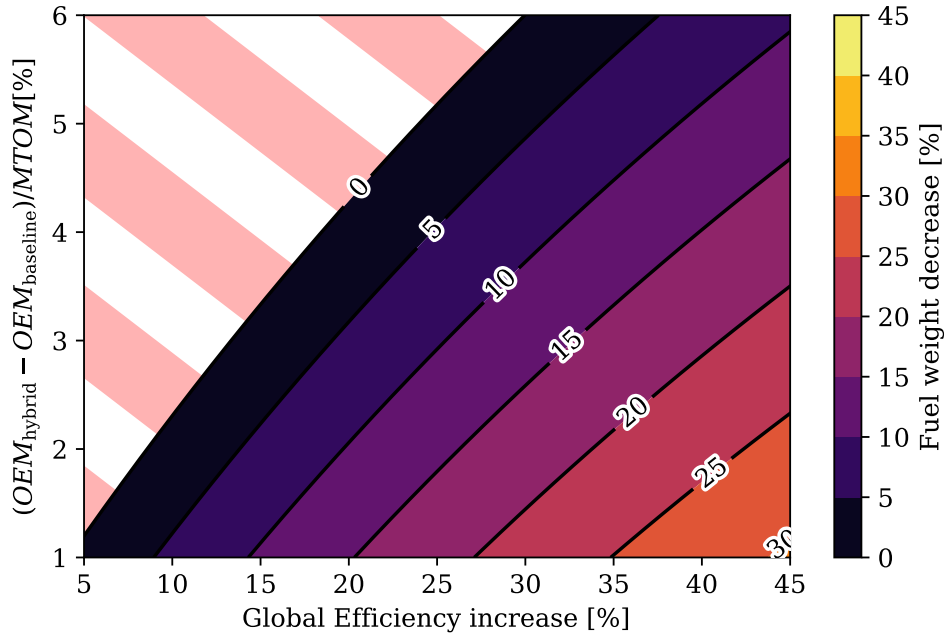

Figure 3.5: Range increase as a function of the increase in weight and global efficiency.

3.5 Summary

This chapter has focused on the selection of components and main design of a UAV with a series hybrid electrical power plant, distributed electric propulsion, and boundary layer ingestion. The first parameter set is the maximum take-off mass adjusting it according to the maximum allowed by Spanish law for aircraft for civil use without certifications.

Most geometric parameters are set depending on the chosen MTOM and similar aircraft, including wing span, aspect ratio, airfoil and chord. With those geometrical parameters set, the main ICE is selected. This ICE is employed in all aircraft described configurations, baseline (without hybridization, DEP and BLI), pure hybrid (without DEP and BLI) and HE DEP BLI aircraft. On the other side of hybridization, the propeller design is also selected for all configurations, considering the blade size change in the DEP BLI case.

A search for commercial components is conducted with the main geometric and power-plant-related aspects defined. This component research aims to estimate the weight increment due to the use of a hybrid configuration. Additionally, a price comparison is performed.

Finally, a preliminary study on the range and fuel benefits is carried out. This quick study is based on the integral Breguet's equations and sets all the efficiencies as constant during the flight, which is not a realistic approach. The study's objective is to know how much efficiency should increase due to the use of hybridization, DEP and BLI, so that the weight gain derived from these systems does not imply a penalty but a benefit. It is concluded that a DEP BLI aircraft needs to increase the product of efficiencies by at least 20 % to obtain a range benefit compared with a baseline case and 25 % to receive a fuel benefit. According to the literature, a BLI system may achieve an efficiency improvement of between 10 % and 45 %. Considering an aircraft with a combination of HE and DEP added to the BLI, it should be enough to decrease the fuel needed in a mission compared with a plane without these systems.

3.6 References

[17] F. G. Harmon, A. A. Frank, and J. J. Chattot. "Conceptual design and simulation of a small hybrid-electric unmanned aerial vehicle". In: *Journal of Aircraft* 43.5 (2006), pp. 1490–1498. ISSN: 00218669. DOI: 10.2514/1.15816 (cit. on pp. 3, 40, 42).

[18] J. K. Ausserer and F. G. Harmon. "Integration, validation, and testing of a hybrid-electric propulsion system for a small remotely-piloted aircraft". In: *10th Annual International Energy Conversion Engineering Conference*. Atlanta, GA, USA: AIAA, Aug. 2012, pp. 1–11. ISBN: 9781624101908. DOI: 10.2514/6.2012-4239 (cit. on pp. 3, 40).

[21] I. H. Mengistu. "A small internal combustion engine testing for a hybrid-electric remotely-piloted aircraft". MA thesis. Wright-Patterson Air Force Base, OH, USA: Air Force Institute of Technology, 2011, p. 124 (cit. on pp. 3, 40).

[27] K. R. Moore and A. Ning. "Distributed electric propulsion effects on traditional aircraft through multidisciplinary optimization". In: *AIAA/ASCE/AHS/ASC Structures, Structural Dynamics, and Materials Conference*. Kissimmee, FL, USA: AIAA, Jan. 2018. ISBN: 9781624105326. DOI: 10.2514/6.2018-1652 (cit. on pp. 4, 42).

[29] M. Amoozgar, M. I. Friswell, S. A. Fazelzadeh, H. H. Khodaparast, A. Mazidi, and J. E. Cooper. "Aeroelastic stability analysis of electric aircraft wings with distributed electric propulsors". In: *Aerospace* 8.4 (2021), pp. 1–12. ISSN: 22264310. DOI: 10.3390/aerospace8040100 (cit. on pp. 4, 42).

[34] L. Teperin. "Investigation on Boundary Layer Ingestion Propulsion for UAVs". In: *International Micro Air Vehicle Conference and Flight Competition (IMAV)*. Aug. 2017, pp. 293–300 (cit. on pp. 5, 45, 63).

[37] M. Elsalamony and L. Teperin. "2D Numerical Investigation of Boundary Layer Ingestion Propulsor on Airfoil". In: *7th European Conference for Aeronautics and Space Sciences (EUCASS)* (2017), pp. 1–11. DOI: 10.13009/EUCASS2017-67 (cit. on pp. 5, 21, 46, 102).

[83] K. Sayler. "A World of Proliferated Drones". In: *Center for a New American Security* June (2015), p. 40 (cit. on p. 37).

[84] España. "Real Decreto 1036/2017". In: *Boletín Oficial del Estado, BOE-A-2017-15721* (2017). ISSN: 0212-033X. URL: https://www.boe.es/eli/es/rd/2017/12/15/1036 (cit. on p. 37).

[85] K. HELNARSKA, J. KRAWCZYK, and G. MOTRYCZ. “Legal regulations of UAVs in Poland and France”. In: *Scientific Journal of Silesian University of Technology. Series Transport* 101 (2018), pp. 89–97. ISSN: 02093324. DOI: 10.20858/sjsutst.2018.101.9 (cit. on p. 37).

[86] EU Commission. “On the rules and procedures for the operation of unmanned aircraft”. In: *Regulation (EU) 2019/ 947* 2019.March (2019). URL: https://skybrary.aero/sites/default/files/bookshelf/4667.pdf (cit. on p. 38).

[87] EU Commission. “Commission delegated regulation 2019/945 on unmmaned aircraft systems and on third-country operators of unmanned aircraft systems”. In: *Regulation (EU) 2019/ 945* 2019.March (2019). URL: https://www.easa.europa.eu/en/document-library/regulations/commission-delegated-regulation-eu-2019945 (cit. on p. 38).

[88] A. Alamouri, A. Lampert, and M. Gerke. “An exploratory investigation of UAS regulations in europe and the impact on effective use and economic potential”. In: *Drones* 5.3 (2021). ISSN: 2504446X. DOI: 10.3390/drones5030063 (cit. on p. 38).

[89] UAV Factory USA LLC. *Penguin C UAS*. https://www.uavfactory.com. Last accessed: 2022-01-12 (cit. on p. 38).

[90] AERTEC Solutions. *RPAS TARSIS 25*. https://aertecsolutions.com/rpas/rpas-sistema-aereos-tripulados-remotamente/rpas-tarsis25/. Last accessed: 2022-01-12 (cit. on p. 38).

[91] C. A. Lyon, A. P. Broeren, P. Giguere, A. Gopalarathnam, and M. S. Selig. *Summary of Low-Speed Airfoil Data - Volume 3*. Vol. 3. Virginia Beach, VA, USA: SoarTech Publications, 1997, p. 315. ISBN: 0964674718 (cit. on p. 38).

[92] S. Schmidt and M. Breuer. “Hybrid LES-URANS methodology for the prediction of non-equilibrium wall-bounded internal and external flows”. In: *Computers and Fluids* 96 (2014), pp. 226–252. ISSN: 00457930. DOI: 10.1016/j.compfluid.2014.03.020. URL: http://dx.doi.org/10.1016/j.compfluid.2014.03.020 (cit. on p. 39).

[93] R. Hain, C. J. Kähler, and R. Radespiel. “Dynamics of laminar separation bubbles at low-Reynolds-number aerofoils”. In: *Journal of Fluid Mechanics* 630 (2009), pp. 129–153. ISSN: 00221120. DOI: 10.1017/S0022112009006661 (cit. on p. 39).

[94] S. Burgmann, J. Dannemann, and W. Schröder. “Time-resolved and volumetric PIV measurements of a transitional separation bubble on an SD7003 airfoil”. In: *Experiments in Fluids* 44.4 (2008), pp. 609–622. ISSN: 07234864. DOI: 10.1007/s00348-007-0421-0 (cit. on p. 39).

[95] M. Galbraith and M. Visbal. "Implicit Large Eddy Simulation of Low-Reynolds-Number Transitional Flow Past the SD7003 Airfoil". In: *40th Fluid Dynamics Conference and Exhibit* January (2010), pp. 1–17. DOI: 10.2514/6.2010-4737. URL: http://arc.aiaa.org/doi/10.2514/6.2010-4737 (cit. on p. 39).

[96] *XFLR5*. Last accessed: 2021-03-10. URL: %7Bhttp://www.xflr5.tech/xflr5.htm%7D (cit. on pp. 40, 64).

[97] M. Drela. *XFOIL Subsonic Airfoil Development System*. Last accessed: 2021-03-10. URL: %7Bhttps://web.mit.edu/drela/Public/web/xfoil/%7D (cit. on pp. 40, 64).

[98] S. Hoerner. *Fluid-Dynamic Drag*. Hoerner Fluid Dynamics, 1965. ISBN: 9789991194448 (cit. on p. 40).

[99] M. Niţă and D. Scholz. "Estimating the Oswald Factor from Basic Aircraft Geometrical Parameters". In: *Deutscher Luft- und Raumfahrtkongress*. Berlin, Germany: DGLR, 2012 (cit. on p. 40).

[100] Honda. *GX-35 Mini 4-stroke engine technical report*. URL: https://www.honda-engines-eu.com/es/productos/motores/gx35 (cit. on p. 40).

[101] J. Schoemann and M. Hornung. "Modeling of hybrid-electric propulsion systems for small unmanned aerial vehicles". In: *12th AIAA Aviation Technology, Integration and Operations (ATIO) Conference and 14th AIAA/ISSMO Multidisciplinary Analysis and Optimization Conference*. Indianapolis, Indiana, USA, Sept. 2012, pp. 1–18. ISBN: 9781600869303. DOI: 10.2514/6.2012-5610 (cit. on p. 40).

[102] F. D. David Willermark. *GT-power simulation report*. Last accessed: 2021-03-10. 2009. URL: http://www.chalmersverateam.se/Rapporter/GTPowerGX35.pdf (cit. on p. 40).

[103] R. W. Deters, G. K. Ananda, and M. S. Selig. "Reynolds number effects on the performance of small-scale propellers". In: *32nd AIAA Applied Aerodynamics Conference*. Atlanta, Georgia, USA, June 2014, pp. 1–43. ISBN: 9781624102882. DOI: 10.2514/6.2014-2151 (cit. on pp. 40, 41, 66, 68).

[104] K. P. Nygren and R. R. Schulz. "Breguet's formulas for aircraft range endurance an application of integral calculus". In: *ASEE Annual Conference Proceedings* (1996), pp. 651–655. ISSN: 01901052 (cit. on p. 45).

[105] O. Atinault, G. Carrier, R. Grenon, C. Verbecke, and P. Viscat. "Numerical and experimental aerodynamic investigations of boundary layer ingestion for improving propulsion efficiency of future air transport". In: *31st AIAA Applied Aerodynamics Conference* (2013), pp. 1–13. DOI: 10.2514/6.2013-2406 (cit. on p. 45).

CHAPTER 4

Methods

Contents

Figures

Tables

4.1 Introduction

ONCE the main geometrical parameters are chosen, as shown in Chapter 3, the study of distributed propulsion and boundary layer ingestion can begin.

The principal analysis tool applied in this work is computational fluid dynamics. CFD, first introduced in chapter 2, allows studying complex thermofluid dynamic problems with a degree of detail defined by the user. Nowadays, Direct numerical simulations (DNS) solve the flow equations entirely without using any model. However, due to the high amount of resources required as well as the cost and application time, it is usually relegated to very small study problems or simple geometries. An alternative is to use Large Eddy Simulation (LES), that model the small turbulence scales but solves the larger ones. This way, a coarser mesh can be used, reducing the cost and time of application. Nevertheless, the cost is still too high for this problem since it is intended to generate a large number of simulations that can be computed simultaneously. Reynolds-averaged Navier-Stokes simulations (RANS) are employed to calculate all cases, where the complete turbulence spectrum is modeled.

In order to further reduce the calculation time and resources required in the simulations, it has been decided to simulate only a portion of the wing with its corresponding propeller. Additionally, the real propeller geometry is not completely included in the simulation, where an actuator disk with blade element method theory (BEMT) models it. Thanks to the use of RANS and the boundary conditions considered, a grid of cases can be calculated by changing the angle of attack, the Reynolds number and geometrical aspects that affect the DEP and BLI, with special attention to the relative height between the wing and the propeller.

The simulations carried out and validated have multiple purposes, and whose application methodology is also described. On the one hand, further analysis is developed using Proper Orthogonal Decomposition (POD). In this way, it is possible to understand better the effect of the propeller position on the BLI, and surrogate models can be created, thus reducing the number of simulations required. On the other hand, the simulations can be used to optimize the flight velocity during a range maximization mission, obtaining this way how much fuel an aircraft with DEP and BLI configuration can save compared to an airplane without these systems, as well as the optimum flight profile. Finally, a lasso method has been employed with a large battery of simulations with the aim of creating useful tools for the preliminary and conceptual design of aircraft with DEP and BLI.

4.2 Computational setup

The same 3D computational domain design is used for all study cases. This way, all cases are modeled as a big "C" shaped domain including a slice of the wing and one single propeller. To aid visualization, a sketch of the wing slice and the propeller is represented in Fig. 4.1.

The main dimensions of the domain are depicted in Fig. 4.2, where every length is dimensionalized with the airfoil chord. A velocity inlet boundary is set 20 chords lengths upstream of the airfoil leading edge. The velocity will be constant in each case and will vary by setting the Reynolds number. The turbulent intensity and the length scale of the turbulence are fixed using a turbulent viscosity ratio. In all cases, the ratio can be neglected, meaning that the turbulence far away from the airfoil can be negligible. The free flow outlet condition is set through a pressure outlet in the opposite direction, 120 chords downstream of the airfoil. Symmetry condition is imposed on top and bottom boundaries, being each boundary equidistantly located at 20 chords from the airfoil. This condition means that the normal derivatives of the velocity are zero. The airfoil skin is considered a smooth wall with a no-slip condition. The remaining lateral boundaries enclose the wing slice and are also set as symmetry conditions.

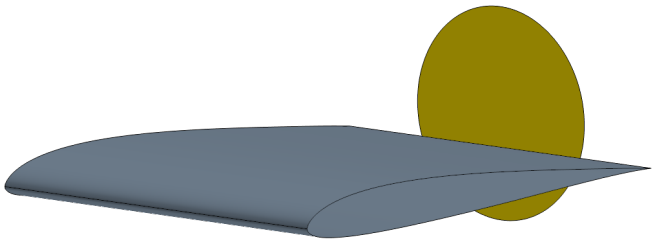

Figure 4.1: 3D detail of the domain containing the portion of the wing with its virtual disk modeling the propeller. This sketch is not to scale.

The domain dimensions are selected in order to ensure that no domain interference is present in the solution. A quick study of the domain is developed under these lines, using the wing lift as main parameter.

First, the lift per unit length (L) is defined for an infinite wing, which is the case of study due to the imposed symmetry conditions, in eq. 4.1.

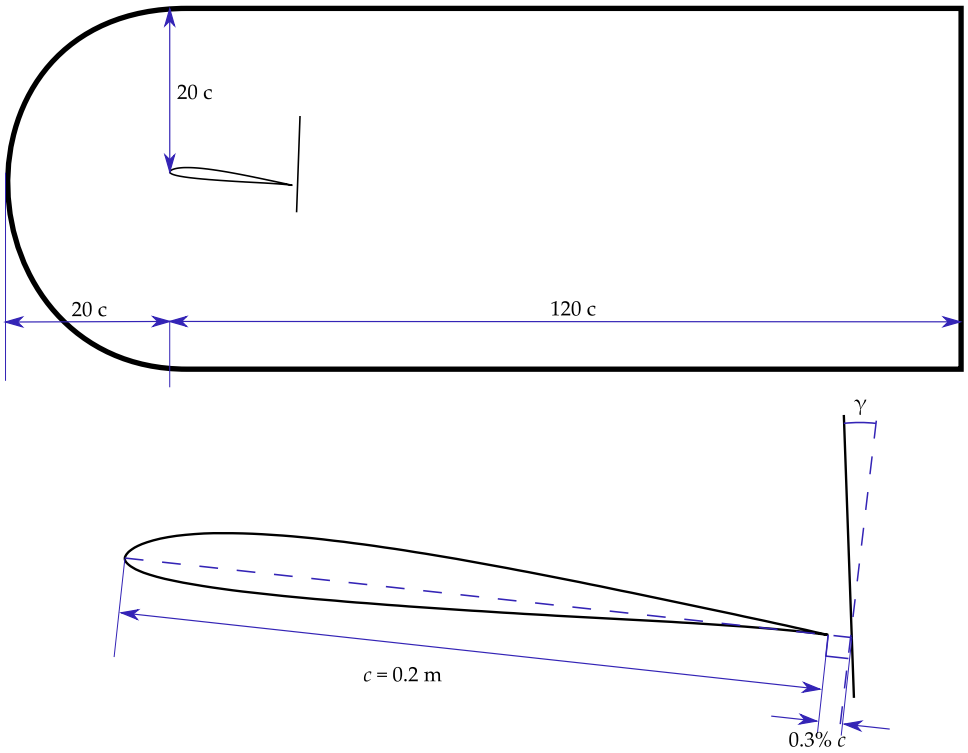

Figure 4.2: CFD calculation domain with main dimensions. c represents the airfoil chord and γ the draft angle. This sketch is not to scale.

$$L = \frac{1}{2}\rho_\infty U_\infty^2 c C_l, \tag{4.1}$$

where C_l is the lift coefficient, ρ_∞ is the air density and U_∞ is the velocity.

In the same way, lift can be expressed as function of the circulation per length unit (Γ) following the Kutta-Joukowski theorem in eq. 4.2.

$$L = \rho_\infty U_\infty \Gamma, \tag{4.2}$$

If the Biot-Savart law is considered, the flow field induced by a vortex filament can be expressed in eq. 4.3.

$$\mathrm{d}U = \frac{\Gamma}{4\pi}\frac{\mathrm{d}l \times r}{|r^3|}, \tag{4.3}$$

where $\mathrm{d}l$ is the length of a segment and r is the radius vector from $\mathrm{d}l$ to an arbitrary point in space. This equation can be discretized considering an infinite vortex filament, obtaining eq. 4.4.

$$U = \frac{\Gamma}{2\pi r}. \tag{4.4}$$

If both eq. 4.1 and 4.2, eq. 4.5 is obtained

$$\Gamma = \frac{1}{2} U_\infty c C_l. \tag{4.5}$$

Considering the symmetry boundary conditions at the upper and lower boundaries at a distance of $r/2$, it is equivalent to assuming that another inverted wing is set at a distance of r. Discretizing for this case, $r/2 = 20c$, so $r = 40c$. Now, combining eq. 4.4 and eq. 4.5, the induced velocity of the reflected wing can be obtained in eq. 4.6.

$$u_i = \frac{1}{2} \frac{U_\infty c C_l}{2\pi 40c} = \frac{U_\infty C_l}{160\pi}. \tag{4.6}$$

This way, the velocity field modification due to applying these boundaries can be calculated, assuming that the lift coefficient is near the unity in eq. 4.7.

$$\frac{u_i}{U_\infty} \approx \frac{C_l}{160\pi} \approx \frac{1}{500}. \tag{4.7}$$

As can be seen, the velocity field modification around the airfoil is near 0.2 % of the incident velocity, which results in a small assumed error.

The inlet boundary condition is analyzed in the same way, considering in this case that $r = 20c$. In this case, the vertical induced velocity is $u_i \approx 1/250 U_\infty$, 0.4 % of the inlet air speed.

Additionally, all domain measures have been validated utilizing a domain dependence study. The study is detailed in section 4.5.

Two strong constraints emerge by limiting the domain to a wing section with only its corresponding propeller. First, because of this lateral limit, the wing tip's aerodynamic effect is not directly taken into account. However, this effect is taken into account when calculating the total drag of the aircraft in Equation 3.3 by introducing a lift-induced drag term. Secondly, because only one propeller is simulated, a hypothesis is made that all distributed propellers contribute to the aircraft thrust in the same way. This condition corresponds to a leveled cruise flight operation.

The main advantage of using this domain is the reduction in computational power needed compared to an entire wing or full aircraft simulation. This way, it is possible to generate a large number of cases changing design parameters in order to obtain an optimized option.

In this work, two different types of simulations have been carried out, analysis simulations and design simulations. Both types share the domain and geometric characteristics already described. The main difference between

them is how the rest of the parameters that each simulated case depends on are varied.

First, the analysis cases are generated, and the changed parameters are described below.

4.2.1 Analysis simulations

During the case generation of the analysis of DEP BLI cases, all parameters described are varied between a few options, usually three. In this way, a controlled parametric study is maintained. Although it does not lead to a definitive optimized design, it does lead to a solution where it is possible to appreciate the improvements caused by using DEP and BLI.

The radii of the propeller is varied between 0.03 m and 0.05 m and the draft angle (γ) is changed between 0° and 3°. The draft angle is defined as the relative angle between the actuator disk surface modeling the propeller with the airfoil chord. Different gap lengths between propeller and airfoil were tested. However, as Smith explains in his work about the benefit on propulsion due to the wake ingestion [62], the best performance is obtained when minimizing this gap. Since a diffusion of the wake occurs downstream of the wing due to viscous and turbulent shear stresses, increasing the gap length translates into more power needed by the propeller since the positive effect of ingestion falls. A constant length gap is set, equal to 0.3 % refered to the chord length.

The propeller height is a parameter studied in detail in this work due to its importance in the boundary layer ingestion mechanism. The propeller height is defined as the relative height between the trailing edge of the airfoil and the center or hub of the propeller. This way, 0 % means that the center of the propeller is at the same height that the trailing edge. At the other end, 100 % means that the propeller is entirely above the trailing edge, and the tip of one blade of the propeller is at the same height that the trailing edge. To aid the visualization, these two positions are depicted in Fig. 4.3.

A different number of propellers has been tested on the distribution between 12 and 25. Since the simulation domain only contemplates one propeller, the number of propellers is changed by growing or decreasing the domain width, in other words, the distance between lateral symmetry boundaries. It must be considered that all the propellers are equally spaced. Setting a propeller radius and the total wingspan described in the Chapter 3, a bigger width domain translates into fewer propellers in the distribution and vice versa. If the number of propellers is altered, changes in the operation of each one are expected. Using fewer propellers expresses that each propeller must rotate faster to propel the entire aircraft to produce the same thrust as the aircraft with more engines. The modification in rotational speed changes the propeller's operational point, producing changes in the propulsive efficiency. Moreover, increasing the distance

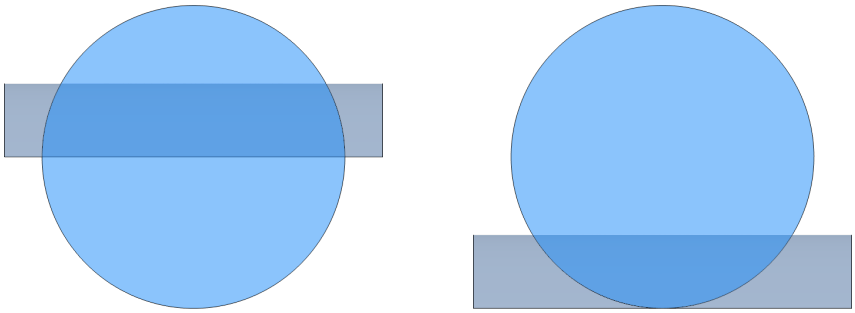

(a) 0% position. (b) 100% position.

Figure 4.3: Maximum and minimum propeller heights above the trailing edge.

between propellers leads to less portion of the wing being affected by the BLI, which can change the aerodynamic efficiency.

As mentioned in the previous chapter, baseline and pure hybrid airplane configurations do not have distributed propulsion or boundary layer ingestion. When studying these cases, the airfoil and the propeller are analyzed separately. The domain has the same dimensions already explained but contains only the airfoil when the wing is studied and an actuator disk when analyzing the propeller.

4.2.2 Design simulations

In the design cases generation, more variables are involved in establishing a dense calculation grid. The seven parameters involved are shown in Table 4.1 with their maximum and minimum value.

	Min	Max
α [°]	0	10
Re	150000	700000
J	0.4	0.8
Propeller radius [m]	0.02	0.07
Distance between shafts [m]	0.045	0.27
θ [°]	-5	5
Propeller position [%]	0	100

Table 4.1: Parameter variation in design cases

The parameters correspond to the angle of attack α, the Reynolds number Re,

the advance ratio defined as $J = U/(n \cdot 2r)$, where n is the propeller rotational speed and r its radius, the propeller radius, the distance between the propeller's blades, and the propeller position as defined in the previous subsection. The propeller's pitch θ is defined in the section 4.4 focused in the implementation of the actuator disk.

A parametric study with seven variables means that the number of cases needed scales with the seventh power of the points chosen to sweep each variable. In this work's scope, it is impossible to solve enough cases to have an adequate resolution, so the parametric study is discarded.

A Latin hypercube sampling (LHS) strategy is proposed. As described by McKay et al. [106], the LHS is a statistical sampling method that generates parameter values to represent a multidimensional distribution. The LHS tries to ensure that the input variables represent all the space sampled. Using this method, 280 cases are generated to describe the design study.

4.3 CFD modelling

All simulations are performed using the CFD commercial software Simcenter STAR-CCM+ [107]. To solve each simulation Reynolds-Averaged Navier-Stokes (RANS) equations are employed with a finite-volume space discretization and a steady-state time discretization scheme.

To compute the Reynolds stress tensor, a Spalart-Allmaras turbulence model is applied. This one-equation turbulence model, based on Boussinesq's eddy viscosity concept, is commonly used in DEP and BLI research, as can be seen in the research of Stoll [24], or the investigation of Brennan et al. [108].

The fluid in all the domain is considered incompressible air. The maximum Reynolds number as defined in Eqn. 3.1 in a simulation is 5×10^5, which translates into a flight velocity of almost 35 m/s. With this velocity, the Mach number defined in Eqn. 4.8 as the relation between flight speed and the sound speed at sea level (u_s), is lower than 0.2. This way, it can be considered that the incompressible flow condition is sufficient, as Anderson explains[109].

$$Ma = \frac{U}{u_s} \tag{4.8}$$

A coupled flow model is set to solve the conservation equations using a pseudo-temporal implicit integration. A variable Courant–Friedrichs–Lewy (CFL) condition is set to limit the residuals and help the convergence. A second-order upwind discretization scheme is selected for evaluating convection terms. A Roe's flux-difference splitting scheme (FDS) [110] is employed when computing the advection terms. An approach to the equations in segregated form might seem logical since the flow is incompressible. However, in practice maintaining a coupled equation scheme proved faster and more stable convergence.

A polyhedral mesh conducts the domain discretization except for the boundary layer near the wing. Additionally, taking into account the airfoil and propeller surface, an automated mesh refinement tool has been applied in the wake. The mesh is depicted in Fig. 4.4. In the boundary layer, a prismatic mesh is applied with 14 layers and total thickness of 3 mm . There is a geometric growth distribution between the first and last layer, and it has been verified that the y^+ is lower than one in 99 % of the wall. This small value of the non-dimensional distance to the centroid of the cells closest to the wall is needed to solve the viscous sublayer of the boundary layer and, thus, produce accurate results for the drag, flow detachment and boundary layer ingestion effects. The boundary layer mesh around the airfoil is detailed in Fig. 4.5.

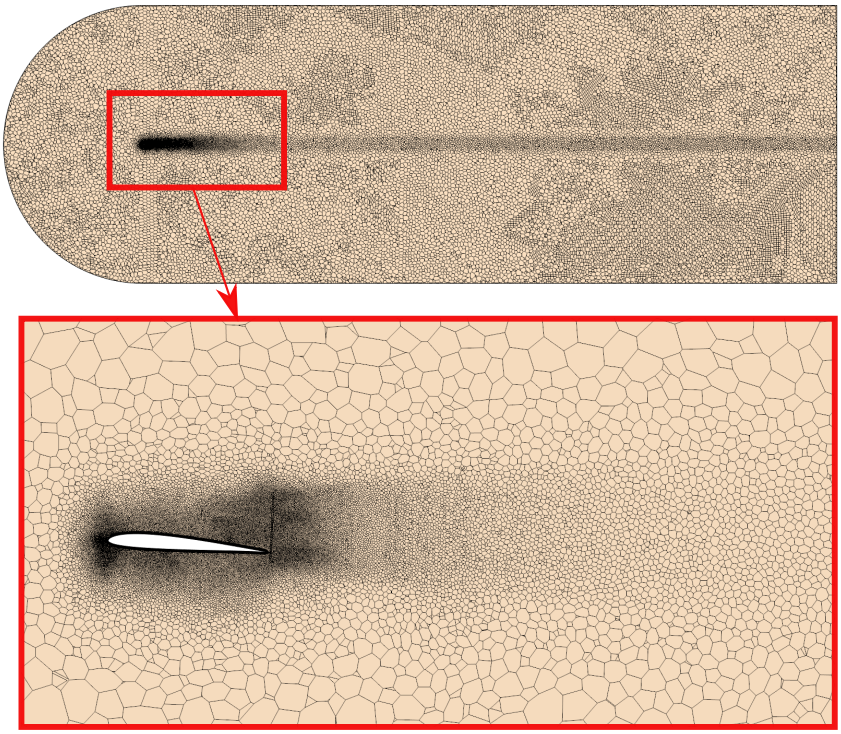

Figure 4.4: Mesh sketch of the entire domain with detailed mesh around the airfoil and wake.

The mesh base size, defined as the minimum size of one cell which is near the airfoil, is set at 1 mm and has been validated with a mesh independence study

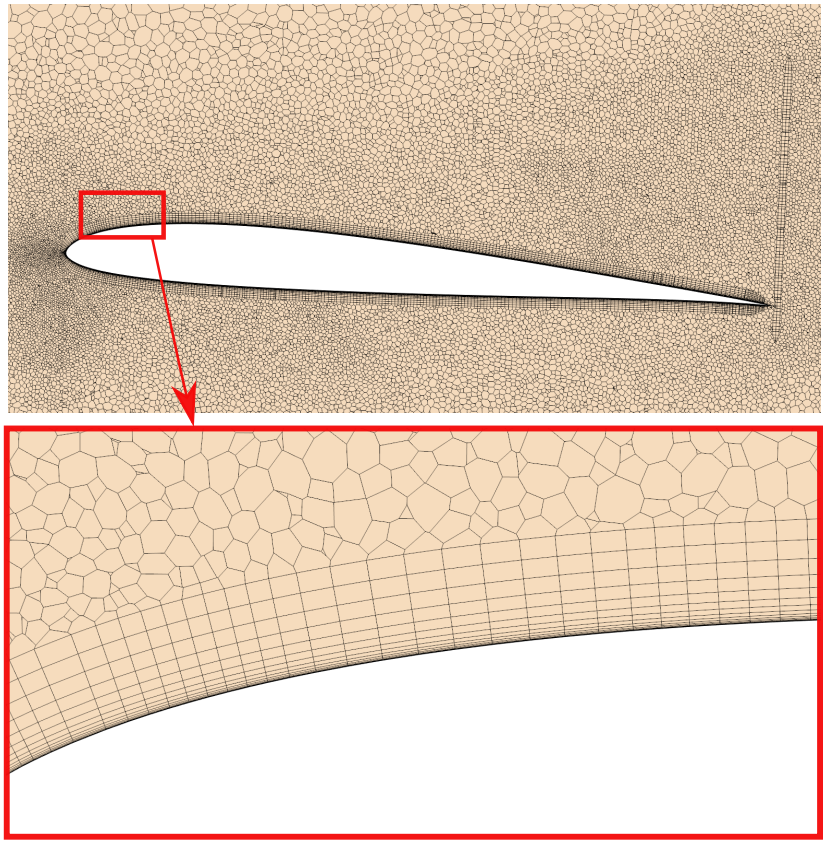

Figure 4.5: Zoom around the airfoil mesh sketch and boundary layer mesh detail.

shown in section 4.5. Also, on each surface of the actuator disk representing the propeller (which will be explained in the Section 4.4), a prismatic layer with a size equivalent to the base size is placed. This prismatic layer does not have the purpose of boundary layer meshing but to ensure that no cell of the polyhedral mesh crosses the actuator disk, which can result in numerical problems during the calculation.

4.4 Actuator disk modelling

The propeller is modeled as an actuator disk in all simulations. Also known as a virtual disk, it is commonly used in the study of DEP and BLI [34, 24]. This disk surface represents the apparent disk generated by the propeller when rotating. The propeller is modeled without incorporating the entire geometry,

corresponding mesh, and rotation into the simulation, making the calculation less expensive. Different models can be applied to this surface. In this case, the blade element method theory (BEMT) model was selected.

Using BEMT, the propeller is modeled as a distribution of momentum sources applied divided both in the radial and in azimuth direction in different sections set by a resolution parameter. The strength of each momentum source is calculated using geometrical parameters of the propeller's blade, such as the chord and twist angle, and takes into account the circulation around the blade airfoil in that section. Instead of resolving the entire blade geometry explicitly, the aerodynamic parameters are computed from interpolation tables for different blade sections as a function of the local angle of attack and Reynolds number, simulating 2D airfoils. These tables of aerodynamic coefficients are calculated using XFLR5 software [96], a potential flow method with interactive boyndary layer correction based on XFOIL [97].

Additionally, a tip loss correction factor is added to the model as proposed by Gur in [111], reducing the effective length of the blade by 3 %.

A small collective pitch θ of $-0.45°$ is set in all the design cases to adjust the obtained results with the experimental results during the validation explained in the next section. This pitch can be translated in a more common term of distance per revolution knowing the diameter of the propeller d and the twist angle of the section correspondent to the 75 % of the blade θ_0. This relation is expressed in eq. 4.9.

$$\theta = \operatorname{atan} \frac{\text{pitch}}{0.75\pi d} - \theta_0. \tag{4.9}$$

It is worth noting again that this parameter is not set as a constant in the design cases.

The rotational speed or the required thrust is usually imposed in the actuator disk model. The setting of this parameter varies between analysis cases and design cases.

On the one hand, in the analysis cases, the total thrust (T_{tot}) produced by all the propellers must be equivalent to the drag of the aircraft (D) as the simulations represent straight, level flight with no accelerations. The total drag is defined in Eqn. 3.3, with this equation the necessary thrust (T) for each propeller can be expressed in 4.10 since every propeller is considered to produce the same amount of individual thrust. In this equation n_{props} represent the number of distributed propellers.

$$T_{\text{tot}} = T \cdot n_{\text{props}} = D = \frac{1}{2} \cdot \rho \cdot U^2 \cdot S \cdot \left(C_{D,0,\text{wing}} + C_{D,0,\text{extra}} + \frac{C_L^2}{\pi \cdot \mathcal{A} \cdot e} \right) \tag{4.10}$$

Since the calculation of drag depends on the different forces on the airfoil, the imposed thrust must vary throughout the simulation so that the condition that the total thrust is equal to the total drag is always fulfilled. This is done by means of a proportional-integral-derivative controller (PID) that regulates this parameter. As the CFD software used for these studies do not include such controllers, a PID had to be programmed.

Constraints are applied to maintain the rotational speed of the propellers lower than the typical maximum speed for thin propellers for electric propulsion, as described in APC's website [112].

On the other hand, in the design cases, the thrust is not directly imposed. As seen in section 4.2, the advance ratio parameter is changed along the incoming flow velocity. This way, the rotational speed set on the actuator disk is extracted. Together with the variation of the rest of the parameters, a thrust will be reached that does not have to be equal to the aircraft's drag.

4.5 CFD validation

As mentioned in section 4.2, a domain dimensions independence analysis has been carried out to ensure that the domain measures do not affect the solution. For doing this, the domain is scaled to obtain two new domains, one bigger by doubling the vertical height to 80 chords and one smaller by decreasing this height to 20 chords. The mesh base size is maintained, and a Reynolds number of 5×10^5 with an angle of attack of 3°is used in the analysis. The results are collected in Table 4.2, where the baseline domain has a C_D variation lower to 1 % compared to the larger domain, so in the selected domain, the error is considered negligible. Although in the smaller domain, the variation of C_L is also lower than 1 %, the variation in C_D is in excess of 2 %, so the dimensions would not be sufficient to not interfere with the solution.

Domain height	C_L **[-]**	C_L **variation [%]**	$C_{D0,\text{wing}}$ **[-]**	$C_{D0,\text{wing}}$ **variation [%]**
$20c$	0.484 96	0.24	0.007 35	2.23
$40c$	0.486 12		0.007 19	
$80c$	0.487 16	0.21	0.007 12	0.97

Table 4.2: Domain independence study

A mesh independence analysis has been conducted to set the mesh base size in section 4.2. A generalized Richardson extrapolation [113] is applied with the same configuration of Reynolds and α that the domain independence study. The main goal of the extrapolation is to estimate the lift coefficient of an infinitely

refined mesh using different grid spacing meshes, in the same way that shows the work of Celik et al. [114]. The data of the study is collected on Table 4.3, and a base size of 0.001 m mesh is set for all cases. Using this base size, the grid convergence index (GCI) is lower than 1 %, where this index estimates the error of the extrapolated C_L and the C_L value for an infinitesimal cell size.

Mesh	**Base Size** [m]	C_L **[-]**
1	0.001	0.48636
2	0.00087	0.48612
3	0.00077	0.48590
	Extrapolated C_L **[-]**	0.48348
	GCI mesh 1 and 2 [%]	0.193
	GCI mesh 2 and 3 [%]	0.183
	GCI ratio	0.9996

Table 4.3: Mesh independence study

Both propeller and airfoil have been compared with experimental data to complete the CFD validation.

In the case of the airfoil, the polar diagram has been validated with experimental data from Princeton and UIUC universities collected by Selig et al. [115]. It is possible to find some discrepancies in the comparison attributed to the manufacture of the airfoils and their surface roughness. The validation has also been carried out on the potential method performed with XFOIL, obtaining a result similar to that of the CFD simulation. The comparison is shown in Fig. 4.6.

For the propeller, the virtual disk is compared with the experimental data of UIUC in the research led by Deters [103, 116] for a couple of rotational speeds. In Fig. 4.7 the propulsive efficiency defined as $\eta_p = (T \cdot U)/P$, where T and P are the propeller thrust and power, respectively, is compared to the advance ratio. Fairly agreement has been found, having coincident data between CFD and experimental methods for different rotation speeds.

4.6 Range mission optimization

When different cases with diverse configurations are tested, the best DEP with BLI cases are selected to estimate the fuel consumed during a maximum range mission. To calculate the fuel savings, it is necessary to define how the maximum range of a baseline case without DEP, BLI, or hybridization is computed.

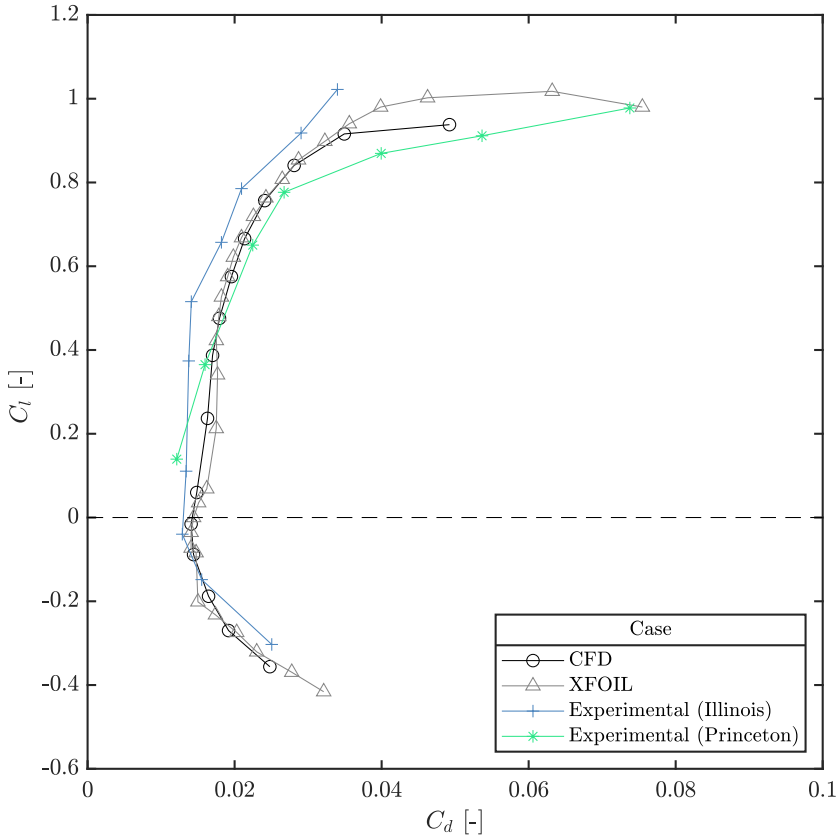

Figure 4.6: Airfoil polar diagram comparisson for validation with XFOIL data and experimental data measured by Selig in University of Illinois in Urbana Champaign (1995) and Princeton University (1989).

A surveillance mission of low altitude should be considered with the fuel expended during non-cruise operations as take-off or landing neglected. Taking into consideration the *MTOM* described in chapter 3, a maximum mass fuel m_{fuel} of 10 kg is set. The range of this baseline configuration R_{baseline} is expressed in the integration of Eqn. 4.11 depending on how the brake specific fuel consumption $BSFC$, the propulsive efficiency η_p and the aerodynamic efficiency C_L/C_D change during flight. A mechanical efficiency η_m is considered due to the use of a gearbox in the baseline configuration, and is set as constant to 90 %.

$$R_{\text{baseline}} = \int_{m_{\text{landing}}}^{m_{\text{landing}}+m_{\text{fuel}}} \frac{\eta_p \cdot \eta_m}{BSFC \cdot g} \cdot \frac{C_L}{C_D} \cdot \frac{\mathrm{d}m}{m}. \tag{4.11}$$

The integration is done supposing that, in the end, all the fuel mass is

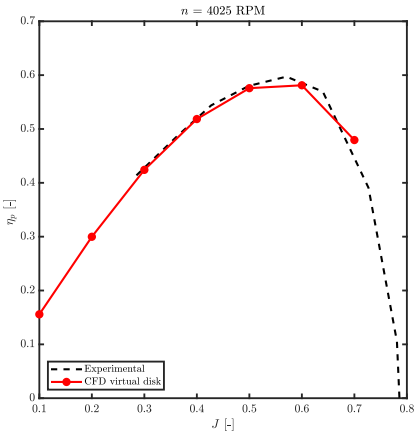

(a) Comparison at 4025 rpm

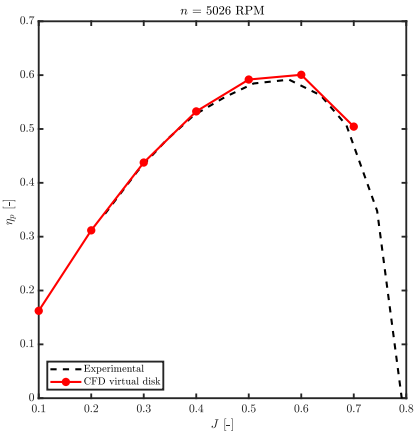

(b) Comparison at 5026 rpm

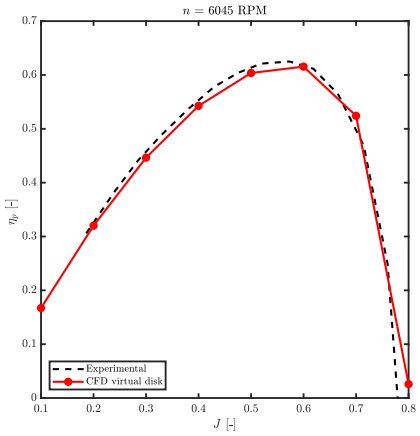

(c) Comparison at 6045 rpm

Figure 4.7: Propeller of 0.1143 m propulsive efficiency comparison between CFD and experimental data. Experimental data provided by Deters et al. [103].

burned, leading to a landing mass m_{landing} of 15 kg. The standard gravity g is equal to $9.806\,65\,\text{m}\,\text{s}^{-2}$.

Each parameter can be expressed as a function of the flight velocity U or the instantaneous mass in every flight moment. To link these two variables, a simple flight speed law is defined in eq. 4.12.

$$U = U_0 + \xi \cdot m. \tag{4.12}$$

In this equation, the flight speed changes as the mass of the aircraft decreases, where U_0 is the speed when all the fuel is burned and ξ is the rate of change of the velocity with the aircraft mass. Both U_0 and ξ are set through a Broyden-Fletcher-Goldfarb-Shanno (BFGS) algorithm to optimize the specific range β with constraints to ensure that the operation is always carried within the *BSFC* map data. The specific range is exposed in eq. 4.13, defined as the integrand of eq. 4.11.

$$\beta = \frac{\eta_p \cdot \eta_m}{BSFC \cdot g} \cdot \frac{C_L}{C_D} \cdot \frac{1}{m}. \tag{4.13}$$

In Fig. 4.8 the specific range is computed for a wide range of flight velocities and aircraft masses, and following the maximization of β through the flight, the flight speed law is depicted.

Every aerodynamic and propulsive parameter is calculated as a function of the flight speed and the aircraft mass. Knowing the flight velocity, the lift coefficient can be calculated. Then the total drag is interpolated using a quadratic surface as a function of the Reynolds number, the lift coefficient and CFD simulations. The next step is estimating the propeller rotational speed, which is calculated with a cubic interpolation of the propeller performance data, and ensuring that the total thrust equals the whole aircraft drag. The propulsive efficiency can be calculated by knowing the propeller's rotational speed. Because the propeller is mechanically coupled with the ICE, the power needed is translated into ICE torque, and ICE rotational speed can also be calculated. The *BSFC* is interpolated with the torque and ICE rotational speed with the ICE operation map set. With all the parameters calculated, it is possible to calculate the specific range for every flight velocity and weight combination, which is translated in the calculation of the contours of Fig. 4.8 using eq. 4.13. Then, the optimal flight speed law can be calculated to maximize β at all times of the flight, which gives the blue line in Fig. 4.8. All variables are known to maximize the range between the initial and the final weight using eq. 4.11.

The equation that gives the operational range in a series of hybrid-electric aircraft is similar to the baseline one and is defined in eq. 4.14

$$R_{\text{hybrid}} = \int_{m_{\text{landing,hybrid}}}^{m_{\text{landing,hybrid}}+m_{\text{fuel}}} \frac{\eta_p \cdot \eta_e}{BSFC \cdot g} \cdot \frac{C_L}{C_D} \cdot \frac{\mathrm{d}m}{m}, \tag{4.14}$$

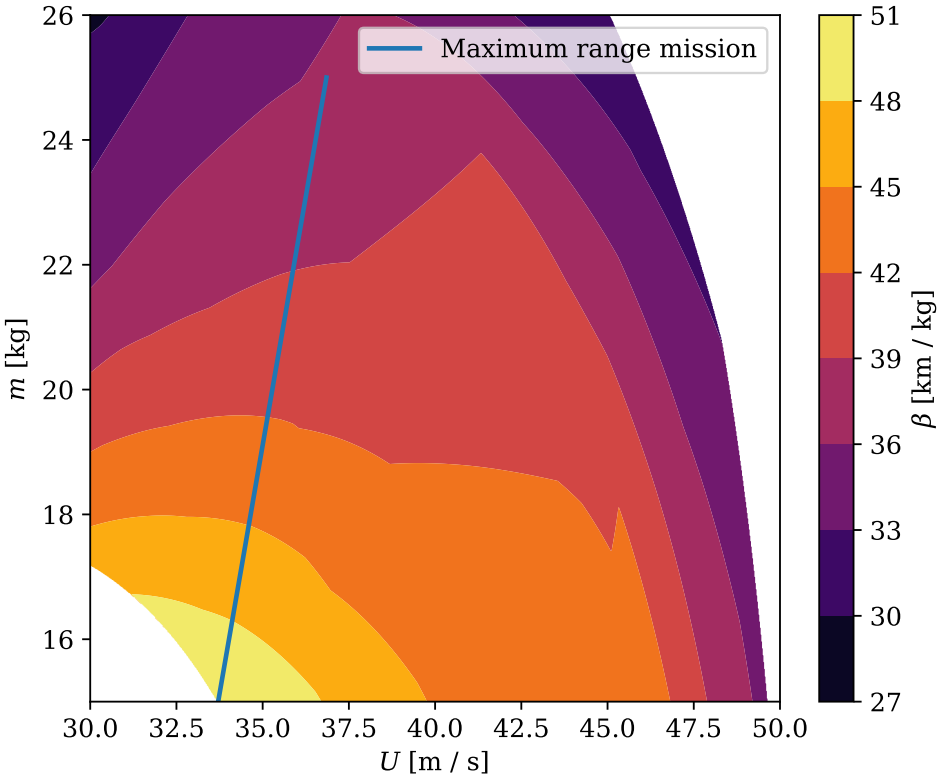

Figure 4.8: In blue line, baseline case velocity law which maximizes the specific range.

Where $m_{\text{landing,hybrid}}$ is the operating empty mass of the hybrid case taking into account the weight increase calculated in chapter 3, and η_e is an electric efficiency. The electric efficiency is typically set to 80 % and is defined as the efficiency of conversion of mechanical energy from the ICE to electric power distributed to each engine and converted back to mechanical power.

To calculate the possible fuel savings in hybrid cases, it is assumed that the range in the hybrid case is the same as that in the baseline case. This way m_{fuel} is an unknown variable.

New ways to maximize specific range emerge in hybrid cases as the propellers are not directly mechanically coupled with the ICE. Because of the decoupling, the flight velocity law can be optimized for every moment of the flight, leading to a non-linear law.

The summary of β calculation in cases with DEP BLI configuration is shown in diagram 4.9.

In the same way as for the baseline case, both propulsive and aerodynamic efficiencies are interpolated from CFD data for each flight operation point. The

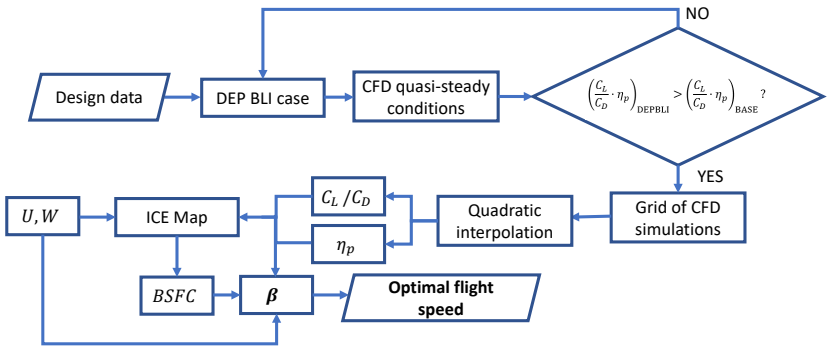

Figure 4.9: Diagram of β calculation in DEP BLI cases.

power needed to propel each electric engine is extracted. However, the rotational speed of the ICE is optimized because the decoupling always leads to a lower BSFC. Fuel savings are calculated by applying Heun's method to integrate the whole mission.

4.7 POD analysis

A Proper Orthogonal Decomposition (POD) has been applied to analyze in detail the influence of the different aerodynamic coefficients on the position of the propeller above the wing. With this method, new pre-design tools are obtained that allow a smaller number of simulations to be carried out.

Most of the geometric parameters in these simulations are fixed, only varying the Reynolds number, the angle of attack α and the relative height h of the disk above the wing. In each simulation, the wing's pressure and friction coefficients are extracted using a midplane.

As defined by Anderson [109], the pressure coefficient can be expressed in eq. 4.15.

$$C_p = \frac{p - p_\infty}{q_\infty}, \tag{4.15}$$

where p is each point around the wing skin, p_∞ is the freestream pressure and q_∞ is the dynamic pressure, defined as a function of the air density ρ_∞ and the velocity U_∞ as $q_\infty = \frac{1}{2}\rho_\infty U_\infty^2$.

The skin friction coefficient is expressed in eq. 4.16.

$$C_f = \frac{\tau}{q_\infty}, \tag{4.16}$$

where τ is the skin shear stress on the surface.

The mentioned plane is shown in Fig. 4.10, and it divides the domain into two symmetrical halves, dividing both the wing and the actuator disk at their center. Applying this midplane limits the number of points in each simulation, limiting this way the collection of data and the complexity of its interpretation.

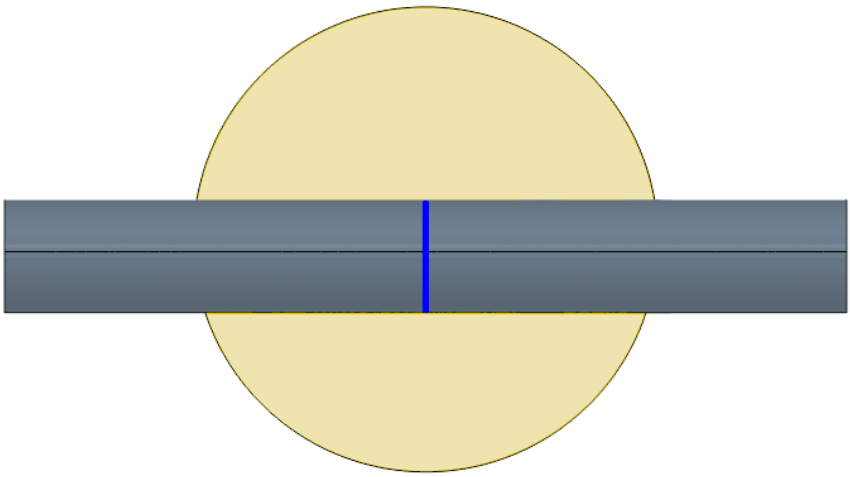

Figure 4.10: Front view of an example case with the dividing mid-plane marked in blue.

For a fixed flight speed, the distribution of cases m is equal to the product of the variables on which it depends. In this case, the product of α and h simulated. For each distribution, n spatial points are extracted from the airfoil surface on which the coefficients are measured. The data of the coefficients calculated are arranged in a matrix $\boldsymbol{U}$ of dimensions $m \times n$ setting in each row the coefficient distribution over the airfoil for one combination of the angle of attack and propeller relative height.

Each coefficient can be expressed as a summation of a series of deterministic spatial functions. These spatial functions are known as spatial modes or egeinvectors (ϕ_k). The eigenvectors depend only on the spatial dimension (x) where the coefficient is studied, where the spatial dimension is referred to as the airfoil chord. In addition, each spatial mode is modulated through another coefficient known as configuration coefficient (a_k). The configuration coefficient depends only on the problem distribution, in this case α and h. The pressure

coefficient is expressed in those terms in Eqn. 4.17, and is analogous to the friction coefficient.

$$C_p(x,\alpha,h) = \sum_{k=1}^{\infty} a_k(\alpha,h)\phi_k(x). \tag{4.17}$$

The relationship between terms can be obtained first by calculating the covariance matrix $\boldsymbol{C}$ of the original data. The covariance matrix is constructed in Eqn. 4.18 and is a square matrix, that contains the variability between terms.

$$\boldsymbol{C} = \frac{1}{m-1}\boldsymbol{U}^{\mathrm{T}}\boldsymbol{U}, \tag{4.18}$$

With the covariance obtained, the eigenvectors arranged as columns in matrix $\boldsymbol{\Phi}$ and the eigenvalues (λ) placed on the diagonal of the matrix $\boldsymbol{\Lambda}$ can be expressed in Eqn. 4.19.

$$\boldsymbol{C} = \boldsymbol{\Phi}\boldsymbol{\Lambda}\boldsymbol{\Phi}^{-1}. \tag{4.19}$$

Once obtained, the eigenvalues are sorted from the largest to the smallest value. The modes are sorted by their influence on the aerodynamical coefficients. Also, it is interesting to define the total fluctuating kinetic energy (*TKE*). This term written in Eqn. 4.20 expresses the percentage of the energy content of each sorted mode and allows estimating how many modes are necessary to explain with a certain percentage the problem studied. The name comes from the fact that this method was introduced to process turbulent velocity flows.

$$TKE_j = \frac{\lambda_j}{\sum_{j=1}^{n}\lambda_j}. \tag{4.20}$$

With the eigenvectors of the problem sorted, the configuration coefficients are expressed in a matrix $\boldsymbol{A}$ related to the projection of the original data $\boldsymbol{U}$ projected on each spatial mode. This relationship is shown in Eqn. 4.21, where every coefficient a_{ij}, is the projection of the original data in a configuration i (combination of α and h) on mode j.

$$\boldsymbol{A} = \boldsymbol{U}\Phi = \begin{pmatrix} a_{11} & \dots & a_{1n} \\ a_{21} & \dots & a_{2n} \\ \vdots & & \vdots \\ a_{m1} & \dots & a_{mn}. \end{pmatrix} \tag{4.21}$$

The original dataset $\boldsymbol{U}$ can be reconstructed from the summation seen in 4.17 of spatial contribution modes and the configuration coefficients that model them. Benefiting of *TKE* data, the summatory can be expressed only using the initial modes that explain the more significant part of the problem instead of using all modes. The reconstruction is described in Eqn. 4.22.

$$\boldsymbol{U} = \boldsymbol{A}\boldsymbol{\Phi}^{-1} = \sum_{k=1}^{n} \tilde{\boldsymbol{U}}^k = \sum_{k=1}^{n} \begin{pmatrix} \tilde{u}^k_{11} & \dots & \tilde{u}^k_{1n} \\ \tilde{u}^k_{21} & \dots & \tilde{u}^k_{2n} \\ \vdots & & \vdots \\ \tilde{u}^k_{m1} & \dots & \tilde{u}^k_{mn} \end{pmatrix} = \sum_{k=1}^{n} \begin{pmatrix} a_{1k} \\ a_{2k} \\ \vdots \\ a_{mk} \end{pmatrix} \begin{pmatrix} \phi_{1k} & \dots & \phi_{nk}. \end{pmatrix} \quad (4.22)$$

Once the reconstruction of the C_p and C_f is performed with the desired number of modes, lift and drag coefficients can be integrated as presented respectly in equations 4.23 and 4.24.

$$C_L = \frac{1}{c}\left[\int_0^c \left(C_{p,ps} - C_{p,ss}\right) \mathrm{d}x + \int_0^c \left(C_{f,ss}\frac{\mathrm{d}y_{ss}}{\mathrm{d}x} + C_{f,ps}\frac{\mathrm{d}y_{ps}}{\mathrm{d}x}\right) \mathrm{d}x\right], \quad (4.23)$$

$$C_D = \frac{1}{c}\left[\int_0^c \left(C_{p,ss}\frac{\mathrm{d}y_{ss}}{\mathrm{d}x} - C_{p,ps}\frac{\mathrm{d}y_{ps}}{\mathrm{d}x}\right) \mathrm{d}x + \int_0^c \left(C_{f,ss} + C_{f,ps}\right) \mathrm{d}x\right], \quad (4.24)$$

where the subtitle ss and ps allude to the airfoil suction side and pressure side respectively.

4.8 Lasso application

A least absolute shrinkage and selection operator method, commonly known as “lasso”, is applied with the data extracted in the design cases to develop tools that can aid the DEP BLI aircraft conceptual and preliminary design.

The lasso, first introduced by Tibshirani [117], is a linear model that estimates coefficients fitted as a least-squares regression with a given regularization term λ, as function of a predictor and a response data. The idea behind the application of this model is to reduce the number of variables that describe the solution. This way, the lasso shrink some coefficients while set other to zero, trying to retain the features of both subset selection and regression.

The lasso solves the problem expressed in eq. 4.25, minimizing the objective function.

$$\min_{\beta}\left(\frac{1}{2N}\sum_{i=1}^{N}(y_i - x_i^T\beta)^2 + \lambda\sum_{j=1}^{p}|\beta_j|\right), \quad (4.25)$$

where N is the number of observations, y_i is the response or target at observation i, x_i is the predictor or training data of length p at observation i, and β is a vector of length p with the stimated coefficients. λ is a constant parameter between 0 and 1. As this parameter decreases and has a value near zero, the number of nonzero components of the list β increases.

The lasso regression is applied to the design dataset, and only the main effects that affect the aerodynamic and propulsive performance parameters are retained. The final model keeps a reduced amount of complexity, which is important during aircraft conceptual and preliminary design phases, and, hopefully, keeps good generalization capabilities.

4.9 Summary

This chapter discusses all the methods and computational tools applied to obtain the results presented in Chapter 5.

It contains an extensive explanation of the diverse computational setup, with all the dimensions and boundaries that define the problem. Also, the mesh and models selected to solve all cases are presented, with special attention to the definition of the actuator disk that model the propeller. The CFD is accompanied by a complete validation, where experimental data found in the literature is employed to check the accurate modeling of the wing and the propeller.

The chapter continues with an explanation of the calculation of velocity optimization to improve the range and obtain fuel benefits using DEP and BLI configuration-aircraft based on the previously calculated simulations.

Additionally, the general line of application of the proper orthogonal decomposition method to the problem is explained. It is shown how to discretize the problem in representative modes, as well as how to reconstruct aerodynamic coefficients from the information obtained.

Finally, a lasso method has been explained and employed with the design dataset, serving as a tool to help during aircraft conceptual and preliminary design phases.

The applied methodology gives rise to the discussion of the results in the next chapter.

4.10 References

[24] A. M. Stoll. “Comparison of CFD and experimental results of the leap tech distributed electric propulsion blown wing”. In: *15th AIAA Aviation Technology, Integration, and Operations Conference*. Dallas, TX, USA: AIAA, June 2015, pp. 22–26. ISBN: 9781624103698. DOI: 10.2514/6.2015-3188 (cit. on pp. 4, 61, 63).

[34] L. Teperin. “Investigation on Boundary Layer Ingestion Propulsion for UAVs”. In: *International Micro Air Vehicle Conference and Flight Competition (IMAV)*. Aug. 2017, pp. 293–300 (cit. on pp. 5, 45, 63).

[62] L. H. Smith. “Wake ingestion propulsion benefit”. In: *Journal of Propulsion and Power* 9.1 (1993), pp. 74–82. ISSN: 07484658. DOI: 10.2514/3.11487 (cit. on pp. 21, 59).

[96] *XFLR5*. Last accessed: 2021-03-10. URL: %7Bhttp://www.xflr5.tech/xflr5.htm%7D (cit. on pp. 40, 64).

[97] M. Drela. *XFOIL Subsonic Airfoil Development System*. Last accessed: 2021-03-10. URL: %7Bhttps://web.mit.edu/drela/Public/web/xfoil/%7D (cit. on pp. 40, 64).

[103] R. W. Deters, G. K. Ananda, and M. S. Selig. “Reynolds number effects on the performance of small-scale propellers”. In: *32nd AIAA Applied Aerodynamics Conference*. Atlanta, Georgia, USA, June 2014, pp. 1–43. ISBN: 9781624102882. DOI: 10.2514/6.2014-2151 (cit. on pp. 40, 41, 66, 68).

[106] M. D. McKay, R. J. Beckman, and W. J. Conover. “A comparison of three methods for selecting values of input variables in the analysis of output from a computer code”. In: *Technometrics* 42.1 (2000), pp. 55–61. ISSN: 15372723. DOI: 10.1080/00401706.2000.10485979 (cit. on p. 61).

[107] *Simcenter STAR-CCM+ Documentation*. Siemens. 2019 (cit. on p. 61).

[108] B. T. Blumenthal, A. A. Elmiligui, K. A. Geiselhart, R. L. Campbell, M. D. Maughmer, and S. Schmitz. “Computational investigation of a boundary-layer-ingestion propulsion system”. In: *Journal of Aircraft* 55.3 (2018), pp. 1141–1153. ISSN: 00218669. DOI: 10.2514/1.C034454 (cit. on p. 61).

[109] J. D. Anderson. *Fundamentals of Aerodynamics (6th edition)*. Vol. 1984. 3. 2011, p. 1128. ISBN: 9780071289085 (cit. on pp. 61, 71).

[110] P. L. Roe. “Approximate Riemann Solvers, Parameter Vectors, and Difference Schemes”. In: *Journal of Computational Physics* 43 (1981), pp. 357–372. DOI: 10.1016/0021-9991(81)90128-5 (cit. on p. 61).

[111] O. Gur and A. Rosen. "Comparison between blade-element models of propellers". In: *Aeronautical Journal* 112.1138 (2008), pp. 689–704. ISSN: 00019240. DOI: 10.1017/S0001924000002669 (cit. on p. 64).

[112] APC. "APC Propeller RPM Limits". In: *APC website* 95776.530 (2016), p. 95776. URL: https://www.apcprop.com/technical-information/rpm-limits/ (cit. on p. 65).

[113] W. L. Oberkampf and T. G. Trucano. "Verification and validation in computational fluid dynamics". In: *Progress in Aerospace Sciences* 38 (2002), pp. 209–272. DOI: 10.1201/b19031-50 (cit. on p. 65).

[114] I. B. Celik, U. Ghia, P. J. Roache, C. J. Freitas, H. Coleman, and P. E. Raad. "Procedure for estimation and reporting of uncertainty due to discretization in CFD applications". In: *Journal of Fluids Engineering, Transactions of the ASME* 130.7 (2008), pp. 0780011–0780014. ISSN: 00982202. DOI: 10.1115/1.2960953 (cit. on p. 66).

[115] Selig, Donovan, and Fraser. *Airfoils at Low Speeds*. Virginia Beach, VA, USA: H.A. Stokey, 1989, pp. 1–408 (cit. on p. 66).

[116] R. W. Deters. *Performance and Slipstream Characteristics of Small-scale propellers at low Reynolds Numbers*. 2014 (cit. on p. 66).

[117] R. Tibshirani. "Regression Shrinkage and Selection via the Lasso". In: *Journal of the Royal Statistical Society. Series B (Methodological)* 58.1 (1996), pp. 267–288. ISSN: 00359246. URL: http://www.jstor.org/stable/2346178 (visited on 10/17/2022) (cit. on p. 74).

CHAPTER 5

Results

Contents

Figures

Tables

5.1 Introduction

THE extensive methodology described and discussed in Chapter 4 is fully employed to develop the results.

First, an analysis of the CFD data obtained is performed to understand the importance of the location of the propeller on the wing when performing boundary layer ingestion. With that information, a near-optimal propeller position is sought and analyzed.

This research is followed by a deeper analysis of the position using proper orthogonal decomposition methods. The aerodynamic coefficients can be better-understood thanks to the modal decomposition, and the data can be used in surrogate models to estimate aerodynamic coefficients in non-simulated cases.

Then the optimum aircraft configuration obtained is compared in terms of range to similar aircraft with more classical power plant configurations.

Finally, the design cases developed in the previous chapter are used to fit a least-squares regression, creating simple linear equations based on a series of selected predictors with which to feed more complex optimization models.

5.2 Propeller position CFD analysis

The relative height or propeller position above the trailing edge is one of the most influential parameters in the BLI mechanisms. Nevertheless, to close the problem and optimize the propeller position it is necessary to set the rest of the geometrical parameters. A quick study is conducted to set the number of propellers distributed on the wing and the radius of each propeller. The simulations are performed at near cruise condition of 3° α and 5×10^5 Reynolds. An extensive parametric study was carried out with a fixed propeller position of 75 %, and an optimum was found at 13 propellers with 0.04 m radius. In Table 5.1 results of the product of aerodynamic efficiency and propulsive efficiency are shown near the optimum found. Following a similar study, a draft angle γ equal to 1.5° was set on all cases.

Table 5.1: Comparison of results varying the number of propellers and their radius.

Nº propellers	**Blade radius [mm]**	C_{D0}	C_L	$\frac{C_L}{C_D}$
Optimum case 13	40	0.008055	0.5366	17.58
13	30	0.008940	0.5731	17.36
13	50	0.009885	0.5551	16.74
12	40	0.009734	0.5739	16.96
14	40	0.009741	0.5623	16.87

With the optimum distribution obtained, the gap length between the trailing edge and the propeller set in chapter 4 is also tested in a quick study, testing two additional gap positions. If the distance in chord direction is increased to 4 % of the chord, the product of efficiencies is decreased by 4 %. If this distance is increased by an additional 4 %, the product decreases 0.5 % more. In view of the results, the gap length is maintained.

The propeller position was modified between 0 % and 100 % with 25 % intervals. For each position, the angle of attack is varied between 1° and 9°. At a higher angle of attack, the airfoil is in stall conditions.

Combining this spectrum of propeller position and angle of attack, the product of efficiencies is plotted in Fig. 5.1 for a Reynolds number of 5×10^5.

This Reynolds number is maintained in all the studies because, as seen in Fig. 4.8 of section 4.6, the baseline flight speed oscillates around 35 m/s and corresponds to the selected Reynolds number for the described aircraft dimensions.

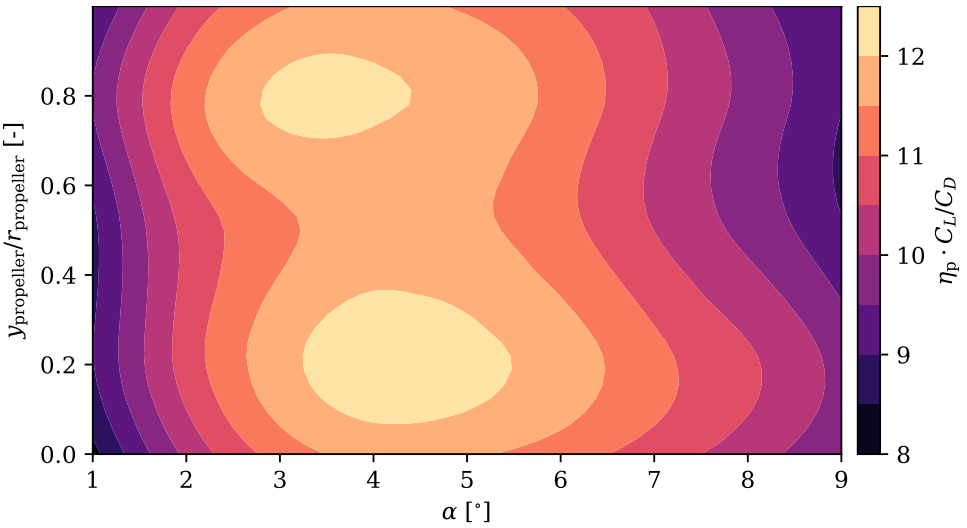

Figure 5.1: Aerodynamic and propulsive efficiency product as a function of each propeller position above the trailing edge (Y axis) and the angle of attack (X axis) at a Reynolds number of 5×10^5.

Two optimum zones emerge shown in Fig. 5.1, meaning that two different propeller positions maximize the product of efficiencies. The highest zone, near 80 % corresponds to higher aerodynamic efficiency, and by contrast, the lower position zone corresponds to a higher propulsive efficiency. This result is more obvious if the efficiencies are plotted separately for each position and angle of attack in Fig. 5.2 and 5.3.

The aerodynamic efficiency is represented in fig 5.2 and, as anticipated, the

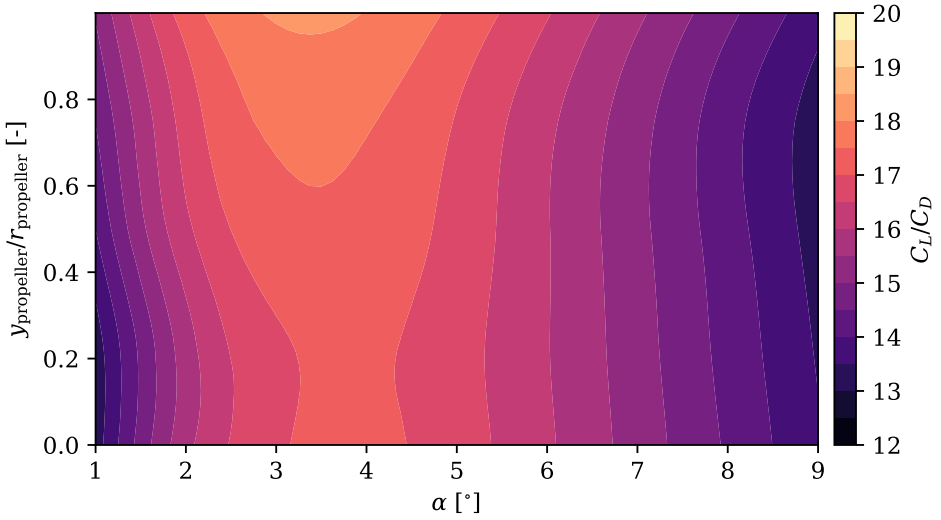

Figure 5.2: Aerodynamic efficiency as a function of each propeller position above the trailing edge (Y axis) and the angle of attack (X axis) at a Reynolds number of 5×10^5.

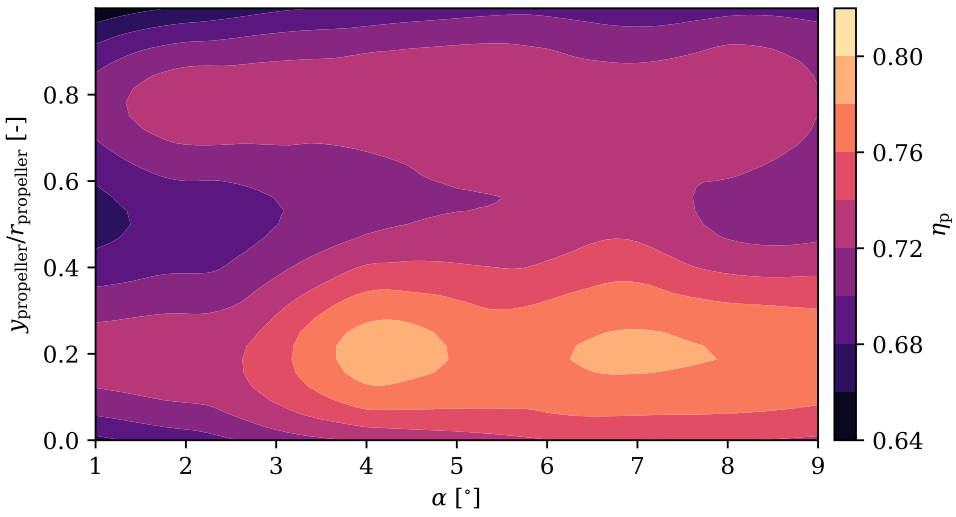

Figure 5.3: Propulsive efficiency as a function of each propeller position above the trailing edge (Y axis) and the angle of attack (X axis) at a Reynolds number of 5×10^5.

higher values correspond to the most elevated propeller position. This trend is valid for every angle of attack and is confirmed when representing both drag and lift coefficients separately in figs. 5.4 and 5.5, respectively.

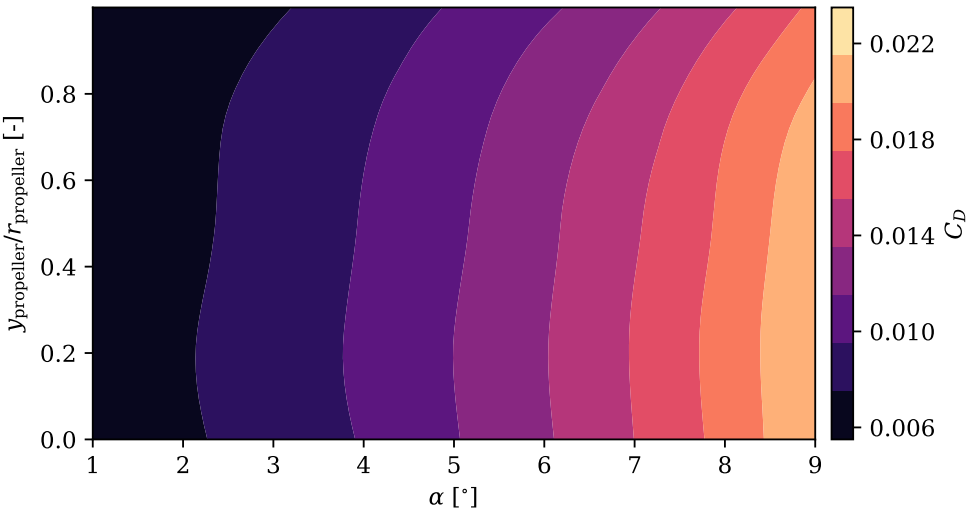

Figure 5.4: Drag coefficient as a function of each propeller position above the trailing edge (Y axis) and the angle of attack (X axis) at a Reynolds number of 5×10^5.

In Fig. 5.4 and 5.5 an improvement of the coefficient can be seen when the highest propeller position is set and the angle of attack is frozen. Taken as an example an α of 4°, the lift coefficient increases almost 10 % when comparing the lowest position with the highest. Meanwhile, the drag coefficient decreases more than 10 % at the same points.

Both coefficients vary to a more significant extent with the angle of attack. For example, increasing the angle of attack from 5° to 6°, the C_L grows around 16 %, while changing the propeller position from 50 % to 75 % corresponds to a 3.5 % growth of this coefficient.

The pressure coefficient for each propeller position and an angle of attack of 5° is depicted in Fig. 5.6 in order to understand the change in aerodynamic coefficients when moving the propeller.

According to Fig. 5.6, setting a higher propeller position translates directly to a greater suction peak on the suction side, keeping unaltered a significant part of the pressure side of the airfoil. Around a point at 20 % of the chord, the laminar separation bubble or LSB can be spotted. To aid the visualization, two C_p detailed zones have been represented in Fig. 5.7.

In Fig. 5.7(a), it can be seen that the suction peak varies between −1.7 in the lower position and −1.9 in the highest position. However, the variation is

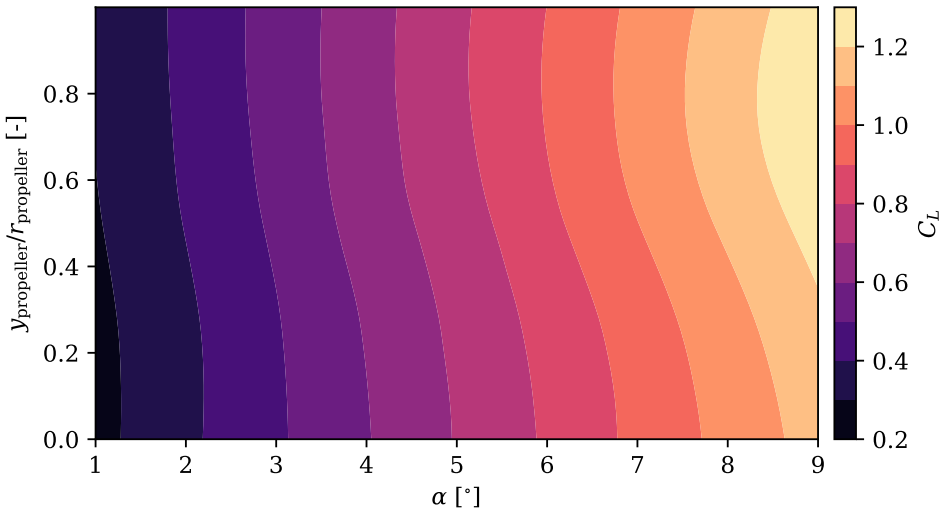

Figure 5.5: Lift coefficient as a function of each propeller position above the trailing edge (Y axis) and the angle of attack (X axis) at a Reynolds number of 5×10^5.

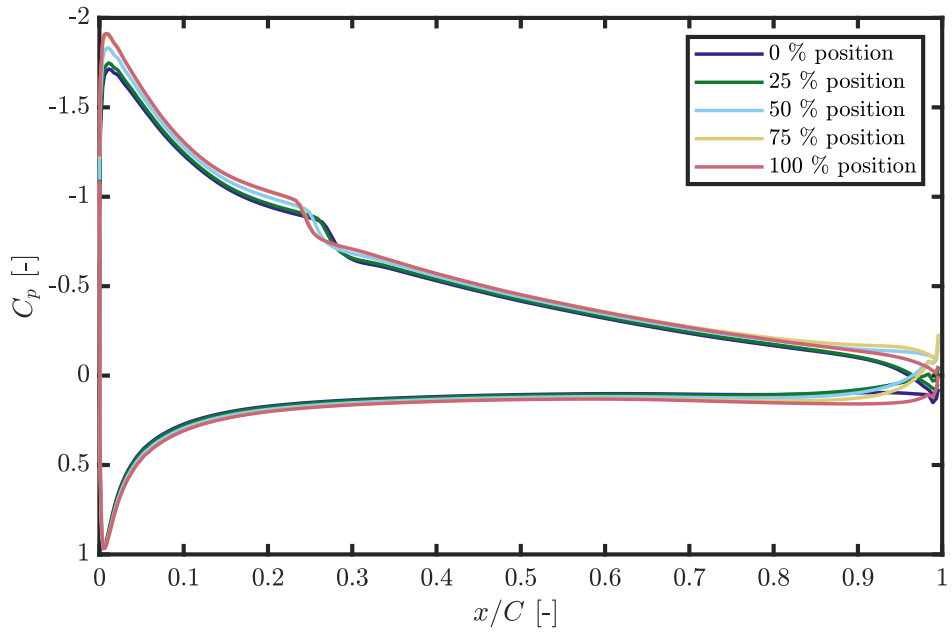

Figure 5.6: Pressure coefficient around the airfoil at 5° of angle of attack and 5×10^5 Reynolds number for each propeller position relative to the trailing edge.

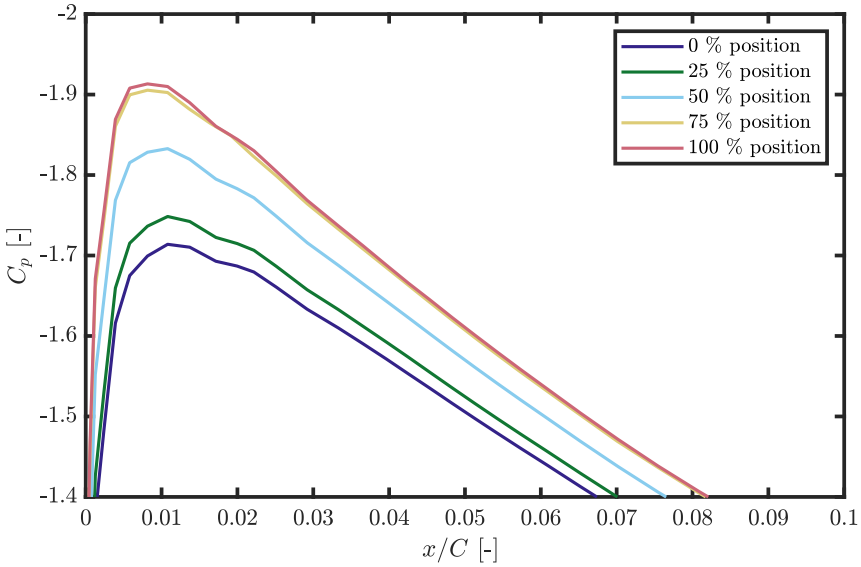

(a) Detailed pressure coefficient near the suction peak.

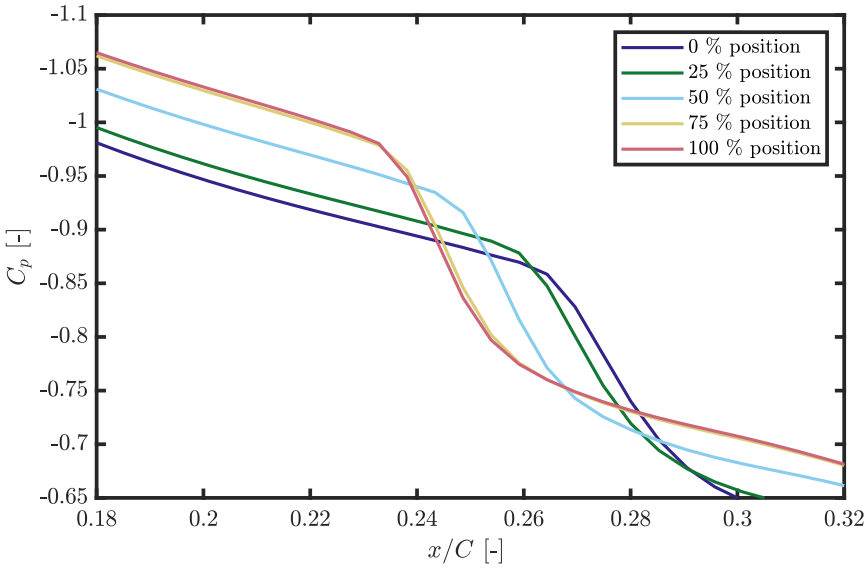

(b) Detailed pressure coefficient near the LSB.

Figure 5.7: Detailed pressure coefficient around the airfoil at 5° of angle of attack and 5×10^5 Reynolds number for each propeller position relative to the trailing edge.

not linear between positions. It can be seen that the increase in suction peak between the two highest positions (75 % and 100 %) is much less than between the lowest or intermediate positions.

An increase in the position of the propeller is also reflected in the advancement of the separation bubble. In Fig. 5.7(b) a trend similar to that mentioned in the suction peak is observed. There is a difference in the appearance of the LSB between the lowest and the highest position of 3 % of the chord. In the same way, a greater distance is appreciated between the lowest and intermediate propeller positions, with the advancement of the LSB being much smaller comparatively between the highest positions.

Raising the propeller position have a similar effect to increasing the angle of attack, a result that can be perceived in the wing when an aircraft flies inside the upwash of another plane. Furthermore, a higher position means that a smaller propeller part is recirculating the pressure side flow. Although this effect is marginal, it contributes to increasing the airfoil's lift.

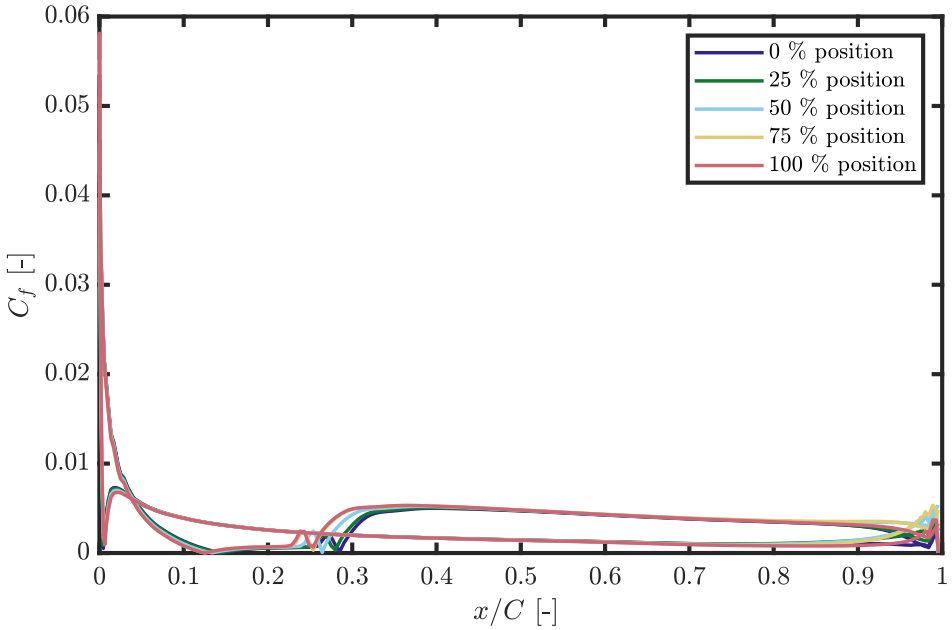

Figure 5.8: Pressure coefficient around the airfoil at 5° of angle of attack and 5×10^5 Reynolds number for each propeller position relative to the trailing edge.

In Fig. 5.8 the friction coefficient is plotted in the same way. Using this coefficient it is easier to see how the LSB moves upstream as the propeller position increases in height. The coefficient behaves similarly in all positions except for the last airfoil section. On the suction side, the friction increases as

the position increases, giving rise to higher parasitic drag. There is an exception for the most elevated position where the effect of the propeller decreases and the C_f decreases as a consequence. This effect occurs because the last percentage of the blade corresponding to the outermost section of the virtual disk does not produce efective thrust. This imposition is made to consider the effects of the blade tip, as discussed in section 4.4. The conclusions obtained for C_p in the pressure side can be extrapolated to the C_f in this airfoil side. When the propeller is set in a lower position, the flow recirculation of the pressure side increases, thus increasing the friction.

Once the BLI effect of the propeller position over the aerodynamic efficiency is understood, this effect is studied over the propulsive efficiency. Fig. 5.3 shows the propulsive efficiency for every value of α and propeller position.

In this figure, it can be seen that the propulsive efficiency is less homogenous than the aerodynamic efficiency. At first sight, an opposite graph to that obtained in Fig. 5.2, should be expected, where the propulsive efficiency should improve if the actuator disk is located more centered concerning the trailing edge. However, the propulsive efficiency results from the combination of several phenomena, leading to an optimization of this parameter between a position of 15 % and 35 %.

Better values of η_p are expected at a lower position because of a geometrical aspect. In this position, the center or hub of the propeller is located near the trailing edge, and the wet propeller area affected by the boundary layer increases. This way, the propeller will be ingesting more boundary layer. Since the speed is lower in this area than the flight speed, the propeller will need less power to produce the same thrust and increase the propulsive efficiency. Nevertheless, the CFD simulations are performed by fixing the flight velocity and not the lift coefficient. As a result, the propeller operating point between different heights will vary even if the angle of attack is kept the same. Because the aerodynamic efficiency changes with the propeller position, the total thrust computed in each simulation is not the same as explained in eq. 4.10, meaning changes in the rotational speed and therefore in the advance parameter J.

In Fig. 5.9 the advance ratio parameter for each propeller position is represented.

As mentioned, with a set angle of attack, J varies if the propeller position change. In the lower positions, the advance parameter remains higher since, being the positions with the highest propulsive performance, it is not necessary to increase the rotational speed as much to reach the thrust request.

5.2.1 Optimal position CFD analysis

A single case is selected for further analysis based on the previous results. From now on, this case will be referred to as the optimal case since, of those

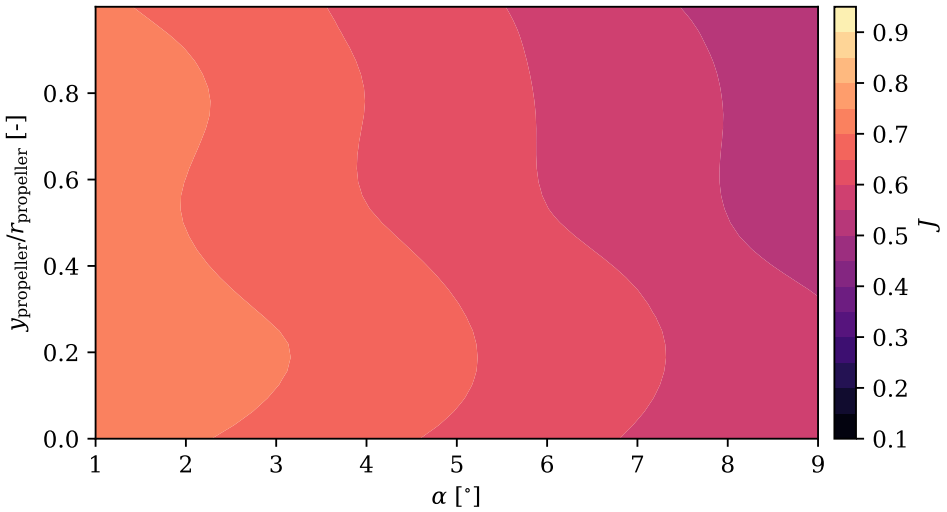

Figure 5.9: Advance ratio for each propeller position above the trailing edge and angle of attack at a Reynolds number of 5×10^5.

tested, it is the one that achieves the best efficiencies product and with which more significant fuel savings are achieved, as can be seen in Section 5.3. However, there may likely be untested configurations that further improve the efficiencies product, becoming even more optimal.

The selected case has a propeller with a radius of 0.04 m in a 31.5 % position, with a distribution of 13 engines and a draft angle of 1.5° and would be compared with other suboptimal cases.

Near-cruise conditions are considered with a Reynolds number of 5×10^5 and an angle of attack of 3°. In fig 5.10 the velocity contours of this case are compared to the baseline case (without propeller).

As can be seen in both cases, the boundary layer is completely attached to the airfoil and has a moderate growth due to the lower angle of attack. The velocity contours around both cases are very similar in magnitude, but a reacceleration exists near the trailing edge due to the propeller. To see the propeller reacceleration properly, a close look at the trailing edge of both cases is represented in Fig. 5.11.

The velocity isolines are remarked in blue in these figures to aid in the comparison. Although the effect of the reacceleration under the airfoil is not very significant, since a small portion of the disk remains below the airfoil trailing edge, it can be seen that the last percentage of the airfoil's chord has a higher speed when the propeller is present.

The pressure coefficient contours are compared in Fig. 5.12.

Fig. 5.12 shows that, at first glance, the propeller does not significantly

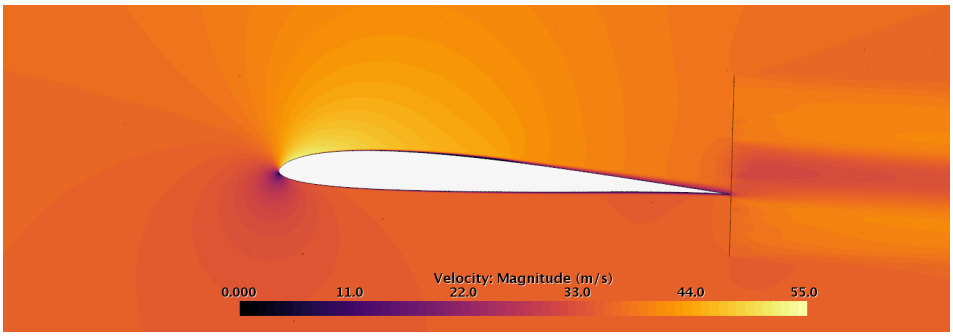

(a) Velocity contours in DEP BLI optimal case in a 31.5 % position. The actuator disk that models the propeller can be seen behind the trailing edge.

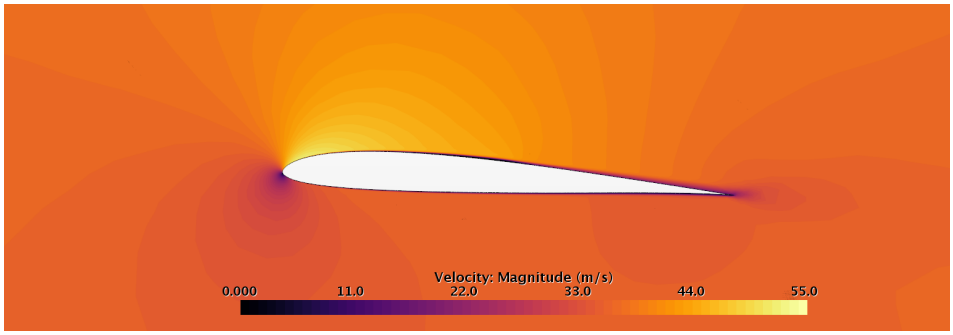

(b) Velocity contours in baseline case without DEP.

Figure 5.10: U contours in mid-plane for best DEP BLI configuration and baseline case comparison at an angle of attack of 3° and a Reynolds number of 5×10^5.

change the pressure coefficient contours around the airfoil. Of course, they are different in the immediate vicinity of the actuator disk, since this virtual disk simulates a pressure jump in flow across its surface.

The optimal case is now compared in Fig. 5.13 with a suboptimal case with a propeller position at 75 % and a case without BLI. For the sole purpose of generating a comparison, in this last case, the same height of the propeller has been maintained. As an additional disclaimer, since the objective of this work is not to optimize a case with DEP but without BLI, it is very likely that this case is far from being optimized.

It is immediate to observe in Fig. 5.13 how, when placing the propeller in a higher position, there is less reacceleration in the pressure side. Around the airfoil, the velocity contours, in this case, are similar. The velocity contours in the case without BLI have a different nature. Placing the propeller near the leading edge projects a wake faster than the free inlet flow onto the surface of

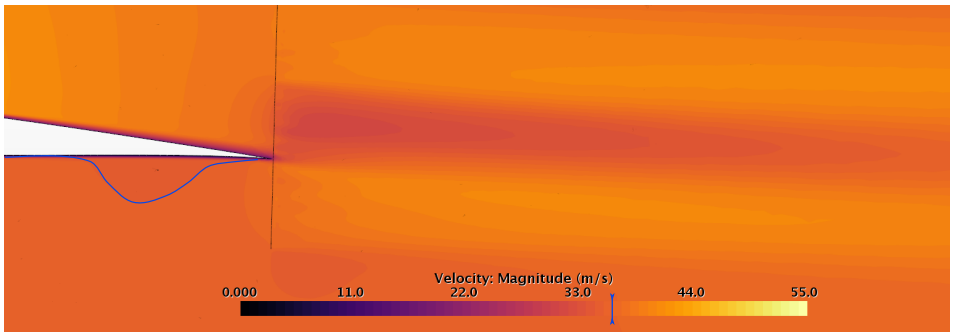

(a) Detail of velocity contours in DEP BLI optimal case in a 31.5 % position.

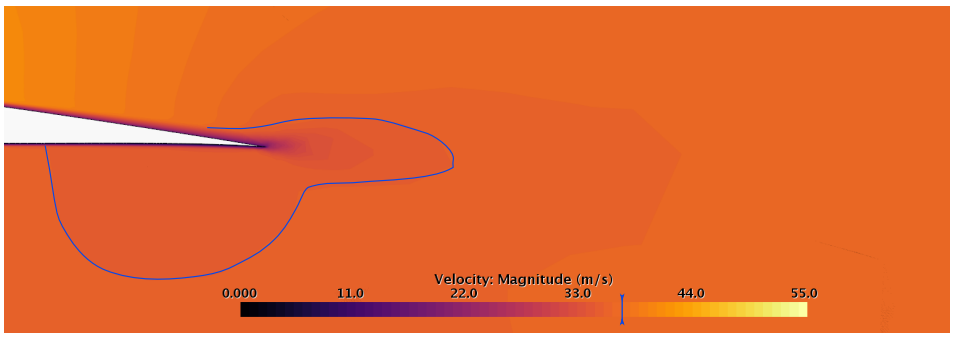

(b) Detail of velocity contours in baseline case without DEP.

Figure 5.11: Detail of U contours using a midplane for best DEP BLI configuration and baseline case with isovelocity lines under the pressure side for better comparison.

the airfoil.

In Fig. 5.14 the pressure coefficient contours are plotted for the same cases than in Fig. 5.13. As anticipated, the optimal position disturbs the flow around the pressure side to a greater extent than the suboptimal DEP BLI setting. As an overall comment, the C_p contours are similar in the three cases.

An additional simulation containing only the propeller is carried out, imposing in the simulation the same advance ratio and velocity as the DEP BLI case.

The results of all cases are collected in Table 5.2. The reacceleration of the flow due to the BLI increases the angle of attack perceived. Therefore, the lift coefficient is higher than the baseline case. As a counterpart, because the height of the propeller is not high enough, in the optimal case the aerodynamic efficiency is not optimized, being 1 % lower than the baseline case. The main cause is the increase in the friction due to the acceleration, leading to a rise in parasitic drag. Meanwhile, this propeller position benefits from a greater area

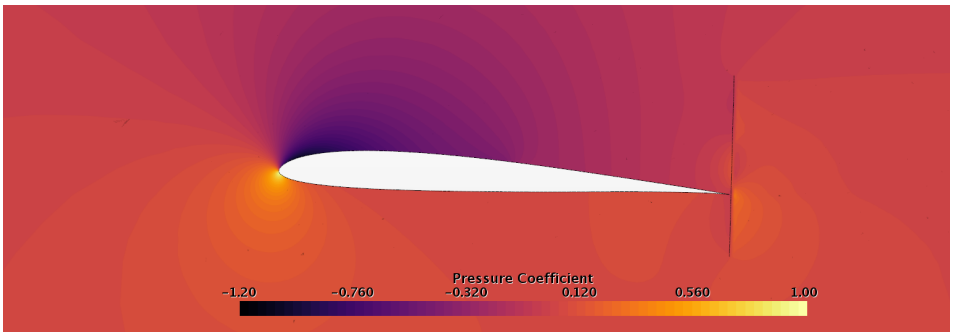

(a) Pressure coefficient contours in DEP BLI optimal case in a 31.5 % position.

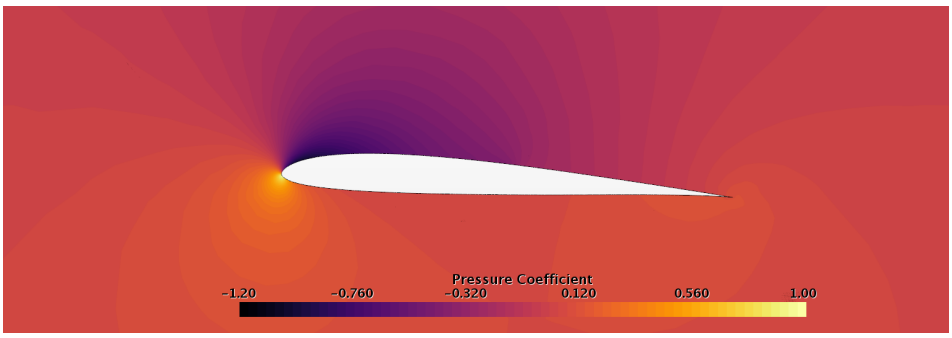

(b) Pressure coefficient contours in baseline case without DEP.

Figure 5.12: C_p contours in mid-plane for best DEP BLI configuration and baseline case comparison at an angle of attack of 3° and a Reynolds number of 5×10^5.

wetted by the boundary layer, thus optimizing the propulsive efficiency. In the end, the product of both efficiencies is around 6 % higher in the DEP and BLI case with respect to the baseline case. The suboptimal DEP BLI configuration absorbs the rise in drag produced in the pressure side with the propeller height. This way, the drag increases but to a lesser extent, which is accompanied by an increase in C_L. This gives rise to higher aerodynamic efficiency than the base case. However, the propeller position slightly penalizes propulsive efficiency giving rise to a lower efficiencies product as seen in 5.2, but very close to the optimal position.

The case with DEP but without BLI has a higher propulsive efficiency than expected. The reason for this increase is the position of the propeller. As can be seen in Fig. 5.14(c), the propeller is located very close to the leading edge and in a relatively low position. This way, a significant part of the actuator disk benefits from the low velocity near the stagnation point, increasing the propulsive efficiency. However, the reacceleration of both the pressure side and the suction

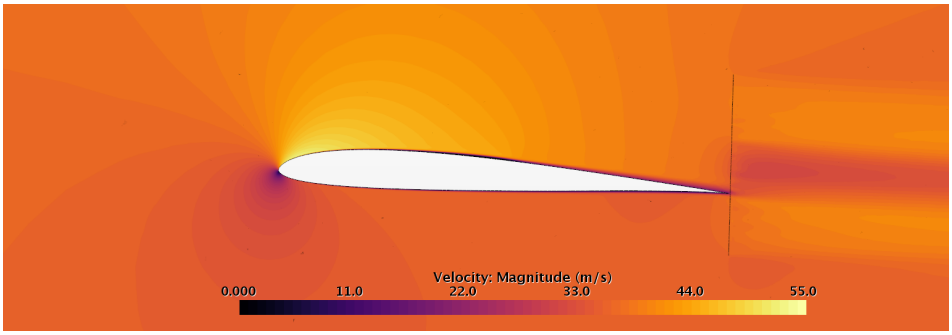

(a) Velocity contours in DEP BLI optimal case in a 31.5 % position.

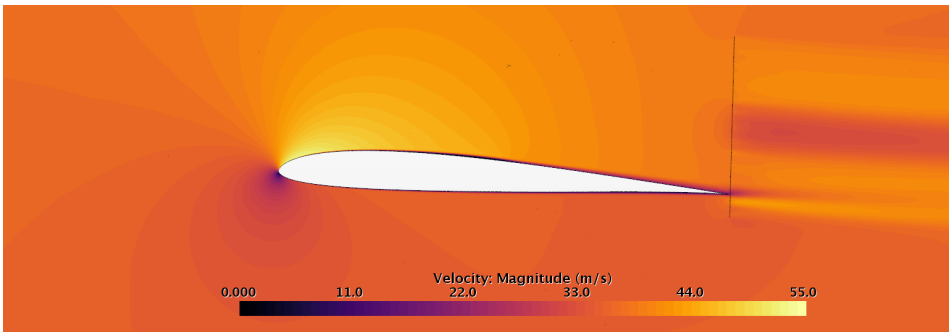

(b) Velocity contours in in DEP BLI optimal case in a 75 % position.

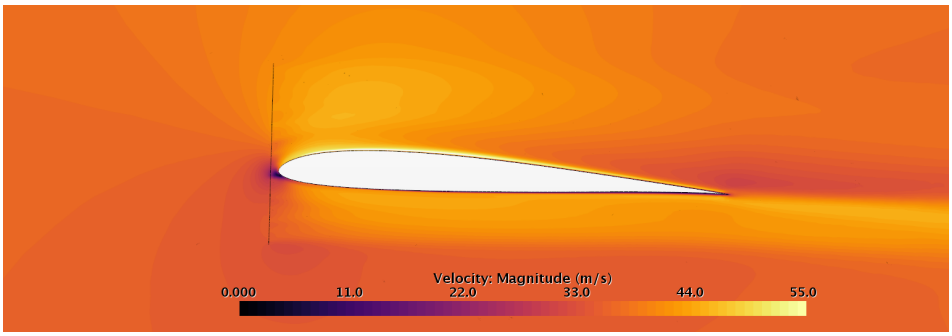

(c) Velocity contours in DEP without BLI case in a 31.5 % position.

Figure 5.13: U contours in mid-plane for best DEP BLI configuration, a suboptimal DEP BLI setting and a case with DEP configuration in leading edge, at an angle of attack of 3° and a Reynolds number of 5×10^5.

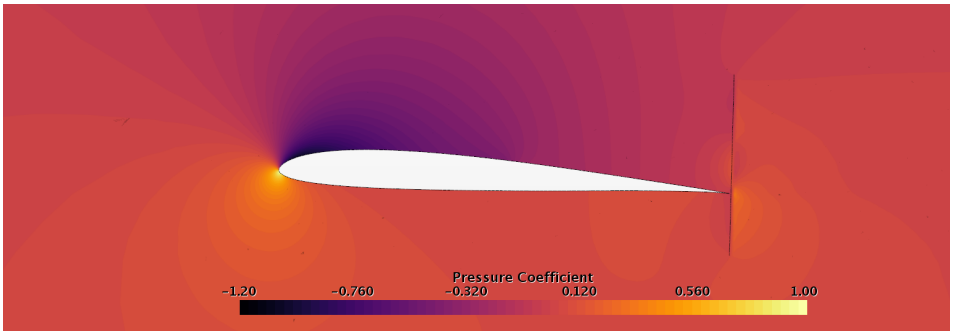

(a) Pressure coefficient contours in DEP BLI optimal case in a 31.5 % position.

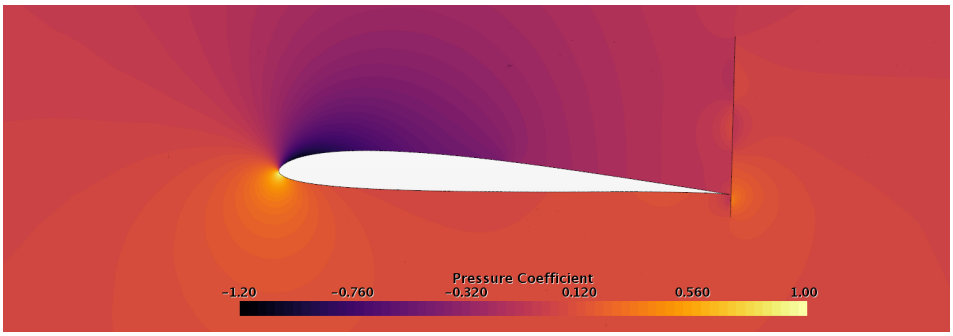

(b) Pressure coefficient contours in in DEP BLI optimal case in a 75 % position.

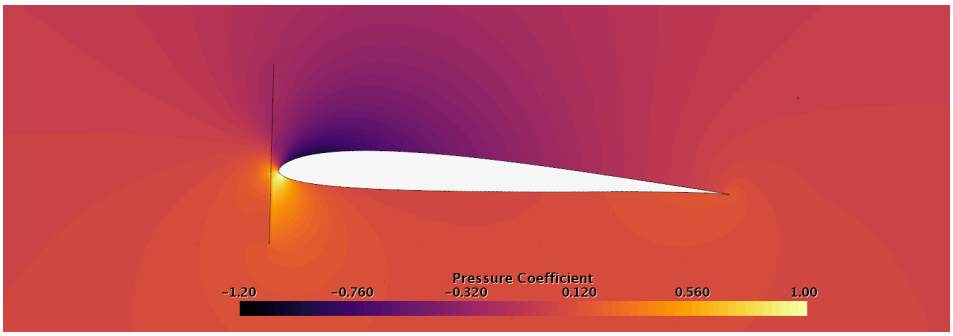

(c) Pressure coefficient contours in DEP without BLI case in a 31.5 % position.

Figure 5.14: C_p contours in mid-plane for best DEP BLI configuration, a suboptimal DEP BLI setting and a case with DEP configuration in leading edge, at an angle of attack of 3° and a Reynolds number of 5×10^5.

side decreases the pressure gap, reducing the lift coefficient. At the same time, the friction drag increases, significantly reducing the aerodynamic efficiency. In conclusion, the product of efficiencies gives the worst result compared to the rest of the cases.

	C_L	$C_{D,0,\text{wing}}$	C_L/C_D	η_p	$C_L/C_D \cdot \eta_p$
Baseline	0.484	0.00769	17.280	0.692	11.96
DEP BLI optimal	0.505	0.00841	17.08	0.748	12.77
DEP BLI 75 %	0.540	0.00798	17.56	0.726	12.74
DEP no BLI	0.509	0.015	13.81	0.859	11.86

Table 5.2: Coefficient comparison between optimal DEP and BLI case with propeller in a 31.5 % position, and baseline case without DEP, a suboptimal DEP BLI with propeller in a 75 % position and a DEP setting without BLI. All simmulations have been carried out at an angle of attack of 3° and a Reynolds number of 5×10^5.

For a better understanding of the impairment in aerodynamic efficiency, the pressure coefficient of this case is compared with the baseline case in Fig. 5.15.

In Fig. 5.15(b) C_p is plotted from three different planes corresponding to three wing span positions. The first one in blue corresponds to the already mentioned (section 4.7) midplane that divides the domain into two symmetrical parts through the propeller center. In red, a parallel plane is plotted crossing by the middle of the radius of the actuator disk. This position corresponds to the middle of the propeller blade. Last, another parallel plane cuts the domain where the virtual disk ends, just at the tip of the propeller blade. To aid in the visualization, a frontal view of the wing with the actuator disk is depicted in Fig. 5.15(a), with the three different planes marked.

In Fig. 5.16 the detailed suction peak is represented. The inclusion of BLI prompted a more significant suction peak, almost 4 % higher than the baseline case. Additionally, the value of the C_p for the BLI case is also higher on all the suction side, explaining the growth in C_L.

The pressure coefficient has the same value in each span up to about 60 % of the chord, as can be seen in Fig. 5.17, wherefrom this point discrepancies are found. As the analysis plane is located away from the mid-plane, the C_p obtained has a behavior similar to the baseline case.

As seen, the propeller effect over the boundary layer near the trailing edge is more significant near the center of the actuator disk compared with the tip. Therefore, it is expected to observe non-uniformities along the wing span as the angle of attack increases and the boundary layer detaches.

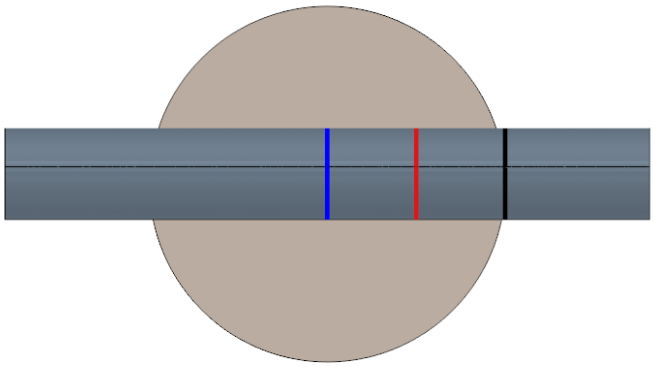

(a) Span positions in frontal view.

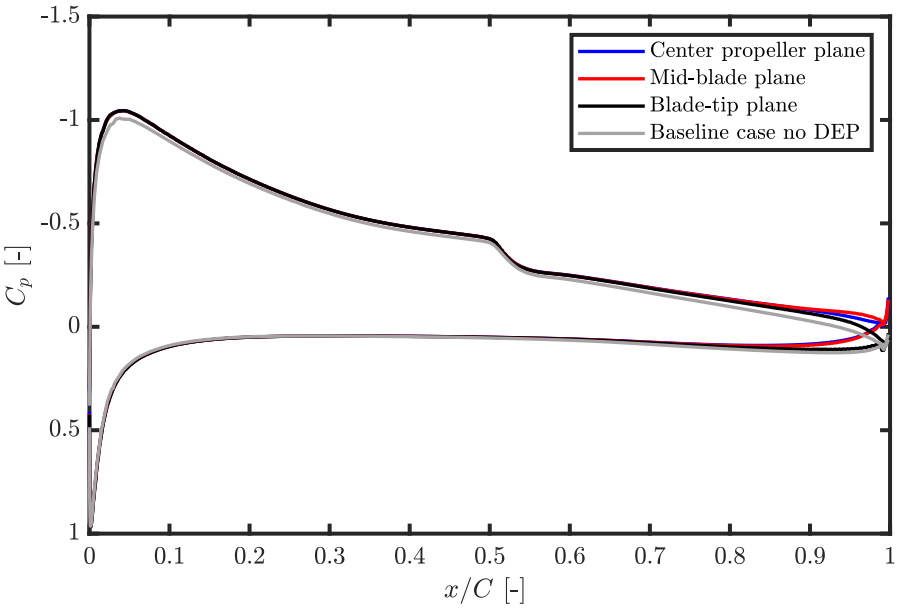

(b) Pressure coefficient distribution at three different spans and baseline case comparisson.

Figure 5.15: Cp comparison for optimal DEP BLI configuration case with propeller in a 31.5 % position in different wing spans, and baseline case middle plane.

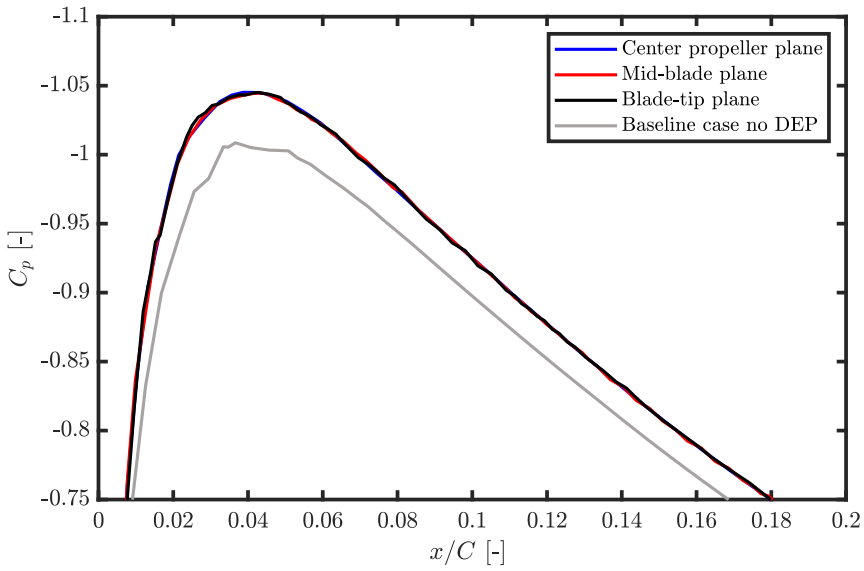

Figure 5.16: Detailed Cp near suction peak for optimal DEP BLI configuration case with propeller in a 31.5 % position in different wing spans, and baseline case middle plane.

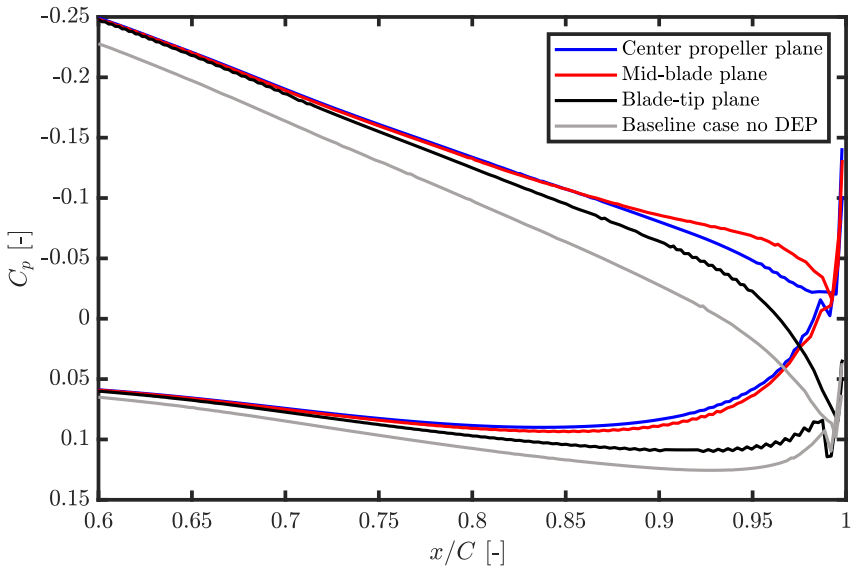

Figure 5.17: Detailed Cp in last chord percent for optimal DEP BLI configuration case with propeller in a 31.5 % position in different wing spans, and baseline case middle plane.

Although it is possible to see the LSB appearance in Fig. 5.15(b), it is easy to perceive it if the C_f is plotted. The friction coefficient is represented both for the DEP BLI and baseline case only using the mid-plane described in fig 5.18.

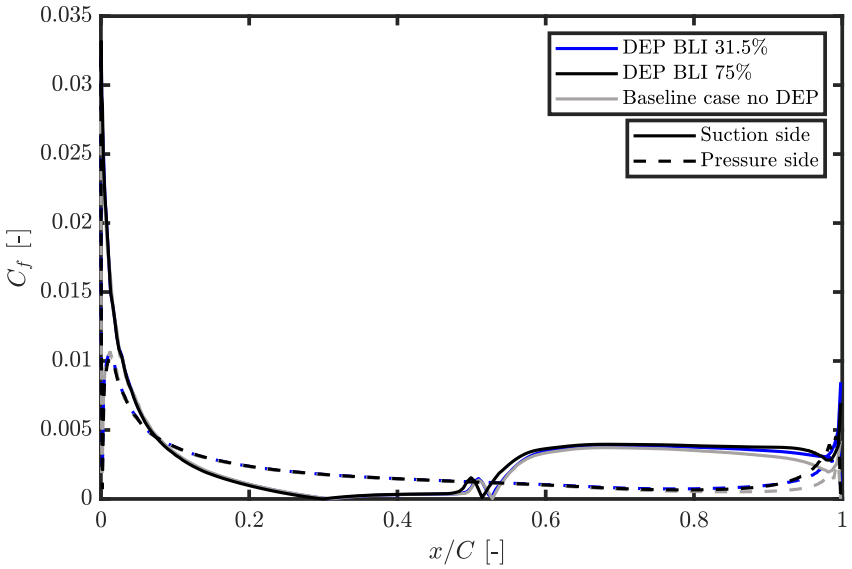

Figure 5.18: Friction coefficient comparison for DEP BLI optimal case with propeller in 31.5 %, a DEP BLI case with propeller in in 75 % and baseline case without DEP and BLI distinguishing between suction side and pressure side.

In the DEP BLI case, the LSB shows earlier on the suction side. As mentioned before, placing a propeller behind the wing alters the flow around the wing, increasing the apparent angle of attack. When α increases, the LSB tends to move upstream. This trend has been previously observed experimentally in [118], where it is shown that if the angle of attack increases, the pressure force resultant is displaced towards the leading edge. By doing this, the lift increases and the boundary layer transition moves upstream.

Analyzing the friction coefficient of the suction side, the first thing that stands out is the difference in the absolute value of friction just before and after the LSB. In the DEP BLI case, the flow reacceleration creates a smaller bubble. If the length of the bubble decreases, the effective inviscid flow shape changes around the airfoil, as Sutton explains [119].

As a result, the pressure drag decreases and higher suction peaks are obtained, matching a higher C_L. The reacceleration of the flow has a counterpart explained by Tepperin [37]. The air suctioning near the trailing edge lowers the pressure and accelerates the flow before the propeller, increasing the shear force in this zone. Increasing the shear force means that the friction drag also

grows, which can be seen after the LSB in Fig. 5.18. On the pressure side, the same comment can be said. Because a large part of the actuator disk is located under the trailing edge, the pressure side is also reaccelerated, increasing the friction drag. In overall terms, the increase in drag due to the friction of the reacceleration outweighs the decrease in pressure drag produced by the flow change around the airfoil.

As commented in the previous section, it is foreseeable that the propulsive efficiency of the optimal position is higher than the efficiency of a case with a propeller set in a higher position because of the geometrical situation, since the propeller set in a higher position have a smaller area wetted by the boundary layer.

In Fig. 5.19, a frontal view similar to the one presented in Fig. 4.10 is plotted, where only the velocity contours in the actuator disk surface are sketched. The plot also contains a transparent wing to aid in the visualization.

As shown in Fig. 5.19, if a lower propeller position is set, a higher boundary layer washed area is captured in the actuator disk. Also, the overall velocity in the propeller's plane is lower in the optimal position compared with the higher one, which leads to better propulsive efficiency.

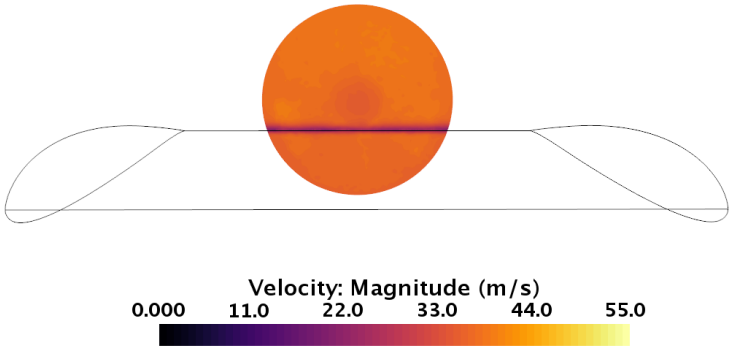

(a) Velocity contours in the actuator disk of DEP BLI optimal case in a 31.5 % position.

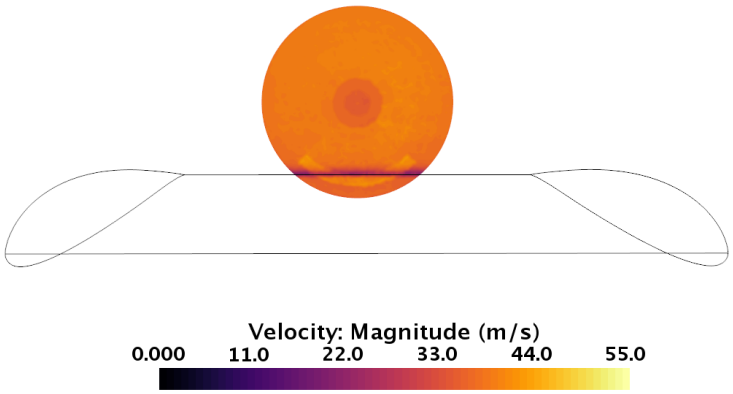

(b) Velocity contours in the actuator disk of DEP BLI optimal case in a 75 % position.

Figure 5.19: U contours in the actuator disk plane for best DEP BLI configuration and suboptimal DEP BLI case comparison at an angle of attack of 3° and a Reynolds number of 5×10^5.

5.3 Aircraft range optimization

The case with 13 engines, 40 mm propellers set in a 31.5 % position above the trailing edge, and 1.5° draft angle is employed in the range optimization as a result of the CFD analysis of section 5.2.1, and compared with suboptimal cases.

In chapter 4, the range calculation method was introduced (equations 4.11 and 4.14) for both baseline and hybrid cases. Now that the optimal case is selected the velocity law which maximizes the specific range can be depicted and compared in Fig. 5.20.

Different specific range contours are observed between the baseline and the best HE DEP BLI case. In both cases, at the beginning of the flight (at 25 kg of *MTOM*), the optimal velocity is always higher than at the end of the flight (near 15 kg). However, the maximum β of each contour in the DEP BLI case is displaced to higher velocities compared with the baseline case. The change in the contours is derived from the product of efficiencies variation but mainly from the ICE operation. As explained before in section 4.6, the flight velocity is imposed in the baseline case to change parametrically with the aircraft mass. Nevertheless, in the DEP BLI case, the velocity is changed in every moment of the flight in order to maximize the specific range. This is possible thanks to the decoupling between the ICE and the electric motors of the series hybrid configuration. At first sight, the velocity changes throughout the flight might seem abrupt. But as anticipated, the total range calculated surpasses the 4000 km, and combined with an average velocity of 40 $\mathrm{m\,s^{-1}}$ the accelerations resulting from changes in speed during the flight are very small.

Because all the hybrid cases optimize the ICE torque and rotational speed in the same way, the *BSFC* behavior is almost the same in the ICE map. However, fluctuations are observed when the specific range of diverse hybrid cases is plotted, due to different flight velocities between cases chosen during the optimization.

In Fig. 5.21 the specific range of a pure hybrid case (without DEP or BLI) and a suboptimal DEP BLI case with a propeller position of 75 % are compared. This case will be referred as DEP BLI 75 in the rest of the section. In the pure hybrid case, all possible β improvement is due to the *BSFC* optimization. In this case, the map is shifted to the left compared with the DEP BLI cases, meaning that a lower velocity law optimizes the specific range. In contrast, the DEP BLI cases have a more expansive β map, with the mean velocity shifted to higher values. Also, in these cases, the higher value of β, situated in the lower values of *MTOM* comprises a wider range; therefore, with the same amount of fuel, a DEP BLI case will reach a more extensive flight range. In the DEP BLI cases, it is possible to observe that, although the optimal case with a 31.5 % propeller position maximizes the range, the β map is narrower and deteriorates

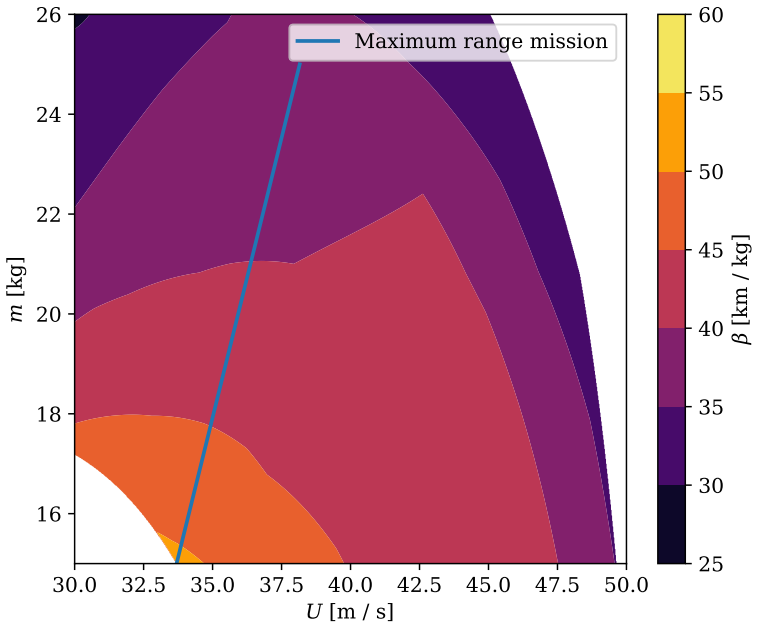

(a) Specific range map for baseline case with velocity which maximises β.

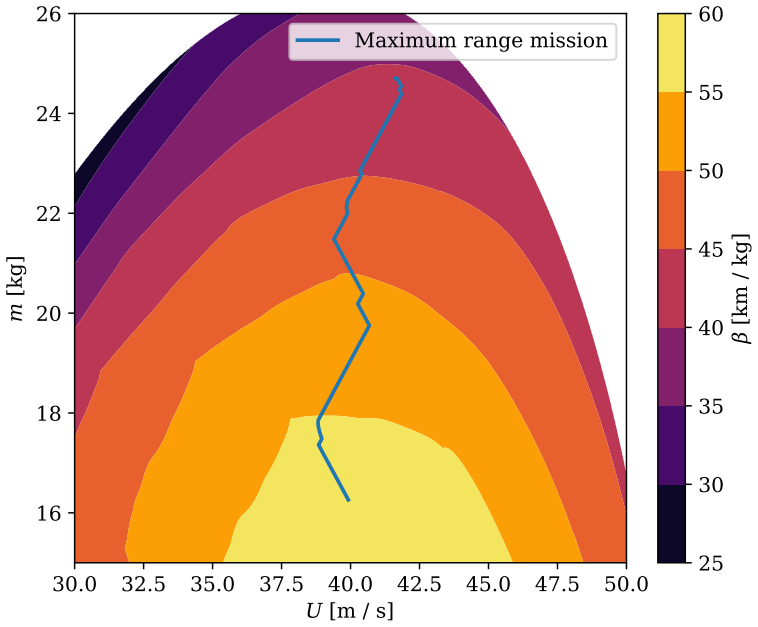

(b) Specific range map for DEP BLI optimal case with velocity which maximises β.

Figure 5.20: Specific range map for the baseline and DEP BLI optimal cases. In blue is marked the velocity which maximises β depending of the flight velocity law.

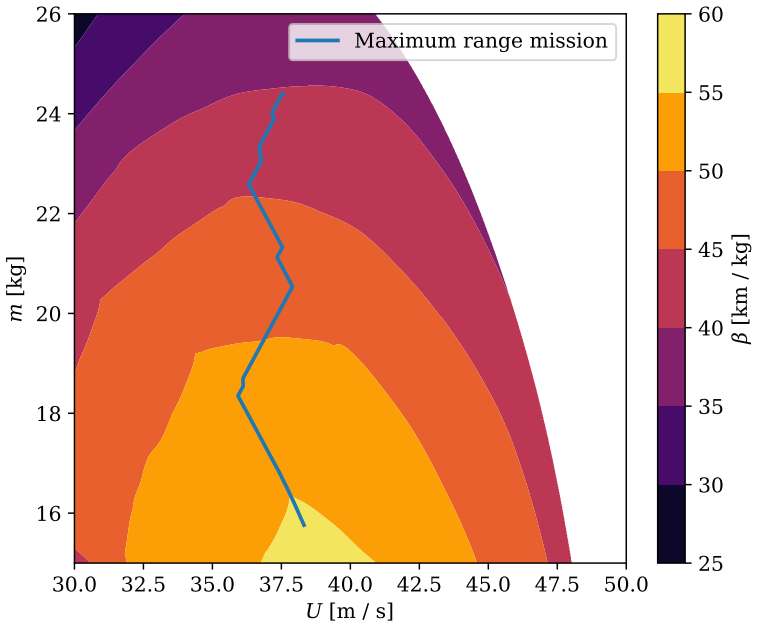

(a) Specific range map for the pure hybrid case without DEP and BLI, with velocity which maximises β.

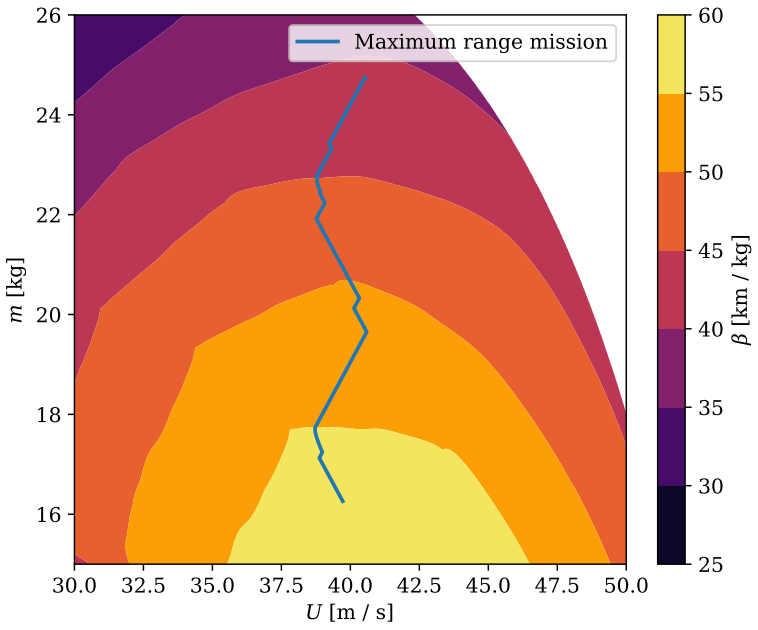

(b) Specific range map for DEP BLI suboptimal case with the propeller in a 75 % position above the trailing edge, with velocity which maximises β.

Figure 5.21: Specific range map for the pure hybrid and DEP BLI suboptimal cases. In blue is marked the velocity which maximises β depending of the flight velocity law.

the specific range quickly if the velocity drops. This does not occur so abruptly if the propeller is set in a higher position.

The leading cause for this is how the improvement of β is produced. In a lower position, the main variable of the product of efficiencies that optimize the range is the propulsive efficiency. If the flight velocity change, the advance parameter of the propeller also varies, impairing this efficiency quickly, as seen in Fig. 5.22.

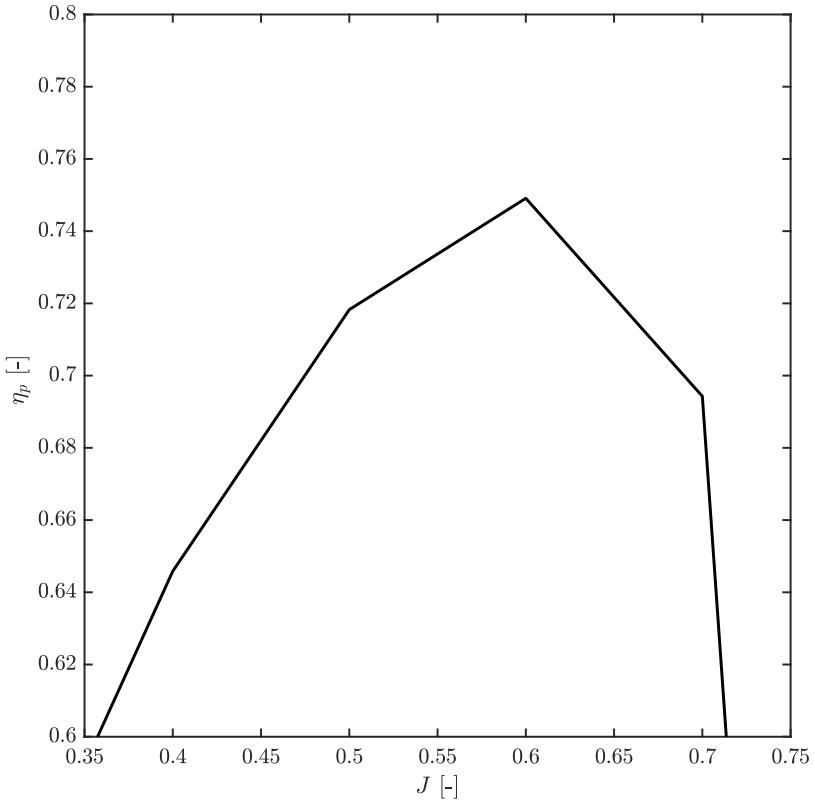

Figure 5.22: Propeller of 0.1143 m propulsive efficiency at a Reynolds number of of 5×10^5.

The propulsive efficiency is independent of the Reynolds number when this number and the propeller size are large enough. The single-blade propeller used in the baseline case illustrates the fall of propulsive efficiency as the advance ratio parameter progresses.

In this figure, the maximum propulsive efficiency corresponds to an advance parameter of 0.75. To illustrate the quick drop in propulsive efficiency, if the aircraft has a J equal to 0.6 at a Re equal to 5×10^5 (i.e. 35 m/s) and the flight

velocity increases by 3 m/s, maintaining the rotational speed, the J changes between 0.65 and 0.7. With this small change in the advance parameter, the propulsive efficiency drops 5 %.

The operation from both baseline and optimal DEP BLI case is translated to the ICE map in Fig. 5.23.

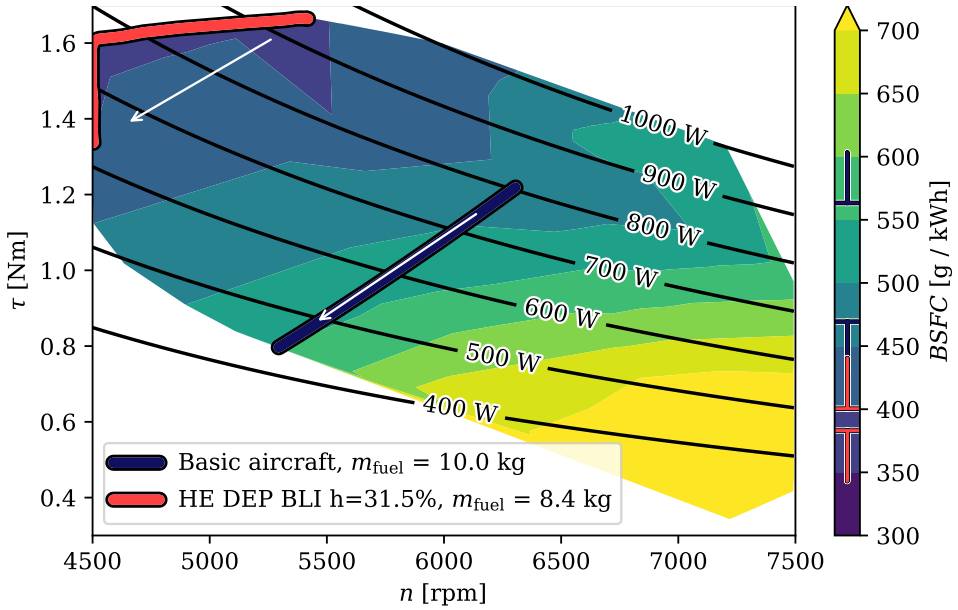

Figure 5.23: Maximum range mission evolution over the ICE map for the baseline case in blue and for the DEP and BLI optimal case in red. White arrows indicate the direction of the ICE operation through the flight.

The operation throughout the flight is tagged with a blue line in the baseline case and using a red line in the optimal case. The operation in the baseline case requires more fuel than the hybrid because both propeller and ICE are mechanically coupled through the rotational speed parameter. The operation is always kept within a stable region of the ICE map using a constant multiplication factor for the gearbox and additional constraints in the limits of the optimization of the velocity law. The optimal DEP BLI case operation is represented with a red line. In this case, the line saturates the map because of the decoupling between ICE and propellers, which allows working at a more optimal point of the engine with more power produced and less fuel burned. In Fig. 5.23, a white arrow indicates the direction of the operation throught the flight.

It should be noted that independently of the propeller distribution, if the power plant is series-hybrid, the engine operates almost in the same zone, towards high torques and low engine speeds. In Fig. 5.24 the operation throughout the flight of the pure hybrid and the DEP BLI 75 case are represented.

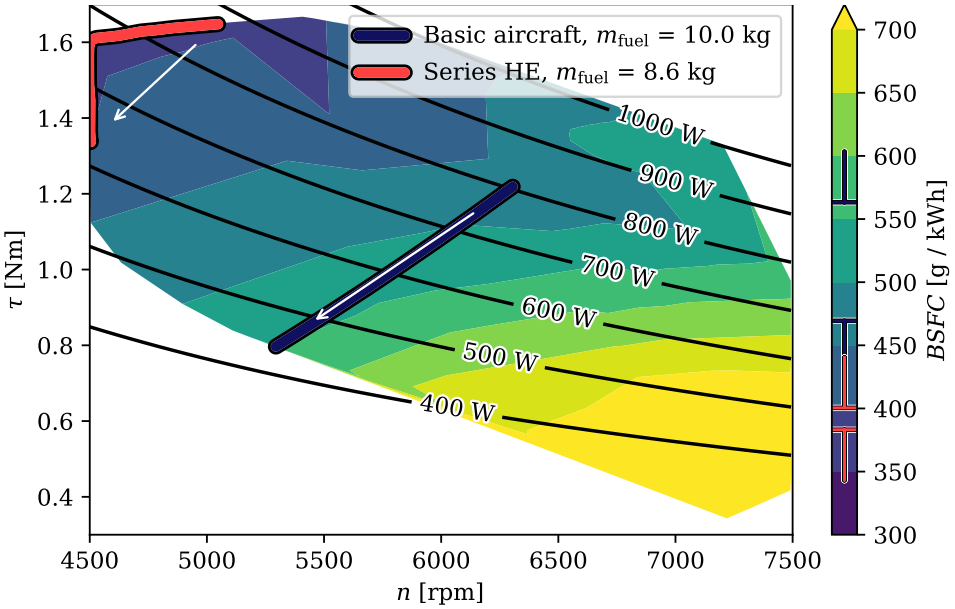

(a) Maximum range mission evolution over the ICE map for the baseline case in blue and for the pure hybrid case without DEP and BLI in red.

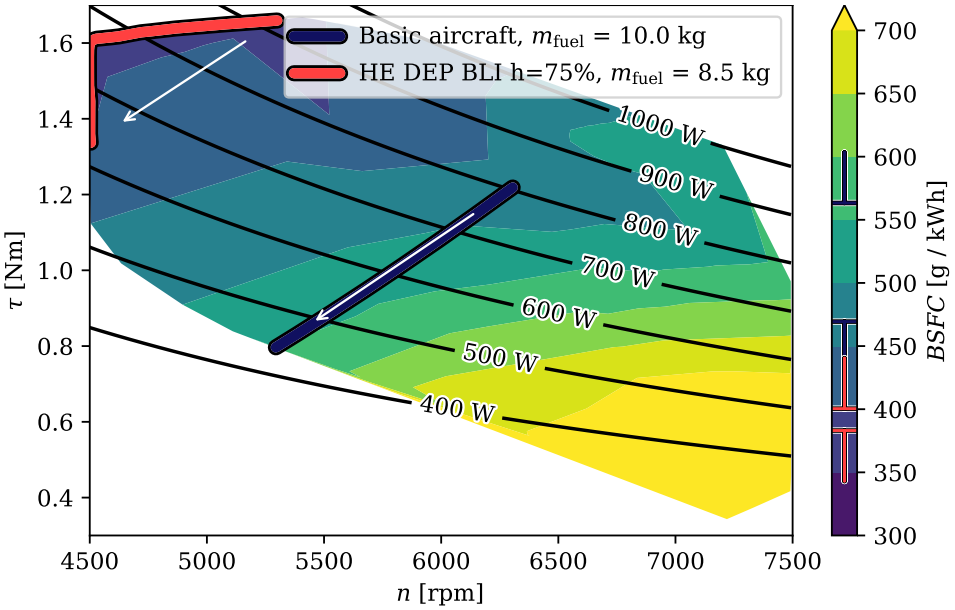

(b) Maximum range mission evolution over the ICE map for the baseline case in blue and for the DEP BLI suboptimal case with the propeller in a 75 % position above the trailing edge in red.

Figure 5.24: Maximum range mission evolution over the ICE map for the baseline case in blue and for the pure hybrid and the DEP and BLI suboptimal cases in red. White arrows indicate the direction of the ICE operation through the flight.

As mentioned before, the fuel reduction during the flight will depend on the improvement in aerodynamic and propulsive efficiency derived from the correct use of DEP and BLI.

A velocity comparison between cases is depicted in Fig. 5.25 as a function of the aircraft covered range. For a better understanding of the velocity variation, the velocity is plotted in Fig. 5.26 as a function of the aircraft mass decrement as the fuel is burned.

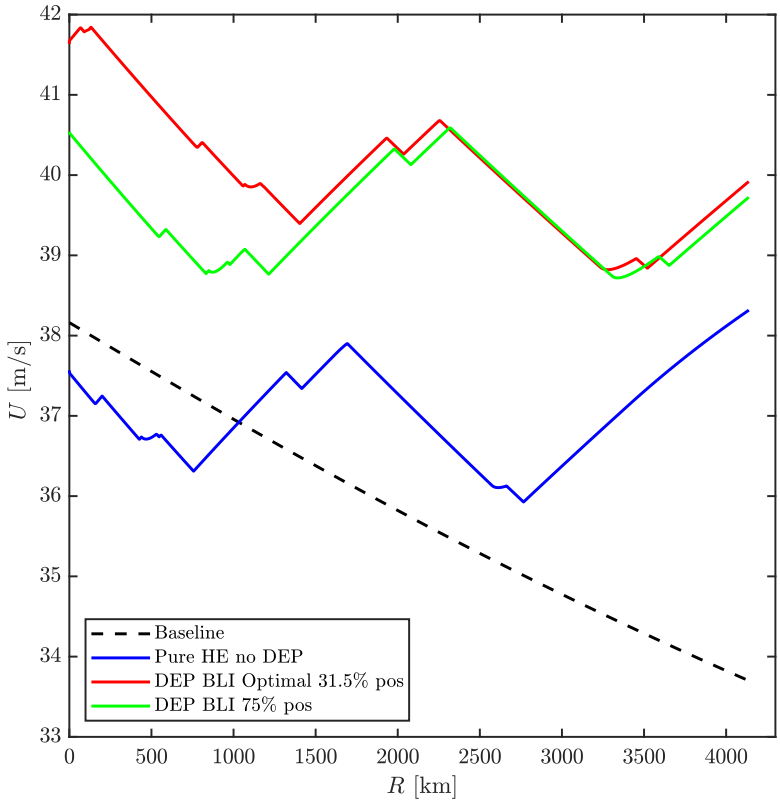

Figure 5.25: Comparison of flight velocity during the mission by aircraft with different propulsion plant setting.

As the mission progresses and the fuel is burned, the weight of the aircraft decreases. Looking at the baseline case, as the mass decreases, the power needed also decreases. The velocity strategy is to progressively be lowered to ensure that the *BSFC* is at the minimum possible, matching the required rotational velocity of the propeller. Meanwhile, in the hybrid cases, the speed increases and decreases around almost a constant speed. This way, the optimum specific fuel consumption is kept nearly constant at an optimum point, cushioning the

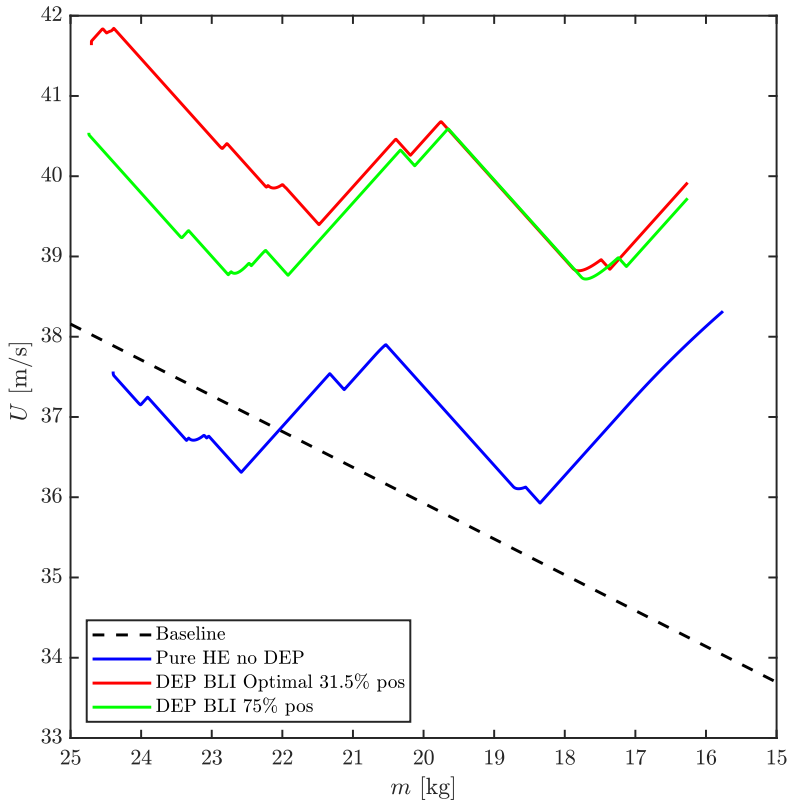

Figure 5.26: Comparison of flight velocity during the mission as function of the aircraft mass by aircraft with different propulsion plant setting.

drop in power. Despite all hybrid cases having equivalent velocity trends, the main velocity in each case is different. The pure hybrid is the case with a lower velocity, even starting the flight under the baseline case. The DEP and BLI cases optimize the range at a higher speed, starting the optimal case at the higher velocity. Since the fuel calculation matches the range of the baseline case with 10 kg of fuel, all cases have the same operational range, as seen in Fig. 5.25. However, as they don't burn the same amount of fuel to reach that range, the initial and final mass is different in Fig. 5.26. The range calculation takes into account that all the fuel will burn, leading to a final weight equivalent to the operative empty weight (OEW). The graph finishes early in the hybrid cases since their OEW is higher, as mentioned in chapter 3. Also, the graph of all hybrid cases starts before the baseline case meaning that fuel saving is happening.

Different velocities between cases mean that the total flight time will change.

In Fig. 5.27, the accumulative time of flight is plotted against the mission range.

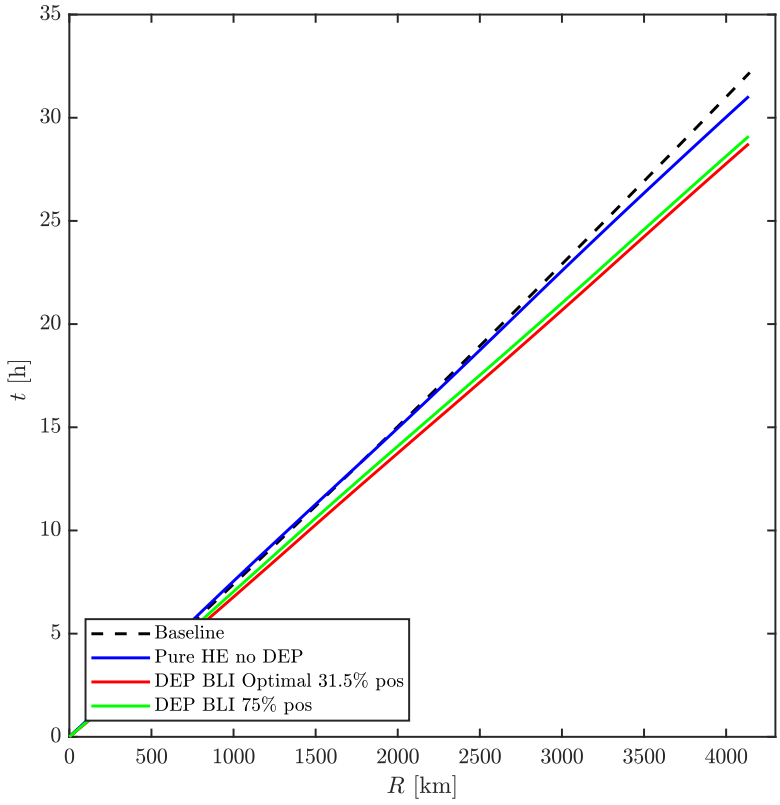

Figure 5.27: Comparison of the time flight mission by aircraft with different propulsion plant setting.

Because the speed is higher in the DEP BLI cases, the mission is completed early. In the optimal case, the mission is finished in less than 29 hours; meanwhile, in the baseline case, 32 hours are needed. It should be remembered that the mission to be optimized is the range of the aircraft and not its flight time. A mission based on maximizing endurance could produce significant changes.

Setting a flight velocity law directly impacts the plane's efficiencies. Fig. 5.28 shows the aerodynamic efficiency evolution through the flight for all the cases.

As the flight progresses, the velocity is lowered in the baseline case to cushion the aerodynamic efficiency drop. This tendency is also observed in the DEP BLI cases, but the pure hybrid does not minimize enough the speed at low aircraft mass to maintain a good propeller performance. As a result, the pure hybrid has worse aerodynamic efficiency than the baseline case. The optimal DEP BLI

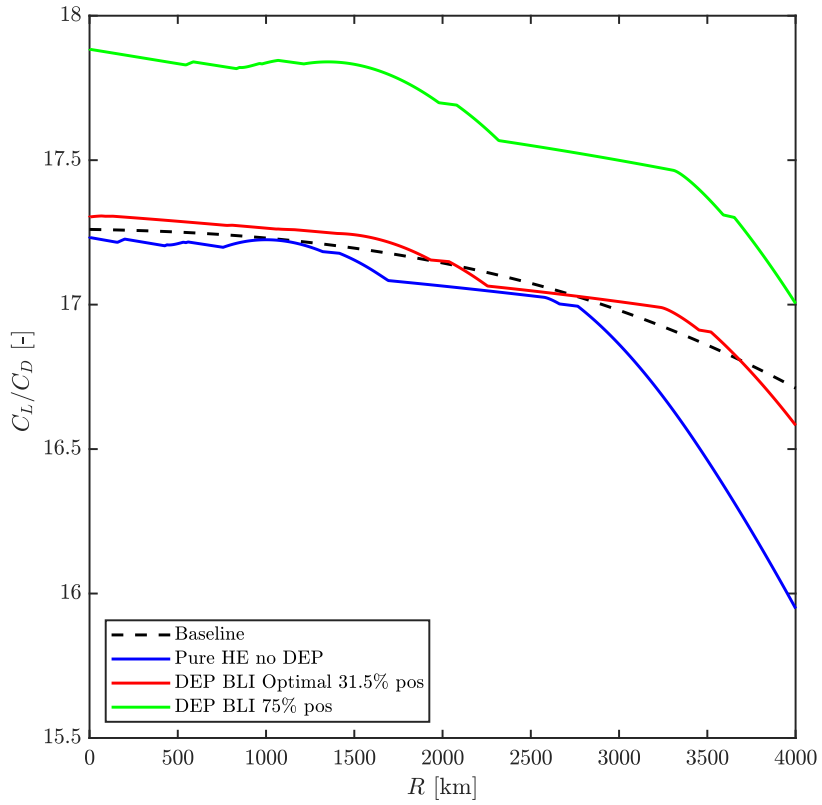

Figure 5.28: Comparison of the aerodynamic efficiency during the flight by aircraft with different propulsion plant setting.

case has a slight improvement in the aerodynamic efficiency compared with the baseline case. Nevertheless, a higher propeller position translates to better aerodynamic efficiency. As an example of that, the DEP BLI 75 case has almost a 3 % higher lift-to-drag ratio at all times of the flight.

In Fig. 5.29 the propulsive efficiency through the flight is plotted for all the cases.

The flight speed set by the velocity law maintains an almost constant propulsive efficiency in all cases. It can be seen that the cases without distributed propulsion, the baseline and the pure hybrid cases, have the same efficiency for much of the flight, only being lowered in the pure hybrid in the last thousand kilometers. In the DEP BLI cases, the optimal position is more efficient because of the lower propeller setting. This case has a greater propeller area affected by the boundary layer ingestion developed above the wing, which translates to higher efficiencies compared to the suboptimal case. This case has worse

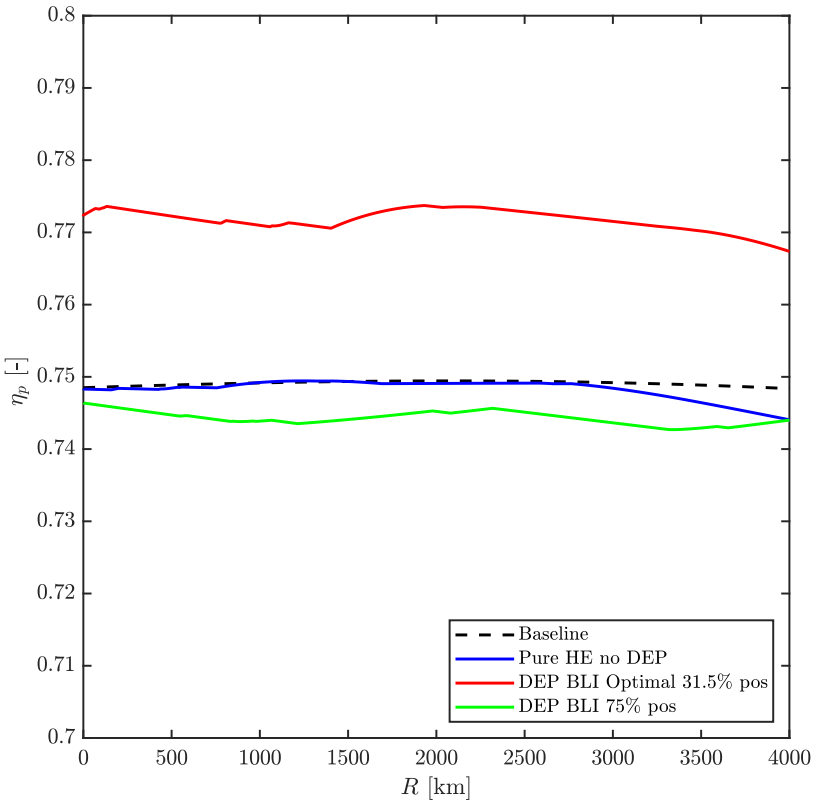

Figure 5.29: Comparison of the propulsive efficiency during the flight by aircraft with different propulsion plant setting.

propulsive efficiency with the flight velocity law setting than the non-DEP cases. Plotting the same graph as a function of the advance ratio in Fig. 5.30 is useful.

In Fig. 5.30 , the gray curve represents the original performance of the propeller as a function of the advance ratio parameter J. Since the pure hybrid and the baseline cases are studied with a propeller not affecting the wing aerodynamics, these cases are situated at the curve's peak overlapping each other. However, in the DEP BLI cases the maximum is shifted to higher advance parameters.

This shift is produced by the combination of small propellers and the effect of the BLI. Of course, it can be seen again that the lower propeller position grows this efficiency by more than 2.5 % compared with non-DEP cases.

The optimal DEP case has more than 3 % higher propulsive efficiency than the higher propeller position setting case. Since this increase is more significant than the improvement in aerodynamic efficiency, the optimal case with the

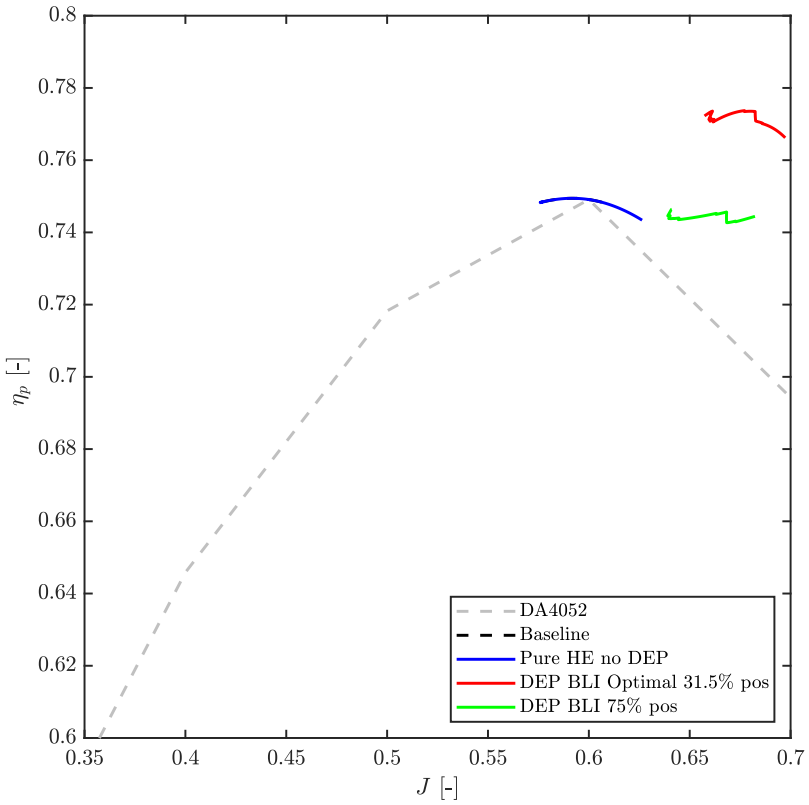

Figure 5.30: Comparison of the propulsive efficiency as function of the advance ratio parameter during the flight by aircraft with different propulsion plant setting.

propeller position at 31.5 % saves more fuel at the same range mission. The best way to verify the improvement is to draw the product of efficiencies in Fig. 5.31.

The product of aerodynamic and propulsive efficiency is plotted in Fig. 5.31. The optimal case tops the product of efficiencies, followed by the DEP BLI 75 case. This graph confirms that the gain in propulsive efficiency achieved by the lower propeller position case is more significant than the increase in lift-to-drag ratio reached in a higher propeller position. As the ICE is not taken into account in this plot, both baseline and pure hybrid cases behave similarly, having a worse product of efficiencies in the pure hybrid due to the flight velocity, as mentioned before. This plot changes if the fuel consumption is introduced in Fig. 5.32.

There is a dramatic change in the plot when the *BSFC* is introduced in Fig. 5.32. Due to the ICE optimization, all hybrid cases experiment a higher product

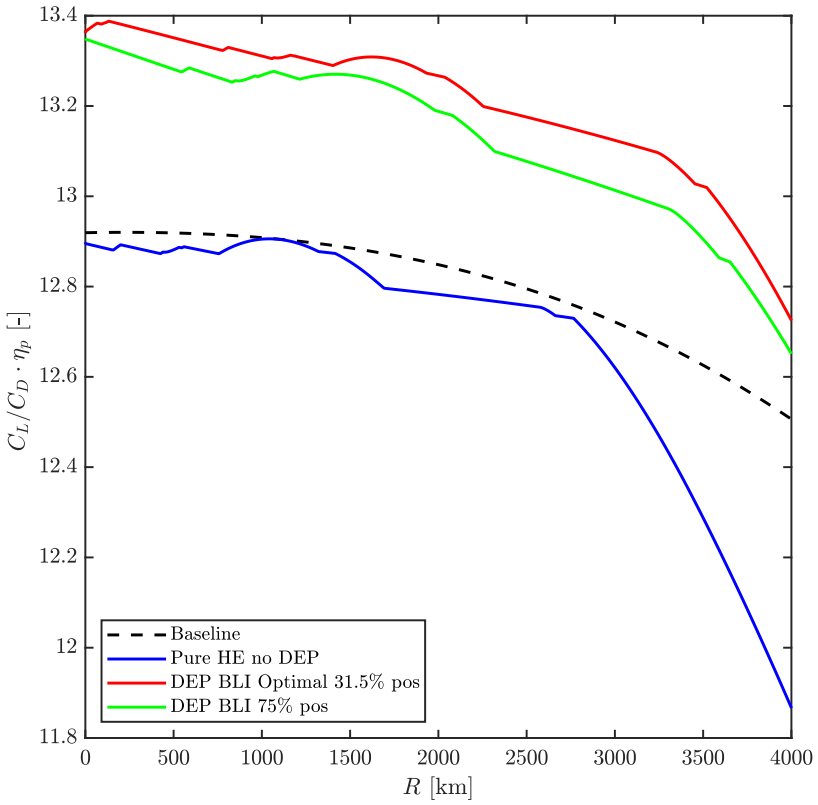

Figure 5.31: Comparison of the product of lift-to-drag ratio and propulsive efficiency during the flight by aircraft with different propulsion plant setting.

of efficiencies compared with the baseline case. Combining that the *BSFC* is the most critical factor in the range optimization and that the ICE performance is practically equal in all hybrid cases results in close curves for these cases. Nevertheless, the DEP BLI cases improve the product, translating into fuel savings for the same range. With the *BSFC* involvement, both DEP BLI cases behave similarly until approximately 1500 km. From this point, the optimal case gives rise to better performance. In addition, it should be noted that the final product of efficiencies considering the *BSFC* is relatively independent of the aircraft's weight.

The instantaneous CO_2 emitted during the flight is plotted in Fig. 5.33, considering only perfect stoichiometric combustion, in which each kilogram of fuel burnt produces 3.05 kg of CO_2.

All the hybrid cases emit less CO_2 through the mission than the baseline case. At first sight, it could seem that the pure hybrid case emits CO_2 in a lesser

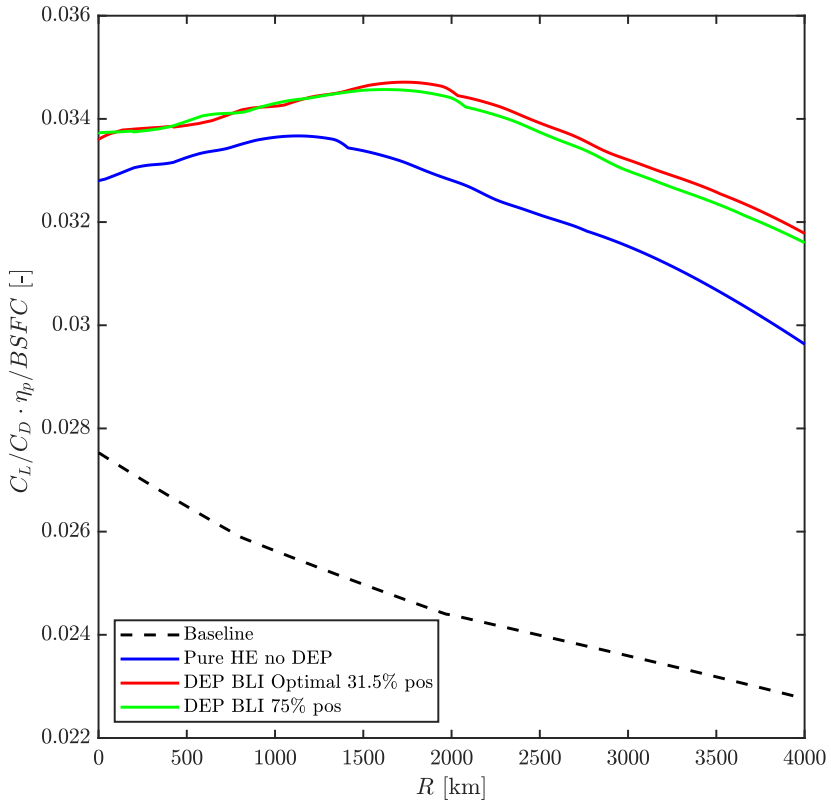

Figure 5.32: Comparison of the product of lift-to-drag ratio, propulsive efficiency and specific brake fuel consumption during the flight by aircraft with different propulsion plant setting.

way than the DEP BLI cases. However, as seen before in Fig. 5.27 the DEP BLI cases achieve the same range mission in a lower time. To check if the emission of CO_2 is lower in the optimal case, it is necessary to graph this parameter in an accumulated way in Fig. 5.34.

As seen in Fig. 5.34, the CO_2 emissions through the flight in the optimal case are slightly lower than in the other cases. CO_2 emissions are mainly influenced by the *BSFC*. Because all hybrid cases optimize the ICE map similarly, all hybrid curves appear close to each other. Of course, because the optimal DEP BLI case has a higher product of efficiencies, lower overall greenhouse gases will be delivered to the atmosphere using this configuration.

The main results of all cases are collected in Table 5.3. This table includes the fuel savings as a function of the mass of fuel of the baseline case $m_{\text{fuel,baseline}}$. The fuel savings are introduced in equation 5.1, where m_{fuel} corresponds to the

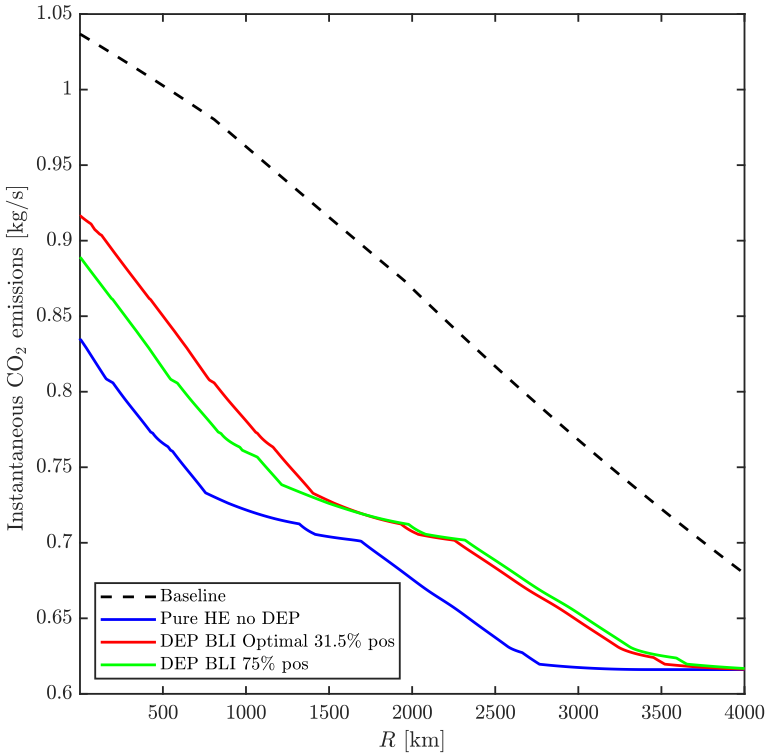

Figure 5.33: Comparison of instantaneous CO_2 emitted during the flight by aircraft with different propulsion plant setting.

mass of fuel needed to complete the mission in every scenario.

$$\text{Fuel savings} = \frac{m_{\text{fuel,baseline}} - m_{\text{fuel}}}{m_{\text{fuel,baseline}}} \tag{5.1}$$

Case	**Fuel mass** [kg]	CO_2 **emissions** [kg]	**Fuel saved** [%]
Baseline	10.00	30.53	0
Hybrid no DEP	8.65	26.41	13.5
HE with DEP and BLI h =75%	8.49	25.92	15.1
HE with DEP and BLI h =31.5%	8.45	25.72	15.6

Table 5.3: Comparison of fuel savings between different propulsion plant setting cases

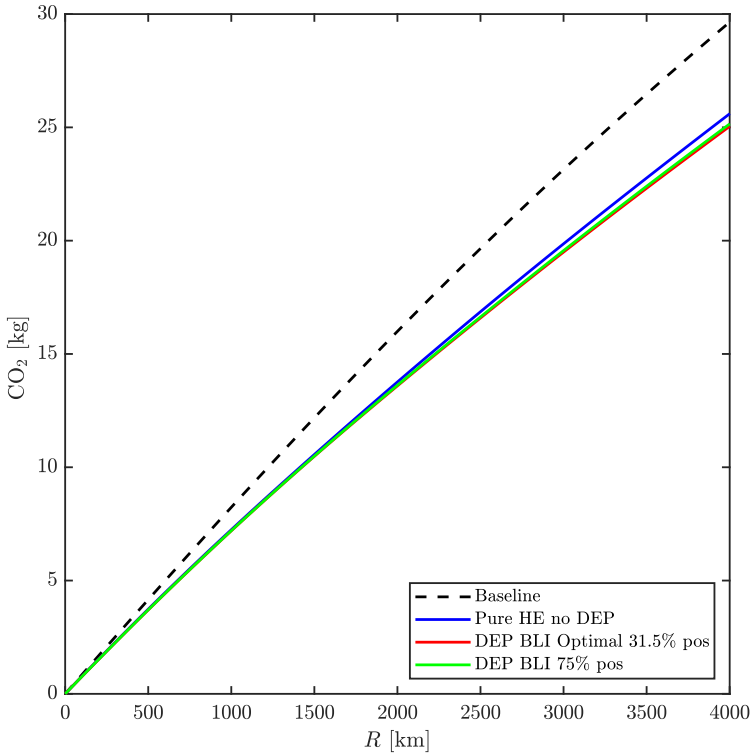

Figure 5.34: Comparison of CO_2 emitted during the flight by aircraft with different propulsion plant setting.

All the hybrid cases consume less fuel than the baseline case since the optimization of the ICE is the factor that most influences the consumption. Comparing the hybrid cases, a DEP and BLI case can achieve greater fuel economy and lower associated emissions. The DEP BLI case with a propeller setting position of 31.5 % allows an improvement of fuel consumption near 16 %, 2 % more than when using a pure hybrid configuration.

5.4 Propeller position POD analysis

In this section, a proper orthogonal decomposition method has been applied in the propeller position study. A first look at the POD tool was first introduced in chapter 2, and the methodology of application to this particular case was developed in chapter 4.

The POD method has multiple applications. First, it is employed as a pure analysis tool of the pressure and friction coefficients. Then lift and drag coefficients are reconstructed and analyzed using the method. Finally, the information obtained is used in a surrogate model to estimate the aerodynamic coefficients of non-calculated cases.

5.4.1 Pressure Coefficient Analysis using POD

As seen in the Section 5.2, the pressure coefficient is influenced by the angle of attack, but also the propeller position above the trailing edge. In Fig. 5.35, a comparison between a DEP BLI with a 75 % position and a baseline case is represented for two different angles of attack.

Looking at Fig. 5.35 it is evident that the C_p changes strongly with the angle of attack, but the propeller position effect is not negligible. The modal decomposition introduced in section 4.7 is applied to study the effect of the combination of propeller height and angle of attack. First, through the TKE, an estimation of how many modes are significant for the problem is depicted in Fig. 5.36.

In Fig. 5.36, the C_p from the suction side and pressure side are studied separately, a trend that will continue in the rest of the study. This way, a different number of modes can be used to reconstruct the aerodynamic coefficients of each airfoil side, optimizing the problem. The TKE of the first sorted modes is represented in blue for the suction side and red for the pressure side. As a result of sorting the eigenvalues by their value in descending order, most of the energy of the problem is contained in the first modes. Looking at the suction side, 96 % of the energy is explained in the first mode, and a 3 % by the second. 1 % of the information is contained in the rest of the modes, much less energetic. On the pressure side, a similar trend is observed, where the first mode explains 86 % of the coefficient. It can be seen that in this case, the energy is shared by more modes, explaining the second one 12 % of the C_p behavior.

More information can be recovered if the eigenvector is represented in a spatial dimension. In Fig. 5.37, the first four spatial modes that concern the suction side C_p are described.

The first two modes have a homogeneous shape on the suction side compared to the following modes. These two modes explain a significant part of the pressure coefficient, as seen in Fig. 5.36. However, it is possible to appreciate

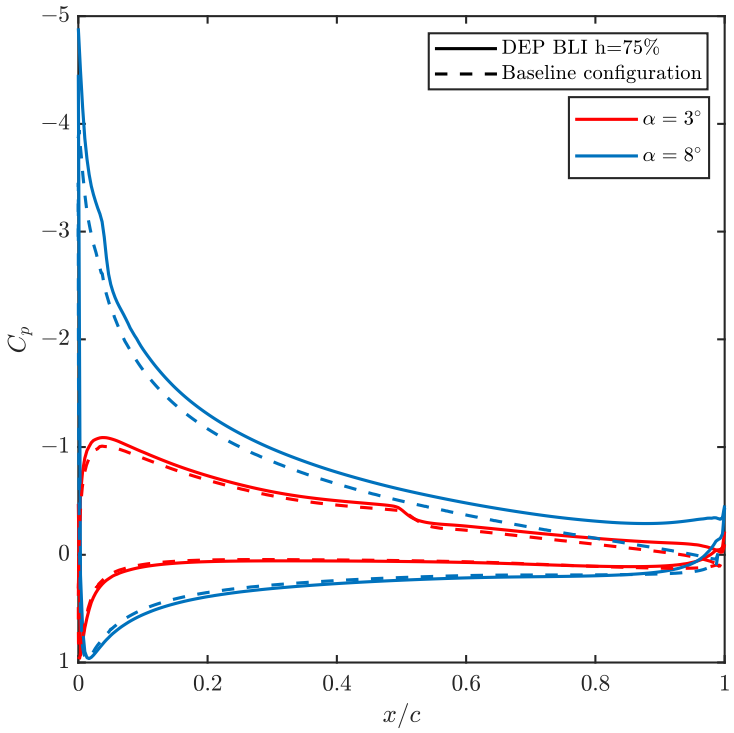

Figure 5.35: Comparison of the pressure coefficient distribution between baseline case without DEP and DEP BLI case with a propeller position of 75% at two angles of attack for a Reynolds number of 5×10^5.

that these modes contain information of the first 20 % of the chord. Consequently, the first two modes resolve the pressure coefficient near the suction peak, while the less energetic modes explain the pressure in the rest of the airfoil. In this case, the third mode information core is in the trailing edge, and the fourth mode contribution to the coefficient is in all the chord length.

Equivalently, the first four spatial modes of the pressure side are depicted in Fig. 5.38.

In this case, the three first initial modes contain most of the information of the coefficient near the leading edge, while the fourth one group its data near the trailing edge. Although the trend is similar to that seen on the suction side, all four modes behave homogeneously.

In Fig. 5.39, a different number of modes are used in the C_p reconstruction

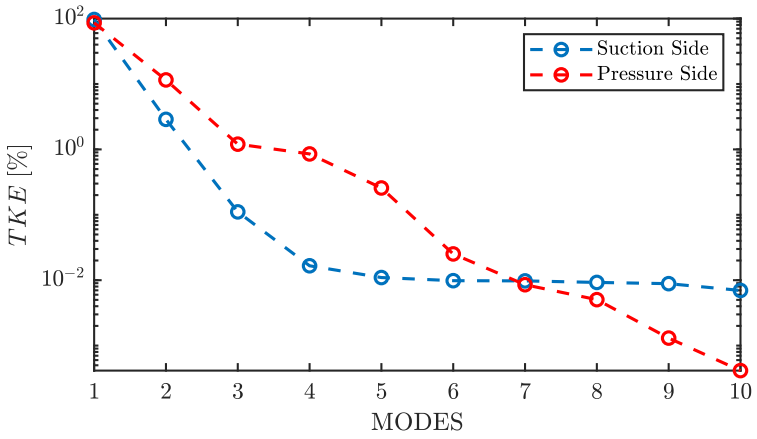

Figure 5.36: *TKE* of the different C_p modes for both the suction side (in blue) and pressure side (in red).

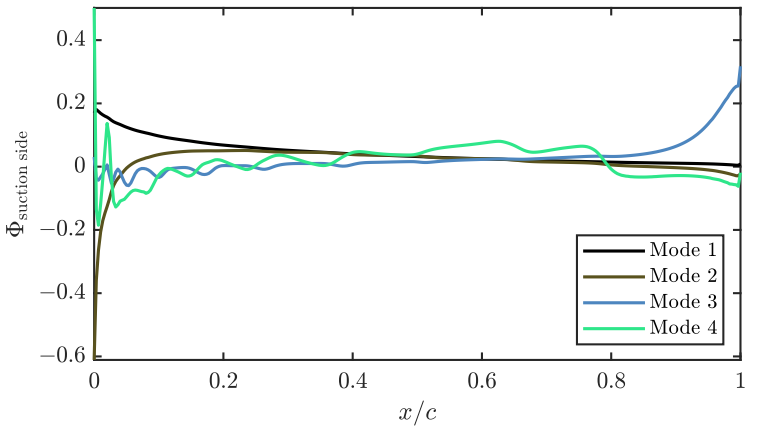

Figure 5.37: First four modes of the pressure coefficient of the suction side.

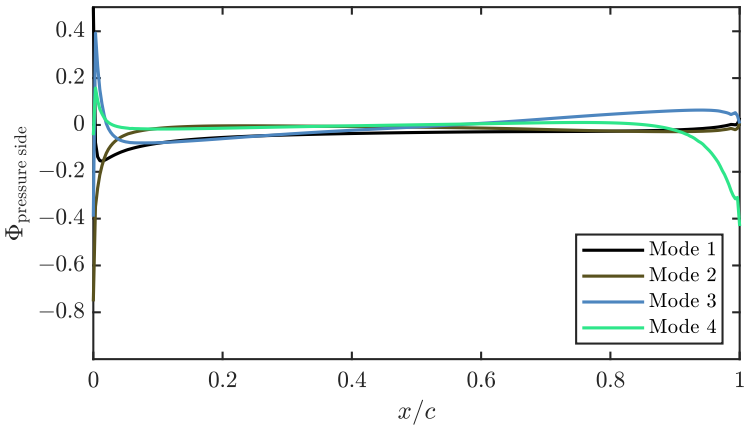

Figure 5.38: First four modes of the pressure coefficient of the pressure side.

of a case at 3° of angle of attack and a propeller position of 50 %.

As can be seen, three modes are enough to capture the information of the suction peak and almost all the C_p of the pressure side. Nevertheless, it is not enough to reconstruct the LSB, despite that three modes explain 99.5 % of the TKE. The LSB appears near the trailing edge with reduced intensity with three modes. Increasing the number of modes to nine, the C_p behavior is completely captured, including the reconstruction of the transitional bubble over the suction side. In any case and according to the TKE calculated in Fig. 5.36, using only three modes is enough to reproduce almost the complete shape of this coefficient. This way, the pitching moment, structural stresses over the skin, and lift coefficient can be calculated with an acceptable accuracy using limited information, which translates to a quick, effective predesign tool.

The number of modes can also be used as a proxy for the complexity of the phenomena being studied. The actual complexity of the effects of the propeller over the pressure coefficient distribution and the nonlinearities against the angle of attack is slight if only three modes are needed. More information is required to assess the actual complexity of this behavior, of course, so the configuration coefficients must also be studied.

The configuration coefficients are presented in Fig. 5.40 to obtain more information about the different modes.

Fig. 5.40 shows the first two configuration modes of the pressure coefficient corresponding only to the suction side. $A1$ is the first configuration coefficient

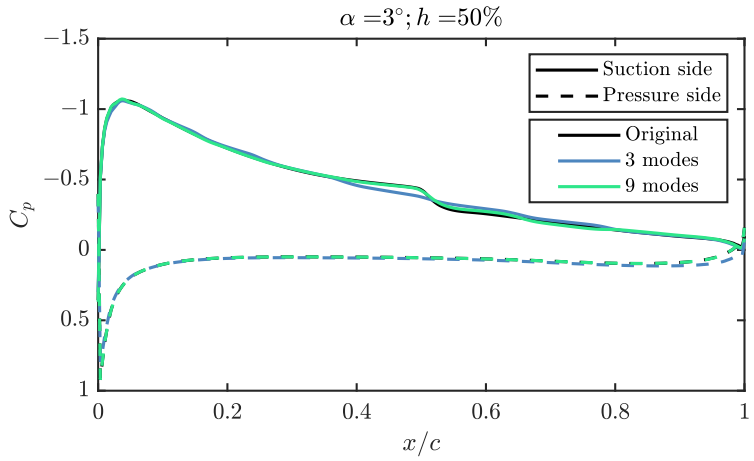

Figure 5.39: Pressure coefficient over the airfoil for an angle of attack of 3°, a propeller position of 50%. The results for the reconstruction with the first 3 and 9 eigenvectors are also included.

and offers a slight coefficient variation with the propeller height setting an angle of attack. Seeing the problem with another perspective, if the propeller height is set, the first configuration coefficient changes considerably when the angle of attack also changes. The value of the coefficient has a negative value in every possible distribution, so it always modulates the spatial modes independently of the angle of attack and propeller position. It can be remarked that when fixing the angle of attack and a propeller position above the 75 % is set, the value of $A1$ decreases as the propeller decreases its boundary layer ingestion effect due to the height. It has its absolute peak value when the angle of attack and propeller position is also maximum.

The influence in the first mode is the cause of having an increment in the lift when the propeller is set in a higher position. Maintaining an angle of attack, the value of the C_p can be increased from 10 % to 20 % just by raising the propeller around a 75 % position and ensuring that the thrust is equal to the drag.

The position where the first mode reaches the minimum value is analyzed in Fig. 5.41.

Representing the suction side C_p for α equal to 9° and h equal to 100 %, it can be seen that the first mode almost manages to fit the coefficient. If both first and second modes are applied, the C_p is perfectly reconstructed.

The second configuration coefficient $A2$ behaves similarly to the first one. The coefficient value changes due to the angle of attack to a larger extent than

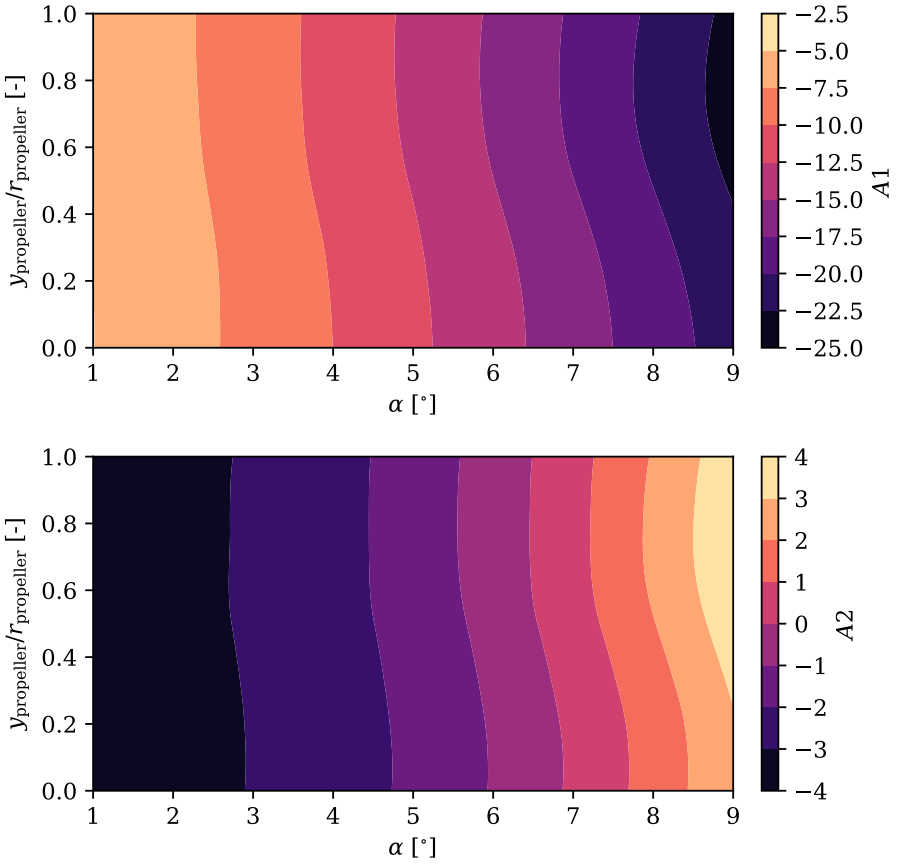

Figure 5.40: Configuration coefficients for the first two modes of the pressure coefficient over the suction side of the airfoil, as a function of the angle of attack and the relative propeller position.

the variation due to the propeller position. However, in this coefficient, the absolute maximum and minimum values are lower, tuned with the lower TKE. Additionally, $A2$ goes from positive to negative values when the angle of attack is increased, reaching a null value around 7°.

The configuration coefficient varies with the angle of attack more nonlinearly than $A1$, making the suction peak narrower and more intense when α increases. This commentary can be transferred to the propeller position, where $A2$ increases as the position height also moves up. As a result, the suction peak is moved towards the leading edge. There is a change in the tendency of the configuration coefficient with the propeller position around the 50 %. This change is produced due to the high effect that the propeller has in a lower position on the pressure, as a bigger section of the wing is directly affected by it.

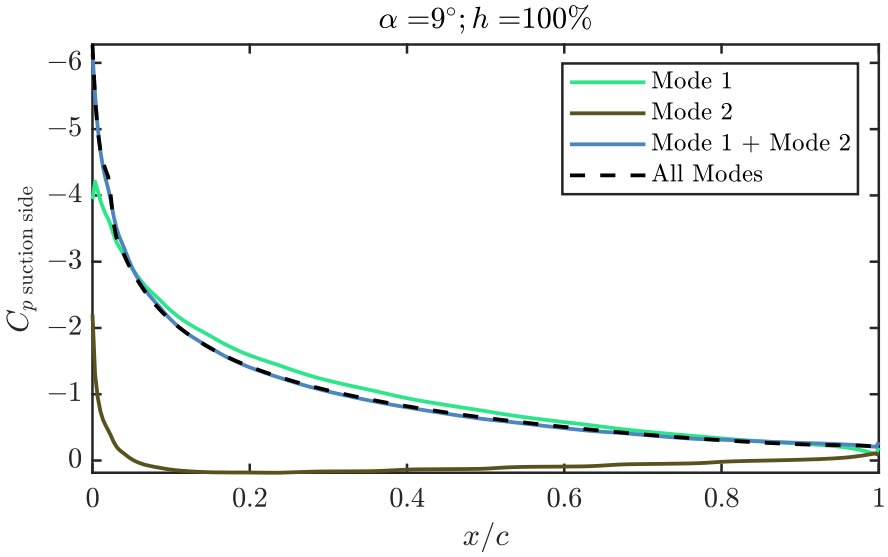

Figure 5.41: Contribution of the two first modes in the case of maximum relative height of the propeller over the trailing edge and maximum angle of attack simulated.

In the same way, the configuration coefficients that correspond to the pressure side are represented in Fig. 5.42.

The first configuration coefficient has a similar trend to that seen on the suction side regarding the propeller position and angle of attack. However, it behaves more nonlinearly and with smaller absolute values, reaching a null value at a low angle of attack. Fixing α, the value of $A1$ is lowered as the propeller position is minimized. As explained before, in a lower propeller position, there is a large area of actuator disk reaccelerating the flow of the pressure side, reducing the pressure coefficient.

The same can not be said of the second and third configuration coefficients. These modes have more complex structures and explain a bigger percentage of TKE compared to the suction side. However, it should be taken into account that their contribution to global aerodynamic coefficients is limited as the absolute value of C_p on the suction side is more important.

Looking at each configuration coefficient, they have an absolute value peak near α equal to 4°. Nevertheless, around this value, the behavior of each coefficient is different. In $A2$ the maximum is found around this α, reaching null values near it and negative values at a high angle of attack. Meanwhile, in $A3$ at 4° the value is minimum, reaching maximum values at a lower angle of attack and zero values at higher angles. At the mentioned angle of attack, $A2$ maximizes the value of C_p at the leading edge stagnation point, widening it. $A3$

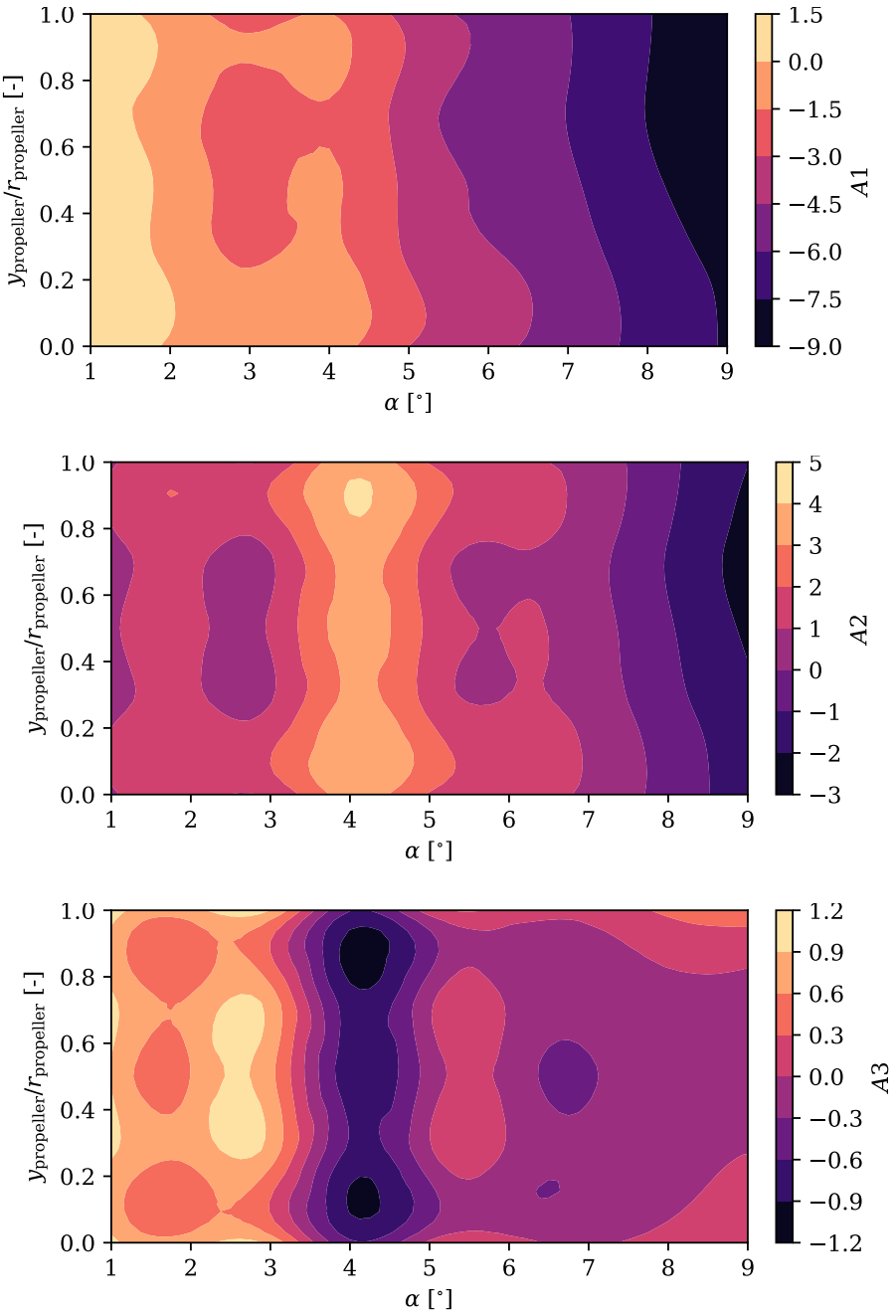

Figure 5.42: Configuration coefficients for the first three modes of the pressure coefficient over the pressure side of the airfoil, as a function of the angle of attack and the relative propeller position.

acts oppositely, making the stagnation zone narrower.

5.4.2 Friction Coefficient Analysis using POD

The friction coefficient is analyzed using the same tools as the pressure coefficient case. Representing the C_f for a propeller position of 50 % and with different angle of attack in fig . 5.43, the apparition of the LSB and its movement upwind with α can be seen. The transitional bubble is characterized by the fast growth of the coefficient and consequent null value. The changes in C_f due to the variation of α are small on the pressure side, maintaining the same form and values.

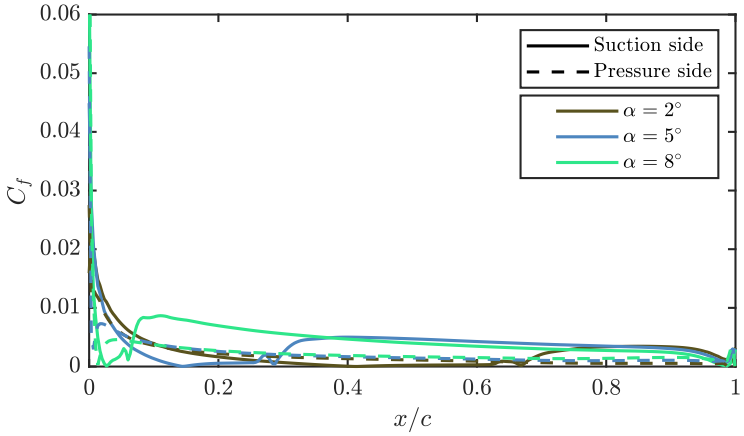

Figure 5.43: Friction coefficient over the airfoil with the propeller in 50% position.

As done for the pressure, the TKE of the first ten modes is depicted in Fig. 5.44, divided into two airfoil sides.

The energy explained by the first mode of the suction side is below 83 %, meaning that more modes are needed to reconstruct the C_f. Meanwhile, the first mode of the pressure side excess 91 %, which is consistent with a reduced complexity of the flow. This commentary can be validated when the friction coefficient is depicted at a fixed propeller position and angle of attack. In Fig. 5.45, an α of 3° and a propeller position of 50 % are represented for each airfoil side and a different summation of modes.

Using two modes in the suction side, the primary trend of the C_f is averaged. Increasing the number of modes to five, the coefficient is better captured in

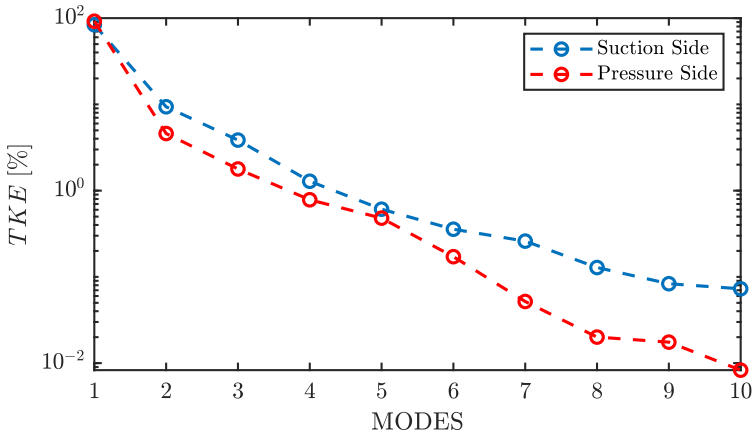

Figure 5.44: *TKE* of the friction coefficient.

all the chord length, but the LSB is neglected. To see the LSB correctly reconstructed, at least ten modes are needed. This does not apply to the pressure side due to its homogeneous trend. Only using two modes is enough to represent the original coefficient correctly.

The configuration coefficients are also represented in Fig. 5.46 to obtain more information.

The main behavior of the two first modes of the suction side mirrors the trend seen for the C_p in Fig. 5.40. In both $A1$ and $A2$, the value is maximized when the angle of attack grows, and again a lower variation is produced due to the propeller position.

Looking the first graph of Fig. 5.46 that corresponds to $A1$, the value of the coefficient remains almost constant with the position until reaching 5°. From this angle of attack, the value of the coefficient varies in a pronounced way with the position, obtaining greater values at higher positions.

What has been obtained agrees with what was commented in section 5.2. If the propeller position is raised, the friction coefficient of the suction side also grows along the parasitic drag.

The majority of the C_f effect can be explained using only one mode. However, there is a lack of information in order to rebuild the transitional separation bubble. Anyway, using a few modes, it is expected to have enough information to interpolate the skin friction over the suction side on non-simulated cases (with non-simulated angles of attack or propeller positions) even if the LSB is not

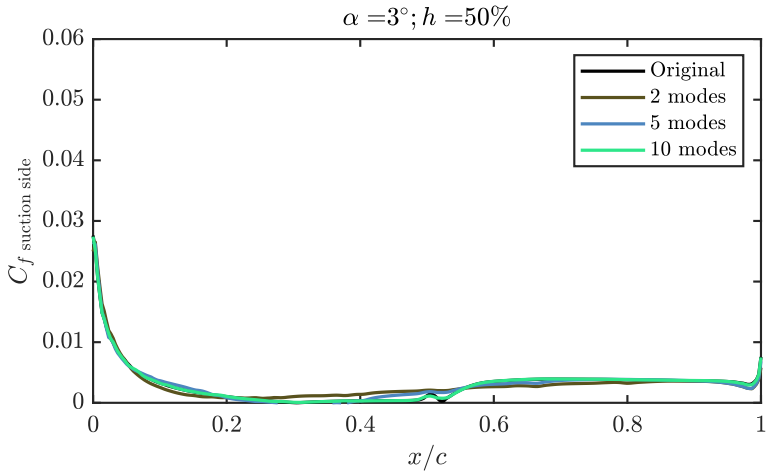

(a) Friction coefficient reconstruction over the suction side of the airfoil.

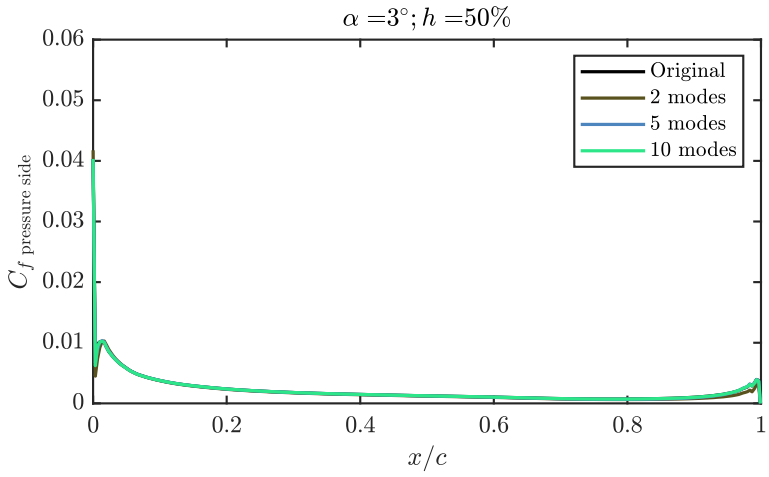

(b) Friction coefficient reconstruction over the pressure side of the airfoil.

Figure 5.45: Friction coefficient reconstruction over the airfoil, for an angle of attack of 3° and a propeller relative height of 50%.

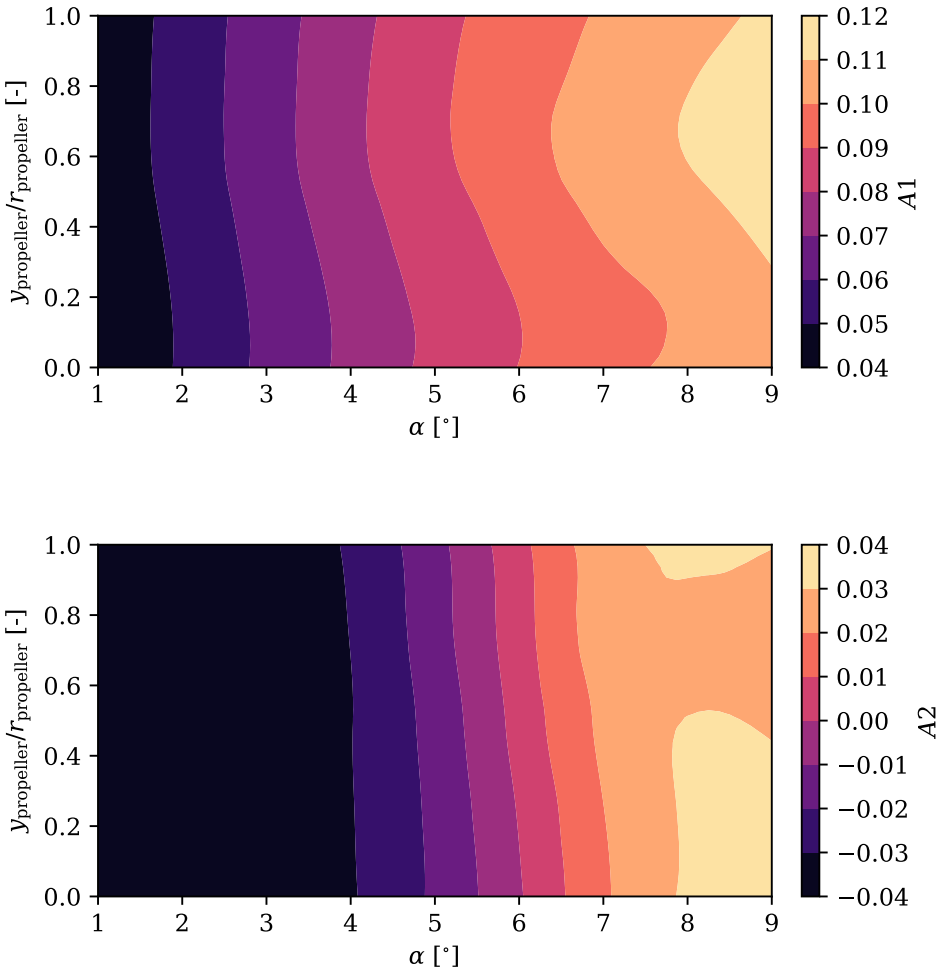

Figure 5.46: Configuration coefficients for the first two modes of the friction coefficient over the suction side of the airfoil, as a function of the angle of attack and the relative propeller position.

adequately resolved. The parasitic drag due to the skin friction will be obtained with this information.

The second mode seems to contribute less to the skin friction as a function of the propeller position. If an angle of attack is set, $A2$ does not vary significantly with the propeller height, and it is only possible to observe some variation at a high angle of attack. For angles of attack between 1° and 6°, the value of $A2$ is negative, cushioning the positive value of the first mode. From this point on, the value of $A2$ is positive, leveraging the skin friction caused by the first mode. Of course, finding higher skin friction values at higher angles of attack makes sense. At high angle of attack, near stall conditions, the LSB moves upstream and the portion of the skin wetted by a turbulent boundary layer over the suction side increases, further increasing the C_f.

The configuration coefficients that correspond to the pressure side are depicted in Fig. 5.47.

On the pressure side, the first mode imitates the one obtained for the suction side but with negative values. The value of $A1$ decreases as the angle of attack increases. On the pressure side, as the angle of attack increases, the transition point is moved downstream. This way, the fraction of the skin affected by a laminar boundary layer increases, reducing the skin friction drag.

However, the first configuration coefficient of the pressure side affects the first mode to a lesser extent than the suction side. Even if both coefficients have opposite trends, the net flow around the airfoil becomes more turbulent when the angle of attack is increased, increasing the global skin friction coefficient.

Also, $A1$ is more negative as the propeller position rises, reaching its minimum at the maximum angle of attack and position measured. This trend corresponds to having a smaller portion of the wing surface affected by the propeller in higher positions. This way, the reacceleration of the flow decreases and the friction drag on the pressure side decreases too.

As observed for the suction side, $A2$ does not have significant variations with the propeller position at low angles of attack and is only modified at higher angles. In the same way, it seems to cushion the first mode in most of the operating range.

As discussed for the suction side, the skin friction over the pressure side should be accurately interpolated to obtain the parasitic drag in non-calculated cases. Also, the pressure side is easier to rebuild since there is no transitional bubble in this airfoil side and more TKE is contained in the first modes.

5.4.3 Lift and drag coefficient analysis and reconstruction

The pressure and friction coefficients obtained over the airfoil have been integrated using a different number of modes to obtain a reconstruction of the lift and drag coefficients. Based on the C_L and C_D results obtained in section

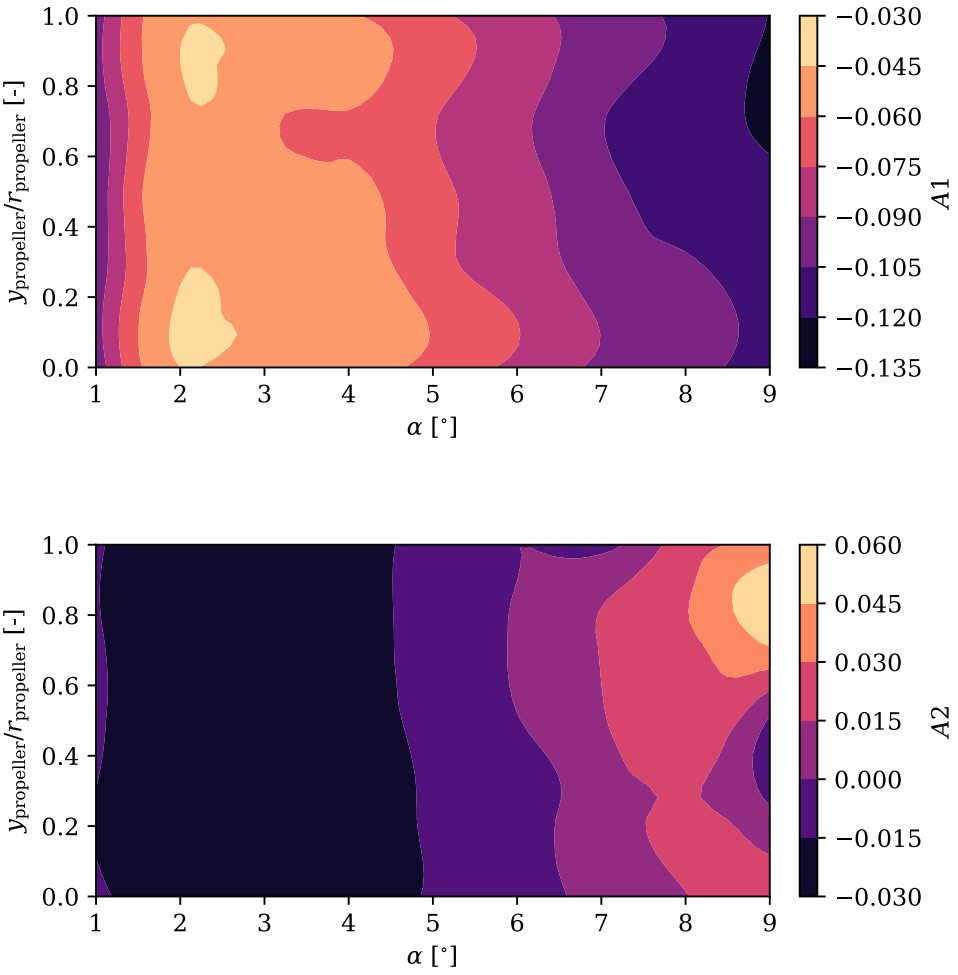

Figure 5.47: Configuration coefficients for the first two modes of the friction coefficient over the pressure side of the airfoil, as a function of the angle of attack and the relative propeller position.

5.2 (Fig. 5.4 and 5.5), the fraction between the reconstruction and the original data is plotted in figs. 5.48 and 5.49. For each coefficient, three different angles of attack are depicted.

In Fig. 5.48, the error between the lift coefficient using up to nine modes ($C_{L,\text{modes}}$) and the original CFD lift obtained is represented for every position and three angles of attack, equal to 1°, 5° and 9°. The relative error using at least two modes in the reconstruction is under 3 % for almost all positions, except for higher propeller positions at a low angle of attack. This commentary is valid for every position and angle of attack. The error varies more with the angle of attack than with the propeller position, as more modes are needed to lower the error at low α. Generalizing the three graphs, at least five modes are needed to reduce the relative error to around a 1 %.

However, more modes are needed to reconstruct the C_D as can be seen in Fig. 5.49, where the same positions and angles of attack used before in Fig. 5.48 are represented. While using only one mode in the C_L reconstruction is translated to an error of 10 %, in the drag reconstruction, the error increases to 50 %. Using two or three modes during the reconstruction gives rise to an error around 3 % for every angle of attack. But if the propeller position changes, the C_D varies between underestimating the coefficient in higher positions to overestimating it at lower propeller positions. Generalizing again for every angle of attack and propeller position, at least six modes are needed to ensure that the relative error is always under 3 %.

Oppositely, the error between lift and drag coefficient using up to nine modes compared with the original CFD data can be represented for every angle of attack and three propeller positions.

Fig. 5.50 corresponds to the lift coefficient and is plotted for propellers positions of 0 %, 50 % and 100 %.

The commentary made for all positions (Fig. 5.48) can be applied in this figure. More than two modes are needed for all three positions to maintain the C_L error below 3 %. Only at very low angles of attack (between 1° and 3°) at least more than three modes are needed to maintain the error.

There is a similar trend in all three positions represented. With few modes, if the angle of attack is less than 7°, the C_L calculated is underestimated. However, at a high angle of attack, this coefficient is overestimated.

In Fig. 5.51 the equivalent graph is plotted for the drag coefficient.

As seen in Fig. 5.49, correctly representing the C_D requires more modes. Independently of the propeller position, more than five modes are needed to lower the error below 3 %. It should be noted that higher angles of attack require fewer modes for their correct representation. If only an angle of attack superior to 4° is needed in a study, four modes can correctly represent the drag coefficient.

If only a pair or fewer modes are employed, the error tendency is the same that is observed in the lift coefficient. The trend from the second mode is

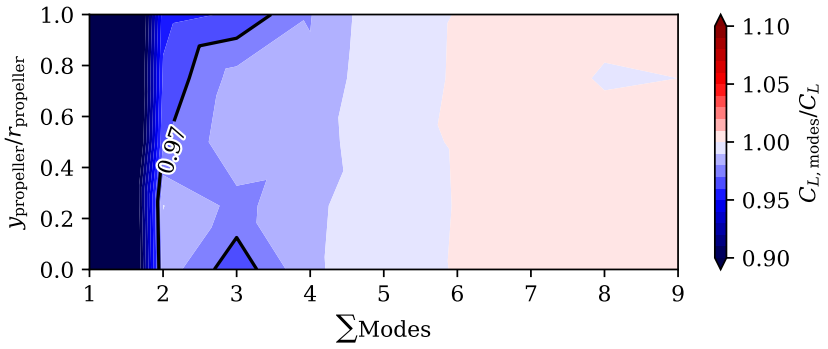

(a) Lift coefficient computed using from 1 to 9 modes for an angle of attack of 1°.

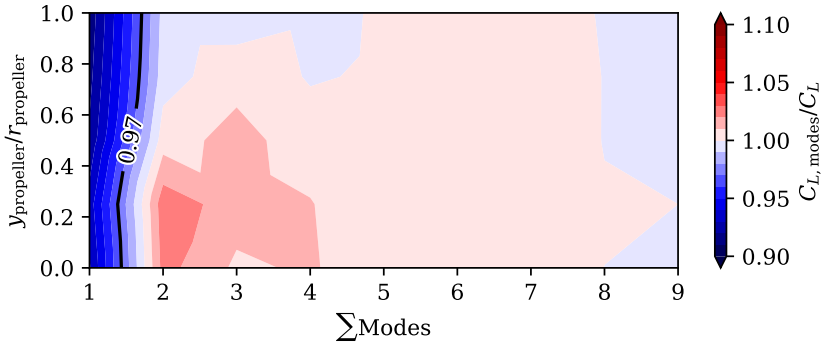

(b) Lift coefficient computed using from 1 to 9 modes for an angle of attack of 5°.

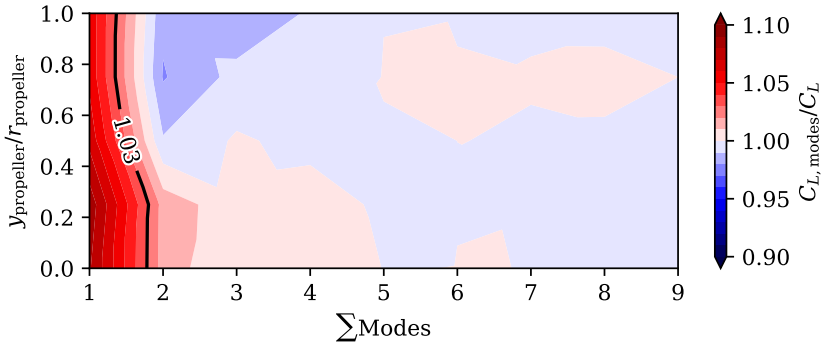

(c) Lift coefficient computed using from 1 to 9 modes for an angle of attack of 9°.

Figure 5.48: Fraction of lift coefficient computed using from 1 to 9 modes, using both the pressure coefficient and friction coefficient distributions for all propeller positions and three angles of attack.

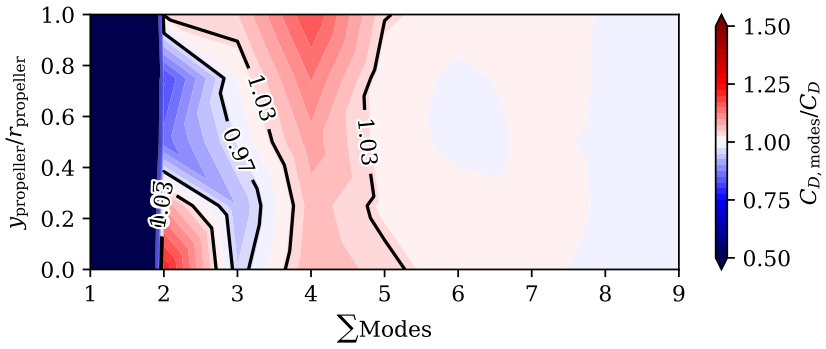

(a) Drag coefficient computed using from 1 to 9 modes for an angle of attack of 1°.

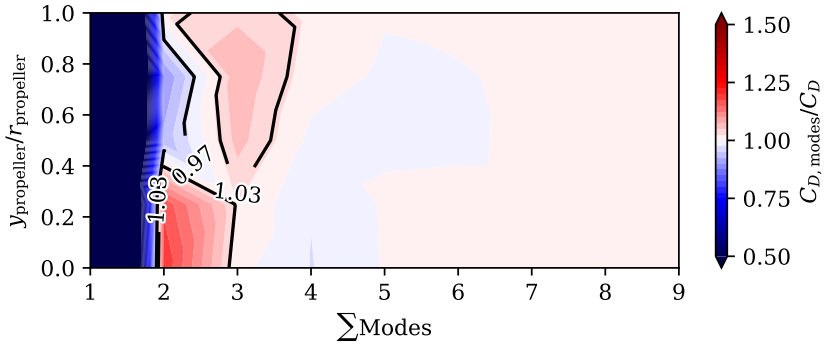

(b) Drag coefficient computed using from 1 to 9 modes for an angle of attack of 5°.

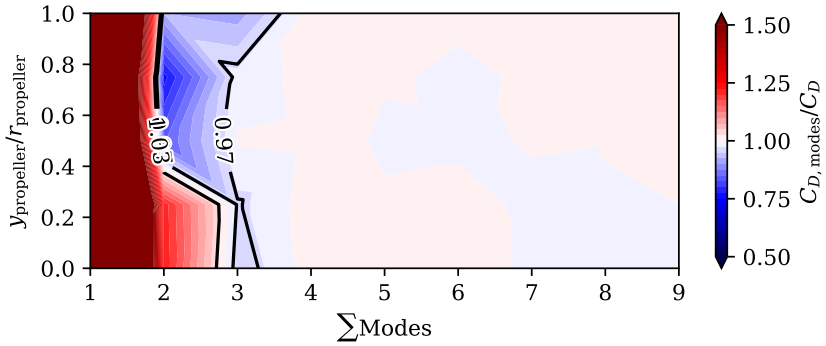

(c) Drag coefficient computed using from 1 to 9 modes for an angle of attack of 9°.

Figure 5.49: Fraction of drag coefficient computed using from 1 to 9 modes, using both the pressure coefficient and friction coefficient distributions for all propeller positions and three angles of attack.

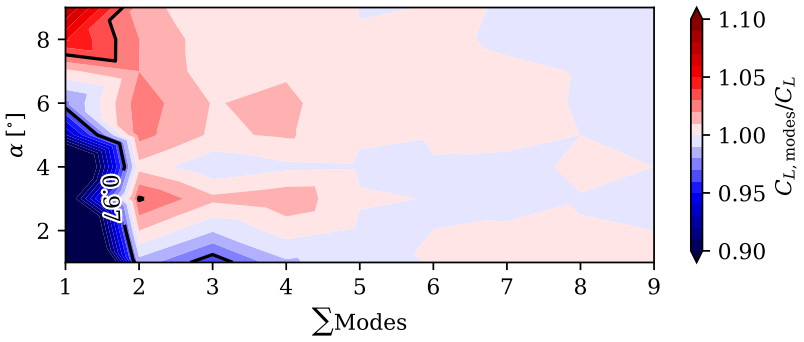

(a) Lift coefficient computed using from 1 to 9 modes for a propeller position of 0 %.

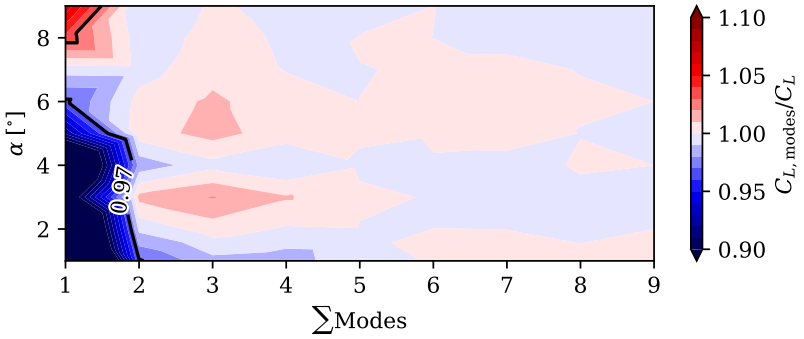

(b) Lift coefficient computed using from 1 to 9 modes for a propeller position of 50 %.

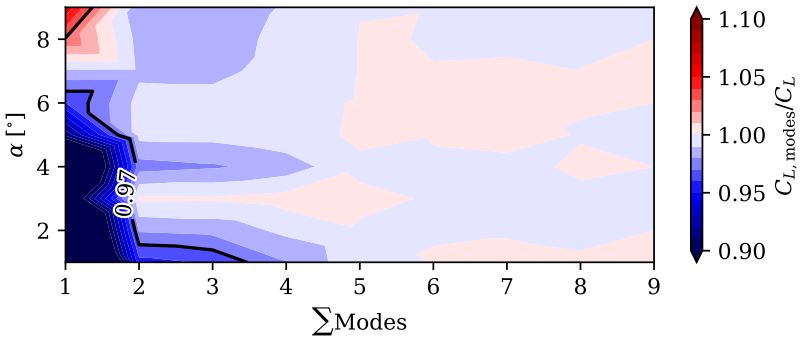

(c) Lift coefficient computed using from 1 to 9 modes for a propeller position of 100 %.

Figure 5.50: Fraction of lift coefficient computed using from 1 to 9 modes, using both the pressure coefficient and friction coefficient distributions for all angles of attack and three propeller positions.

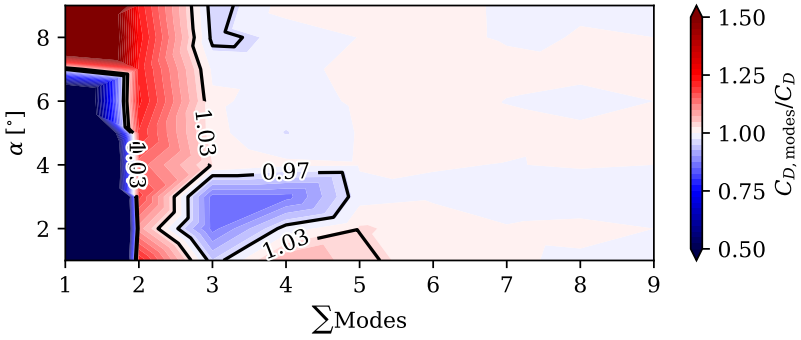

(a) Drag coefficient computed using from 1 to 9 modes for a propeller position of 0 %.

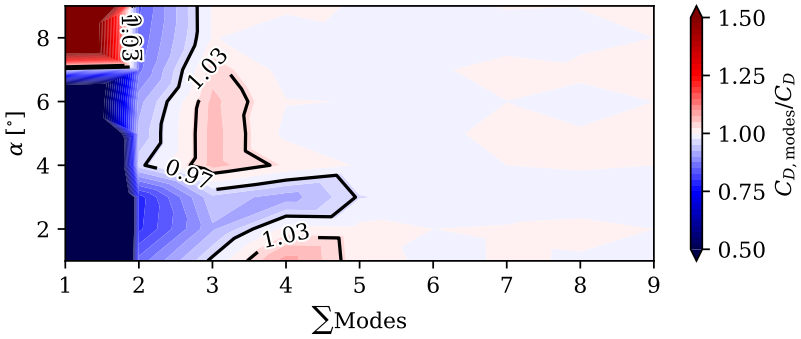

(b) Drag coefficient computed using from 1 to 9 modes for a propeller position of 50 %.

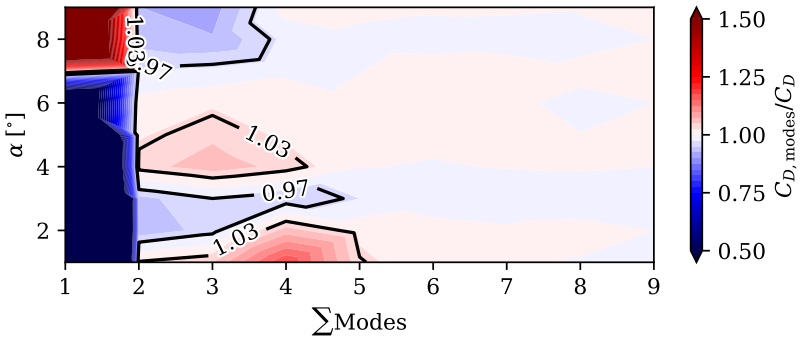

(c) Drag coefficient computed using from 1 to 9 modes for a propeller position of 100 %.

Figure 5.51: Fraction of drag coefficient computed using from 1 to 9 modes, using both the pressure coefficient and friction coefficient distributions for all angles of attack and three propeller positions.

alternated in all positions, between overestimating or underestimating the error.

A higher degree of complexity in the drag coefficient than in the lift coefficient can be inferred from these results. When generating surrogate models for conceptual and preliminary design, as described in the next sections 5.4.4 and 5.5, a higher error for the same model complexity is expected when predicting the drag than when computing the lift.

5.4.4 Coefficient interpolation using a surrogate model

POD can be used as a tool to reduce the number of high fidelity simulations needed for fitting a surrogate model. With enough distributions calculated, it is possible to interpolate and reconstruct the aerodynamic coefficient for not-simulated intermediate cases. In Fig. 5.52, the pressure coefficient of a non-simulated propeller position is plotted and compared with an original simulation out of the model.

Using an angle of attack of 3° and a Reynolds number of 5×10^5 , two propellers positions are reconstructed, one at 30 %, and another at 65 %.

As the propeller effect modifies less the pressure coefficient and the angle of attack set belongs to the original data, the coefficient is perfectly reconstructed in both propeller positions. The reconstruction only has a small representation error in the last section of the airfoil, near the propeller.

Looking at the C_p reconstruction it can be stated that the aerodynamic coefficients (lift, drag and pitching moment) can be properly estimated over the wing, assuming a small amount of error. In the same way, it is possible to compute with high accuracy the stress over the airfoil skin.

A similar comment can be done if the angle of attack is the variable interpolated with some nuances. In Fig. 5.53, an α of 5.5° is interpolated for two propeller positions: one belonging to the calculation grid (50 %), and the other also interpolated (65 %), with the same Reynolds.

The main behavior of the C_p is correctly captured in both the suction and pressure side, including the magnitude of the suction peak and the coefficient near the trailing edge. It is true that the reconstruction of the bubble is not obtained properly. Nevertheless, it is still possible to compute correctly and with a low error the stresses over the wing skin.

In the same way, the friction coefficient can also be interpolated. Using the same distributions as figures 5.52 and 5.53, the C_f is plotted in figs. 5.52 and 5.55.

The commentary extracted from the C_p figures are also valid in the C_f case. In Fig. 5.54, where only the propeller position is interpolated, the friction coefficient interpolation is almost perfect. Meanwhile, in Fig. 5.55 when the α is interpolated both alone or paired with the propeller position, the reconstruction

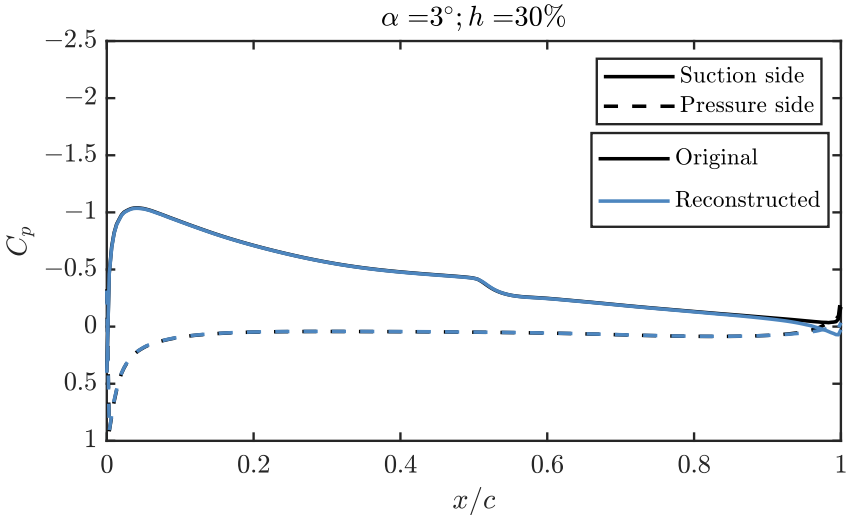

(a)

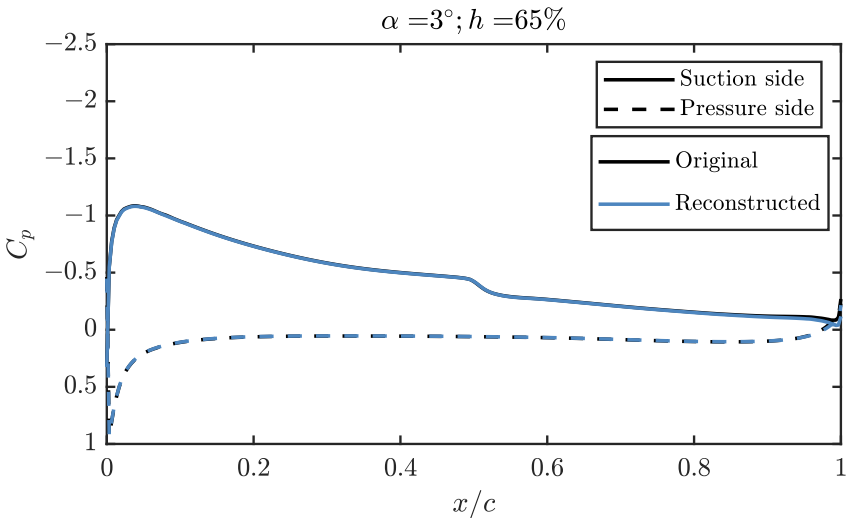

(b)

Figure 5.52: Pressure coefficient reconstructed in a propeller position not used to fit the surrogate model, compared with data from a CFD simulation. (**a**) Pressure coefficient reconstructed an angle of attack of 3° and a propeller position of 30%. (**b**) Pressure coefficient reconstructed for an angle of attack of 3° and a propeller position of 65%.

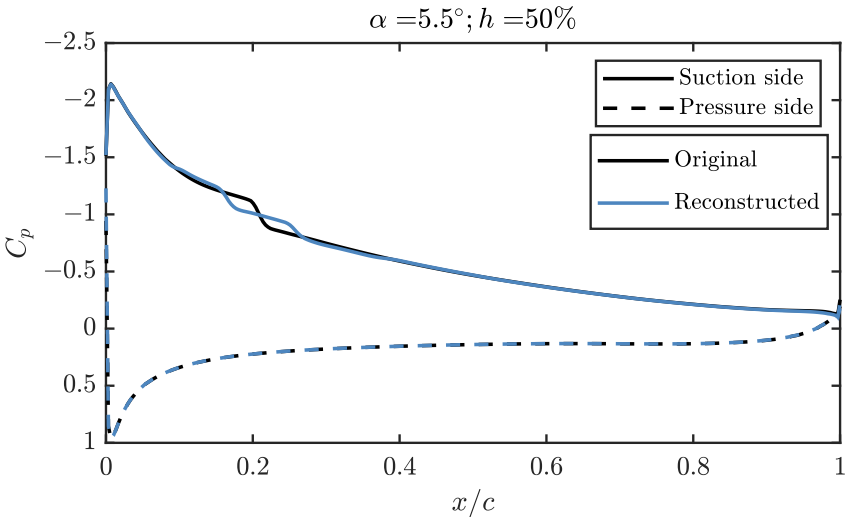

(a)

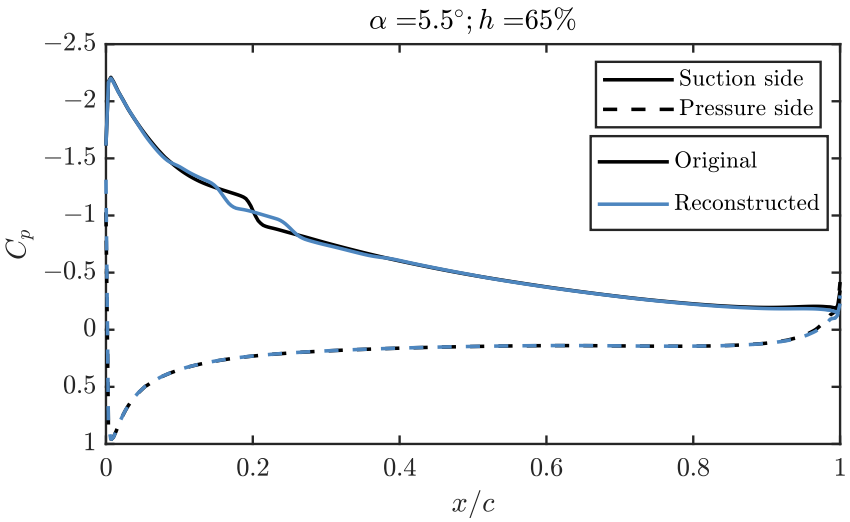

(b)

Figure 5.53: Pressure coefficient reconstructed in a propeller position and angle of attack not used to fit the surrogate model, compared with data from a CFD simulation. (**a**) Pressure coefficient reconstructed for an angle of attack of 5.5° and a propeller position of 50%. (**b**) Pressure coefficient reconstructed for an angle of attack of 5.5° and a propeller position of 65%.

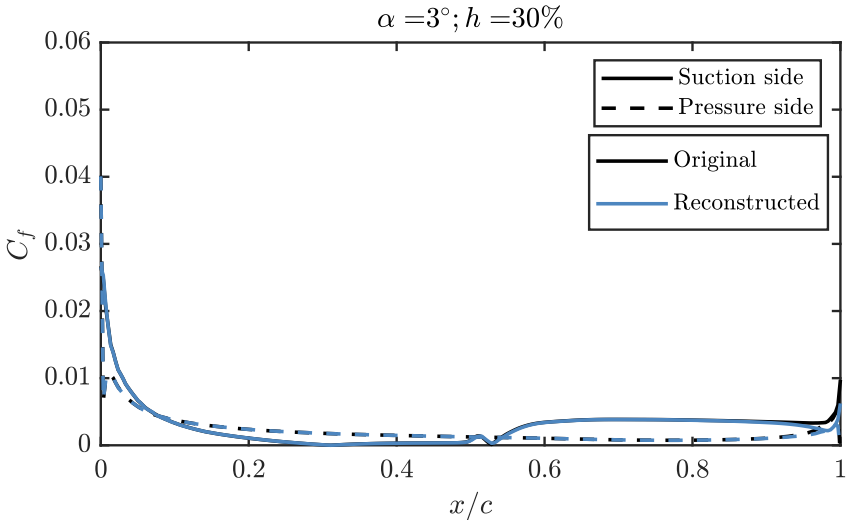

(a)

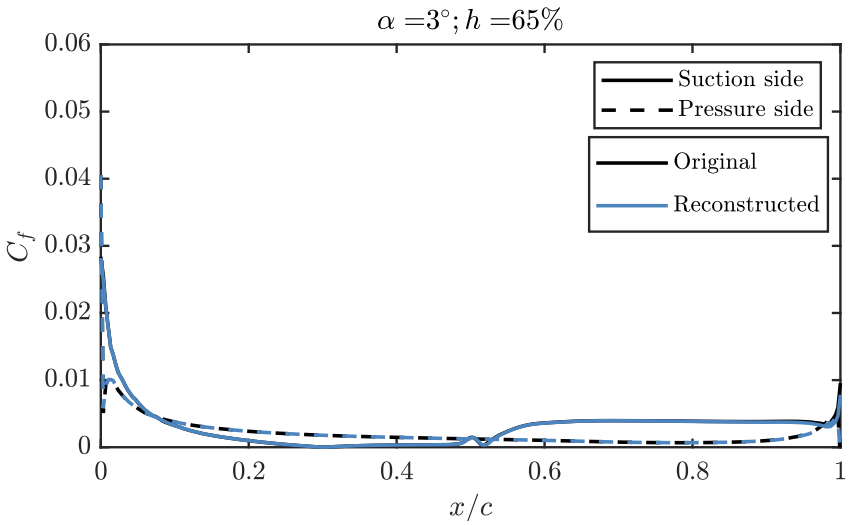

(b)

Figure 5.54: Friction coefficient reconstructed in a propeller position not used to produce the surrogate model, compared with data from a CFD simulation. (**a**) Friction coefficient reconstructed an angle of attack of 3° and a propeller position of 30%. (**b**) Friction coefficient reconstructed for an angle of attack of 3° and a propeller position of 65%.

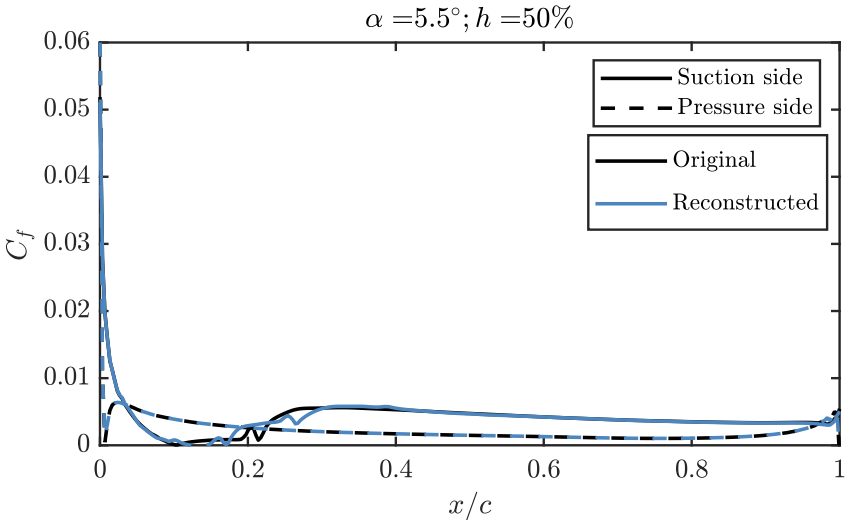

(a)

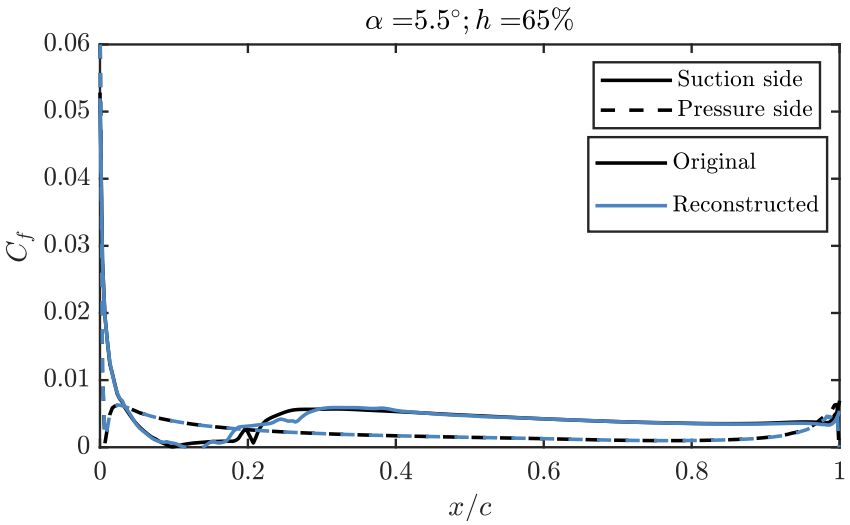

(b)

Figure 5.55: Friction coefficient reconstructed in a propeller position and angle of attack not used to fit the surrogate model, compared with data from a CFD simulation. (**a**) Friction coefficient reconstructed for an angle of attack of 5.5° and a propeller position of 50%. (**b**) Friction coefficient reconstructed for an angle of attack of 5.5° and a propeller position of 65%.

struggles to reconstruct correctly the C_f near the LSB at the suction side. However, the rest of the distribution is properly reconstructed.

In conclusion, POD is a helpful tool when rebuilding aerodynamic coefficients. The interpolation of a surrogate model with a low error may be employed in designing and optimizing small aircraft. The application of small aircraft stands out because, beyond being the central design of this work, it is a field where the final weight is decisive. Because these aircraft types are usually built using light materials with low stiffness, it is vital to know the exact pressure distribution over the wing. This way, optimizing the structure without incurring in prohibitve wing deformations is possible.

5.5 Design optimization

The design cases developed in the previous chapter and shown in subsection 4.2.2, are selected to create models that optimize aircraft design with DEP and BLI.

First, the lasso method explained in section 4.8 is applied to obtain the equation that expresses every coefficient. This method returns an equation with a series of chosen variables, so each coefficient is expected to be related in some way to the seven selected variables during the creation of the simulations. However, the coefficients do not have to vary in a directly proportional way to the variables.

Based on the observation of the previous analysis, the aerodynamic coefficients will be a function of the seven parameters expressed in eq. 5.2,

$$C_L, C_{D0} = f\left(\alpha, \log Re, \frac{1}{J}, \theta, \frac{d}{x}, \frac{h}{d}, \frac{d}{c}\right), \tag{5.2}$$

where α is the angle of attack, Re is the Reynolds number, J is the advance parameter, θ is the geometrical pitch angle of propeller, d is the propeller diameter, h is the distance between the propeller shaft and the trailing edge, c is the airfoil chord, and x is the distance between propeller shafts.

The following hypothesis are used based on the aforementioned observations:

- The behaviour is probably proportional to the angle of attack, as in a case without boundary layer ingestion.
- An increase of the Reynolds number increases the lift coefficient and decreases the drag coefficient, but with diminishing returns, so a logarithm is used.
- The effect due to the propeller thrust becomes more important as J decreases, so $1/J$ is used.
- The propeller thrust is, as a first approximation, proportional to the pitch, and the effect of the thrust on the aerodynamic coefficients may be approximated by a linear trend.
- The effect of the propeller increases as the relative distance between propeller shafts is decreased: this effect is introduced as d/x.
- Higher propeller heights increase the effect up to a point, so h/d is used.
- Finally, bigger propellers have a bigger effect, so d/c is introduced.

The propulsive coefficients can be expressed as a function of the same parameters in eq 5.3.

$$C_T, C_P = f\left(\alpha, \frac{1}{\log Re}, J, \theta, \frac{x}{d}, \frac{h}{d}, \frac{c}{d}\right). \tag{5.3}$$

Similar hypotheses to those considered for the aerodynamic coefficients are now employed for the propulsive coefficients:

- The behaviour is probably proportional to the angle of attack, as in a case without boundary layer ingestion.
- An increase of the Reynolds number should not affect in a high degree the thrust coefficient and power coefficient, but it could be manifested in a slight decrease in these values, so the inverse of the logarithm is used.
- Both propeller thrust and power decrease in a linear way with the advance ratio parameter. The term J is used as a direct relationship and is expected to obtain negative coefficients accompanying it.
- The propeller thrust and power are, as a first approximation, proportional to the pitch, so the effect is kept in a linear trend.
- The effect of the propeller increases as the relative distance between propeller shafts is decreased: this effect is introduced as x/d.
- Higher propeller heights increase the effect up to a point, so h/d is used.
- Finally, smaller propellers tend to have higher rotational speeds achieving higher thrust at lower J. The parameter c/d is introduced to keep these phenomena.

These variables will be the predictors for the lasso method. Still, to ensure that the method has enough information, a matrix of predictors is built containing a constant term, the linear terms, the interaction between every variable, and a squared term of every predictor. This way, the total number of predictors p employed can be expressed in eq. 5.4 as:

$$p = 1 + 2n + \sum_{j=1}^{n+1} (j-1). \tag{5.4}$$

Considering that $n = 7$ are the original predictors, a total of 36 variables are introduced in the method.

For the use of the lasso, half of the randomly chosen simulations are used. This way, the rest of the simulations will validate the regression obtained. As explained in section 4.8, the λ parameter of the method controls how many

variables will ultimately be used to perform the regression. In this case, the regression has been obtained by performing a sweep of this parameter. The bounds of this sweep correspond to a value that gives a solution that contains the use of all the predictors and another with the application of only one.

For choosing the correct number of predictors, the regression's mean squared error (MSE) is analyzed in Fig. 5.56.

Of course, if the number of predictors is minimized, the regression will have a more significant error. To maintain a low MSE for every coefficient, different predictors are chosen in each case.

Six predictors are chosen to explain the C_L, maintaining a good compromise solution between model complexity (and, thus, expected generalization capabilities and low overfitting) and MSE. The expression of the C_L is shown in eq. 5.5, and the value of each coefficient is collected in Table 5.4 along with the corresponding coefficient for the other aerodynamical and propulsive coefficients.

$$C_L = C1 \cdot \alpha \log Re + C2 \cdot \frac{\alpha}{J} + C3 \frac{\alpha d}{x} + C4 \cdot \frac{\alpha h}{d} + C5 \cdot \frac{\alpha d}{c} + C6 \cdot \frac{h}{dJ} + C7. \quad (5.5)$$

In the equation, all the original predictors appear, although, except for the angle of attack, they all appear related to each other. The angle of attack is the most critical parameter, which was already inferred from the results shown in section 5.2 when the vertical position of the propeller and the angle of attack were analyzed. It should be noted that the position of the propeller is related to the diameter of the actuator disk and the advance parameter, remaining independent of the angle of attack.

The C_L can be plotted against the angle of attack α in Fig. 5.59(a) using the original data from the simulations and the predicted data.

As can be seen, the main tendency of the parameter is maintained. An additional way to understand this data is by plotting the C_L predicted versus the C_L from the simulations in Fig. 5.58.

As shown in Fig. 5.58, almost all the predicted C_L data collapses with the data stored from the simulations to validate the model between an error margin of 5 %. This prediction seems to work better in an intermediate range of C_L since, at a low lift coefficient, the prediction gives a C_L higher than the one obtained in the simulations. It is more widespread at higher lifts, with some points outside the error margins: this is expected, as the complexity of the behavior of the lift coefficient was found to be higher in the POD analysis.

The exact process carried out for the C_L can be applied to the rest of the aerodynamic and propulsive coefficients. In the drag coefficient case, the equation obtained is expressed in eq. 5.6.

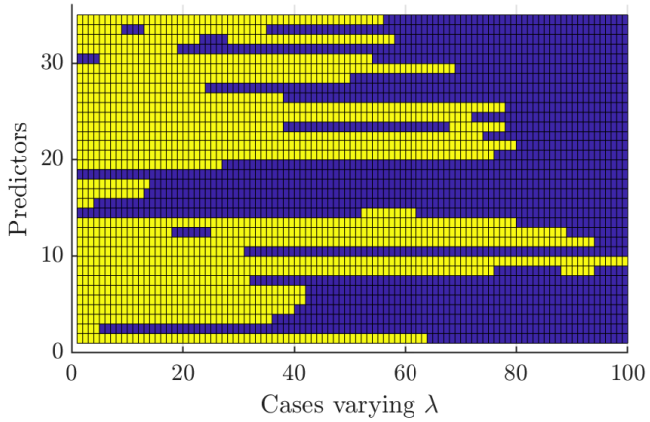

(a) Predictors with non-null (yellow) and null value (blue) as λ parameter grows.

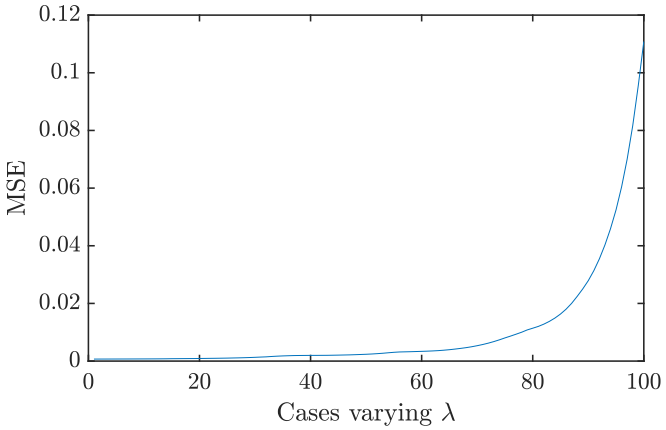

(b) MSE evolution as α parameter grows.

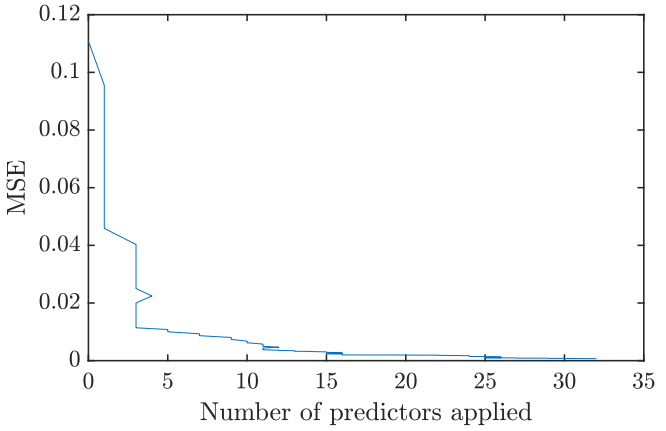

(c) MSE evolution as the number of predictors with non-null value are applied.

Figure 5.56: Lasso method aplication to obtain the lift coefficient regression.

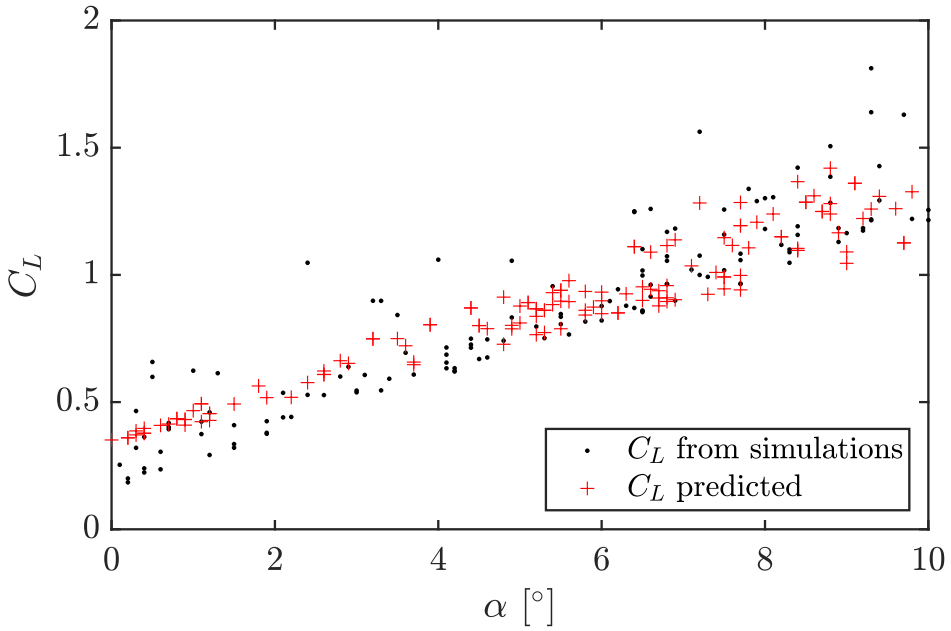

Figure 5.57: Lift coefficients obtained through simulations and from the application of the lasso method in a wide range of angle of attack.

$$C_{D0} = C1 \cdot \alpha + C2 \cdot \log Re + C3 \cdot \frac{\alpha}{J} + C4 \cdot \frac{h}{dJ} + C5 \cdot \frac{\theta d}{x} + C6 \cdot \frac{h}{c} + C7 \cdot \alpha^2 + C8 \cdot \frac{h^2}{d^2} + C9. \tag{5.6}$$

Again, the angle of attack is the most weighted predictor to explain this coefficient, although more predictors are needed in this case. The propeller vertical position also seems to gain importance as discussed in the previous sections.

Representing the C_{D0} in Fig. 5.59 as seen for the C_L, it is appreciated that the drag coefficient predicted collapses with the C_{D0} from the simulations between the same error.

In this case, the prediction is inside the error margins at intermediate drag, with a more significant widespread at higher drag where some points are outside the margin. At low drag, the prediction has higher values than the simulated drag, so the points are close to the upper limit of the error margin.

Following the lasso method's application, the propulsive coefficients are obtained in the same way. The expressions for the thrust coefficient and power coefficient are shown in eq. 5.7 and 5.8, respectively.

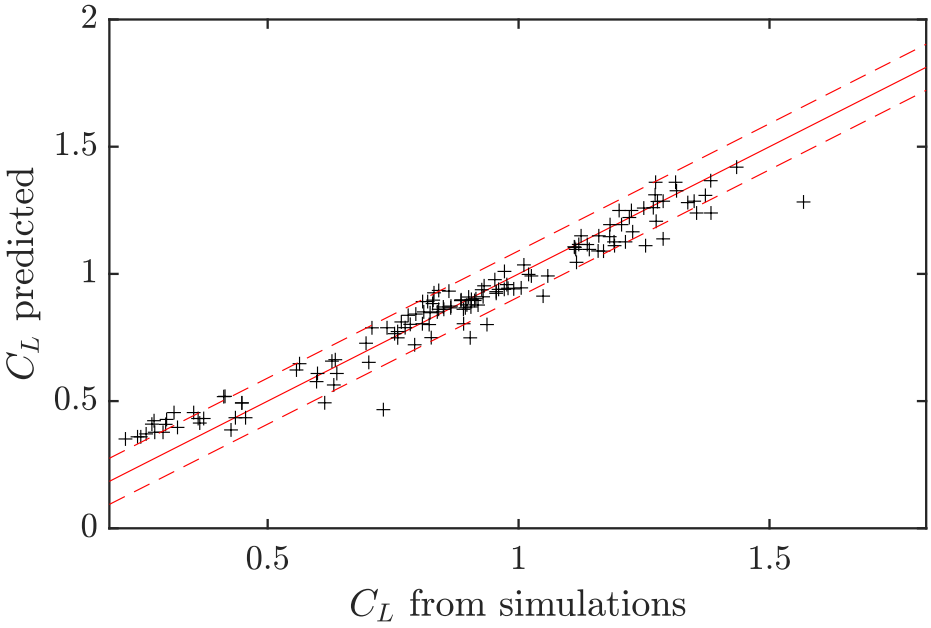

Figure 5.58: Lift coefficient obtained from the application of the lasso method versus the lift coefficient obtained directly in the simulations. The dashed bars set a 5 % of deviation from the maximum value.

$$C_T = C1 \cdot J + C2 \cdot \theta + C3 \cdot \frac{J}{\log Re} + C4 \cdot J\theta + C5 \cdot \frac{Jh}{d} + C6 \cdot J^2 + C7, \tag{5.7}$$

$$C_P = C1 \cdot J + C2 \cdot \theta + C3 \cdot \frac{\theta}{\log Re} + C4 \cdot J\theta + C5 \cdot \frac{Jh}{d} + C6 \cdot \frac{xc}{d^2} + C7 \cdot J^2 + C8 \cdot \theta^2 + C9. \tag{5.8}$$

Contrary to what happened with the aerodynamic coefficients, both propulsive coefficients depend to a great extent on the advance parameter ratio. In this case, the influence of the angle of attack is negligible for the regression. This may seem unexpected, as it is not what was shown in previous results. However, during level flight, the advance parameter is a function of the angle of attack, as varying the angle of attack means changes in the drag coefficient and, thus, the needed thrust coefficient. The other most important predictor is the pitch angle.

Again, both coefficient regressions are plotted in Fig. 5.60 and Fig. 5.61. This time, the coefficients are plotted versus the advance parameter ratio. Both thrust and power coefficients are inside the set error margin compared with the simulations' data and with a minor dispersion compared with the aerodynamic

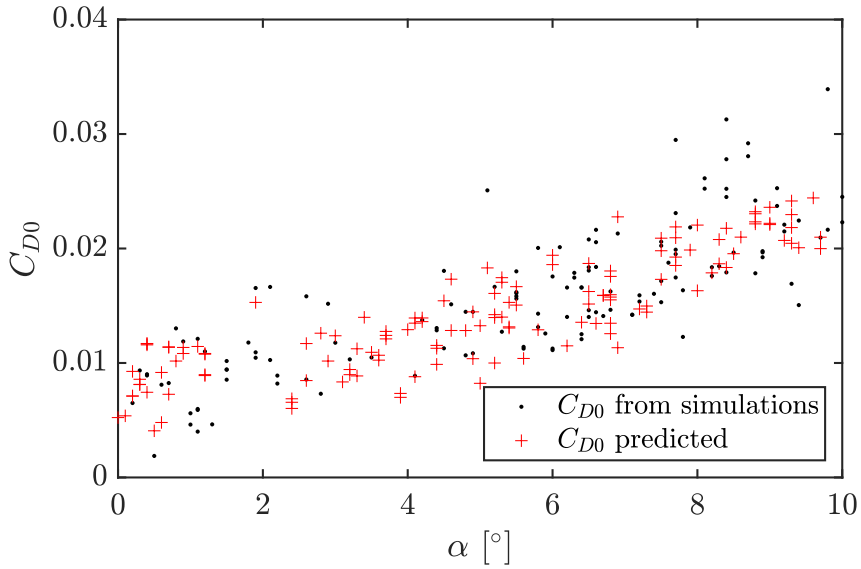

(a) Drag coefficients obtained through simulations and from the application of the lasso method in a wide range of angle of attack.

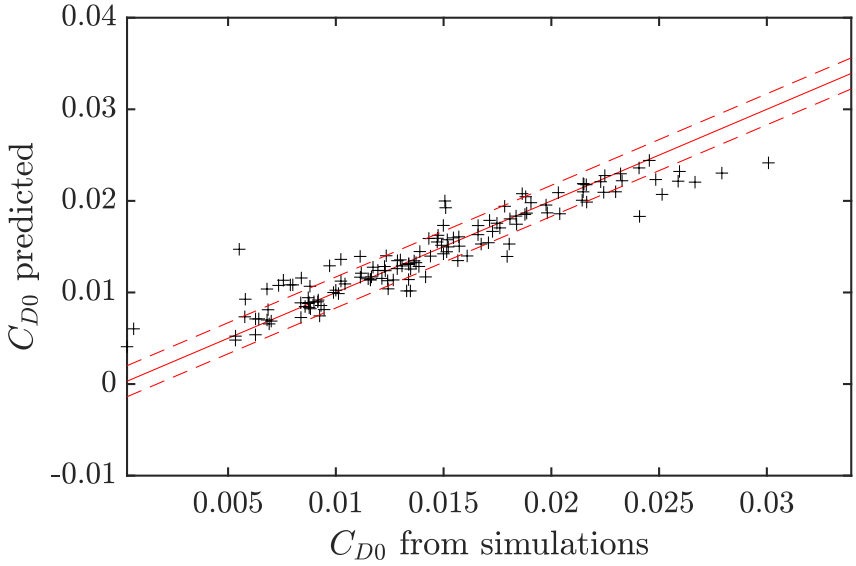

(b) Drag coefficient obtained from the application of the lasso method versus the drag coefficient obtained directly in the simulations. The dashed bars set a 5 % of deviation from the maximum value.

Figure 5.59: Drag coefficient lasso method aplication.

coefficients. The prediction gives higher coefficient values at low C_T and C_P, while with a high value, it tends to underestimate them.

Below these lines, a table with all the coefficients for each equation is shown. The present data have the objective of being helpful in designing and creating new aircraft that combine distributed electric propulsion and boundary layer ingestion.

	C_L	C_{D0}	C_T	C_P
C1	0.031	0.0074	-0.1341	-0.0092
C2	1.9664	-0.0034	0.4355	0.2091
C3	1.4498	0.0238	-0.2402	1.5938
C4	1.8702	-0.0007	0.0182	0.0301
C5	0.2342	0.0072	-0.0114	-0.0013
C6	0.0230	-0.0149	-0.0032	0.0001
C7	0.2523	1.0053	0.1534	-0.0580
C8		-0.0080		0.1248
C9		0.0549		0.0687

Table 5.4: Coefficients needed to complete the equations 5.5, 5.6, 5.7 and 5.8.

5.5.1 Practical Example

Now that the different expressions for each aerodynamic and propulsive coefficient are obtained through the lasso, it is possible to express the aerodynamic efficiency in eq. 5.9 and the propulsive efficiency in eq. 5.10 as a function of the same predictors.

$$\frac{C_L}{C_D} = \frac{C_L}{C_{D0} + C_{D0,\text{extra}} + \dfrac{C_L^2}{\pi \cdot \mathcal{AR} \cdot e}} = f\left(\alpha, \log Re, \frac{1}{J}, \theta, \frac{d}{x}, \frac{h}{d}, \frac{d}{c}\right), \tag{5.9}$$

$$\eta_p = \frac{C_T J}{C_P} = f\left(\alpha, \log Re, \frac{1}{J}, \theta, \frac{d}{x}, \frac{h}{d}, \frac{d}{c}\right). \tag{5.10}$$

A practical example using the coefficients obtained is proposed. In this case, the predictors will be optimized in order to maximize the product of both efficiencies, obtaining a new DEP BLI configuration. For this task, the same geometrical parameters described in chapter 3 are considered (chord length, wing span length, Oswald factor...). Additionally, a constant mass of 25 kg is considered, similar to assuming that the aircraft flies with 10 kg of batteries in this case.

The maximization of the product of efficiencies can be found using a nonlinear programming solver. An interior-point algorithm that calculates the Hessian

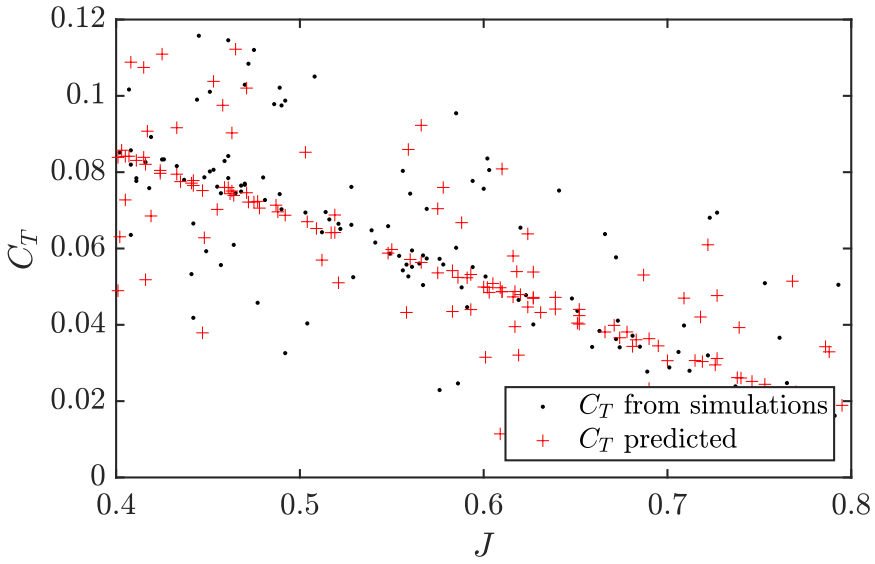

(a) Thrust coefficients obtained through simulations and from the application of the lasso method in a wide range of advance ratio parameter.

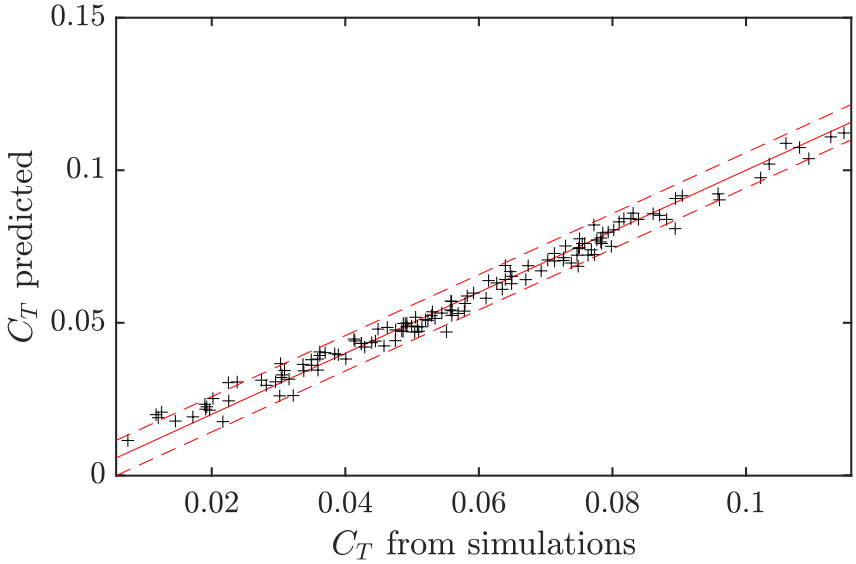

(b) Thrust coefficient obtained from the application of the lasso method versus the thrust coefficient obtained directly in the simulations. The dashed bars set a 5 % of deviation from the maximum value.

Figure 5.60: Thrust coefficient lasso method aplication.

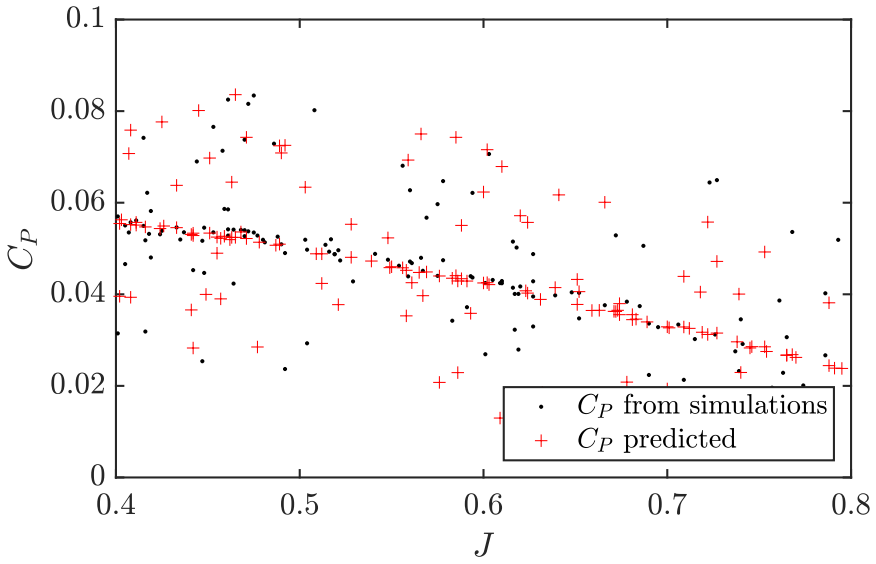

(a) Power coefficients obtained through simulations and from the application of the lasso method in a wide range of advance ratio parameter.

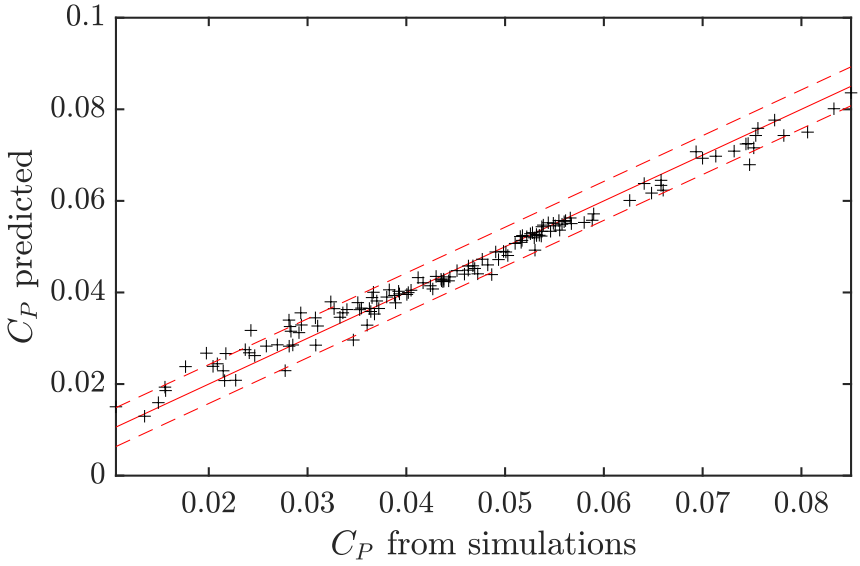

(b) Power coefficient obtained from the application of the lasso method versus the power coefficient obtained directly in the simulations. The dashed bars set a 5 % of deviation from the maximum value.

Figure 5.61: Power coefficient lasso method aplication.

by a dense quasi-Newton approximation is employed. More information about the algorithm is provided by Byrd et al. [120].

As limits of the optimization, the maximum and minimum values set during the generation of the design cases are applied. Those limits can be observed in section 4.2.2 and Table 4.1.

The optimization is applied only in cruise condition, considering constant velocity and sea level altitude. Two extra restrictions are added: the aircraft drag must be equal to the total thrust, and the aircraft lift must be equal to the aircraft weight. These two restrictions are expressed also in terms of the proposed predictors and they are shown respectively in eq. 5.11 and eq. 5.12.

$$T \cdot n_{\text{props}} - D = \rho \cdot \frac{U^2}{J^2} \cdot d^2 \cdot C_T \cdot n_{\text{props}} - \frac{1}{2} \cdot \rho \cdot U^2 \cdot S \cdot \left(C_{D,0,\text{wing}} + C_{D,0,\text{extra}} + \frac{C_L^2}{\pi \cdot AR \cdot e} \right) = 0, \tag{5.11}$$

$$L - W = \frac{1}{2} \cdot \rho \cdot U^2 \cdot S \cdot C_L^2 - m \cdot g = 0, \tag{5.12}$$

where n_{props} is the total number of engines of the configuration, J is the advance ratio, d is the propeller diameter, and U is the velocity. These variables must be expressed as a function of the selected predictors. The oswald parameter e, the aspect ratio AR, the wing surface S, the chord lenght c and total mass m remain constant in this study.

The optimal configuration obtained has an aerodynamical efficiency of 17.42 and a propulsive efficiency of 86 %. All the data of this optimal configuration are summarized in Table 5.5. The data from the optimal case selected through the CFD analysis in section 5.2.1 is also included for comparison in this table. The data for this case is extracted at the beginning of the mission described in section 5.3, in order to have the same aircraft mass. The pitch in both cases is evaluated through eq. 4.9 and using the data shown in Table 3.2, which sets the θ_0 of the 75 % blade section at 17.6°.

In this case, the DEP BLI configuration differs significantly from the optimal configuration selected during the propeller position analysis in section 5.2. Nevertheless, reaching a different solution is expected as additional variables and cases are employed. The main variable of change is the pitch of the propellers. Taking this variable into account, a new distribution of propellers in terms of diameter used, the number of propellers, and rotational velocity are possible.

This optimal solution opts for a configuration with smaller propellers closer to each other, which are set at high vertical positions above the trailing edge. On the one hand, a smaller propeller is translated into higher rotational velocities. On the other hand, a more significant number of propellers need a lower rotational velocity to generate the same thrust as a smaller number of propellers.

	Optimal case from lasso	Case from CFD analysis
α [°]	2.17	3.42
Re	610740	566630
Speed [m/s]	44.92	41.63
J	0.61	0.66
Rotational speed [rev/s]	633.76	853.07
Propeller radius [m]	0.033	0.04
Distance between shafts [m]	0.066	0.15
Number of propellers	29	13
θ [°]	-4.87	-0.45
Pitch [m/rev]	0.0356	0.0292
Propeller position [%]	95.06	31.5

Table 5.5: Parameters obtained during the optimization of the efficiency product using the coefficients from the lasso vs the parameters used at the begining of the flight of the optimal selected case from CFD analysis in section 5.3.

This case optimizes the rotational velocity by setting a negative collective pitch angle.

It is worth stressing that this optimization should not be fully comparable to the one obtained by the CFD analysis. This case shown here is only optimizing the product of efficiencies without taking into account any variation of operative empty weight due to this new distribution.

The developed tool can be helpful for also determining an aircraft performance chart as a function of the wing loading (W/S) and the power-to-weight ratio (P/W). Using the chart, optimizing the geometrical parameters set as a constant and evaluating a potential power plant optimization is possible. However, it should be noted that in a DEP BLI case, the aerodynamics and the propulsion plant are strongly coupled, so the evaluation of the limitations in the performances is not so simple. In this case, there is no explicit equation that relates the wing loading with the power-to-weight ratio, increasing the number of variables involved.

5.6 Summary

In this chapter, the main results obtained in the entire work have been discussed.

The first result discussed is the CFD analysis of the propeller position. In this study, all the propulsive and aerodynamic coefficients are analyzed as a function of the angle of attack and the position of the propeller above the trailing edge, with particular emphasis on the product of aerodynamic and propulsive efficiency. The main result is that the propulsive efficiency is maximized in lower positions while the aerodynamic efficiency acts reversely. With the previous data in mind, an optimal configuration with a propeller of 0.04 m in a 31.5 % position with 13 engines is selected for further analysis. This optimum case obtains a product of efficiencies 6 % higher than a baseline case with a classical configuration without DEP or BLI.

A proper orthogonal decomposition has been carried out to examine the propeller position effect on the aircraft's aerodynamics. The most energetic modes have been isolated to see their contribution to the pressure and friction coefficients. Then, these modes have been employed to obtain the lift and drag coefficients with low error. Last, POD has been presented as a tool to interpolate the aerodynamic coefficients, reducing the number of simulations needed for fitting a surrogate model.

Following with the optimal aircraft selected, fuel optimization for a range mission is carried out and compared with the other configurations. To do that, the specific range of every case is computed, and the velocity law that maximizes that specific range is obtained using the efficiencies from the simulations and the ICE map. With this, the maximum range of a baseline aircraft with 10 kg of fuel is calculated. Then, the possible fuel savings for the hybrid cases are computed, maintaining the same operational range. The optimal case saves almost 16 % of fuel compared with the baseline case, 3 % more than a pure hybrid case.

Finally, the cases where seven design parameters were changed are employed to fit a lasso method. Every aerodynamic and propulsive coefficient is fitted using a list of low error predictors, which are analyzed. The simplified equations obtained for each coefficient can be used to feed optimization models to design DEP and BLI aircraft in different missions and conditions. An example using the obtained the equations is provided. In this example, a cruise flight with the same geometrical parameters presented in chapter 3 and a constant aircraft mass is optimized, obtaining a different DEP BLI configuration to that selected in the previous sections.

All these conclusions are contained in Chapter 6, along with a general summary of all of them. A discussion about the limitations when carrying out this work and possible future work is also included.

5.7 References

[37] M. Elsalamony and L. Teperin. “2D Numerical Investigation of Boundary Layer Ingestion Propulsor on Airfoil”. In: *7th European Conference for Aeronautics and Space Sciences (EUCASS)* (2017), pp. 1–11. DOI: 10.13009/EUCASS2017-67 (cit. on pp. 5, 21, 46, 102).

[118] G. K. Ananda, P. P. Sukumar, and M. S. Selig. “Measured aerodynamic characteristics of wings at low Reynolds numbers”. In: *Aerospace Science and Technology* 42 (2015), pp. 392–406. ISSN: 12709638. DOI: 10.1016/j.ast.2014.11.016 (cit. on p. 102).

[119] D. M. Sutton. “Experimental Characterization of the Effects of Freestream Turbulence Intensity on the SD7003 Airfoil at Low Reynolds Numbers”. MA thesis. Univeristy of Toronto, 2015 (cit. on p. 102).

[120] R. H. Byrd, J. C. Gilbert, and J. Nocedal. “A trust region method based on interior point techniques for nonlinear programming”. In: *Mathematical Programming, Series B* 89.1 (2000), pp. 149–185. ISSN: 00255610. DOI: 10.1007/PL00011391 (cit. on p. 156).

CHAPTER 6

Conclusions and future works

Contents

6.1 Introduction

THE growth of the UAV fleet, together with the unsustainable climatic situation, forces design solutions for these aircraft to be sought to reduce the associated polluting and greenhouse emissions as much as possible. Multiple investigations on various technologies try to alleviate the polluting and greenhouse effects of aircraft thanks to the improvement of both its aerodynamics and propulsion plant. In this work, it is proposed to use three technologies simultaneously. Through a correct setting, it is possible to obtain better propulsive and aerodynamic efficiencies while reducing specific consumption. These technologies are series hybridization, distributed electric propulsion, and boundary layer ingestion.

Throughout this work, the inclusion of these technologies has been analyzed to analyze their feasibility with promising results. Additionally, simple tools have been provided to favor the future design of these aircraft.

This chapter focuses on the final conclusion of this work. First, the main conclusions obtained in the previous chapter will be shown. Next, a summary of these conclusions will be discussed. The chapter ends with a discussion of the work's limitations and future proposed projects.

6.2 CFD analysis conclusions

The product of aerodynamic and propulsive efficiency is the best way to evaluate an aircraft's performance with DEP and BLI with a range mission. Because both efficiencies are the main parameters along the BSFC involved in maximizing the range, the product of efficiencies must be the highest possible. This way, higher ranges can be flown or, for the same range, more fuel savings can be achieved. A preliminary study of the possible fuel benefits was performed in Chapter 3, where the main conclusion drawn was that if the overall efficiencies and specific fuel consumption improve by 25 % by combining series hybridization, distributed electric propulsion, and boundary layer ingestion, a fuel benefit can be achieved despite the gain in weight by using those systems.

Multiple design parameters affect the aircraft's aerodynamics or propulsive efficiency. Most of these parameters were set at a quick parametric study maximizing the product of efficiencies to study the vertical propeller position, which significantly affects the aircraft's performance involving how the boundary layer ingestion is produced.

The propeller position is defined in percentage above the trailing edge, meaning that the lower position (0 %) sets the propeller center at the same height as the trailing edge. Conversely, in the higher position (100 %), the

propeller is set fully above the airfoil, with the blade tip at the same height as the trailing edge.

When the product of efficiencies is studied at a fixed angle of attack and Reynolds number, two propeller positions emerge as candidates for maximizing it: one position between 70 % and 85 % and another between 15 % and 35 %. Both places maximize the efficiencies for diverse reasons.

On the one hand, the propulsive efficiency is maximized at a lower position due to a geometrical aspect, where the area affected by the BLI of the propeller increases compared with a higher position. As the wet area increases, a more significant part of the propeller benefits from the BLI effects, thus improving the propulsive efficiency. More than 10 % of propulsive efficiency benefit can be achieved by setting the propeller in a lower position than the higher one.

On the other hand, higher propeller positions achieve better aerodynamic efficiencies. As the position increases, the airfoil circulation changes so that the apparent angle of attack is greater. This is reflected by a rise in the suction peak on the suction side and an advancement of the laminar separation bubble. Although increasing the position raises the parasitic drag in the last segment of the airfoil, the effect is marginal between positions and counterbalanced by the fact that a smaller portion of the propeller recirculates the flow on the pressure side. At a constant angle of attack, the lift coefficient increases by 10 % between the lower and higher position while the drag decreases by more than 10 %.

Knowing how both efficiencies are improved, an optimal case is defined with propellers of radius of 0.04 m and a position of 31.5 %, with a distribution of 13 engines and a draft angle of 1.5°. This case is compared at near cruise conditions with other cases with more classic configurations and a DEP BLI suboptimal case with the propeller position at 75 %.

Because the optimal case has the propeller set in a lower position, the aerodynamic efficiency is not optimized, being lower than the baseline case without DEP and BLI. Nevertheless, this optimal case benefits from high propulsive efficiency, with a final rise of almost 3 % percent in the product of efficiencies compared with the baseline case. The suboptimal case attains a lower but close product of efficiencies compared with the optimal case. In this case, the propulsive efficiency is lower than the optimal case, but this decrease is accompanied by an aerodynamic efficiency higher than the baseline case. Also, its operational specific range map is wider, which means that its behavior can become better than that of the optimal case outside the design conditions.

6.3 Range mission optimization conclusions

The optimal configuration with DEP BLI and a propeller position of 31.5 % obtained in the first conclusion is compared in terms of mission with other

arrangements achieving promising results.

Thanks to the implementation of series hybridization, where the ICE is mechanically decoupled to the propeller, it is possible to optimize the fuel consumption of these aircraft. Since the rotational speed of the propeller and the same speed from the ICE do not need to be related, all the hybrid configurations reach a similar $BSFC$. Therefore, the differences between those cases will depend on the product of the efficiencies.

The objective is to obtain fuel savings when comparing configurations. First, the maximum range that the baseline case achieves with 10 kg of fuel is computed. This range obtained exceeds 4000 km. Then the fuel of all the hybrid cases, including the optimal case, is calculated for the same range.

The velocity is set linked to the aircraft mass in the baseline case, while in the hybrid cases, the velocity changes during the flight, trying to maximize always the specific range. This way, all the hybrid cases fly with higher velocities than the baseline case, reducing the time of flight. The optimal case completes the mission in 29 hours, 3 hours less than the baseline configuration.

Thanks to the optimization of the product of efficiencies, the optimal case reduces the fuel mass needed to 8.45 kg, thanks to the improvement in propulsive efficiency. This reduction is translated to fuel savings of nearly 16 %, more than 3 % compared with a pure hybrid case without DEP and BLI.

The suboptimal case with DEP and BLI but with a higher propeller position (75 %) is also analyzed, obtaining slightly lower results but very similar to those of the optimal configuration. In this case, the improvement is given by the optimization of aerodynamic efficiency.

Regarding CO_2 emissions, the $BSFC$ is slightly better optimized in the pure hybrid case, which is reflected in a lower instantaneous emission from this configuration. However, since the flight time is shorter in the optimal case, the global emissions turn out to be lower.

6.4 POD analysis and design conclusions

The first propeller position analysis is continued by using proper orthogonal decomposition methods, and a better understanding of the aerodynamic coefficients is achieved. Both pressure and friction coefficients behavior are explained in more than 90 % by using only one mode. This means that the primary behavior of the coefficients can be analyzed by utilizing that mode, leaving the details to high-order modes, which indicates that it is possible to use this data to create simple models.

In this study, it is determined that the main parameter that affects the pressure coefficient is the angle of attack. Nevertheless, the effect of the propeller position is not negligible. If the position of the propeller is raised, the suction

over the suction side increases at the same time that the overpressure on the pressure side also increases. This effect was already observed in the first study, producing the same effect as increasing the angle of attack, and is reflected in a rise in the lift coefficient. However, suppose the position is at its maximum, with the propeller shaft at a radius distance of the trailing edge. In that case, the trend is inverted, and the extra lift is decreased, which is consistent with a decrease in the boundary layer ingestion effects. At the same time, the suction peak is displaced upstream, near the leading edge. By doing that, the form drag produced by the pressure distribution is reduced.

When analyzing higher modes, the nonlinear effect of the propeller position challenges a correct interpretation. In the friction coefficient, it is possible to observe the maximum effect at around 70 % position, which coincides with the CFD analysis. Even though, as already mentioned, the first modes include the majority of the information to reconstruct these coefficients, if it is also desired to rebuild the LSB, it will be necessary to apply around ten modes.

The lift and drag coefficients can be obtained for any combination of the angle of attack and propeller position by integrating the pressure and friction coefficients using a few modes. This way, it is possible to have an error in the C_L lower than 1 % using five modes. Because of the importance of the C_f reconstruction, the C_D is slightly more sensitive, needing at least six modes to reduce the error below 3 %.

POD is an interesting tool to rebuild aerodynamic coefficients that can be used to feed surrogate models with a low error when designing and optimizing small DEP BLI aircraft. Having enough information, additional tools to help the design can be obtained. A lasso method has been applied with a more extensive database of simulations varying seven design parameters. Using the simulations, linear regression is calculated through a lasso method. The method produces an equation for each aerodynamic coefficient with some adjusted predictors, which gives correct results with less than 5 % deviation of the maximum value obtained. These equations can be useful to feed optimization algorithms applied when designing DEP BLI aircraft with conditions different from those presented in this work. As there is no public database of similar aircraft with DEP and BLI, classic statistical methods for conceptual and preliminary aircraft design can not be used directly. The regression presented in this document is, thus, an interesting addition to the toolbox of UAV designers.

6.5 General Conclusions

The main conclusion of this work is that it shows the feasibility of combining series hybridization, distributed electric propulsion, and boundary layer ingestion in the design of small aircraft up to 25 kg.

Despite the fact of having a greater operative empty weight due to the additional systems, a correct distribution and setting of the propellers may achieve important fuel savings.

The propeller's vertical position plays an important role that directly affects how the BLI works. On the one hand, a higher propeller position can improve the aerodynamic efficiency by changing the circulation around the airfoil. This way, the suction peak increases, and the laminar separation bubble is moved toward the leading edge. Although the friction coefficient also increases, it is mitigated by a decrease of the form drag, similar to the observed when having upwash effects. On the other hand, in a lower propeller position, the washed propeller's area by the boundary layer increases, thus benefiting from this effect and increasing the propulsive efficiency.

An optimal configuration with 13 engines, 40 mm propellers set in a 31.5 % position above the trailing edge, and 1.5° draft angle with a series-hybrid power plant is studied in detail in this thesis. The range of this aircraft is equal to the maximum range that an aircraft of the same $MTOM$ with a baseline configuration (single-engine without DEP and BLI) can fly with 10 kg of fuel. For the same mission, the optimal aircraft needs 16 % less fuel, 3 % less compared to a pure hybrid aircraft without DEP and BLI. This reduction in fuel required is immediately translated into fewer polluting and greenhouse emissions produced.

6.6 Limitations and future works

The objectives described in Chapter 1 have been successfully completed, which opens the door to future work based on the limitations of this work.

Although it has been possible to use experiments to validate the simulations of the propeller and the wing, at the time of writing of this work, it has not been possible to obtain experiments that validate the interaction of the wing employed with the propulsion system at the same time. One of the main future works should focus on designing a wind tunnel experiment with both systems mounted simultaneously. In this way, it would be possible to validate further the study of the position of the propeller and the results of product improvement of efficiencies.

Since an extensive battery of simulations was used in this work, they have been simplified as much as possible in order to reduce the required computational resources and calculation time. For this reason, two types of simulations are proposed that help provide greater realism and also help to validate the results obtained. On the one hand, it is proposed to simulate the complete wing with the distribution of all the propellers in the position obtained in this work. This simulation will be more significant than the ones used here. It is intended to observe better the possible interaction between propellers and better consider

the induced drag component on the wing. On the other hand, to better solve the propeller simulation, it is proposed to simulate the actual geometry of the rotating propeller in an unsteady simulation. With this, it would be possible to analyze the limitations coming from the BEMT model.

Additionally, there is still room for improvement in optimizing systems integration, not only in a deeper analysis of all the geometric variables that are part of the problem but also in the selection of all components, from the airfoil to the propeller employed. There are important optimization opportunities in the generator and power distribution, but also in the structure design and in the engine matching. The engine may even be downsized a bit more, using batteries as an energy buffer for climbing and high-C_L maneuvers.

Finally, it would be interesting to apply the tools that have been developed in this work to help designing DEP BLI aircraft, either with new weight or size limitations, or destined for a different mission than the one that has been presented. Indeed, at the time of finishing writing this document, there are two aircraft being designed using the method described here.

Bibliography

[1] **García-Cuevas, L. M., Quintero, P., Bares, P., and Varela, P.**
"Optimisation of the flight speed in a hybrid RPAS with distributed electric propulsion and boundary layer ingestion"
in: *1st INGENIADRON Conference*. Seville, Spain: INGENIADRON May 2021, pp. 10–11 (cit. on p. vii)

[2] **Serrano, J. R., Tiseira, A. O., García-Cuevas, L. M., and Varela, P.**
"Computational Study of the Propeller Position Effects in Wing-Mounted, Distributed Electric Propulsion with Boundary Layer Ingestion in a 25 kg Remotely Piloted Aircraft"
in: *Drones* 5.3 (2021). ISSN: 2504-446X. DOI: 10.3390/drones5030056 (cit. on p. vii)

[3] **Tiseira, A. O., García-Cuevas, L. M., Quintero, P., and Varela, P.**
"Series-hybridisation, distributed electric propulsion and boundary layer ingestion in long-endurance, small remotely piloted aircraft: Fuel consumption improvements"
in: *Aerospace Science and Technology* 120 (2022). DOI: 10.1016/j.ast.2021.107227 (cit. on p. vii)

[4] **Serrano, J. R., García-Cuevas, L. M., Bares, P., and Varela, P.**
"Propeller Position Effects over the Pressure and Friction Coefficients over the Wing of an UAV with Distributed Electric Propulsion: A Proper Orthogonal Decomposition Analysis"
in: *Drones* 6.2 (2022). ISSN: 2504-446X. DOI: 10.3390/drones6020038. URL: https://www.mdpi.com/2504-446X/6/2/38 (cit. on p. vii)

[5] **Agency, E. U. A. S.**
Study on the societal acceptance of Urban Air Mobility in Europe
2021 (cit. on p. 2)

[6] **Single European Sky ATM Research**
European Drones Outlook Study
Last accessed: 2022-01-12 2016. URL: http://www.sesarju.eu/sites

/default/files/documents/reports/European_Drones_Outlook_Study_2016.pdf (cit. on p. 2)

[7] **Amoukteh, A., Janda, J., and Vicent, J.**
"Drones Go to work"
in: *Harvard Business Review* (2017), pp. 77–94. URL: https://hbr.org/cover-story/2017/05/drones-go-to-work (cit. on p. 2)

[8] **Nickol, C. L. and Haller, W. J.**
"Assessment of the performance potential of advanced subsonic transport concepts for NASA's environmentally responsible aviation project"
in: *54th AIAA Aerospace Sciences Meeting*. San Diego, CA, USA: AIAA Jan. 2016, pp. 1–21. DOI: 10.2514/6.2016-1030 (cit. on p. 2)

[9] **Rostami, M. and Farajollahi, A. hamzeh**
"Aerodynamic performance of mutual interaction tandem propellers with ducted UAV"
in: *Aerospace Science and Technology* 108 (2021), p. 10. ISSN: 12709638. DOI: 10.1016/j.ast.2020.106399 (cit. on p. 2)

[10] **Zhang, H., Song, B., Li, F., and Xuan, J.**
"Multidisciplinary design optimization of an electric propulsion system of a hybrid UAV considering wind disturbance rejection capability in the quadrotor mode"
in: *Aerospace Science and Technology* 110 (2021), p. 20. ISSN: 12709638. DOI: 10.1016/j.ast.2020.106372 (cit. on p. 2)

[11] **McKinney, K. E.**
"Evaluation of Hybrid-Electric Power System Integration Challenges for Multi-rotor UAS"
B.Sc. thesis. Stilwater, OK, USA: Oklahoma State University 2018 (cit. on pp. 2, 3)

[12] **Fredericks, W. J., Moore, M. D., and Busan, R. C.**
"Benefits of hybrid-electric propulsion to achieve 4x increase in cruise efficiency for a VTOL aircraft"
in: *2013 International Powered Lift Conference*. Los Angeles, California, USA 2013, pp. 1–21. DOI: 10.2514/6.2013-4324 (cit. on p. 2)

[13] **Payri, F. and Desantes, J.**
Motores de Combustión Interna Alternativos
Valencia, Spain: Editorial Reverté and Editorial UPV 2011, pp. 800–822. ISBN: 978-84-291-4802-2 (cit. on p. 2)

[14] **Heywood, J.**
Internal Combustion Engine Fundamentals
McGraw-Hill Education 1988, pp. 668–712. ISBN: 978-1259002076
(cit. on p. 2)

[15] **Benajes, J., Novella, R., Gómez-Soriano, J., Barbery, I., Libert, C., Rampanarivo, F., and Dabiri, M.**
"Computational assessment towards understanding the energy conversion and combustion process of lean mixtures in passive pre-chamber ignited engines"
in: *Applied Thermal Engineering* 178 (2020). DOI: 10.1016/j.applthermaleng.2020.115501 (cit. on p. 3)

[16] **Nagasawa, T., Okura, Y., Yamada, R., Sato, S., Kosaka, H., Yokomori, T., and Iida, N.**
"Thermal efficiency improvement of super-lean burn spark ignition engine by stratified water insulation on piston top surface"
in: *International Journal of Engine Research* 22 (5 2021), pp. 1421–1439. DOI: 10.1177/1468087420908164 (cit. on p. 3)

[17] **Harmon, F. G., Frank, A. A., and Chattot, J. J.**
"Conceptual design and simulation of a small hybrid-electric unmanned aerial vehicle"
in: *Journal of Aircraft* 43.5 (2006), pp. 1490–1498. ISSN: 00218669. DOI: 10.2514/1.15816 (cit. on pp. 3, 40, 42)

[18] **Ausserer, J. K. and Harmon, F. G.**
"Integration, validation, and testing of a hybrid-electric propulsion system for a small remotely-piloted aircraft"
in: *10th Annual International Energy Conversion Engineering Conference*. Atlanta, GA, USA: AIAA Aug. 2012, pp. 1–11. ISBN: 9781624101908. DOI: 10.2514/6.2012-4239 (cit. on pp. 3, 40)

[19] **Hiserote, R. M.**
"Analysis of Hybrid-Electric Propulsion System Designs for Small Unmanned Aircraft Systems"
MA thesis 2010. URL: https://scholar.afit.edu/etd/2044
(cit. on p. 3)

[20] **Kim, C., Namgoong, E., Lee, S., Kim, T., and Kim, H.**
Fuel economy optimization for parallel hybrid vehicles with CVT
SAE Technical Paper 1999-01-1148. SAE International 1999. DOI: 10.4271/1999-01-1148 (cit. on p. 3)

[21] **Mengistu, I. H.**
"A small internal combustion engine testing for a hybrid-electric remotely-piloted aircraft"
MA thesis. Wright-Patterson Air Force Base, OH, USA: Air Force Institute of Technology 2011, p. 124 (cit. on pp. 3, 40)

[22] **Lieh, J., Spahr, E., Behbahani, A., and Hoying, J.**
"Design of hybrid propulsion systems for unmanned aerial vehicles"
in: *47th AIAA/ASME /SAE/ASEE Joint Propulsion Conference and Exhibit 2011*. San Diego, California, USA Aug. 2011, pp. 1–14. DOI: 10.2514/6.2011-6146 (cit. on pp. 3, 14)

[23] **Stoll, A. M., Bevirt, J., Moore, M. D., Fredericks, W. J., and Borer, N. K.**
"Drag Reduction Through Distributed Electric Propulsion"
in: *14th AIAA Aviation Technology, Integration, and Operations Conference*. Atlanta, GA, USA: AIAA June 2014, pp. 1–10. DOI: 10.2514/6.2014-2851 (cit. on p. 4)

[24] **Stoll, A. M.**
"Comparison of CFD and experimental results of the leap tech distributed electric propulsion blown wing"
in: *15th AIAA Aviation Technology, Integration, and Operations Conference*. Dallas, TX, USA: AIAA June 2015, pp. 22–26. ISBN: 9781624103698. DOI: 10.2514/6.2015-3188 (cit. on pp. 4, 61, 63)

[25] **Xue, C. and Zhou, Z.**
"Propeller-wing coupled aerodynamic design based on desired propeller slipstream"
in: *Aerospace Science and Technology* 97 (2020), p. 16. ISSN: 12709638. DOI: 10.1016/j.ast.2019.105556 (cit. on p. 4)

[26] **Ko, Y.-Y. A.**
"The Multidisciplinary Design Optimization of a Distributed Propulsion Blended-Wing-Body Aircraft"
PhD thesis. Virginia Tech 2003, pp. 1–222. URL: https://vtechworks.lib.vt.edu/handle/10919/27257 (cit. on p. 4)

[27] **Moore, K. R. and Ning, A.**
"Distributed electric propulsion effects on traditional aircraft through multidisciplinary optimization"
in: *AIAA/ASCE /AHS/ASC Structures, Structural Dynamics, and Materials Conference*. Kissimmee, FL, USA: AIAA Jan. 2018. ISBN: 9781624105326. DOI: 10.2514/6.2018-1652 (cit. on pp. 4, 42)

[28] **Kirner, R., Raffaelli, L., Rolt, A., Laskaridis, P., Doulgeris, G., and Singh, R.**
"An assessment of distributed propulsion: Part B - Advanced propulsion system architectures for blended wing body aircraft configurations"
in: *Aerospace Science and Technology* 50 (2016), pp. 212–219. ISSN: 12709638. DOI: 10.1016/j.ast.2015.12.020. URL: http://dx.doi.org/10.1016/j.ast.2015.12.020 (cit. on p. 4)

[29] **Amoozgar, M., Friswell, M. I., Fazelzadeh, S. A., Khodaparast, H. H., Mazidi, A., and Cooper, J. E.**
"Aeroelastic stability analysis of electric aircraft wings with distributed electric propulsors"
in: *Aerospace* 8.4 (2021), pp. 1–12. ISSN: 22264310. DOI: 10.3390/aerospace8040100 (cit. on pp. 4, 42)

[30] **Kim, H. D., Perry, A. T., and Ansell, P. J.**
"A Review of Distributed Electric Propulsion Concepts for Air Vehicle Technology"
in: *AIAA/IEEE Electric Aircraft Technologies Symposium*. Cincinnati, OH, USA: AIAA/IEEE July 2018, pp. 1–21. ISBN: 9781624105722. DOI: 10.2514/6.2018-4998 (cit. on p. 4)

[31] **Budziszewski, N. and Friedrichs, J.**
"Modelling of a boundary layer ingesting propulsor"
in: *Energies* 11.4 (2018). ISSN: 19961073. DOI: 10.3390/en11040708 (cit. on p. 4)

[32] **Lv, P., Ragni, D., Hartuc, T., Veldhuis, L., and Rao, A. G.**
"Experimental investigation of the flow mechanisms associated with a wake-ingesting propulsor"
in: *AIAA Journal* 55.4 (2017), pp. 1332–1342. ISSN: 00011452. DOI: 10.2514/1.J055292 (cit. on p. 4)

[33] **Hall, D. K., Huang, A. C., Uranga, A., Greitzer, E. M., Drela, M., and Sato, S.**
"Boundary layer ingestion propulsion benefit for transport aircraft"
in: *Journal of Propulsion and Power* 33.5 (2017), pp. 1118–1129. ISSN: 15333876. DOI: 10.2514/1.B36321 (cit. on pp. 5, 21)

[34] **Teperin, L.**
"Investigation on Boundary Layer Ingestion Propulsion for UAVs"
in: *International Micro Air Vehicle Conference and Flight Competition (IMAV)* Aug. 2017, pp. 293–300 (cit. on pp. 5, 45, 63)

[35] **Martínez Fernández, A. and Smith, H.**
"Effect of a fuselage boundary layer ingesting propulsor on airframe forces and moments"
in: *Aerospace Science and Technology* 100 (2020), p. 105808. ISSN: 12709638. DOI: 10.1016/j.ast.2020.105808 (cit. on p. 5)

[36] **Samuelsson, S. and Grönstedt, T.**
"Performance analysis of turbo-electric propulsion system with fuselage boundary layer ingestion"
in: *Aerospace Science and Technology* 109 (2021), p. 10. ISSN: 12709638. DOI: 10.1016/j.ast.2020.106412 (cit. on p. 5)

[37] **Elsalamony, M. and Teperin, L.**
"2D Numerical Investigation of Boundary Layer Ingestion Propulsor on Airfoil"
in: *7th European Conference for Aeronautics and Space Sciences (EUCASS)* (2017), pp. 1–11. DOI: 10.13009/EUCASS2017-67 (cit. on pp. 5, 21, 46, 102)

[38] **Leifsson, L., Ko, A., Mason, W. H., Schetz, J. A., Grossman, B., and Haftka, R. T.**
"Multidisciplinary design optimization of blended-wing-body transport aircraft with distributed propulsion"
in: *Aerospace Science and Technology* 25.1 (2013), pp. 16–28. ISSN: 12709638. DOI: 10.1016/j.ast.2011.12.004 (cit. on p. 5)

[39] **Goldberg, C., Nalianda, D., MacManus, D., Pilidis, P., and Felder, J.**
"Installed performance assessment of a boundary layer ingesting distributed propulsion system at design point"
in: *52nd AIAA/SAE/ASEE Joint Propulsion Conference*. Salt Lake City, Utah, USA 2016, pp. 1–22. DOI: 10.2514/6.2016-4800 (cit. on p. 5)

[40] **Capata, R., Marino, L., and Sciubba, E.**
"A hybrid propulsion system for a high-endurance UAV: configuration selection, aerodynamic study, and gas turbine bench tests"
in: *Journal of Unmanned Vehicle Systems* 02.01 (2014), pp. 16–35. ISSN: 2291-3467. DOI: 10.1139/juvs-2013-0005 (cit. on p. 14)

[41] **Jurecka, R. and Bencalik, K.**
"Airplanes with an electric motor"
in: *Aviation* 16.3 (2012), pp. 63–68. ISSN: 16487788. DOI: 10.3846/16487788.2012.732304 (cit. on p. 14)

[42] "Fuel cell/battery hybrid UAV takes off in Taiwan"
in: *Fuel Cells Bulletin* 2010.6 (2010), pp. 4–5. ISSN: 1464-2859. DOI: https://doi.org/10.1016/S1464-2859(10)70177-2. URL: https://www.sciencedirect.com/science/article/pii/S1464285910701772 (cit. on p. 14)

[43] **Hoogreef, M. F., Vos, R., Vries, R. de, and Veldhuis, L. L.**
"Conceptual assessment of hybrid electric aircraft with distributed propulsion and boosted turbofans"
in: *AIAA Scitech 2019 Forum* May 2020 (2019). DOI: 10.2514/6.2019-1807 (cit. on p. 14)

[44] **Ehsani M. Gao Y., G. S. and A., E.**
Modern Electric, Hybrid Electric, and Fuel Cell Vehicles
CRC Press 2010, pp. 120–136. ISBN: 0-8493-3154-4 (cit. on p. 14)

[45] **Schömann, J.**
Hybrid-electric Propulsion Systems for Small Unmanned Aircraft
Verlag Dr. Hut 2014. ISBN: 9783843918473. URL: https://books.google.es/books?id=idECrgEACAAJ (cit. on p. 15)

[46] **Kim, H. D., Berton, J. J., and Jones, S. M.**
"Low noise cruise efficient short take-off and landing transport vehicle study"
in: *Collection of Technical Papers - 6th AIAA Aviation Technology, Integration, and Operations Conference* 1.February (2006), pp. 362–372. DOI: 10.2514/6.2006-7738 (cit. on p. 18)

[47] **Insititute, T. C.-M.**
The 'Silent' Aircraft Initiative
Last accessed: 2022-09-01. URL: %7Bhttp://silentaircraft.org/%7D (cit. on p. 18)

[48] **Liu, Y., Dowling, A. P., Hileman, J. I., and Quayle, A. R.**
"Surface roughness noise prediction for silent aircraft experimental design SAX-40"
in: *46th AIAA Aerospace Sciences Meeting and Exhibit* January (2008). DOI: 10.2514/6.2008-45 (cit. on p. 18)

[49] **Siliang, D., Qijun, Z., and Bo, W.**
"Research on Distributed Jet Blowing Wing Based on the Principle of Fan-Wing Vortex-Induced Lift and Thrust"
in: *International Journal of Aerospace Engineering* 2019 (2019). ISSN: 16875974. DOI: 10.1155/2019/7561856 (cit. on p. 18)

[50] **Goeksel, B.**
"Novel Distributed Air-Breathing Plasma Jet Propulsion Concept for All-Electric High-Altitude Flying Wings"
in: April 2017, pp. 2016–2017 (cit. on p. 18)

[51] **Goharadani, A. S.**
Distributed Propulsion Technology
Nova Science Publishers 2014, pp. 173–1174 (cit. on p. 19)

[52] **Felder, J. L., Kim, H. D., and Brown, G. V.**
"Turboelectric distributed propulsion engine cycle analysis for hybrid-wing-body aircraft"
in: *47th AIAA Aerospace Sciences Meeting including the New Horizons Forum and Aerospace Exposition*. Orlando, Florida, USA 2009, pp. 1–25. ISBN: 9781563479694. DOI: 10.2514/6.2009-1132 (cit. on p. 19)

[53] **Clarke, S. and Redifer, S.**
"NASA ' s X -57 Maxwell All-Electric Aircraft"
in: 2020 (cit. on p. 19)

[54] **Kim, H. D., Perry, A. T., and Ansell, P. J.**
"A Review of Distributed Electric Propulsion Concepts for Air Vehicle Technology"
in: *2018 AIAA/IEEE Electric Aircraft Technologies Symposium, EATS 2018* (2018). DOI: 10.2514/6.2018-4998 (cit. on p. 19)

[55] **Smith, A. M. O. and Roberts, H. E.**
"The Jet Airplane Utilizing Boundary Layer Air for Propulsion"
in: *Journal of the Aeronautical Sciences* 14.2 (1947), pp. 97–109. DOI: 10.2514/8.1273 (cit. on p. 20)

[56] **Douglass, W. M.**
Propulsive Efficiency with Boundary Layer Ingestion
1970 (cit. on p. 20)

[57] **Uranga, A. et al.**
"Boundary layer ingestion benefit of the D8 transport aircraft"
in: *AIAA Journal* 55.11 (2017), pp. 3693–3708. ISSN: 00011452. DOI: 10.2514/1.J055755 (cit. on p. 20)

[58] **Uranga, A., Drela, M., Hall, D. K., and Greitzer, E. M.**
"Analysis of the aerodynamic benefit from boundary layer ingestion for transport aircraft"
in: *AIAA Journal* 56.11 (2018), pp. 4271–4281. ISSN: 00011452. DOI: 10.2514/1.J056781 (cit. on p. 20)

[59] **Hardin, L. W., Tillman, G., Sharma, O. P., Berton, J., and Arend, D. J.**
"Aircraft system study of boundary layer ingesting propulsion"
in: *48th AIAA/ASME/SAE/ASEE Joint Propulsion Conference and Exhibit 2012* December 2015 (2012). DOI: 10.2514/6.2012-3993 (cit. on p. 20)

[60] **Welstead, J. R. and Felder, J. L.**
"Conceptual design of a single-aisle turboelectric commercial transport with fuselage boundary layer ingestion"
in: *54th AIAA Aerospace Sciences Meeting* 0.January (2016), pp. 1–17. DOI: 10.2514/6.2016-1027 (cit. on p. 20)

[61] **Angelique, P.**
"Performance of a Boundary Layer Ingesting Propulsion System by Angelique Plas"
MA thesis 2006, p. 114 (cit. on p. 20)

[62] **Smith, L. H.**
"Wake ingestion propulsion benefit"
in: *Journal of Propulsion and Power* 9.1 (1993), pp. 74–82. ISSN: 07484658. DOI: 10.2514/3.11487 (cit. on pp. 21, 59)

[63] **Lv, P., Rao, A. G., Ragni, D., and Veldhuis, L.**
"Performance analysis of wake and boundary-layer ingestion for aircraft design"
in: *Journal of Aircraft* 53.5 (2016), pp. 1517–1526. ISSN: 15333868. DOI: 10.2514/1.C033395 (cit. on p. 21)

[64] **Sato, S.**
"The Power Balance Method For Aerodynamic Performance Assessment"
MA thesis 2012. ISBN: 978-1-4244-7992-4. DOI: 10.1109/ICIP.2010.5649226 (cit. on p. 21)

[65] **Drela, M. and Kohler, T. J.**
"Power balance in aerodynamic flows"
in: *AIAA Journal* 47.7 (2009), pp. 1761–1771. ISSN: 00011452. DOI: 10.2514/1.42409 (cit. on p. 22)

[66] **Drela, M.**
"Version Terms of Use Power Balance in Aerodynamic Flows"
in: *AIAA Journal* 47 (2009). ISSN: 1533-385X. DOI: http://dx.doi.org/10.2514/1.42409 (cit. on p. 22)

[67] **Meseguer, J. and Sanz, A.**
Aerodinámica básica
Universidad Politécnica de Madrid 2005. ISBN: 84-921113-8-0 (cit. on p. 22)

[68] **Hendricks, E. S.**
"A Review of Boundary Layer Ingestion Modeling Approaches for use in Conceptual Design"
in: July 2018 (2018). URL: http://www.sti.nasa.gov (cit. on p. 25)

[69] **John D. Anderson, J.**
Computational Fluid Dynamics: The Basics with Applications
McGraw-Hill 1995. ISBN: 0-07-113210-4 (cit. on p. 25)

[70] **Verstappen, R. and Veldman, A.**
"Direct Numerical Simulation of Turbulence at Lower Costs"
in: *Journal of Engineering Mathematics* 32 (Oct. 1997). DOI: 10.1023/A:1004255329158 (cit. on p. 25)

[71] **Spalart, P. and Allmaras, S.**
"A One-Equation Turbulence Model for Aerodynamic Flows"
in: *AIAA* 439 (Jan. 1992). DOI: 10.2514/6.1992-439 (cit. on p. 26)

[72] **Menter, F. R., Langtry, R., and Völker, S.**
"Transition Modelling for General Purpose CFD Codes"
in: *Flow, Turbulence and Combustion* 77.1-4 (2006), pp. 277–303. ISSN: 15731987. DOI: 10.1007/s10494-006-9047-1 (cit. on p. 26)

[73] **Rajagopalan, R. and Mathur, S. R.**
Three dimensional analysis of a rotor in forward flight
1989. DOI: 10.2514/6.1989-1815 (cit. on p. 27)

[74] **Lumley, J.**
"The structure of inhomogeneous turbulent flows."
in: *Atmospheric turbulence and radio wave propagation* (1967). DOI: 10.2514/1.C033395 (cit. on p. 28)

[75] **Torregrosa, A. J., Broatch, A., García-Tíscar, J., and Gomez-Soriano, J.**
"Modal decomposition of the unsteady flow field in compression-ignited combustion chambers"
in: *Combustion and Flame* 188 (2018), pp. 469–482. ISSN: 15562921. DOI: 10.1016/j.combustflame.2017.10.007. URL: https://doi.org/10.1016/j.combustflame.2017.10.007 (cit. on p. 28)

[76] **Zhu, Z., Midlam-Mohler, S., and Canova, M.**
"Development of physics-based three-way catalytic converter model for real-time distributed temperature prediction using proper orthogonal decomposition and collocation"
in: *International Journal of Engine Research* 22.3 (2021), pp. 873–889. ISSN: 20413149. DOI: 10.1177/1468087419876127 (cit. on p. 28)

[77] **Shen, L., Teh, K. Y., Ge, P., Zhao, F., and Hung, D. L.**
"Temporal evolution analysis of in-cylinder flow by means of proper orthogonal decomposition"
in: *International Journal of Engine Research* 22.5 (2021), pp. 1714–1730. ISSN: 20413149. DOI: 10.1177/1468087420917246 (cit. on p. 28)

[78] **Rulli, F., Fontanesi, S., D'Adamo, A., and Berni, F.**
"A critical review of flow field analysis methods involving proper orthogonal decomposition and quadruple proper orthogonal decomposition for internal combustion engines"
in: *International Journal of Engine Research* 22.1 (2021), pp. 222–242. ISSN: 20413149. DOI: 10.1177/1468087419836178 (cit. on p. 28)

[79] **Broatch, A., García-Tíscar, J., Roig, F., and Sharma, S.**
"Dynamic mode decomposition of the acoustic field in radial compressors"
in: *Aerospace Science and Technology* 90 (2019), pp. 388–400. ISSN: 12709638. DOI: 10.1016/j.ast.2019.05.015. URL: https://doi.org/10.1016/j.ast.2019.05.015 (cit. on p. 28)

[80] **Malouin, B., Trépanier, J. Y., and Gariépy, M.**
"Interpolation of transonic flows using a proper orthogonal decomposition method"
in: *International Journal of Aerospace Engineering* 2013 (2013). ISSN: 16875966. DOI: 10.1155/2013/928904 (cit. on p. 28)

[81] **Mifsud, M. J., MacManus, D. G., and Shaw, S. T.**
"A variable-fidelity aerodynamic model using proper orthogonal decomposition"
in: *International Journal for Numerical Methods in Fluids* 82.10 (2016), pp. 646–663. ISSN: 10970363. DOI: 10.1002/fld.4234 (cit. on p. 28)

[82] **Mifsud, M., Zimmermann, R., and Görtz, S.**
"Speeding-up the computation of high-lift aerodynamics using a residual-based reduced-order model"
in: *CEAS Aeronautical Journal* 6.1 (2015), pp. 3–16. ISSN: 18695590. DOI: 10.1007/s13272-014-0125-0 (cit. on p. 28)

[83] **Sayler, K.**
"A World of Proliferated Drones"
in: *Center for a New American Security* June (2015), p. 40
(cit. on p. 37)

[84] **España**
"Real Decreto 1036/2017"
in: *Boletín Oficial del Estado, BOE-A-2017-15721* (2017). ISSN: 0212-033X. URL: https://www.boe.es/eli/es/rd/2017/12/15/1036
(cit. on p. 37)

[85] **HELNARSKA, K., KRAWCZYK, J., and MOTRYCZ, G.**
"Legal regulations of UAVs in Poland and France"
in: *Scientific Journal of Silesian University of Technology. Series Transport* 101 (2018), pp. 89–97. ISSN: 02093324. DOI: 10.20858/sjsutst.2018.101.9
(cit. on p. 37)

[86] **EU Commission**
"On the rules and procedures for the operation of unmanned aircraft"
in: *Regulation (EU) 2019 / 947* 2019.March (2019). URL: https://skybrary.aero/sites/default/files/bookshelf/4667.pdf
(cit. on p. 38)

[87] **EU Commission**
"Commission delegated regulation 2019/945 on unmmaned aircraft systems and on third-country operators of unmanned aircraft systems"
in: *Regulation (EU) 2019 / 945* 2019.March (2019). URL: https://www.easa.europa.eu/en/document-library/regulations/commission-delegated-regulation-eu-2019945
(cit. on p. 38)

[88] **Alamouri, A., Lampert, A., and Gerke, M.**
"An exploratory investigation of UAS regulations in europe and the impact on effective use and economic potential"
in: *Drones* 5.3 (2021). ISSN: 2504446X. DOI: 10.3390/drones5030063
(cit. on p. 38)

[89] **UAV Factory USA LLC.**
Penguin C UAS
https://www.uavfactory.com. Last accessed: 2022-01-12
(cit. on p. 38)

[90] **AERTEC Solutions**
RPAS TARSIS 25
https://aertecsolutions.com/rpas/rpas-sistema-aereos-tripulados-remotamente/rpas-tarsis25/. Last accessed: 2022-01-12
(cit. on p. 38)

[91] **Lyon, C. A., Broeren, A. P., Giguere, P., Gopalarathnam, A., and Selig, M. S.**
Summary of Low-Speed Airfoil Data - Volume 3
vol. 3. Virginia Beach, VA, USA: SoarTech Publications 1997, p. 315. ISBN: 0964674718 (cit. on p. 38)

[92] **Schmidt, S. and Breuer, M.**
"Hybrid LES-URANS methodology for the prediction of non-equilibrium wall-bounded internal and external flows"
in: *Computers and Fluids* 96 (2014), pp. 226–252. ISSN: 00457930. DOI: 10.1016/j.compfluid.2014.03.020. URL: http://dx.doi.org/10.1016/j.compfluid.2014.03.020 (cit. on p. 39)

[93] **Hain, R., Kähler, C. J., and Radespiel, R.**
"Dynamics of laminar separation bubbles at low-Reynolds-number aerofoils"
in: *Journal of Fluid Mechanics* 630 (2009), pp. 129–153. ISSN: 00221120. DOI: 10.1017/S0022112009006661 (cit. on p. 39)

[94] **Burgmann, S., Dannemann, J., and Schröder, W.**
"Time-resolved and volumetric PIV measurements of a transitional separation bubble on an SD7003 airfoil"
in: *Experiments in Fluids* 44.4 (2008), pp. 609–622. ISSN: 07234864. DOI: 10.1007/s00348-007-0421-0 (cit. on p. 39)

[95] **Galbraith, M. and Visbal, M.**
"Implicit Large Eddy Simulation of Low-Reynolds-Number Transitional Flow Past the SD7003 Airfoil"
in: *40th Fluid Dynamics Conference and Exhibit* January (2010), pp. 1–17. DOI: 10.2514/6.2010-4737. URL: http://arc.aiaa.org/doi/10.2514/6.2010-4737 (cit. on p. 39)

[96] *XFLR5*
Last accessed: 2021-03-10. URL: %7Bhttp://www.xflr5.tech/xflr5.htm%7D (cit. on pp. 40, 64)

[97] **Drela, M.**
XFOIL Subsonic Airfoil Development System
Last accessed: 2021-03-10. URL: %7Bhttps://web.mit.edu/drela/Public/web/xfoil/%7D (cit. on pp. 40, 64)

[98] **Hoerner, S.**
Fluid-Dynamic Drag
Hoerner Fluid Dynamics 1965. ISBN: 9789991194448 (cit. on p. 40)

[99] **Niţă, M. and Scholz, D.**
"Estimating the Oswald Factor from Basic Aircraft Geometrical Parameters"
in: *Deutscher Luft- und Raumfahrtkongress*. Berlin, Germany: DGLR 2012 (cit. on p. 40)

[100] **Honda**
GX-35 Mini 4-stroke engine technical report
URL: https://www.honda-engines-eu.com/es/productos/motores/gx35 (cit. on p. 40)

[101] **Schoemann, J. and Hornung, M.**
"Modeling of hybrid-electric propulsion systems for small unmanned aerial vehicles"
in: *12th AIAA Aviation Technology, Integration and Operations (ATIO) Conference and 14th AIAA/ISSMO Multidisciplinary Analysis and Optimization Conference*. Indianapolis, Indiana, USA Sept. 2012, pp. 1–18. ISBN: 9781600869303. DOI: 10.2514/6.2012-5610 (cit. on p. 40)

[102] **David Willermark, F. D.**
GT-power simulation report
Last accessed: 2021-03-10 2009. URL: http://www.chalmersverateam.se/Rapporter/GTPowerGX35.pdf (cit. on p. 40)

[103] **Deters, R. W., Ananda, G. K., and Selig, M. S.**
"Reynolds number effects on the performance of small-scale propellers"
in: *32nd AIAA Applied Aerodynamics Conference*. Atlanta, Georgia, USA June 2014, pp. 1–43. ISBN: 9781624102882. DOI: 10.2514/6.2014-2151 (cit. on pp. 40, 41, 66, 68)

[104] **Nygren, K. P. and Schulz, R. R.**
"Breguet's formulas for aircraft range endurance an application of integral calculus"
in: *ASEE Annual Conference Proceedings* (1996), pp. 651–655. ISSN: 01901052 (cit. on p. 45)

[105] **Atinault, O., Carrier, G., Grenon, R., Verbecke, C., and Viscat, P.**
"Numerical and experimental aerodynamic investigations of boundary layer ingestion for improving propulsion efficiency of future air transport"
in: *31st AIAA Applied Aerodynamics Conference* (2013), pp. 1–13. DOI: 10.2514/6.2013-2406 (cit. on p. 45)

[106] **McKay, M. D., Beckman, R. J., and Conover, W. J.**
"A comparison of three methods for selecting values of input variables in the analysis of output from a computer code"

in: *Technometrics* 42.1 (2000), pp. 55–61. ISSN: 15372723. DOI: 10.1080/00401706.2000.10485979 (cit. on p. 61)

[107] *Simcenter STAR-CCM+ Documentation*
Siemens 2019 (cit. on p. 61)

[108] **Blumenthal, B. T., Elmiligui, A. A., Geiselhart, K. A., Campbell, R. L., Maughmer, M. D., and Schmitz, S.**
"Computational investigation of a boundary-layer-ingestion propulsion system"
in: *Journal of Aircraft* 55.3 (2018), pp. 1141–1153. ISSN: 00218669. DOI: 10.2514/1.C034454 (cit. on p. 61)

[109] **Anderson, J. D.**
Fundamentals of Aerodynamics (6th edition)
vol. 1984. 3 2011, p. 1128. ISBN: 9780071289085 (cit. on pp. 61, 71)

[110] **P. L. Roe**
"Approximate Riemann Solvers, Parameter Vectors, and Difference Schemes"
in: *Journal of Computational Physics* 43 (1981), pp. 357–372. DOI: 10.1016/0021-9991(81)90128-5 (cit. on p. 61)

[111] **Gur, O. and Rosen, A.**
"Comparison between blade-element models of propellers"
in: *Aeronautical Journal* 112.1138 (2008), pp. 689–704. ISSN: 00019240. DOI: 10.1017/S0001924000002669 (cit. on p. 64)

[112] **APC**
"APC Propeller RPM Limits"
in: *APC website* 95776.530 (2016), p. 95776. URL: https://www.apcprop.com/technical-information/rpm-limits/ (cit. on p. 65)

[113] **Oberkampf, W. L. and Trucano, T. G.**
"Verification and validation in computational fluid dynamics"
in: *Progress in Aerospace Sciences* 38 (2002), pp. 209–272. DOI: 10.1201/b19031-50 (cit. on p. 65)

[114] **Celik, I. B., Ghia, U., Roache, P. J., Freitas, C. J., Coleman, H., and Raad, P. E.**
"Procedure for estimation and reporting of uncertainty due to discretization in CFD applications"
in: *Journal of Fluids Engineering, Transactions of the ASME* 130.7 (2008), pp. 0780011–0780014. ISSN: 00982202. DOI: 10.1115/1.2960953 (cit. on p. 66)

[115] **Selig, Donovan, and Fraser**
Airfoils at Low Speeds
Virginia Beach, VA, USA: H.A. Stokey 1989, pp. 1–408 (cit. on p. 66)

[116] **Deters, R. W.**
Performance and Slipstream Characteristics of Small-scale propellers at low Reynolds Numbers
2014 (cit. on p. 66)

[117] **Tibshirani, R.**
"Regression Shrinkage and Selection via the Lasso"
in: *Journal of the Royal Statistical Society. Series B (Methodological)* 58.1 (1996), pp. 267–288. ISSN: 00359246. URL: http://www.jstor.org/stable/2346178 (visited on 10/17/2022) (cit. on p. 74)

[118] **Ananda, G. K., Sukumar, P. P., and Selig, M. S.**
"Measured aerodynamic characteristics of wings at low Reynolds numbers"
in: *Aerospace Science and Technology* 42 (2015), pp. 392–406. ISSN: 12709638. DOI: 10.1016/j.ast.2014.11.016 (cit. on p. 102)

[119] **Sutton, D. M.**
"Experimental Characterization of the Effects of Freestream Turbulence Intensity on the SD7003 Airfoil at Low Reynolds Numbers"
MA thesis. Univeristy of Toronto 2015 (cit. on p. 102)

[120] **Byrd, R. H., Gilbert, J. C., and Nocedal, J.**
"A trust region method based on interior point techniques for nonlinear programming"
in: *Mathematical Programming, Series B* 89.1 (2000), pp. 149–185. ISSN: 00255610. DOI: 10.1007/PL00011391 (cit. on p. 156)